Development of a test of Newton's law of gravitation at micrometer distances using a superconducting spherical torsion balance

by

Emanuele Rocco

A thesis submitted to
The University of Birmingham
for the degree of
Doctor of Philosophy

Centre for Space and Gravity Research
School of Physics and Astronomy
The University of Birmingham
May 2008

Abstract

To solve the theoretical problems associated with quantum gravity and the unification with the other forces, many theories have been proposed such as string theory, which predict violations of the inverse square law of gravity (ISL) at sub-millimetre distances. To search for such experimental signatures we developed a magnetically levitated cryogenic torsion balance, the SSTB, and a set of masses with modulated mass density across their surfaces. The lateral force has to be measured as one mass is moved in front of the other with a micropositioner without any electrostatic shield interposed between them. The expected Newtonian and electromagnetic forces have been studied to optimise the design of the masses. The torque sensitivity of the SSTB has been modelled, including the servo loop controlling the float rotation and the effect of the seismic noise. The performances at $4.2K$ of the SSTB are discussed, from the effective damping of its parasitic modes to its tunable natural stiffness, and a torque sensitivity of $2 \times 10^{-10} Nm/\sqrt{Hz}$ at $30mHz$ has been measured. This noise limit is most probably due to coupling with ground tilt. Two tests with the manufactured prototypes of the masses have been performed. During the first test a torque due to electrostatic and magnetic forces of $8.4 \times 10^{-11} \pm 1.5 \times 10^{-11} Nm$ has been measured at a mass spacing of $42 \pm 14 \mu m$ at the spatial periodicity of the density modulation. During the second test by covering both masses with a $1 \mu m$ gold layer the detected signal was reduced to $1.91 \times 10^{-11} \pm 4.7 \times 10^{-12} Nm$ at a spacing of $30 \pm 10 \mu m$. To look for new violations of the ISL of gravity the torque sensitivity of the SSTB has to be further improved.

To Andrea.
My better half

Acknowledgements

Firstly I have to thank my supervisor, Prof. Clive C. Speake, for giving me the opportunity to join the group and work on this challenging project of experimental gravity. His extensive knowledge and flow of ideas were, for me, a constant inspiration and opportunity to learn. Secondly, I must thank Dr. Giles D. Hammond, who had been working on the study and development of the torsion balance for few years already before I joined the group. His work was essential to the success of the experiment. I have to thank him also as a friend and mentor, for his great patience during these years, while we taught me almost everything I now know about experimental physics.

The results presented in this thesis about the SSTB and the first tests of the ISL of gravity at micrometer distances are due to a very intensive team work, which made possible the experiment and which I am proud to be part of. Within this thesis the following nomenclature will be used: "*we*" will refer to the work which has been done in collaboration with my colleagues within the gravitational group of the University of Birmingham; "*I*" will refer to all the work of which I am solely the author or of which I am the principal investigator.

I worked in strict collaboration with Dr. Hammond and Dr. Matthews during all the phases of the assembly and preparation of the experimental chamber containing the SSTB, of which I was, in particular, in charge of all the wiring, all the temperature sensors and heaters, the capacitive transducer and the setting up of the float with the test masses. I helped Dr. Hammond to build the magnetic actuator circuit of the SSTB and, in parallel (to check for consistency), we created its analytical model. I also helped Dr. Matthews with the polishing and final assembly of test mass B. I characterised the metrology of all the test masses with the CMM. With Dr. Hammond and Dr. Matthews, I performed all the low temperature runs to characterize the performances of the SSTB and to conduct the first ISL tests of gravity.

I took the lead of the study and development of most of all the analytical models describing the expected forces, which are acting between the masses. I developed the model of the Newtonian forces and I took charge of optimising the

design of the test masses. I also designed and optimised the copper support of the mass C, according to the gravitational force acting between the masses and their supports. Inspired on an early work of Dr. Matthew, I created the model of the electrostatic forces due to surface corrugations and included the effect of the presence of contact potentials on one or on both masses. I also modelled the Casimir forces acting between the masses at short distances. Starting from an early work of Prof. Speake, I developed and debugged the numerical model of the possible Yukawa forces acting between our masses. I used such model to further optimise the geometry of the test masses. I developed the theoretical model to set up the upper limits on the parameters describing the Yukawa type forces given by the experimental results.

I independently developed the analytical model describing the 3D dynamics of the SSTB, which predicts the coupling between the seismic noise and the torque acting on the float and the effect of the tilt noise on the torque sensitivity of the SSTB. I modelled and measured the transfer functions and noise sources for all the subsystems of the SSTB, and I predicted the closed loop transfer function of the instrument and its expected torque sensitivity.

I performed all the data analysis of the experiments on the performances of the SSTB and of the first ISL tests of gravity. I analysed all the results of the ISL tests of gravity and compared them with the developed theoretical models of the expected forces.

I have to greatly thanks Dr. Hammond for the development and manufacture of the SSTB and, in particular, of the levitation and damper circuit and of the capacitive bridge of the measurement mode. I also own many thanks to Dr. Peña-Arrellano for the development of the capacitive bridge of the calibration mode and Prof. Speake for the model of the para-diamagnetic forces acting between our masses. I have to thank Dr. Matthews for the polishing and gold coating of the test masses A and C, for the implementation of the current source, the HP Vee servo compensator and the custom electronics controlling the SSTB. Many thanks go also to Mr. Matthew Stiff for his work on the electronics during the early stages of our experiment.

This work would have not been possible without the inspiring discussions I had with Prof. Speake, whom I have to specially thank for his very useful comments on my models of the float dynamics and of the expected forces acting between the masses and on the interpretation on the ISL results.

I would further like to acknowledge the work done at the Millimiter Wave group at Rutherford Appleton Laboratory, where under the supervision of Dr. P. G. Huggard our test masses have been manufactured. Thanks also goes to Plansee Metals, Austria, for the manufacture of the niobium float. I am greatly thankful to Dr. Chris Eyles for letting me use the coordinate measurement machine to characterise the topographies of the test masses. None of the hardware for the experiment would exist without the work done by the technical support staff of the University. I want to thank the staff in the main mechanical workshop under the supervision of Steeve Brookes. Special thanks must also go to Tony Barnes who taught me how to use some of the tools by myself. I like to thank the staff of the condensed matter workshop who helped with cryogenics and the vacuum testing of the torsion balance: Gary Walsh, Michael Parkes and Dave Brester.

My gratitude also goes to Mr. Walter Del Pozzo, Mr. Antonio Perreca and Dr. Ludovico Carbone for their friendship and for the fruitful discussions, which had while I have been working alongside them. Many thanks go to Dr. Alberto Sesana for suggesting me the best location where to write up this PhD thesis. I am also very grateful to Mrs. Norma A Simpson for her help with all the University bureaucracy during all these years and to Dr. Ray Jones for his helpful advice during the first year of my PhD.

Most of the costs of my PhD work have been financed by my parents, Laura and Luigi Rocco, whom I sincerely thanks. I have also to thank the School of Physics for its much-appreciated financial help during the most difficult years of my PhD. I am especially thankful to some of my friends, now family, who, in many ways, help me during the difficult period of the writing up: Rosaria Simoniello, Marco Tucci, Puvan Tharmanathan, Maria Jose Mato. Thanks also to my friend Claire Boydell for proofreading this thesis and helping me to improve its English.

Finally I do not have the words to thanks all the Saiani - Andrea, Daniela and Loris - who gave me a home and who, with great patience, supported me along the long way. Thanks.

Contents

List of Figures

List of Tables

Chapter 1

Testing gravity at micrometre distances: motivations and current results

1.1 Introduction

In this PhD thesis I will discuss a test of the inverse square law (ISL) of gravity at micrometre distances that we are developing at the School of Physics and Astronomy of the University of Birmingham. The gravitational law of Newton was discovered more than three hundreds years ago, however it has no experimental proofs for distances between masses, which are shorter than a fraction of a millimetre. This lack of evidence is due to the extreme weakness of gravity with respect to the other known forces, such as, for example, the electrostatic or the magnetic force. In recent years experimental efforts to test Newton's law at sub-millimetre distances have increased worldwide, because of the opportunity they offer to verify possible experimental signatures of proposed theories of quantum gravity. In the last few years many theoretical works, which are mainly, but not exclusively, related to string theory, have indicated that the gravitational interaction does not follow the $1/r^2$ law at distances as large as tens of microns. Such violations are accessible by present table-top experiments.

During the last few years at the University of Birmingham, motivated by these theoretical interests, we have been developing a novel test of Newton's law of gravity at micrometre distances. Our experiment uses a spherical superconducting torsion balance, the SSTB, which has been developed by our group and

which is currently in its second version (MKII), to measure the lateral forces between two test masses. Our masses have mass density modulations across their surfaces as source of the gravitational signal. Our test of the ISL of gravity will, we think, let us explore many of the hypothesised violations of Newton's law within the next few years.

This chapter is divided into three sections: the first section is a review of all the theoretical motivations which have been the catalyst for this particular field of research field. The second section is a review of all past, current and possible future experimental tests of the Newtonian law at sub-millimetre distances including our table-top experiment. The third section presents a synopsis of this PhD thesis.

1.2 Theoretical motivations

In the following section I will present the theoretical framework which has motivated renewed interest in the experimental search for violations of the ISL of gravity at micrometre distances. I will start with a brief historical introduction of the gravitational force, beginning with Kepler and ending with Einstein's theory of General Relativity. I will also discuss the open problems of gravity, which are related to the lack of a complete quantum theory of the gravitational force. I will discuss the possible experimental signatures associated with the violation of the ISL of gravity at sub-millimetre distances, which might prove or constrain possible approaches to quantum gravity. Such signatures of quantum gravity will be accessible by the next generation of table-top experiments testing the ISL of gravity at micrometre distances.

1.2.1 Brief history of gravity

I will begin the history of classical gravity with the astronomical observations of planetary orbits, which were carefully documented by the Danish astronomer Tycho Brahe (1546-1601). These observations were used by the German mathematician and astronomer Johannes Kepler (1571-1630) to establish his three famous eponymous laws modelling the planetary motions. Kepler stepped away from the Ptolemaic conception that nature should be described by perfect geometries, as circles, and modelled the motions of the planets as ellipses with the

Sun at one of the foci. In the same period Galileo Galilei (1564-1642) studied the effect of gravity on bodies on Earth and established that their acceleration in free fall is independent of their mass. Galileo also defined the first principle of relativity, by stating that the laws of physics are unchanged in any system which is moving at any constant speed and in any directions. The British physicist Sir Isaac Newton (1643-1727) in his 1687 treatise "Philosophiæ Naturalis Principia Mathematica" presented his three laws of motions, which explained and extended Galileo's observations about the motion of objects on Earth, and the universal law of gravitation. The Newtonian law of gravity explained Kepler laws of the planetary orbits in terms of an attractive force which is inversely proportional to the square of the distance between the planets. By stating that the motion of the objects on Earth and the motion of the planets are governed by the same physical laws, Newton made the first unification in the history of physics. For more than 300 years Newton's law of gravitation stood unchallenged, successfully explaining the motion of the known planets and even predicting the existence of two new ones, Neptune and Pluto. However small inconsistencies between the theory and the observations remained unexplained. For example, Newtonian gravity was not able to fully model the precession of the perihelion of Mercury, which was 43 *sec* per century larger than expected. At the beginning of the 20^{th} century, the gravitation theory was revolutionised by the work of the German physicist Albert Einstein (1879-1955), who was not satisfied by the tacitly supposed instantaneous action at a distance of gravity. In 1905 Einstein extended the principle of Galilean or Newton's relativity to all the physical laws including electromagnetism, accordingly modifying the laws of mechanics and the concept of space-time to satisfy a new additional principle that the speed of light is constant and the same when measured by any inertial observer. In 1915-1916, with his theory of General Relativity, Einstein stated that the acceleration due to the gravitational force is locally equivalent to the effect of an accelerated reference frame. Einstein remodelled the gravitational field as the consequence of the local curvature of the space-time geometry which is deformed by the presence of mass-energy distribution. The new theory of gravity not only successfully explained the precession of the Mercury orbit but also predicted new effects, which were verified during the following years. First, the deflection of light due to the Sun, which was predicted by General Relativity, was verified by Eddington and coworkers in 1919 during a solar eclipse. Then the time delay of light due to the presence of the

gravitational field, which was predicted by Shapiro in 1964, was verified by radar measurements in the following years. Many more tests of GR followed (see [91] for a review) of which perhaps the most famous is the study of the binary pulsar B1913+16 by Joseph Taylor and Russell Hulse, in 1974, where the effect of the possible emission of gravitational waves was first observed.

The history of gravity however was not, and is not, over yet, because as I will discuss, fundamental experimental and theoretical issues are still not understood or explained within GR. It is possible that a new thought revolution, like those of Kepler, Galilei, Newton or Einstein is still to come.

1.2.2 Problems with gravity

The problems with GR arose as soon as physicists started to compare its prediction with the ones derived from the Standard Model of particle physics, which describes all the forces apart from gravity and all the particles within a quantum field theory. For example, GR predicts black hole singularities which are forbidden by the fundamental principles of quantum mechanics, such as the Heisenberg uncertainty principle. As we will see, there are also other open issues, which are all related to the fact that, despite the formidable efforts of several generations of physicists, there is not yet a quantum theory of gravity which is theoretically complete and experimentally verified.

The small cosmological constant and dark energy

General Relativity has faced significant problems since its advent when it was first used to predict the evolution of the Universe. The solution of GR predicted a dynamic universe, which was in contrast with the conception of a static universe, current at that time. This dynamic solution forced Einstein to introduce an additional free parameter into his equations, called the cosmological constant, which theoretically lead to the conception of a static universe. However after the discovery of the redshift of distant galaxies by Slipher (see [89] for review) and the formulation of the Hubble law describing an expanding universe, the cosmological constant was quickly dropped from Einstein equations. Quantum field theory suggested that would instead be necessary to include a cosmological constant. This cosmological constant has to be associated with the energy density of the quantum vacuum, which would theoretically not be empty anymore and which

would give origin to other experimentally verified effects such as the Casimir force. Unfortunately the predicted vacuum energy density is extremely high, $\rho_{vac} \approx 10^{92} g/cm^3$ [15]. From the simple cosmological constraints given by the Hubble expansion, the experimental upper bound on the vacuum energy density is $|\rho_{vac}| \lesssim 10^{-29} g/cm^3$ [89], which is approximately 10^{120} smaller than the theoretical value. Because it is possible to model the cosmological constant as three terms [16] (a bare cosmological constant added to the metric tensor in the GR action, a cosmological constant given by a dynamic scalar field and a cosmological constant given by the zero point fluctuations of the quantum fields), it was thought that in some way the total cosmological constant might be exactly balanced and equal to zero. The puzzle has become much more intricate during the last ten years because of the growing experimental evidence of a non-null cosmological constant. In 1998 the observation of the redshift of Type I supernovae [64][63] showed that the universe is going through an accelerated expansion. This expansion was attributed to a new repulsive form of energy, which was christened dark energy and which constitutes approximately 76% of the total mass of the universe. Dark energy was immediately associated with a non-null cosmological constant. The energy density of this reborn cosmological constant is $\approx 8 \times 10^{-30} g/cm^3$ [93], which is extremely small and still unexplained by the quantum field theory. Additional independent evidence of a non null cosmological constant was found in the following years through the study of the cosmic microwave background by WMAP [10][80][79], which confirmed the supernovae results. (for a review see [16] and [68]).

The hierarchy problem

Another theoretical problem which afflicts gravity, is that of the hierarchy problem: we do not understand why gravity is so much weaker than all the other known forces or equivalently why two of the fundamental energy scales in nature, the electroweak scale and the Planck scale, are so different. The electroweak scale is $m_{EW} \approx 250 GeV\ /c^2$ [93], while the Planck scale $m_{Pl} = \sqrt{\hbar c/G} = 2.43 \times 10^{18} GeV/c^2$. To try to understand the reasons for the small ratio m_{EW}/m_{Pl} is one of the open questions of contemporary physics.

The renormalisation problem

It is also well know that General Relativity is a non-renormalizable theory. This means that, if we try to quantise it as we do for the electromagnetic field, we can not reformulate the theory in such a way that all the divergent integrals associated with the exchange of multi virtual particles become finite and calculable [3]. We do not have, therefore, a consistent way to quantify gravity within the usual framework of the quantum field theory.

The problem of quantum gravity

For many years a large amount of work has been undertaken worldwide to develop a quantum theory of gravity and to unify the gravitational interaction with the Standard Model of particle physics. Many different theoretical approaches have been followed in these years, of which we should at least mention the string/superstring/M theory and loop quantum gravity. In simple terms string theories substitute point-like particles with strings, which vibrate in space-time with added extra dimensions giving origin to the observed particles and naturally reproducing gravity (see [70] for an introduction). A principal feature of string theories is that there are not only the 3+1 dimensions of the Standard Model and General Relativity, but many more (now up to a total of 11, including the known ones). These extra dimensions have not yet been observed, because they are generally thought to be closed on themselves with dimensions near the Plank length. The idea of extra dimensions is not new in physics. In 1921, Kaluza-Klein in their attempt to unify electromagnetism with General Relativity, had already added a fifth extra dimension to space-time. Extra dimensions might have some possible experimental signatures which could be tested by future table-top experiments or by upcoming particle accelerators [27].

In the attempt to merge General Relativity with Quantum Mechanics, loop quantum gravity tries instead to quantise space-time itself by using the technique of loop quantisation [67].

However all these attempts to quantise the gravitational field have one feature in common one feature: the lack of any experimental evidence confirming their validity. On the one hand all these theories are still being developed and are only recently at the stage of predicting experimental signatures. On the other hand any experimental test of the gravitational force is extremely difficult because of

the extreme weakness of this force with respect to all the other known forces. As we will see, there has especially recently been high expectation that some of these signatures of quantum gravity scenarios will be experimentally tested in the near future.

1.2.3 Possible violations of Newton's law at small distances

Many theoretical solutions to the previous issues, which are mainly, but not exclusively, associated with the string theory, predict violations of the inverse square law of gravity at submillimetre distances (for a detailed review see [1] and [25]). Even if these possible deviations can take many different analytical forms, in this preliminary study we will adopt only the most common and standard parametrisation. The model, which is used to compare the theoretical predictions with experimental results, is a Yukawa type potential, which at the distance r from a source mass m is given by the equation:

$$V(r) = -\frac{Gm}{r}(1 + \alpha e^{-r/\lambda}) \tag{1.1}$$

G is the gravitational constant measured at infinite distance. α and λ are respectively the strength and the range of the force violating the inverse square law of Newton. The constraints on the possible couples (α, λ) can be plotted in a figure as fig.1.1, where the grey upper area is the experimentally excluded area of the parameter space. I will here review the expected violations of the ISL of gravity presented in fig.1.1, while in the next section I will describe the experimental efforts, present and future, to constrain these theoretical expectations.

Compactified Large Extra Dimensions

To solve the hierarchy problem Arkani-Hamed et al. [6][7] proposed that there are in reality not two different energy scales, the Planck and the electroweak scales, but just one: the electroweak one in a higher dimensional space-time. Their motivations reside in the fact that, while electroweak interactions have been probed almost at the distance associated to the electroweak scale, $l_{EW} \approx 10^{-18}m$, we have no experimental evidence that gravity exists and follows the Newtonian law at distances smaller than a fraction of a mm. The Planck scale was derived

by assuming that gravity is unchanged down to distances comparable with the Planck length of $10^{-35}m$ and which are more than 30 orders of magnitude smaller than any experimental evidence of the gravitational interaction. Arkani-Hamed et al. assumed that there are n extra dimensions compactified on a torus of radius R. The new Planck scale within these $4+n$ dimensions, $M_{Pl(4+n)}$, is assumed to be equal to the string electroweak scale, $M^* \approx 1TeV/c^2$ [54][1] and is related to the usual Planck scale in the 4 dimensions by the equation:

$$M_{Pl}^2 \simeq M_{Pl(4+n)}^{2+n} \cdot R^n \tag{1.2}$$

In this scenario, the gravitation potential at distances which are comparable with the radius R takes the form of a Yukawa potential with $\alpha = 8n/3$ and $\lambda = R$ [1]. The radius R of n equal compact dimensions, for $n = 1$, is $\approx 10^{12}m$, which had already been excluded by the observations within the solar system. For $n = 2$ R is expected to be $\approx 100\mu m$, which had been ruled out by recent table-top experiments [40] and by astrophysical bounds [37]. For $n > 2$ there is no experimental evidence excluding or confirming the existence of such extra dimensions. However if the compactification is not on a torus but on other geometries, as for example spheres [44], or if the compactifications are not the same among all the different extra dimensions [25] we might expect different (α, λ) values for $n = 2$, which had not yet been excluded by any experiments. Burgess [14] recently presented another scenario with Supersymmetric Large Extra Dimensions (SLED) with a radius of $\approx 10\mu m$, which, within a supersymmetric field theory, allows for a small cosmological constant and which predicts possible violations of the ISL of gravity at micrometre distances.

String moduli

Superstring theory also predicts the existence of scalar particles, called moduli, which describe the size and the shape of all the compact extra dimensions [4]. The masses of these moduli are acquired when the supersymmetry is broken, in which case it is supposed that their masses depend on the scale M^* at which supersymmetry breaking occurs. Some moduli might couple differently with Up and Down quarks, leading to a microscopic force, which would depend on the atomic number of the atoms of the masses, and which violates the Equivalence Principle. In the case of a measured violation of the ISL of gravity, it is possible

to check the dependency of the signal on the atom species of the masses and to discriminate some of these signals from the ones due, for example, to extra dimensions [1]. Different kind of moduli have been postulated:

Radius modulus: this modulus is a low mass spin-0 field, which stabilises the volume of the extra dimensions and fixes their radius. The radius moduli exchange produces a force with Yukawa potential, which is characterized by strength [40]:

$$\alpha = \frac{n}{n+2} \tag{1.3}$$

with n the number of extra dimensions. The range of the interaction is given by:

$$\lambda \approx 2.4 \left[\frac{1TeV}{M_* c^2}\right] mm \tag{1.4}$$

From equation 1.4 it is clear that the force due to the radius exchange does not diminish as the number of new dimensions increases, which instead occurs with the Yukawa potential associated to extra dimensions [1].

Gluon modulus: as the name indicates, the gluon modulus is related to the possible coupling of the moduli field with the gluons of the Standard Model [24]. The expected strength and ranges of the deviations from the ISL of gravity due to the gluon modulus have been recently updated by Dimopoulos and Geraci [25] as plotted in fig.1.1.

Strange modulus: this modulus is responsible for the possible coupling of the modulus field with the strange quarks [24]. Its strength is expected to be always stronger than gravity as plotted in fig.1.1.

Dilaton: string theory also predicts another scalar field, the Dilaton, whose coupling strength, α, is between unity and few thousand as shown in fig.1.1[25].

Fat graviton and vacuum energy scenarios

According to Sundrum [82] one possible solution of the cosmological problem is that the graviton is a "fat" particle which means that it is not a point like particle but has finite size l_{grav}. Sundrum predicted that such a graviton will be insensitive to all the quantum vacuum physics happening at scales smaller than its own size, effectively reducing the theoretical cosmological constant. Assuming that the observed energy density associated with the cosmological constant is given by the usual power counting [15] and limited in this scenario by the graviton

size, Sundrum found that l_{grav} had to be bigger than $20\mu m$. Because in this model the Newtonian force also becomes weaker at distances smaller than l_{grav}, it was recently possible to experimentally set an upper limit on the size of the "fat" graviton as $l_{grav} \leq 98\mu m$ [2]. This scenario can be explored by future experiments. According to Beane [8] there is also another mechanism, which might possibly solve the cosmological problem. The experimental result of the smallness of the vacuum energy might be due to the existence of a new quanta, which has not yet been experimentally found and which, at distances smaller than its Compton wavelength, might prevent gravitational and electromagnetic vacuum fluctuations. Beane shows that this new field is associated with a Yukawa type deviation from the ISL of gravity with $\alpha \approx 1$ and λ between $50\mu m$ and $120\mu m$. Again the experimental results from [43] strongly constrain this scenario to $\lambda < 56\mu m$ with 95% of confidence level.

To explain the smallness of the cosmological constant, Mota and Shaw [59] predicted the existence of a new scalar field, the Chameleon, which is highly non-linear and which acquires mass by interacting with matter. This field might mimic a violation of the ISL at short distances, but its detection may have been missed up till now because the electrostatic shield used during most ISL tests might have possibly shielded the Chameleon field too.

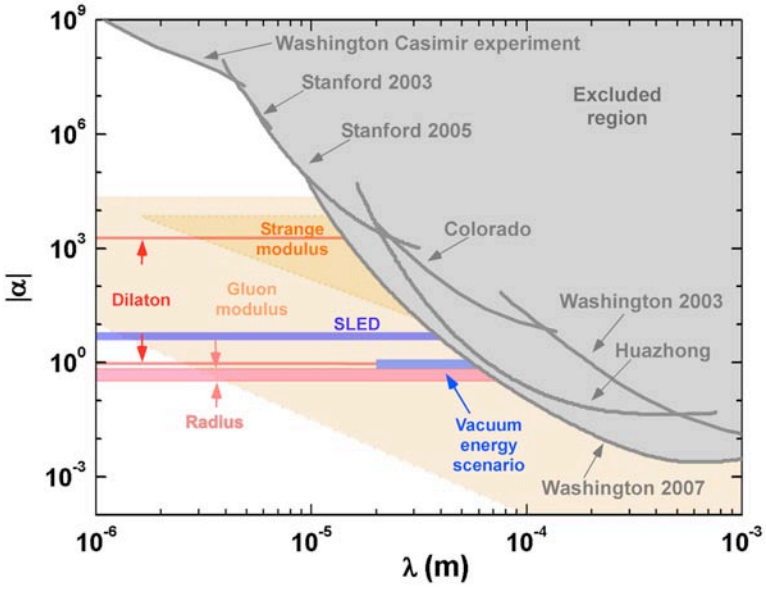

Figure 1.1: Expected violations on the ISL of gravity and current experimental upper limits at 95% confidence level.

1.3 Experimental investigations

Up to now the most stringent constraints on possible Yukawa type deviations from the ISL of gravity are given by astronomical tests for ranges of $10^{12}m$, which are approximately the size of the solar system (see fig.1.2, source [1]). The best constraints down to strengths of $\alpha \approx 10^{-10}$ are given by the Lunar Laser Ranging (LLR), which monitors the Moon orbit by using a laser source on Earth and a few photoreflectors positioned on the Moon surface. At distances smaller than a fraction of a mm we did not have any proof of the existence of Newtonian gravity until a few years ago. Motivated by the reviewed theoretical issues and by an interest in exploring gravity at small distances, a number of experiments have recently been successfully completed and many more are currently planned to test the ISL of gravity at distances between a fraction of a millimetre and a few micrometres.

In the following sections I will review all these experiments, introducing the problems, which make them so difficult to realise, and presenting the solutions they adopted. I will briefly introduce our experimental approach, which I will discuss in detail in the next few chapters.

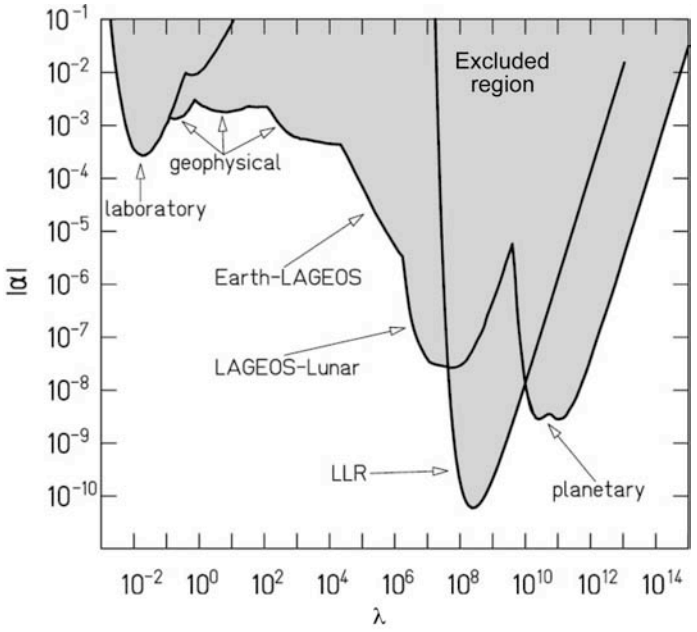

Figure 1.2: Current constraints on Yukawa type violations of the ISL at large distances (source [1]).

1.3.1 Experimental problems

As mentioned previously, we did not have any experimental proof of the existence of the Newtonian gravity at distances, which were smaller than a fraction of a millimetre until a few years ago. This lack of experimental results both was and is due to the extreme weakness of the gravitational interaction, which strongly decreases with the distance and the mass involved in the experimental tests. For example, for two spheres of radius r at a distance proportional to r, the gravitational force acting between them scales as r^4. As we will see in detail in chapter 3, the expected gravitational force is usually weaker than the electrostatic or magnetic forces. At very short distances, less than few microns, it is even weaker than the Casimir force, which is associated with the zero-point vacuum fluctuation of the electromagnetic field.

All the experiments that I will review are in some way designed to minimise these spurious forces. Some of them are also designed to minimise the gravitational force (they are called null experiments) but not to cancel out possible deviations from the ISL of gravity. To minimise the ratio between the expected Newtonian and Yukawa forces (assumed with unit strength), many experiments adopt a planar geometry for their test masses. They therefore reduce as much as possible the thickness of the masses involved in the gravitational interaction. To reduce the effect of the electrostatic forces, all the experiments - which are specifically designed to test the ISL of gravity - interpose an electrostatic shield (a few tens of microns thick) between the masses. This approach, even if successful, strongly limits the minimum achievable distance between the masses and possibly might also shield the expected signals due to the Chameleon fields. Only the Casimir tests, which indirectly derive the results on the violations of the ISL of gravity from Casimir measurements, do not use such shields. All the force measurements are ultimately limited by thermal noise. The power spectrum of thermal noise is inversely proportional to the quality factor Q of the oscillator, which is used for the force measurements, and is directly proportional to the temperature T. Therefore to reduce such thermal noise, the experiments are located inside high vacuum chambers and some of them are cooled down to a few Kelvin.

Micromechanical oscillators with high quality factor had been lately extensively adopted to test the ISL of gravity at micrometre distances and to measure the Casimir forces. Because these oscillators cannot sustain heavy masses, the

strongest constraints on the Yukawa type violations of Newton's law are still given by the experiments, which are based on torsion balances. To increase their sensitivity the torsion balances have in general a very small torsional elastic constant and their torque measurements are usually made at very low frequencies. During these experiments particular care should be taken to isolate the measurements from the low frequency seismic noise, the $1/f$ noise of the electronics and any possible low frequency drift of the ambient parameters, such as the temperature, which may influence the results.

1.3.2 Past experiments

I will present here the experiments which have set the most stringent upper limits on the possible Yukawa type violations of the ISL of gravity in the last few years. I will discuss the technical solutions they adopted to solve the difficulties I mentioned above, and which are associated with testing gravity at sub millimetre distances. I will introduce also a new complementary experimental approach, which is based on condensed atoms and optical lattices. Theses new techniques have very recently been developed to measure weak forces at short distance and might also be used to test Newton's law at micrometre distances.

Casimir force measurements with a torsion balance at the University of Washington

The best upper limits on the Yukawa forces, with ranges between $0.6\mu m$ and $4.2\mu m$, are given by the work of Lamoreaux at the University of Washington [47]. He measured the Casimir force between a spherical lens and a plane by using a torsion balance, which was kept at room temperature and under vacuum. Both masses were made of quartz and coated with a double layer of Copper and Gold. During the torque measurements the masses were positioned at a relative distance between $0.6\mu m$ and $12.3\mu m$. The position of the torsion balance was controlled by using a feedback system, which applied a voltage difference between two compensator plates fixed to the vacuum can and to the pendulum (see fig.1.3). The force between the masses was measured by recording the servo effort, which was necessary to keep the torsion balance at a fixed angular position as a function of the distance between the masses. The force sensitivity of the torsion balance was approximately $2.6 \times 10^{-11} N/\sqrt{Hz}$ and only limited by its thermal noise. Be-

cause no electrostatic shield was set between the masses, the measured dominant force was the electrostatic one, which was fitted to an analytical model at large distances and subtracted from the original data. Lamoureaux [47] found that the resulting force was in good agreement within 5% with the predicted Casimir force between a sphere and a plane. A few years later Bordag et al. [13], in a review of the Casimir experiments, re-analysed the Casimir results and looked for deviations of the ISL of gravity. They concluded that the Lamoreaux work had led to an improvement of the upper limits on the strength α of Yukawa type deviations for ranges λ between $0.6\mu m$ and $4.2\mu m$ (see fig.1.1).

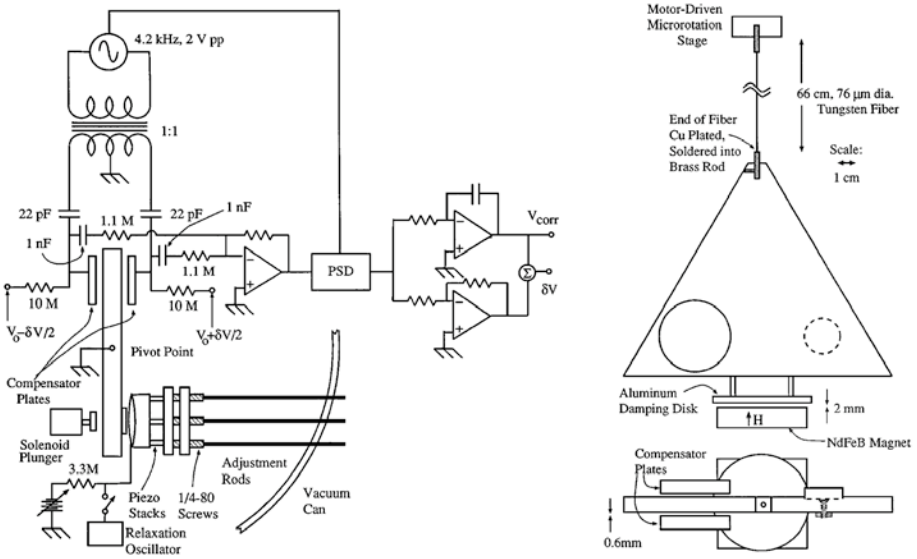

Figure 1.3: Schema of the experiment used by Lamoreaux [47] to measure the Casimir force at distances as small as $0.6\mu m$.

The microcantilever of the University of Stanford

The group of Stanford [22][71] used a micro cantilever, which was kept in vacuum and at a temperature of $10K$, to explore the possible violations of the ISL of gravity at ranges of a few micrometres. They measured the force between a small gold cube ($50\mu m \times 50\mu m \times 30\mu m$, $1.64\mu g$) and a mass made of five alternating gold and silicon bars ($100\mu m \times 100\mu m \times 1mm$). The first mass was mounted on the top of a microcantilever and the second one on a piezoelectric bimorph actuator, which was moved in one direction (see fig.1.4). The two masses were separated by a rigid $3\mu m$ thick electrostatic shield to screen any possible electrostatic or Casimir force acting between them. The screen also set the minimum

reachable distance of $25\mu m$. The source mass was oscillated in the horizontal direction with an amplitude of $\pm 100 - 125\mu m$. In such a way the resulting driving force, which was associated with its density modulation, was at a frequency $(90 - 120Hz)$ which was a subharmonic of the cantilever resonant frequency. It was therefore possible to minimise non-linearity and vibrational couplings of the microcantilever. Additionally, the cantilever and the bimorph were separated by a vibrational isolation stage and the seismic noise was reduced with a passive isolation system. To measure the force between the masses, the displacement of the microcantilever was monitored with a fibre optical interferometer and later converted to an equivalent force measurement. The force sensitivity of this instrument was $2.5 \times 10^{-16} N/\sqrt{Hz}$, which was limited only by the small thermal noise given the high Q of the cantilever. The thermal noise was also used as a reference force to calibrate the force readout. The Stanford group fitted the possible Yukawa forces to their force measurements and set new upper limits on the Yukawa strengths for ranges between 4.2 and $23\mu m$.

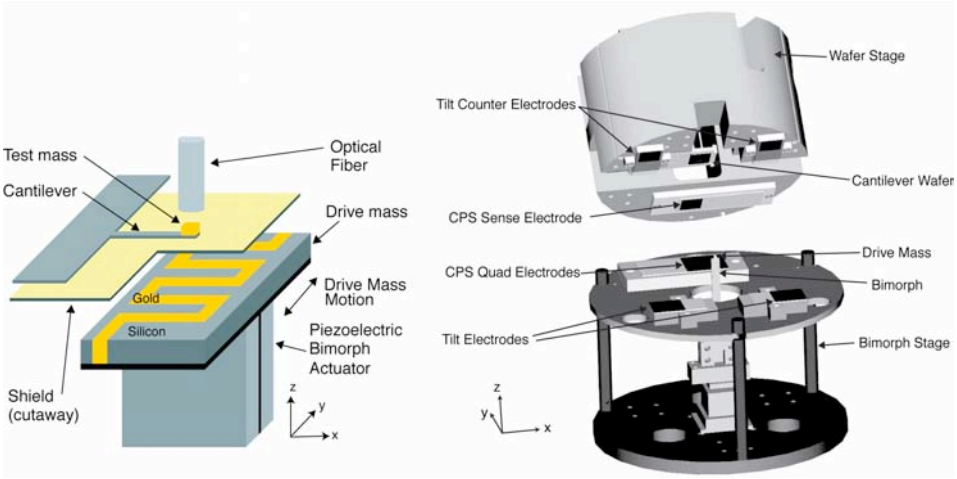

Figure 1.4: Schema of the experiment of the Stanford group [22][71].

The double torsional oscillator of the University of Colorado

The ISL test, which was conducted by Long et al. [51][50][52], had a double torsional oscillator as a force sensor which was kept under vacuum and at constant room temperature ($T = 305K$). The source mass was a tungsten plate $(35mm \times 7mm \times 0.305mm)$, which was driven vertically by a PZT bimorph at the resonant frequency of the torsional oscillator, $\approx 1kHz$. Its oscillation amplitude

was monitored with a capacitive sensor. The force sensitivity of the torsional oscillator was measured to be $2.8 \times 10^{-13} N/\sqrt{Hz}$ [52] and was limited by its thermal noise. As with the previous experiment, the thermal noise was used to calibrate the capacitive readout as torque measurement. The contributions of the acoustic and vibrational background noise to the torque noise were attenuated with passive vibration isolation system. Because the source board and the oscillator were separated by a $60\mu m$ thick conducting shield, the minimum distance between them was $108\mu m$. The geometry of the test masses, being planar with a thickness of $0.2 - 0.3mm$, was optimal to maximise the ratio between a possible Yukawa force (with unit strength) and gravity. The experiment of Long et al. improved the previous upper limits on Yukawa type deviations from the ISL of gravity by many orders of magnitude for λ between $23\mu m$ and $120\mu m$. A cryogenic update of the Colorado experiment [52] would improve its current explored area by a factor of 40 in strength (see fig.1.11).

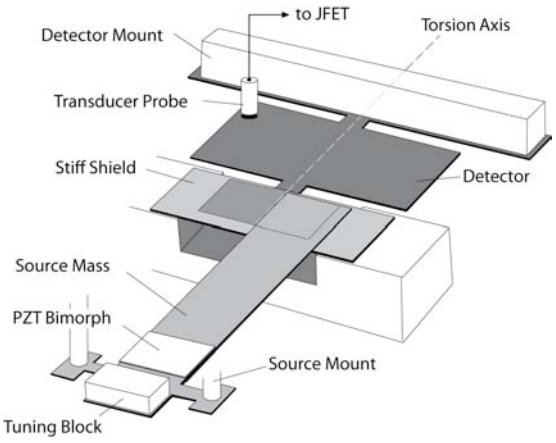

Figure 1.5: Schema of the experiment of Long et al.[51]

The torsion balance of the University of Washington

The experiment of the gravitation group at the University of Washington was one of two experiments to rule out Yukawa type violation of the ISL of gravity for $|\alpha| \leq 1$ for ranges λ as small as $197\mu m$ [40] at 95% confidence level and in a recent update as small as $56\mu m$ [43]. The experiment was based on a room temperature fibre torsion pendulum, which suspended a detector mass over a source mass made of two disks. Both masses had a number, n , of holes, which, machined in circle, constituted the negative masses to test Newton's law. Because

Washington experiment had been designed to be a quasi null test of gravity, the holes in the two disks, which constituted the source mass, were azimuthally displaced in such a way that their Newtonian forces cancelled each other out at a chosen distance between the attractor and the detector mass. At this particular distance only the non Newtonian forces would have been measured by the torsion balance. The source and the detector mass were separated by $20\mu m$ thick electrostatic shield, which screened the electrostatic and Casimir forces between them. The screen constrained the minimum distance between the disks to $55\mu m$. The source mass was rotated at some nominal frequency ω and the corresponding twist of the torsion balance was recorded with an optical autocollimator [40]. Constant torque calibration was given by the gravitational coupling between two sets of three spheres: the first set was positioned on the torsion balance while the second one was on a turntable which rotated at a constant frequency around the vacuum vessel. The rotation speed of the attractor mass was chosen with respect to the natural period of the torsion balance in such a way that the main harmonic of the driving torque signal was at a frequency, $n\omega$, high enough to suppress the $1/f$ noise. The rotation speed was also chosen such that the amplitudes of the second and third harmonics, $2n\omega$ and $3n\omega$, were not too much reduced by the pendulum transfer function of the balance. To reduce possible spurious electrostatic or magnetic interferences, the torsion balance and the source mass were included in an almost complete Faraday cage and partially shielded with mu-metal plates. The torsion balance reached a torque sensitivity of $3.2 \times 10^{-14} Nm/\sqrt{Hz}$ or $10^{-12} N/\sqrt{Hz}$, which was near its thermal noise limit. With this experimental apparatus the Washington group was able to set the strongest constraints on the strength of the possible Yukawa violations of the ISL for ranges $120\mu m \lessapprox \lambda \lessapprox 3.5mm$ [40] and very recently for $9\mu m \lessapprox \lambda \lessapprox 3.8mm$ [43].

The torsion balance of the University of Huazhong

Just after the results of Kapner et al. [43] became known, also the gravitational group from the University of Huazhong [86] published additional results on the violations of the ISL of gravity, which, for ranges between $20\mu m$ and $0.5mm$, confirmed the new constraints given by the Washington group. The Huazhong ISL test was based on planar test masses and on a servo controlled torsion balance working under vacuum. The angular displacement of the balance was monitored by an optical autocollimator. Because their experiment was also designed to

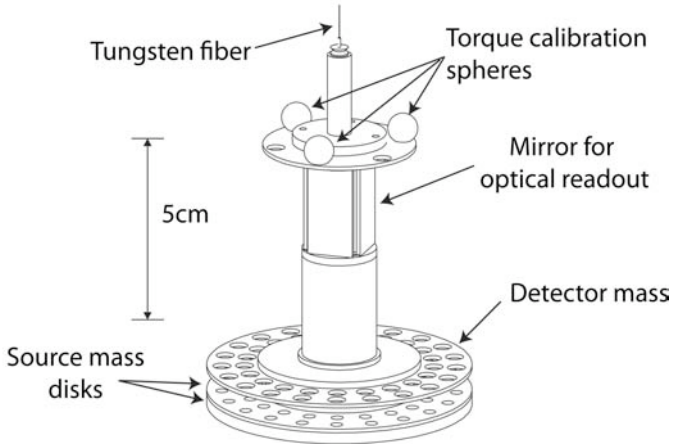

Figure 1.6: Schema of the torsion balance used by Hoyle, Kapner et al [40][43]. The electrostatic shield had not been drawn.

be a quasi null test of gravity, they use two additional masses on the opposite side of the torsion balance with respect to the test ones to cancel out the total Newtonian torque at a chosen distance between the masses. These were separated by a gold coated $56\mu m$ thick glass membrane. A cylindrical mass on a rotating turntable near the vacuum chamber was used to calibrate the voltage servo effort as torque measurement. The driving torque was modulated at the frequency of $0.46mHz$, which was above the resonant frequency of the torsion balance, by moving the source masses in the z direction (see fig.1.7) by $\pm 80\mu m$ using a piezoelectric translator (PZT). With a torque sensitivity of $9.5 \times 10^{-14} Nm/\sqrt{Hz}$, which was limited by electrostatic noise above the thermal noise, the Huazhong group excluded Yukawa violation from the ISL of gravity with $|\alpha| \leq 1$ for $\lambda \geq 66\mu m$ at 95% confidence level.

1.3.3 Possible future experiments

Here I very briefly introduce all the other experiments, which are still in the study phase to possibly test the ISL of gravity at micrometre distances in the near future.

The double-paddle oscillator of the University of Dusseldorf

One group currently developing an experimental test of the ISL of gravity at micrometre distances is based at Dusseldorf University [29][52][30]. Their exper-

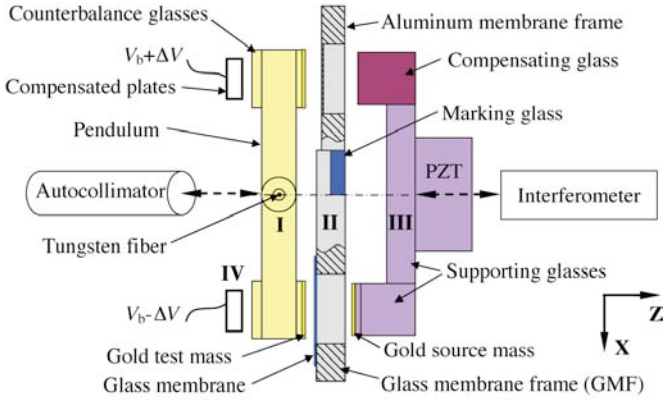

Figure 1.7: Schema of the torsion balance used by Tu et al. [86]

imental approach is based on a planar configuration for the test masses and on the use of a single crystal silicon oscillator as a force sensor. This oscillator has a high quality factor ($Q \approx 10^5$) and has shown torque sensitivity of $10^{-16} Nm/\sqrt{Hz}$, which was limited at the resonance by its thermal noise [29]. The design of Dusseldorf experiment - which has been constructed (see fig.1.8) - has the oscillator as test mass and a series of platinum cylinders on a rotating support as source masses. The cylinders generate a driving gravitational signal at the resonant frequency of the oscillator ($\approx 6kHz$). The source and test masses are separated by a $50\mu m$ thick stainless steel electrostatic shield and are all kept under vacuum. The oscillation amplitude of the oscillator head is monitored by an optical readout system, while the distance between the source and test masses is varied. Even if the experiment had sufficient force sensitivity to explore new possible violations of the ISL of gravity, the results are limited by a systematic signal, which is probably due to a magnetic coupling between the oscillator and the driving motor. The authors have proposed [30] a new experimental design, which will be based on one oscillator detector and two source oscillators, one on each side of the detector (see fig.1.8). The head of the sensor will be covered by a $1\mu m$ gold layer on one side and with a copper layer on the other side. With this new design the gravitational, electrostatic and Casimir forces will counter balance on the oscillator sensor. The sensor will detect only possible deviations from the ISL of gravity, due to the different densities of the copper and gold layer. Dusseldorf group proposes to cool down the new experiment to liquid Helium temperature in order to further enhance the oscillator quality factor up to $Q \approx 10^8$ and in order to lower its thermal noise. With this configuration, if not limited by any other

systematic effect, the possible area of the Yukawa strength, Dusseldorf group will explore is plotted in fig.1.11.

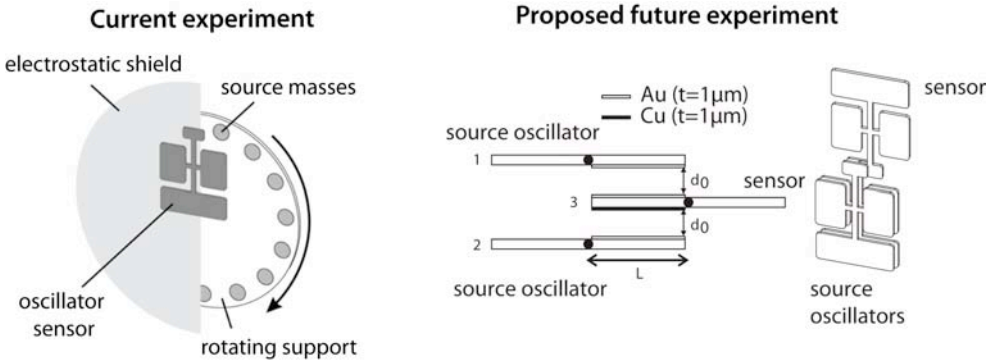

Figure 1.8: Schema of the current and proposed experiments of the Dusseldorf group to test the ISL of gravity at micrometre distances [30].

The differential accelerometer of the University of Maryland

Paik and colleagues [60] of the University of Maryland have proposed a cryogenic space experiment, ISLES, to test the ISL of gravity at distances of $100\mu m$, whose ground version might be able to explore a large area of the Yukawa type deviations at sub-millimetre distances. The concept of the experiment is again for it to be a null experiment. The possible Yukawa forces between a central disk and two lateral superconducting disks will be be detected by using a superconducting circuit, which is sensitive only to differential acceleration. Owning to the short distances between the disks ($\approx 100\mu m$) the gravitational force between the disks will remain constant, when the source mass will be driven along its symmetry axis. Any deviation from the Newtonian gravity would cause a differential acceleration between the two masses. The superconducting test masses will be magnetically coupled with a superconducting circuit and the induced differential acceleration will be picked up by using a few SQUIDS, coupled with the circuit. According to [60] the ground version of ISLES will capable of exploring Yukawa violation of the ISL of gravity for $|\alpha| \leq 1$ for ranges as small as $10\mu m$ (see fig.1.11).

Trapped condensed atoms

In recent years to probe weak forces at micrometre distances a new kind of sensor - based on condensed atoms - has been under study both theoretically and ex-

perimentally [25][38][92][17][26]. Among all the literature on this sensor I should mention particularly the seminal work of Dimopoulos and Geraci [25], who proposes an experiment to test the ISL of gravity at micrometre distances. Their experimental set up is based on an array of Bose-Eistein condensed (BEC) atoms ($\approx 10^6$), which are trapped near a surface at the nodes and antinodes of a laser standing wave (see fig.1.9) perpendicular to the surface. In their project design, after the atoms are loaded in the laser traps in a coherent superimposition of states, the de Broglie phases of the center of mass wave function will develop differently depending on the potential to which they are subjected. After an interrogation time of $1 - 10\,\mathrm{sec}$ the wave functions of their center of mass will have accumulated a relative phase shift because of their different distances from the surface. The laser will then be turned off and the differential phase will be detected by measuring the interference pattern, that the condensate will develop [25]. The surface reflecting the laser is an electrostatic/Casimir shield and a mass with periodic density modulation (see fig.1.9) will be placed behind it. By moving sideway this source mass, a periodic change of the gravitational forces will be detected as a periodic signal by the BEC sensor, while all the Casimir and patch field effects will instead be rejected as common mode. With this experiment the authors [25] predicted that they will be able explore different new areas of the allowed Yukawa deviations for $\lambda \leq 50\mu m$ depending on the phase sensitivity of the instrument (see fig.1.11). Their projections are perhaps optimistic, considering that, for example, they proposed using an electrostatic shield which is only $420nm$ thick. However these new force sensors based on trapped atoms (with either this or an alternative design [26][17][92]) will surely play a key role in the study of weak forces at very short distances. For example, magnetically trapped atoms have recently been used to study the Casimir-Polder force at distance between 6 and 12 μm and to confirm the upper limits on Yukawa deviations [38] for ranges, λ, between 10^{-7} and $10^{-6}m$. Because at present the BEC sensors are not expected to reach enough force sensitivity to explore new interactions for $|\alpha| \leq 1$ at any range, they should be considered as a valid complement to but not substitutive of the current experimental approaches, which are based on torsion balances and microscillators.

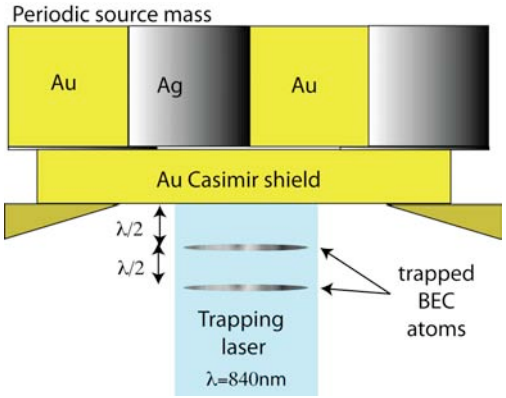

Figure 1.9: Schema of the experiment proposed by Dimopoulos and Geraci [25].

1.3.4 Our approach: the Spherical Superconducting Torsion Balance of the University of Birmingham.

The experimental approach to test the ISL of gravity at micrometre distances, that we are developing at the University of Birmingham, is based on a spherical superconducting torsion balance (SSTB) This balance uses the Meissner effect to levitate a superconducting float over the magnetic field, which is generated by a superconducting coil. The rotation of the float is monitored by using a interferometric or capacitive readout, and is kept at a constant angular position by using a PID feedback loop. The servo effort is applied back to the float by the magnetic field of superconducting coils, which are acting on the float. This actuator circuit is also used to give an arbitrary restoring stiffness to the balance. We use eddy current damping to drastically reduce any spurious oscillations of the torsion balance. The experiment is kept under vacuum and at a temperature of $4.2K$. The design of the torsion balance offers many advantages with respect to the fibre one. Because it has a very short effective pendulum length (a few mm), it is expected to be less sensitive to ground tilt noise. Because it is not based on a fiber, it does not have all the noise sources associated with it, such as the noise due to the mechanical dissipation of the elastic energy in the fibre material. The magnetic levitation can sustain a heavy float ($> 100gr$) with the samples to investigate. We can freely choose its natural resonant frequency and better tune its sensitivity. We can interrupt the levitation to better investigate all the noise sources and the systematics. The first version of the SSTB had already been successfully used to measure the possible coupling between spin and matter,

improving the present measurements of many order of magnitude [34].

It is not only the design of the torsion balance which is very innovative; the design of our ISL test of gravity also offers novel features. The source and test masses are made of alternate stripes of different materials in order to create a density contrast in the x direction (see fig.1.10). The source mass is flat while the test mass, which is attached to the float, is curved. The curvature is chosen such the distance between the two masses does not change even during the pendulum motion of the float. One facet of our design, which is innovative for an experiment specifically designed to test the ISL of gravity, is that we do not to have any rigid electrostatic shield between the two masses. To reduce any electrostatic or Casimir forces we covered the masses with a uniform gold layer $1\mu m$ thick. We do not measure the perpendicular force between the masses, as most of other experiments do, but rather the transversal one. Along this direction some of the spurious forces are expected to be greatly reduced while the gravitational torque is left unchanged. We also use a new kind of commercial micropositioner (Attocube), which is able to move by steps of a fraction of a micrometre up to a maximum distance of few millimetres. We perform long torque scans in the x direction to obtain a large statistics and to extract the signal from the noise. We can also characterise the measured signal versus the frontal distance y between the masses (see fig.1.10). In this way we can try to understand the origin of spurious torques and, if possible, to reduce or fit them out of the data.

We expect that the limiting torque sensitivity of the SSTB , which is given by the thermal noise, is $3.9 \times 10^{-15} Nm/\sqrt{Hz}$ or $9 \times 10^{-14} N/\sqrt{Hz}$ corresponding to a quality factor of $Q \approx 420$ due to residual gas damping.

In fig.1.11 I plotted the expected (α, λ) area that we will be able to explore with the Birmingham SSTB at its thermal noise after 100 days of integration time with two masses, which have a $160\mu m$ pitch of the density modulation and which are positioned at a y distance of $5\mu m$. As shown in the figure, with such a configuration we will be able to either rule out or confirm possible violations to the ISL of gravity due to the strange modulus and the vacuum energy scenario associated with the cosmological constant. We will also be able to set stronger constraints on the dilation, the radius modulus and the SLED scenarios too. It will furthermore be possible to explore smaller strengths of the Yukawa type deviations at shorter ranges, if we develop and adopt new test masses with a much shorter pitch of the density modulation.

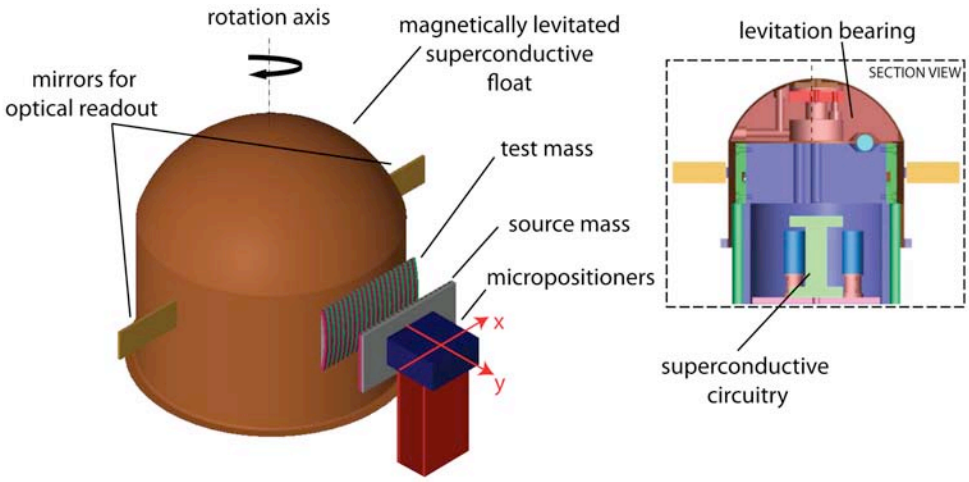

Figure 1.10: Simplified schema of our experiment to test the ISL of gravity at micrometre distances.

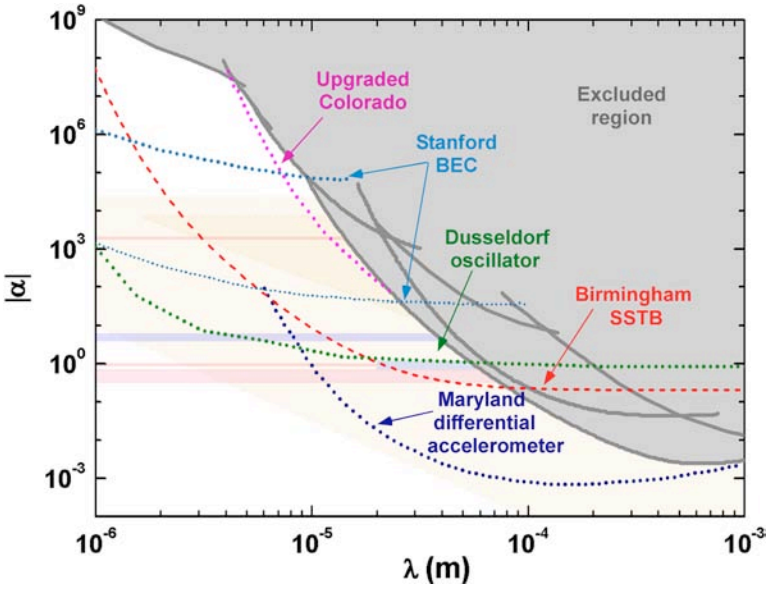

Figure 1.11: Current and expected (α, λ) upper limits accessible by present and future experiments including on the STTB (red dashed line).

1.4 Thesis synopsis

This thesis is devoted to two main goals: on the one hand to present the study, development and first results of our ISL test of gravity; on the other hand to present the expected and measured performances of the SSTB. I review here the synopsis of the following chapters of this PhD thesis.

In *chapter 2* I will present our test masses, which are made of a set of alternating gold and Aluminium stripes coated with a covering gold layer. Their design and manufacture was developed to minimise the spurious forces, which can strongly limit our tests of gravity. One of the two masses is attached to a flat support, which is moved by a micropositioner in two directions. The second mass is glued onto a curved support, which is connected to the float. I will discuss the metrology which characterise the surface topographies of our masses.

In *chapter 3* I will review all the possible forces which, to the best of our knowledge, act between the masses. I will start by discussing the Newtonian signal, which is given by the mass density modulation of gold and aluminum stripes. I will present the analytical model, which I developed to predict such a signal and to optimise the geometry of the masses. I will estimate the spurious electrostatic forces due to periodic corrugations of the surfaces and/or due to surface contact potentials. These forces, if not minimised, will strongly limit our ability to search for violations of the ISL of gravity at micrometre distances. Good knowledge of the expected amplitude and phase of such electrostatic signal will let us fit and effectively subtract them out of the measured data. I will also characterise the expected signals due to the Casimir forces, which are given by the same periodic surface corrugations, and present the magnetic forces due to the contrast in the magnetic susceptibilities of gold and aluminum stripes. I will complete the review of the expected signals by presenting the numerical model, which predict the possible Yukawa-type forces acting between the masses. The Yukawa model is a standard parametrisation of the possible hypothesised violations of Newton's law among the past and current experimental searches for such signals. I will end this chapter by presenting the strengths and ranges of the Yukawa-type deviations that we would potentially explore with our experiment.

In *chapter 4* I will briefly review the experimental apparatus we use to test the ISL of gravity at micrometre distances. I will present all the subsystems which are necessary to magnetically levitate and servo control the SSTB at $4.2K$ and

to modify the relative positions of the test masses during the experiment.

In *chapters 5 and 6* I will discuss the theoretical analysis of all the subsystems of the servo loop, which control the angular position of the SSTB. I will predict the transfer function between the applied and the measured torque and the expected torque noise spectrum. To successfully test the ISL of gravity at micrometre distances, we need not only to reduce all the spurious forces, as much as possible, but also to ensure that the torque sensitivity of the SSTB is as good as possible. A theoretical model of the sensitivity of the SSTB is therefore necessary to optimise the design of the apparatus. This model will also be used to estimate the origins of possible unexpected torque noise levels by comparing them with the analytical predictions. In *chapter 5* I will discuss the analytical model which I developed to predict the dynamic of the SSTB float given its metrology, such as its moments of inertia or the damping and elastic coefficients associated with its angular motions. This model is used to estimate the transfer function between the applied torque and the float angle. The effect of all the possible components of the seismic noise (horizontal, vertical and tilt) on the float will be estimated. I will evaluate their equivalent input torque noise, which is applied to the float. Under certain conditions, that I will define, the torque noise induced by the seismic noise will limit the SSTB torque sensitivity and, ultimately, our ISL tests of gravity.

In *chapter 6* I will analyse in detail the transfer functions and noise sources of all the subsystem of the servo loop controlling the SSTB. I will analyse the capacitive sensor, that we adopted as a temporary solution to monitor the angular position of the float, while the optical readout is still being developed [62]. I will discuss the transfer function of the digital compensator and of the magnetic actuating system. The latter is based on superconducting circuits with permanent currents stored within them. Such currents, which can be modified by an external current source, are used to feedback the torque to the float which is necessary to keep it at a constant angular position. The chapter will end with the analysis of the closed loop transfer function of the servo system between the applied and measured torque and with the discussion of the expected torque noise.

In *chapter 7* I will present the experimental performances of the SSTB which we obtained during our first tests of Newton's law of gravity at micrometre distances. In this chapter I will discuss the protocol we defined to calibrate the servo effort of the SSTB. I will characterise the performances of the SSTB, discussing, for example, the damping of the parasitic oscillations or the tunable natural

stiffness. I will present the measured closed loop transfer function between the applied and the measured torque. In this chapter I will also discuss the torque noise spectrum of the SSTB, which was measured during the ISL tests, and the further measurements we conducted to investigate its origin.

In *chapter 8* I will present the experimental results associated with the first tests of ISL of gravity at micrometre distances, which we obtained with three prototypes of the test masses. The chapter will firstly be dedicated to the methods we defined to characterise the alignment of the masses during the ISL experiments and to minimise the voltage difference between them. I will report the torque signals we measured with such masses above the noise level of the SSTB and all the tests we ran to characterise them.

In *chapter 9* I will discuss the possible origins of the measured signals, given the experimental results and our theoretical models of the expected torques. The thesis will end by discussing which parameter area describing the Yukawa type deviations of the ISL of gravity we actually explored during our first tests of Newton's law at micrometre distances. I will indicate the possible improvements of the SSTB and of the test masses, which are necessary to explore new violations of the ISL of gravity at micrometre distances in future experiments.

1.5 Conclusions

In this chapter I have reviewed all the theoretical motivations behind the renewed interest in testing gravitational law at submillimetre distances. I have discussed the main open issues, which afflict the current theory of gravity such as, for example, the cosmological or hierarchy problems. I have shown how some of the possible solutions to these issues, which are mainly but not exclusively related to string theory, predict violations of the ISL of gravity at submillimetre distances. These violations, which are usually modeled as Yukawa type forces, will be tested by the next generation of table-top experiments. I have reviewed some of the theoretical scenarios which predict such violations of Newton's law, from large supersymmetric extra dimensions to the exchange of scalar particles or to the hypothesised existence of a "fat" graviton. I have reviewed the current experimental tests of the ISL of gravity. I have discussed all the problems of such precision measurements and the solutions which have been developed in the past or are planned for the future. I have shown how these tests are currently based on two classes of instruments: micromechanical oscillators, which look for violations to the ISL of gravity at distances of a few micrometres, and torsion balances, which give the strongest constraints on the violations of Newton's law at distances larger than $\approx 10\mu m$. The current constraints on Yukawa type violations, which have strengths comparable with Newtonian gravity, are set by the torsion balance of Washington University down to a minimum range of roughly $60\mu m$. I also have discussed the emerging approaches which are based on trapped atoms or optical lattices and which will be a complementary method to test the ISL of gravity at micrometre distances. I have briefly introduced our experiment, which is based on a spherical superconducting torsion balance to measure lateral forces between two test masses. The masses have a mass density modulations across their surfaces as source of the gravitational signal. I have discussed some of the innovations of our experiment, such as, for example, the lack of any electrostatic shield between the masses and the counter-measures, which we have taken in its place to reduce spurious forces. I have showed how our experiment will, we think, allow us to explore some of the hypothesised theoretical signatures of quantum gravity in the near future.

Chapter 2

The test masses

2.1 Introduction

For the ISL test of gravity at micrometre distances we needed to fabricate two test masses, which would let us measure gravity within 10% at distances of $5 - 20\mu m$. We manufactured three masses, which were characterised by mass density modulations across their surfaces given by alternating gold and aluminium stripes. This lateral density contrast produced a lateral force between the test masses, which was the gravitational signal we wanted to test. We covered both masses with a uniform $1\mu m$ gold layer to suppress the expected lateral Casimir forces due to the modulation in the gold and aluminium conductivity. We know that the covering gold layer would also suppress the electrostatic forces due to contact potentials, which at micrometre distances limit our sensitivity to violations of the ISL of gravity. One mass was flat while the mass attached to the torsion balance was cylindrical. With this geometry the distance between the masses remained constant even when the float oscillated around an axis parallel to their surfaces. In this chapter I will describe the method we developed to manufacture the test masses and the metrology measurements I took in order to characterise them.

2.2 Manufacture and assembly

The masses were manufactured at the Millimeter Wave group at Rutherford Appleton Laboratory under the supervision of Dr. J. Spencer with a technique which we summarise in fig.2.1 and which lead to aluminium-gold features with periodicity down to $\approx 160\mu m$. The procedure started from an aluminium foil, which was machined to obtain the aluminium ridges according to requirements. The gold was electrodeposited over the aluminium substrate and some of the top layer was skimmed off to obtain a final flat surface. We found that some fissures or crevasses of $\approx 20\mu m$ depth and $\approx 50\mu m$ width were left on the surface of the masses because of non-uniform deposition of the gold layer. To circumvent this problem the test masses were reversed and their new top surface was machined off down to the gold stripes to obtain a uniformly flat surface as shown in fig.2.2. The masses were then transferred to our department, where they were glued to their copper supports. One support was flat, while the other one was curved.

The cylindrical support was obtained by the electrodeposition of copper on an aluminium mandrel by BJS, London. The aluminium was then removed with a solution of potassium hydroxide. One mass was glued onto a semi cylindrical support which was then attached to the float, while the other one was glued on the flat support. The flat and cylindrical masses were polished with a glass slab and a stainless steel tool respectively, and carborundum powder. Afterwards their curvature was measured with a coordinate measurement machine (CMM). We repeated the last two steps till we reached the required curvature. At this point the production procedure became different for the cylindrical and the flat test masses. For the flat mass we thermally evaporated a $1\mu m$ gold layer over the top surfaces of the mass and support obtaining what we called "**mass C**". This mass is shown in fig.2.5. For the cylindrical mass the procedure was not so straightforward: with the first prototype we manufactured we found that it was not possible to directly evaporate the gold layer over the mass, when it was glued onto the cylindrical support. During the evaporation process the thin copper support could not leak enough heat away with the result that the mass became partially detached. We still used this mass however after having cut away its damaged extremes and covered the rest of it with a conductive silver paint (a solvent containing silver particles, the "Acheson Electrodag 1415M"). This curved mass, which was the first of its kind to be manufactured, was called

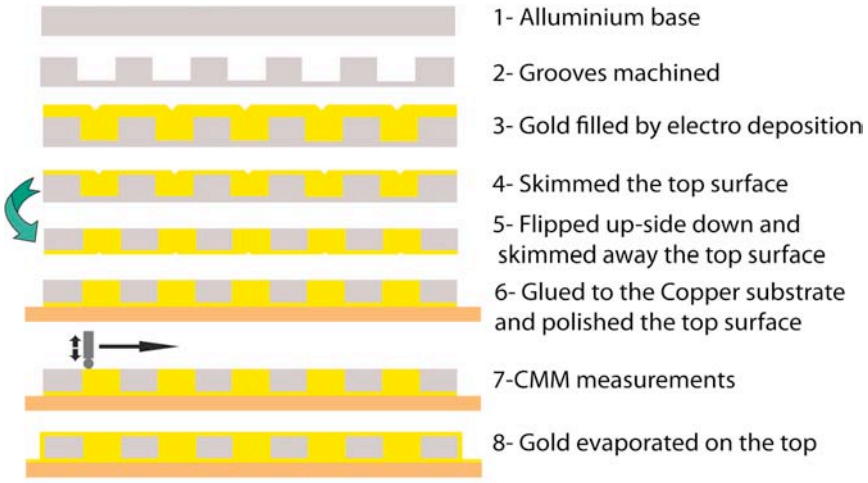

Figure 2.1: Schema illustrating the manufacture of the test masses.

"**mass A**" and is shown in fig.2.3. The assembling procedure was improved with a second prototype we later received. We left the aluminium mandrel under the copper curved support until the mass was with the gold layer in the evaporator. Because the aluminium mandrel was a good heat sink, the test mass was not damaged during the evaporation of the gold layer. To safeguard the integrity of the test mass during the etching process of the aluminium, which followed, the mass was covered with a silicon rubber layer which we later removed. The new curved mass, which I called the "**mass B**", is shown in fig.2.4.

2.3 Metrology

During the process of polishing the masses and after the ISL test of gravity, I characterised the surfaces of the masses by using a Mytutoyo-Crysta-Apex CMM: the procedure consisted of measuring the height of a number of points on the surfaces with respect to a reference plane by means of a $1mm$ radius sphere, which descended onto the mass until touching it. For a hole of $400\mu m$ width the maximum depth the probe was able to measure was $20\mu m$. However because these height measurements relied on the contact between the small sphere and the surfaces of the masses, there was a risk that the surfaces themselves could possibly be damaged during the characterisation process. To avoid compromising the integrity of the surfaces, during the polishing process I took height measurements at a few points only in order to check the long range curvature. After the ISL

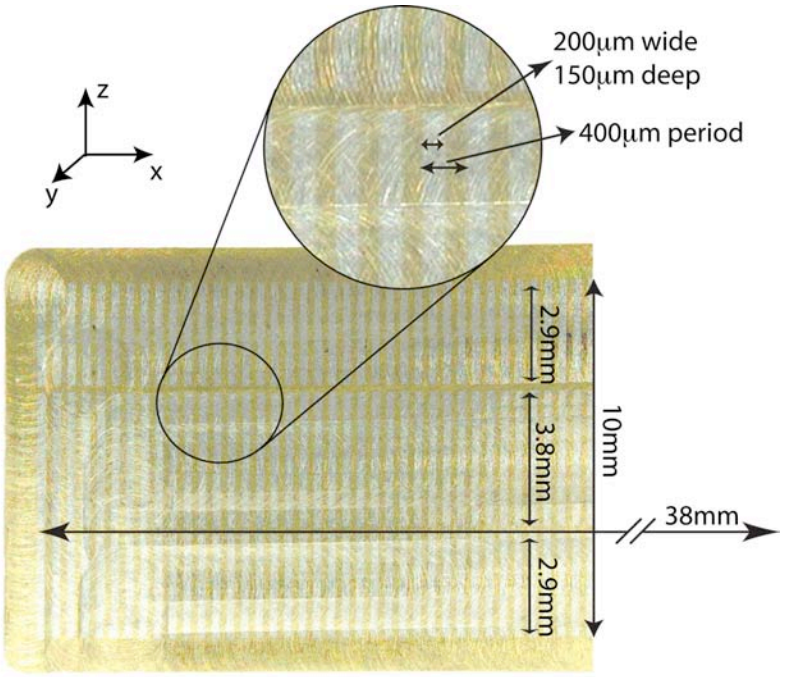

Figure 2.2: Picture of a section of the test mass as it arrived from RAL.

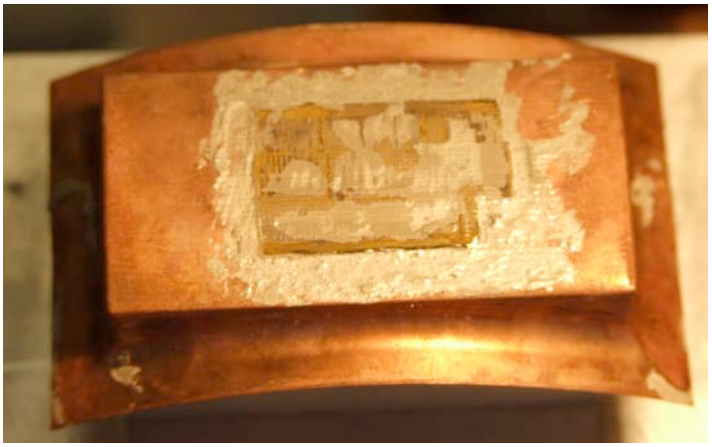

Figure 2.3: Test mass A on the cylindrical support.

Figure 2.4: Test mass B on the cylindrical support attached to the float.

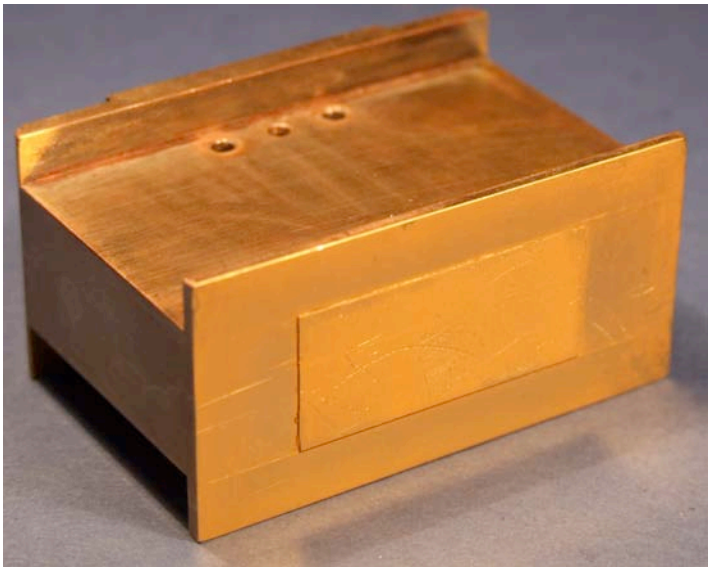

Figure 2.5: Test mass C on the flat support.

experiment I measured the curvature again this time at sufficient points to reveal any corrugation at a pitch of $400\mu m$.

To estimate how much the surfaces deviated from a perfect flat plane or cylinder, I fitted such geometries to the measurements and took the difference between the original data and the fitted one. Because the flat and the cylindrical surfaces were found not to be parallel to the reference plane, which I used during the CMM measurements, it was necessary to fit a possible 3D rotation and one or two translations of the plane or of the cylinder to the experimental data. This was obtained by taking the original data set (x, y, z) (see the reference frame in fig.2.2) and creating the new one defined by the equation:

$$\begin{pmatrix} x_{fit} \\ y_{fit} \\ z_{fit} \end{pmatrix} = A(\theta, \phi, \psi) \cdot \begin{pmatrix} x \\ y_{fig} \\ z \end{pmatrix} \tag{2.1}$$

where $A(\theta, \phi, \psi)$ is 3x3 matrix defining a 3D rotation [36] depending on three Euler angles θ, ϕ and ψ. In the case of the fit to a cylinder of radius r, y_{fig} is defined by the equation:

$$y_{fig} = -y_0 + \sqrt{r^2 + (z - z_0)^2} \tag{2.2}$$

z_0 and y_0 are the two offsets, which define the translations in z and y directions. For the fit to a tilted plate, y_{fig} was simply set to be equal to $-y_0$. The obtained y_{fit} was least squared fitted to the original y data by using the MATLAB function *nlinfit*. I took the difference between the original data sets and the fitted data and obtained the results of fig.2.8, 2.6 and 2.7. I also plotted the height profiles for z constant in the middle of the masses (fig.2.10, 2.12 and 2.13). I found that the central profiles of mass A, B and C are characterised by standard deviations respectively of 13, 9.4 and $3.8\mu m$. I evaluated the amplitude spectrum of all the central scans [83] (fig.2.10, 2.12 and 2.14). For the masses A, B and C the measured amplitude spectrum at the spatial frequency of $k_0 = 1/400\mu m^{-1}$ was respectively 0.54, 0.31 and $0.71\mu m$. The flat mass C had also an amplitude spectrum signal above the noise level at the spatial frequency of $1/200\mu m^{-1}$, which has an amplitude of $0.49\mu m$.

(μm)	**Mass A**	**Mass B**	**Mass C**
Average depth	19.7 ± 13.5	16.2 ± 9.4	9 ± 3.8
k_0 corrugation amplitude	0.54	0.31	0.71

Table 2.1: Average depths and corrugation amplitudes at the spatial frequency of the mass density modulation for the prototypes of the test masses.

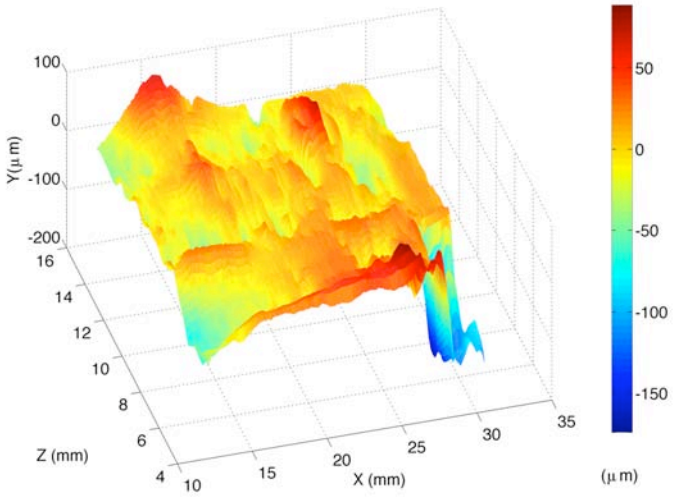

Figure 2.6: 3D topography of the mass A

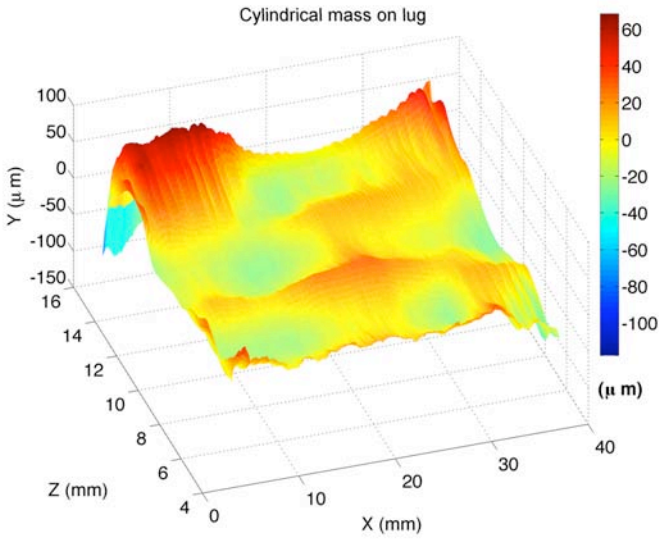

Figure 2.7: 3D topography of the mass B

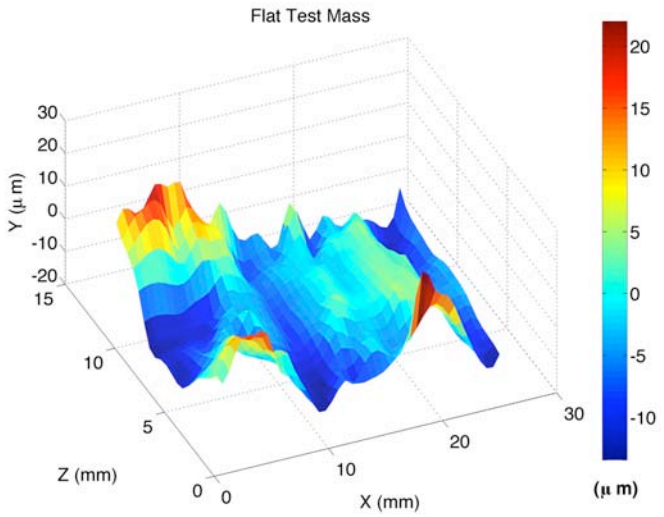

Figure 2.8: 3D topography of the mass C

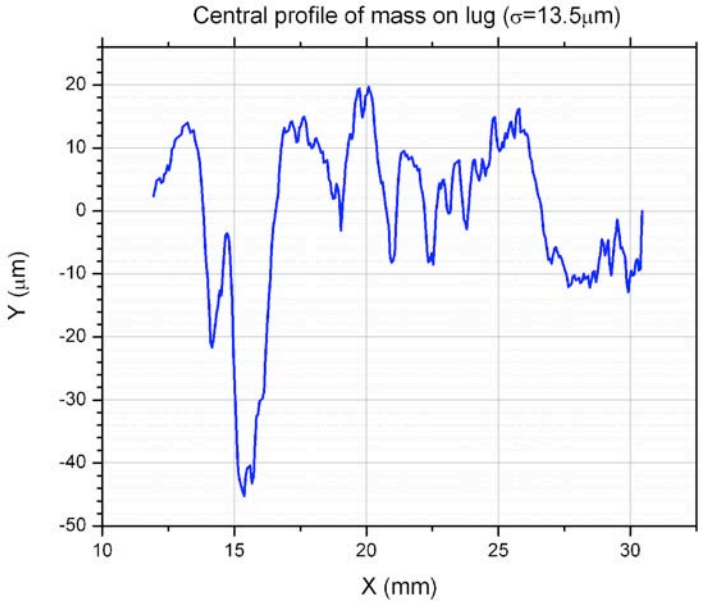

Figure 2.9: Central profile of mass A

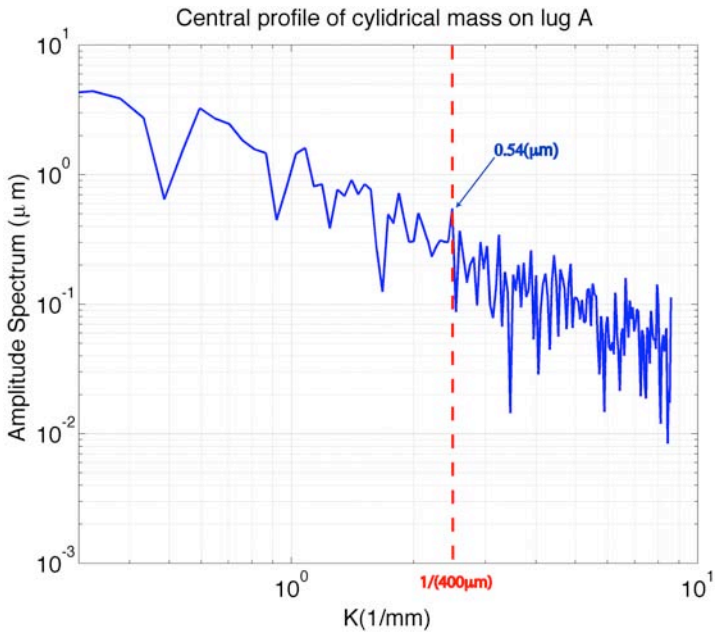

Figure 2.10: Amplitude spectrum of the central profile of mass A.

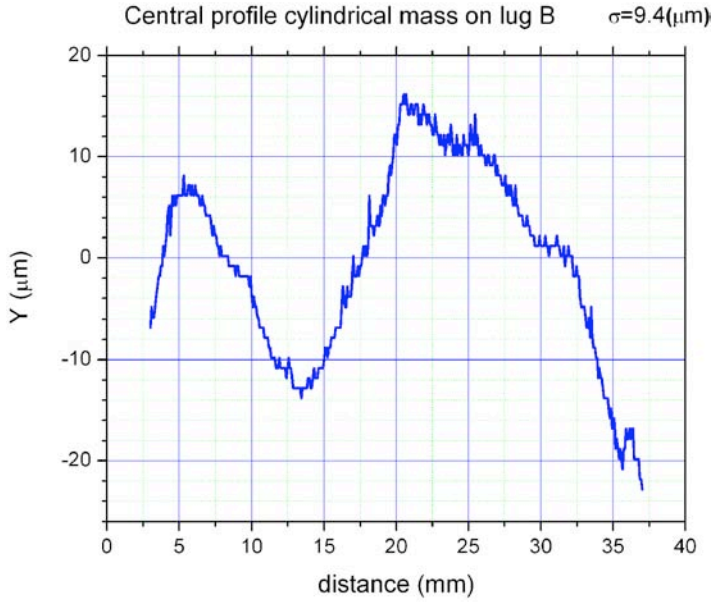

Figure 2.11: Central profile of mass B.

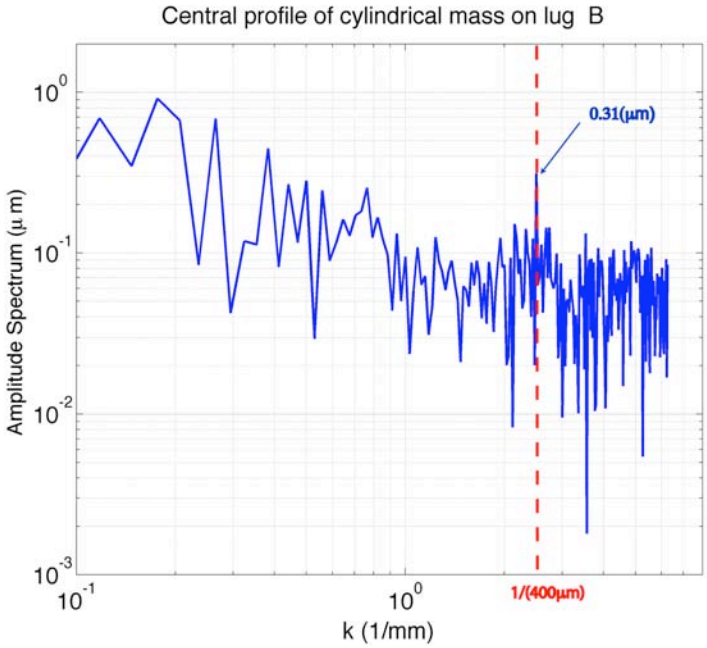

Figure 2.12: Amplitude spectrum of the central profile of mass B.

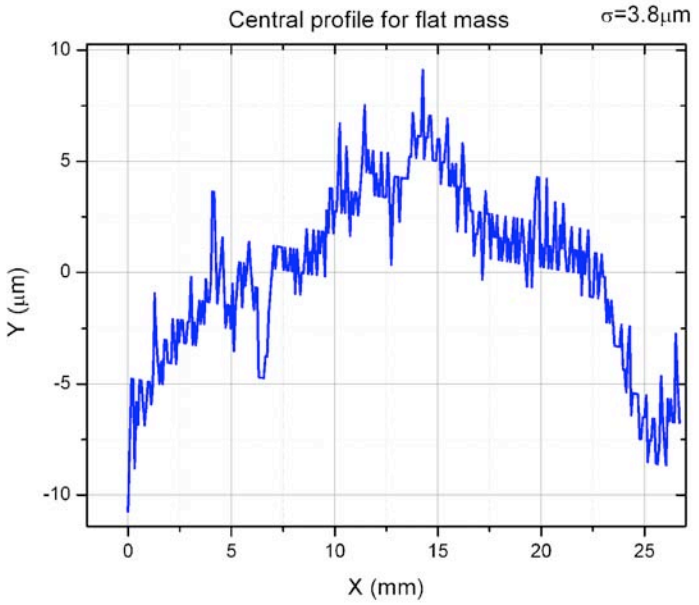

Figure 2.13: Central profile of mass C. This plot is based on a CMM measurements just on the center x axis and with larger number of points per mm with respect to fig.2.8

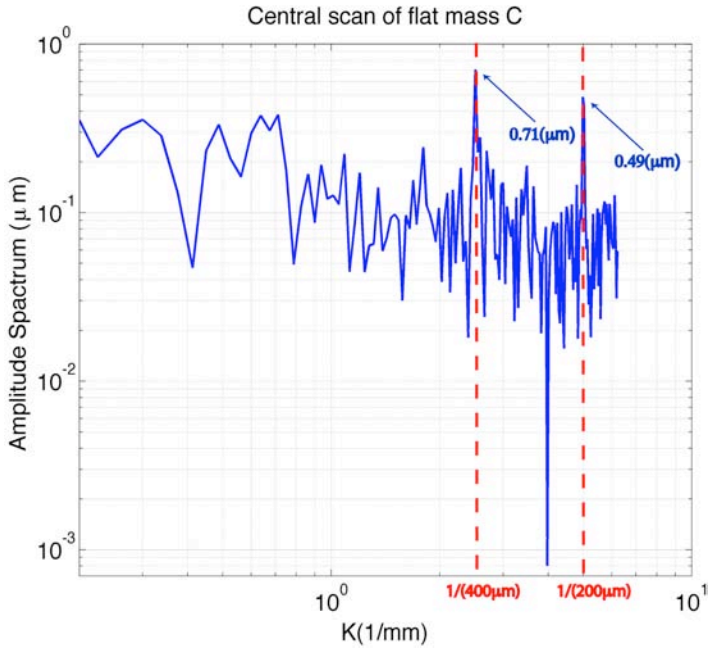

Figure 2.14: Amplitude spectrum of the central profile of mass C.

2.4 Conclusion

I have presented here the first three prototypes of the test masses we manufactured and characterised, which we used for the test of the ISL of gravity at micrometre distances. We defined the method to produce the mass density contrast on the masses by using alternated gold and aluminium stripes. We found that while the manufacture of the flat mass was straightforward, the fabrication of the cylindrical one was more complex due to the low thickness of its copper support. Because of the thin support, the curved mass was easily damaged during the thermal deposition of the gold layer. We finally obtained one flat mass and two cylindrical masses. The first cylindrical mass to be manufactured was partially covered by silver paint, while the second one was uniformly covered by a gold layer. I characterised the topography of the test masses with CMM measurements and found that the amplitude spectrum of the measured corrugations was $0.5\mu m$ at $k_0 = 1/400\mu m^{-1}$. There is a possibility that these CMM measurements may have damaged the test masses and, in future, they should be substituted with non-contact measurements. These first prototypes of the test masses were used to perform the preliminary tests of the ISL of gravity with our experiment.

Chapter 3

The expected torques

3.1 Introduction

This chapter is dedicated to the analysis of all the possible torques which, to the best of our knowledge, I expect we will measure with the torsion balance and the test masses. I will start by presenting an analytical model of the Newtonian force, which is acting between the masses because of the mass density contrast across their surfaces. I will discuss how I used this model to optimise the test mass geometries for the ISL test. I will model the electrostatic forces, which are due to periodic corrugations of the surface topographies of the test masses and/or to periodic surface potentials. These potentials are given by contact potentials between the gold and aluminium stripes. They will give origin to a measurable force in the case they are not well screened by the top gold layer. I will also model the lateral Casimir forces due to surface corrugations, which dominates gravity at distances shorter than $6\mu m$. I will discuss the magnetic force, which are due to the differences in the magnetic susceptibilities of the aluminium and gold stripes. I will discuss the numerical model we developed to predict the possible Yukawa forces, which might act between the masses. I will define the method to set preliminary upper limit on their strength, α, and range, λ, given the experimental results. I will also show how it is possible to optimise the parameters of the test mass geometries according to which (α, λ) area we would like to explore during the experiment.

3.2 Newtonian torques

In this section I will analyse the expected Newtonian torques, which are given by our test masses and their supports. I will start by developing an analytical model of the Newtonian torques, which are due to the mass density modulation of the test masses and I will use the analytical results to define the optimal geometry. I will discuss the models used to predict to Newtonian background torque, due to the interaction between the test masses and their copper supports. Again I will use the obtained results to optimise the geometry of the support of the flat mass and to minimise the background Newtonian torque.

3.2.1 Analytical model for the torque due to the density modulation

I develop here the analytical model of the Newtonian torques, which are due to the mass density modulations. I start by modelling the Newtonian potential, which is given by a periodic mass distribution along the x direction. Then I will integrate the potential over all the dimensions of the source and target mass to get their total gravitational potential. Finally I will differentiate the resulting potential to obtain the torque, which is acting on the torsion balance as a function of the relative position of the test masses in the x direction.

General case:

I start therefore from the Poisson differential equation for the Newtonian potential, ϕ, given a mass density distribution ρ, which is limited to the space of negative y and is infinite along the z direction:

$$\nabla^2\phi(x,y) = 4\pi G\rho \text{ for } y \leq 0 \tag{3.1}$$

$$\nabla^2\phi(x,y) = 0 \text{ for } y > 0 \tag{3.2}$$

where $G = 6.674 \times 10^{-11} m^3 kg^{-1} s^{-2}$ is the gravitational constant. The associated Newtonian fields in the x and y directions are given by the equations:

$$f_x = -\partial_x\phi(x,y), \quad f_y = -\partial_y\phi(x,y) \tag{3.3}$$

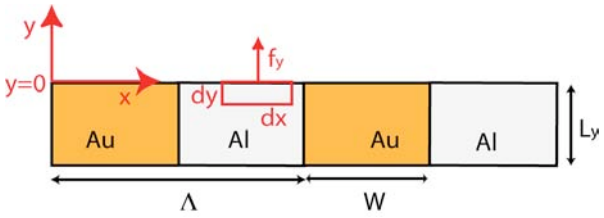

Figure 3.1: Diagram showing the x and y coordinates and the gaussian integration.

From Gaussian integration around an infinitesimal section of the surface (see fig.3.1), it follows that:

$$f_y(x,0) = -2\pi G\rho dy \tag{3.4}$$

I assume that the mass density is periodic in the x direction with period Λ ($\rho(x,y) = \rho(x+n\Lambda, y)$ with $n \in \mathbb{N}$), symmetric with respect to $x = 0$ ($\rho(x,y) = \rho(-x,y)$), separable in the product of two functions depending only on x and y ($\rho(x,y) = \rho_0\rho_x(x)\rho_y(y)$) and independent of z.

I also assume that the gravitation potential is expressed as the product of two functions, of which one is periodic in x with period Λ. The global solution of the Laplace equation 3.2 is obtained by separation of variables [5] and is expressed by the equation:

$$\phi(x,y) = C_0 y + \sum_{l=1}^{\infty} C_l \cos(l\frac{2\pi}{\Lambda}x)e^{-l\frac{2\pi}{\Lambda}y} \tag{3.5}$$

with C_0 and C_l constants, which are set by the boundary conditions. The force fields in the x and y directions are given by the equations:

$$f_x = \sum_{l=1}^{\infty} C_l \frac{2\pi}{\Lambda} \sin(l\frac{2\pi}{\Lambda}x)e^{-l\frac{2\pi}{\Lambda}y} \tag{3.6}$$

$$f_y = -C_0 + l\sum_{l=1}^{\infty} C_l \frac{2\pi}{\Lambda} \cos(l\frac{2\pi}{\Lambda}x)e^{-l\frac{2\pi}{\Lambda}y} \tag{3.7}$$

Now as the density $\rho_x(x)$ is periodic in x, it can be expanded in a Fourier series as:

$$\rho_x(x) = \frac{a_0}{2} + \sum_{n=1}^{\infty} a_n \cos(\frac{n2\pi}{\Lambda}x) \tag{3.8}$$

where [5]:

$$a_n = \frac{2}{\Lambda}\int_{-\Lambda/2}^{\Lambda/2} \rho_x(x)\cos(\frac{n2\pi}{\Lambda}x)dx \tag{3.9}$$

Now eq.3.4 implies that:

$$-C_0 + l\sum_{l=1}^{\infty} C_l \frac{2\pi}{\Lambda}\cos(l\frac{2\pi}{\Lambda}x) = -2\pi G\rho_0 \left(\frac{a_0}{2} + \sum_{n=1}^{\infty} a_n \cos(\frac{n2\pi}{\Lambda}x)\right) dy \tag{3.10}$$

and therefore

$$C_0 = 2\pi G\rho_0 \tfrac{a_0}{2} dy, \quad l = n, \quad C_l \tfrac{2\pi}{\Lambda} = -2\pi G\rho_0 \tfrac{a_n \Lambda}{n2\pi} dy \tag{3.11}$$

The solution for the gravitational potential of eq.3.5 becomes the equation:

$$\phi(x,y) = -2\pi G\rho_0 \left(-\frac{a_0}{2}y + \frac{\Lambda}{2\pi}\sum_{n=1}^{\infty}\frac{a_n}{n}\cos(\frac{2n\pi}{\Lambda}x)e^{-\frac{2n\pi}{\Lambda}y}\right) dy \tag{3.12}$$

and the Newtonian field in the two x and y directions are given by:

$$f_x = -2\pi G\rho_0 \sum_{n=1}^{\infty} a_n \sin(\frac{2n\pi}{\Lambda}x)e^{-\frac{2n\pi}{L}y}dy \tag{3.13}$$

$$f_y = -2\pi G\rho_0 \left(-\frac{a_0}{2} + \sum_{n=1}^{\infty} a_n \cos(\frac{2n\pi}{\Lambda}x)e^{-\frac{2n\pi}{L}y}\right) dy \tag{3.14}$$

Analogous formulae can be calculated for a Fourier integral expansion of a non-periodic density distribution.

Example: In the case $\rho_x(x) = \cos\left(\frac{2\pi}{\Lambda}x\right)$, it follows that $a_{n\neq 1} = 0$ and $a_1 = 1$, which implies from eq.3.13 and 3.14 that f_x and f_y are given by the following equations:

$$f_x = -2\pi G\rho \sin(\frac{2\pi}{\Lambda}x)e^{-\frac{2n\pi}{\Lambda}y}dy \quad (3.15)$$

$$f_y = -2\pi G\rho \cos(\frac{2\pi}{\Lambda}x)e^{-\frac{2n\pi}{\Lambda}y}dy \quad (3.16)$$

Given a sinusoidal mass density distribution in x, the induced force fields are periodical in x as the mass density and they decay exponentially with the distance y.

Torque solution for our test mass geometry

In the following subsection I will present the solution of eq.3.14 and 3.13 in the case of the geometry, that we adopted for our test masses (see fig.3.2). I assume now that the density modulation $\rho_x(x)$ is a square wave function with amplitude 1, symmetric with respect to zero, of width W and periodicity Λ. This function inside the interval $-\Lambda/2 < x < \Lambda/2$ is represented by the equation:

$$\rho_x(x) = \frac{1}{2}\left(\mathrm{Sign}(W + 2x) + \mathrm{Sign}(W/2 - x)\right) \quad (3.17)$$

where the function $\mathrm{Sign}(x)$ gives -1, 0 or 1 depending on whether x is negative, null, or positive.

The transform series of this square wave has the following Fourier coefficients:

$$a_0 = \frac{2W}{\Lambda} \quad (3.18)$$

$$a_{n>0} = \frac{2\sin(\frac{n\pi W}{\Lambda})}{n\pi} \quad (3.19)$$

and therefore its gravitational potential is given by the formula:

$$\phi(x,y) = -2\pi G(\rho_1 - \rho_2)\left(-\frac{W}{\Lambda}y + \frac{\Lambda}{\pi^2}\sum_{n=1}^{K}\frac{\sin(\frac{n\pi W}{\Lambda})}{n^2}\cos(\frac{2n\pi}{\Lambda}x)e^{-\frac{2n\pi}{\Lambda}y}\right)dy \quad (3.20)$$

ρ_1 and ρ_2 are the mass densities of the two metals constituting the mass density contrast, which is associated with the square wave. Because the eq.3.20 has been numerically found to very quickly converge as a function of K, for practical purposes K can be chosen as small as 10.

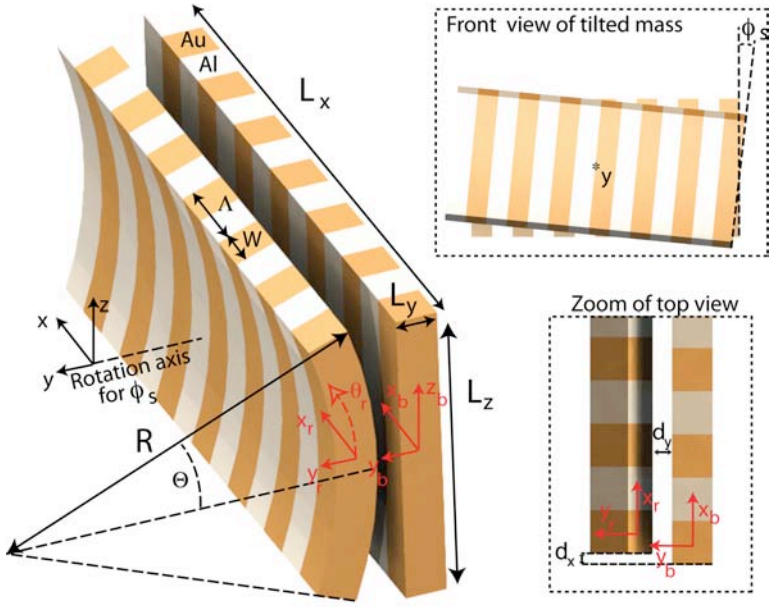

Figure 3.2: Schema representing the test masses (not in scale). The case of the tilt mass is analysed in section 3.6.

Under the small angle hypothesis, I integrate now the previous potential over all the dimensions of the source and test mass: for the flat bar I integrate over its thickness L_y in the y direction; for the curved rib, which has radius R, I integrate over its extension L_z in the z direction and over the width W in the x direction (see fig.3.2). Assuming $\Theta = \arcsin(L_z/R)$, the integral is expressed by the equation:

$$\Phi(d_x, d_y) = \int_{-W/2}^{W/2} \int_{-\Theta}^{\Theta} \int_{\frac{R\theta^2}{2}}^{L_y + \frac{R\theta^2}{2}} \int_{0}^{L_y} R\cos\theta\, \phi(x_r + d_x, d_y + y_b + y_r) dy_b dy_r d\theta_r dx_r \quad (3.21)$$

where d_x and d_y are the distances as shown in fig.3.2. I multiply the integral by the mass density contrast $(\rho_1 - \rho_2)$ of the curved mass and the number of ribs L_x/Λ, where L_x is the total length of the mass in the x direction.

After solving all the integrals of eq.3.21 (see appendix A), I find that the gravitational potential between the masses is expressed by the equation:

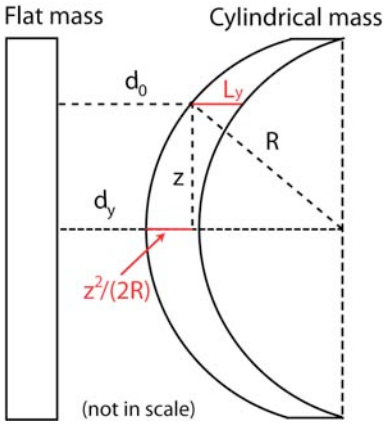

Figure 3.3: Schema of a lateral section ($x = const$) of the test masses.

$$\Phi\left(d_x, d_y\right) = -2\pi G(\rho_1-\rho_2)^2\frac{L_x}{\Lambda}[-\frac{2R\sin\Theta L_y^3 W^2 d_y}{\Lambda}+\sum_{l=1}^{K}\left(\frac{\Lambda}{2n\pi}\right)^4\frac{\left(2\sin(\frac{n\pi W}{\Lambda})\right)^2}{n\pi}$$
$$\cdot\cos(\frac{n2\pi}{\Lambda}d_x)\left(1-e^{-\frac{2\pi n L_y}{\Lambda}}\right)^2 e^{-\frac{2n\pi d_y}{\Lambda}}\sqrt{\frac{\Lambda R}{n}}\,\mathrm{erf}(\sqrt{\frac{n\pi R}{\Lambda}}\Theta)] \qquad (3.22)$$

$\mathrm{erf}(z)$ is the error function or integral of the Gaussian distribution and is given by the equation:

$$\mathrm{erf}(z) = \frac{2}{\sqrt{\pi}}\int_0^z e^{-t^2}dt \qquad (3.23)$$

The final expressions for the x and y components of the gravitational force are given by the equations:

$$F_x = -2\pi G(\rho_1-\rho_2)^2\frac{L_x}{L}\sum_{n=1}^{K}\left(\frac{\Lambda}{2n\pi}\right)^3\frac{\left(2\sin(\frac{n\pi W}{\Lambda})\right)^2\sin(\frac{n2\pi}{\Lambda}d_x)}{n\pi}\left(1-e^{-\frac{2\pi n L_y}{\Lambda}}\right)^2$$
$$\cdot e^{-\frac{2n\pi d_y}{\Lambda}}\sqrt{\frac{\Lambda R}{n}}\,\mathrm{erf}(\sqrt{\frac{n\pi R}{\Lambda}}\Theta) \qquad (3.24)$$

$$F_y = -2\pi G(\rho_1-\rho_2)^2\frac{L_x}{\Lambda}\Big(\frac{2R\sin\Theta L_y^3W^2}{\Lambda}+\sum_{n=1}^{K}\left(\frac{\Lambda}{2n\pi}\right)^3\frac{\left(2\sin(\frac{n\pi W}{\Lambda})\right)^2}{n\pi}$$
$$\cdot\cos(\frac{n2\pi}{\Lambda}d_x)\left(1-e^{-\frac{2\pi nL_y}{\Lambda}}\right)^2 e^{-\frac{2n\pi d_y}{\Lambda}}\sqrt{\frac{\Lambda R}{n}}\,\mathrm{erf}(\sqrt{\frac{n\pi R}{\Lambda}}\Theta)) \quad (3.25)$$

The torque, which is acting on the float, is given by the vector product $\vec{R}\times\vec{F}$. $\vec{R}$ is the vector connecting the center of rotation of the float with the center of mass (CM) of the curved mass and $\vec{F}$ is the force acting on the masses, $\vec{F}=(F_x,F_y,0)$. If R_{float} is the distance between the rotation axis of the float and the center of mass of the curved mass and if (d_x,d_y,d_z) is the vector connecting the centers of mass of the two masses, $\vec{R}$ is simply given by $(d_x,d_y+R_{\mathrm{float}},d_z)$. Therefore the component of the torque on the rotation axis of the float is given by the formula:

$$\Gamma_z = \vec{R}\times\vec{F}\cdot(0,0,1) = d_yF_x+d_xF_y-F_xR_{\mathrm{float}} \quad (3.26)$$
$$\approx -F_xR_{\mathrm{float}} \quad (3.27)$$

The last approximation is possible because d_x (less than $3.5mm$) and d_y ($\sim 10-100\mu m$) are much smaller than R_{float} and because F_x and F_y have similar peak to peak amplitudes. As definition of the peak to peak torque I use the following equation:

$$\Gamma_{pp}(d_y) = R_{\mathrm{float}}\left(\frac{F_x(\Lambda/4,d_y)-F_x(\Lambda/4+\Lambda,d_y)}{2}-F_x(\Lambda/4+\Lambda/2,d_y)\right) \quad (3.28)$$

which will exclude any linear drift in the torque due to the relative displacement of the centers of mass. The analytical model, which I developed here, does not take into account this torque drift, because the number of bars of the test mass is supposed infinite. However the numerical model, which we developed for comparison (see section 3.6), will take it in consideration. So for consistency I use the same definition in both cases, because in the future it might be possible to update the analytical model and include also this extra torque due to the CM displacement.

3.2.2 Results and optimisation of the test masses

In this subsection I present all the results, which are obtained by using the analytical model of eq.3.24, 3.25 and 3.28. When not specified otherwise, the model parameters are chosen as in the table 3.1:

Description	**Parameter**	**Value**
Periodicity of density contrast	Λ	$400\mu m$
Width of the gold bar/ribs	W	$200\mu m$
Components of the Fourier series	K	10
Gold density	$\rho_1 = \rho_{Au}$	$19320 kg/m^3$
Aluminium density	$\rho_2 = \rho_{Al}$	$2700 kg/m^3$
Distance between the masses	d_y	$15\mu m$
Radius of the cylindrical mass and of the float	$R = R_{\text{float}}$	$46.86mm$
Extension of the test masses in the z direction	L_z	$10mm$
Length of the test mass in the x direction	L_x	$4cm$
Thickness of the test mass in the x direction	L_y	$150\mu m$

Table 3.1: Parameters of the test masses which I assumed during the calculations.

First of all I plot the two components of the force, F_x and F_y, over the displacement of the masses in the x direction (fig.3.4), where I did not considere the torque offset of F_y: I find that both forces are out of phase by $\pi/2$ and have the same amplitudes $\sim 2.1 \times 10^{-14} N$. The equivalent torque is given by the eq.3.27 and it is equal to $8.7 \times 10^{-16} Nm$. By looking at the amplitude spectrum of the expected torque in fig.3.5, it is evident that only the odd harmonics of the main spectral component are present and they quickly decay as $n^{-9/2}$ (n is the harmonic number, see eq.3.24). The hypothesis, that it is sufficient to sum until $K = 10$ in eq.3.24, is satisfied. In fig.3.6 I also show the Newtonian signal, which exponentially decreases with the distance. According to eq.3.24, the decay constant of the exponential is $\Lambda/(2\pi)$, which in our case is $\approx 64\mu m$.

Thanks to the analytical model I developed, it was also possible to identify the optimal parameters, which give the maximum Newtonian signal and keep the manufacture of the masses as simple and robust as possible. For example, I found that, for any given choice of the parameters, the maximum gravitational signal is obtained when the width of the gold bars and ribs, W, is half of the pitch Λ (see fig.3.7). From eq.3.24 and fig.3.8 I also found that for a given width W, I obtain 80% of the maximum signal with a thickness, L_y, that is just 3/4 of the width W. In the case of $W = 200\mu m$, the 80% of the maximum signal

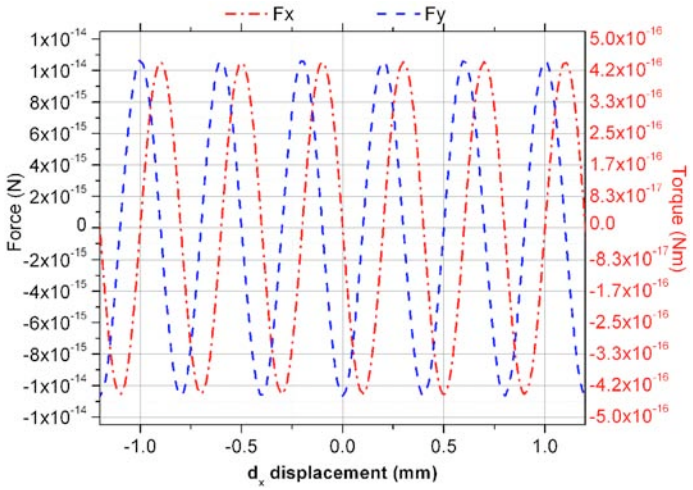

Figure 3.4: F_x and F_y versus the displacement of the test masses in the x direction. The equivalent total torque is reported on the left side of the graph .

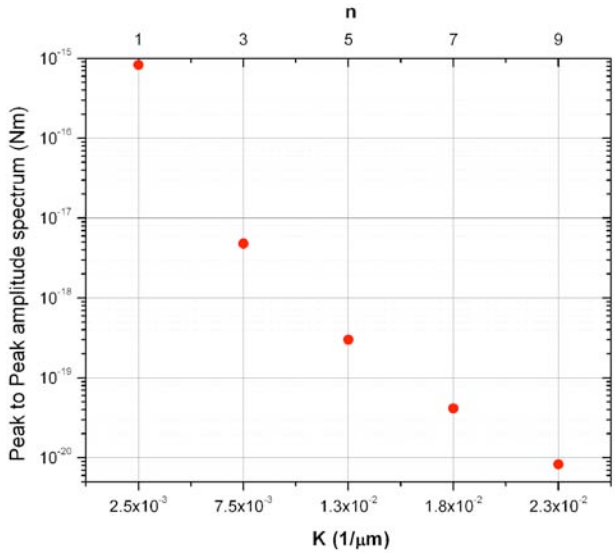

Figure 3.5: Components of the amplitude spectrum of the Newtonian peak to peak torque at the odd harmonics of the main one at $1/400\mu m^{-1}$.

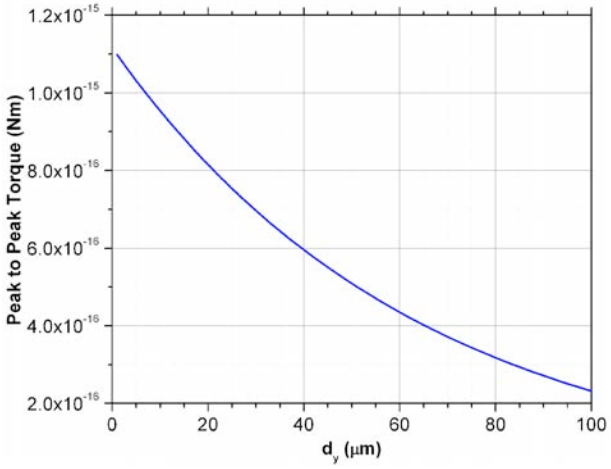

Figure 3.6: Peak to peak Newtonian torque versus the distance d_y between the test masses.

is reached for just $L_y = 150\mu m$. As shown in fig.3.9 the Newtonian torque is expected to increase as I increase the pitch of the mass density modulation. As it will be discussed in section 3.6, the amplitude of possible Yukawa torques at short distances increases as the pitch is decreased, because the total number of bars and ribs per unit of length is increased. Therefore a balanced choice of the pitch Λ has to be made to optimise both the Newtonian and Yukawa signals for the ISL test. I also found that it is not worthwhile to increase the vertical size, L_z, of the test masses beyond $10mm$ (see fig.3.10). In the same figure with the blue rectangular box I also show the signal loss due to the aluminium horizontal bars, which we designed to make the test masses more rigid and robust (see fig.2.2). This signal loss is just a negligible 5%.

As I will discuss in section 3.6, we also developed a numerical model to predict the Newtonian signal in the limit of the Yukawa signal for infinite range, λ. The results of the numerical model are in agreement with the ones of analytical model. With the numerical model I also studied the effect of a possible misalignment angle, ϕ_s, between the bars and ribs of the flat and curved mass (see fig.3.2). From fig.3.11 it is clear that it is possible to tolerate even an misalignment angle $\sim 1^\circ$ without losing more than 10% of the expected Newtonian signal.

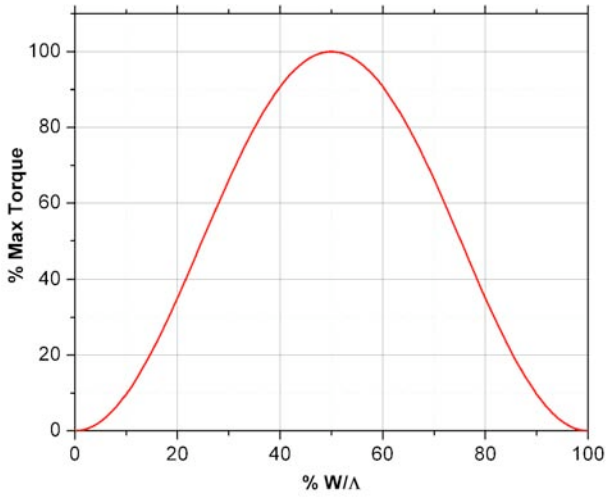

Figure 3.7: Percentage of the maximum torque versus the width percentage of the gold bars-ribs with respect to the pitch Λ.

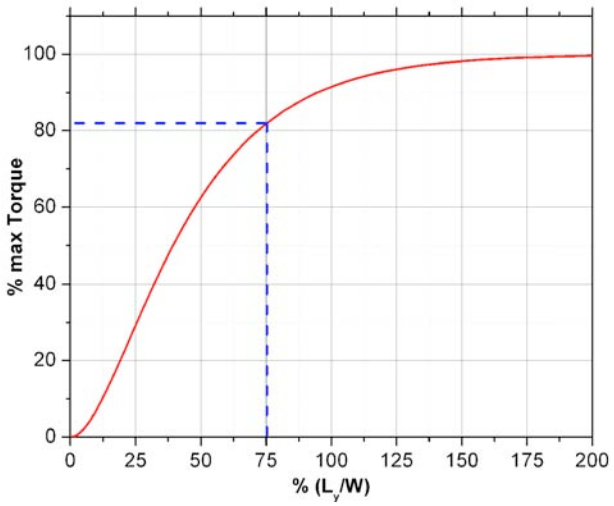

Figure 3.8: Percentage of the maximum torque versus the thickness of the bars and ribs.

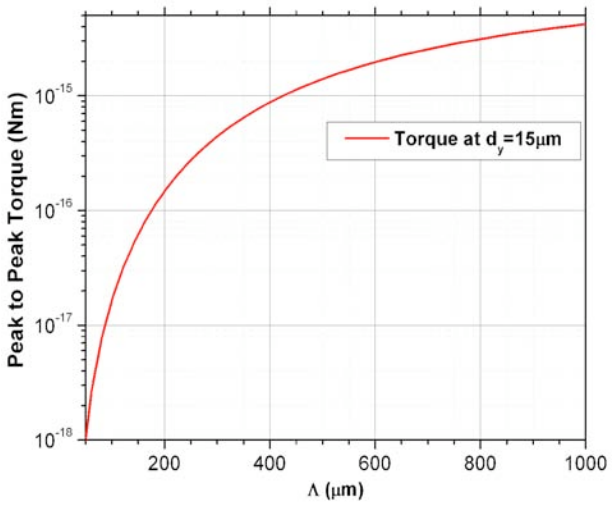

Figure 3.9: Peak to peak torque versus the pitch Λ of the mass density modulation.

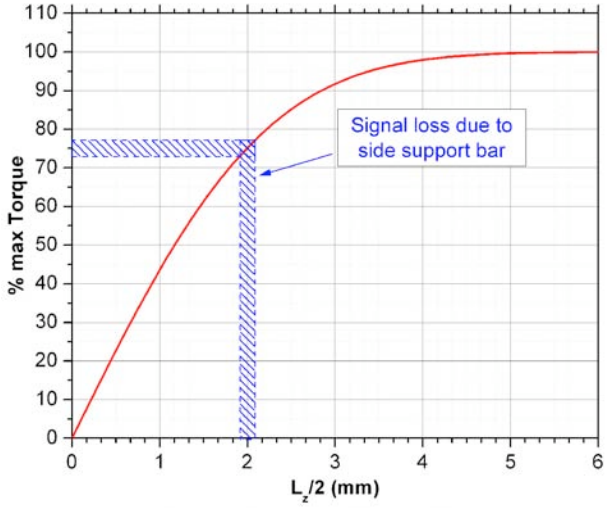

Figure 3.10: Percentage of the maximum torque versus $L_z/2$, half the z-extension of the test masses.

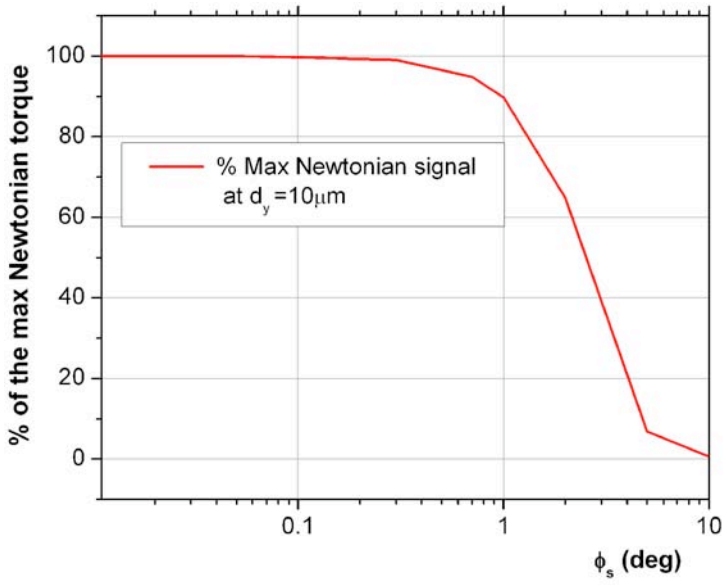

Figure 3.11: Percentage of the signal loss, which is due to a misalignement angle ϕ_s between the facing bar and ribs of the two masses. It was obtained through numerical simulation (see section 3.6).

3.2.3 Error budget on the Newtonian predictions

In this subsection I discuss the error budget for the Newtonian signal of eq.3.24 and 3.28 to evaluate, which are the tolerances to measure gravity within 10% at a distance of $15\mu m$ between the masses.

The percentage error on the Newtonian torque Γ is given by the expression:

$$\frac{\sigma_{\Gamma_{pp}}}{\Gamma_{pp}} = \sqrt{\sum_{\alpha} \left(f_\alpha \frac{\sigma_\alpha}{\alpha} \right)^2} \tag{3.29}$$

where the sum is performed in quadrature on all the parameters α. For all the parameters apart from W and L_z, f_α had been analytically obtained from eq.3.24 and 3.28 according to the next equation:

$$f_\alpha = \frac{\alpha}{\Gamma_{pp}} \frac{\partial \Gamma_{pp}}{\partial \alpha} \tag{3.30}$$

For L_z and W, if $\sigma_{\Gamma_{pp}}$ is defined by:

$$\sigma_{\Gamma_{pp}} = \Gamma_{pp}(\alpha + \sigma_\alpha) - \Gamma_{pp}(\alpha) \tag{3.31}$$

$f_{L_z}$and f_W are given by the dominant term of the equation:

$$f_\alpha = \frac{\Gamma_{pp}(\alpha+\sigma_\alpha)-\Gamma_{pp}(\alpha)}{\Gamma_{pp}(\alpha)}\frac{\alpha}{\sigma_\alpha} \tag{3.32}$$

In fig.3.12 I plot the percentage error on the torque given the error on W and L_z. Given the numerical values of all the parameters α of table 3.1, f_α are shown in table 3.2 for a distance of $15\mu m$ between the masses. In the same table under the label σ_α/α, I report the percentage error on every parameter such that, when they are all summed in quadrature according to eq.3.29, the total error on the Newtonian signal is 10%. I supposed that the contributions of each parameter on the total Newtonian error are all the same. Therefore because there are 10 parameters, in table 3.2 I report the percentage error on each α such that:

$$\frac{\sigma_\alpha}{\alpha}f_\alpha = \frac{10\%}{\sqrt{10}} = 3.16\% \tag{3.33}$$

In the same table, under the label σ_α, I reported the actual errors on each parameter, which correspond to the previously defined σ_α/α

$\boldsymbol{\alpha}$	f_α	σ_α/α	σ_α
ρ_{Au}	2.32	1.36%	$253 g/m^3$
Λ	2.16	1.45%	$6.3\mu m$
L_x	1	3.2%	$1.26mm$
R_{float}	1	3.2%	$1.6mm$
L_y	0.5	6.3%	$9.5\mu m$
R	0.5	6.3%	$3.2mm$
ρ_{Al}	0.32	9.5%	$253 kg/m^3$
W	$(-1+\sin(\pi/2\frac{\sigma_W}{W})^3)/\frac{\sigma_W}{W}$	$\approx 10\%$	$20\mu m$
d_y	0.15	20.2%	$3.2\mu m$
L_z	$(-1+19Erf(0.1+0.1\cdot\frac{\sigma_{Lz}}{Lz}))/\frac{\sigma_{Lz}}{Lz}$	27%	$2.7mm$
	TOTAL	10%	

Table 3.2: Table of all the coefficients f_α to estimate the percentage total error on the estimate of the Newtonian signal. σ_α/α is the percentage error on each parameter α, such that their sum in quadrature gives 10% error of the Newtonian signal according to eq.3.29. σ_α is the numerical error on α corresponding to each percentage error σ_α/α.

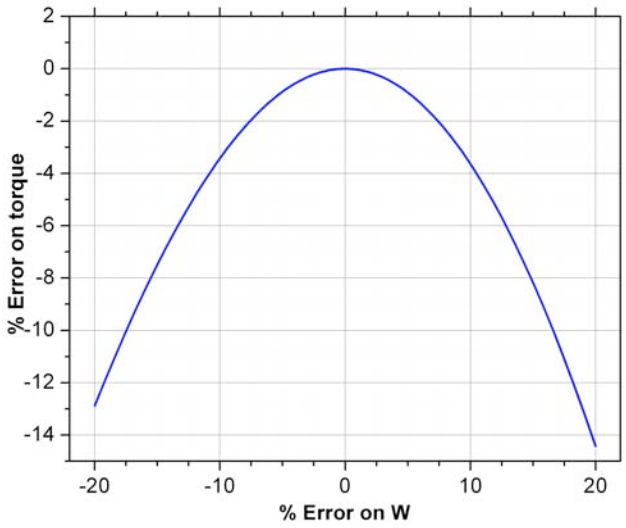

Figure 3.12: Percentage error on the torque due to the percentage error on the width of a gold stripe, W.

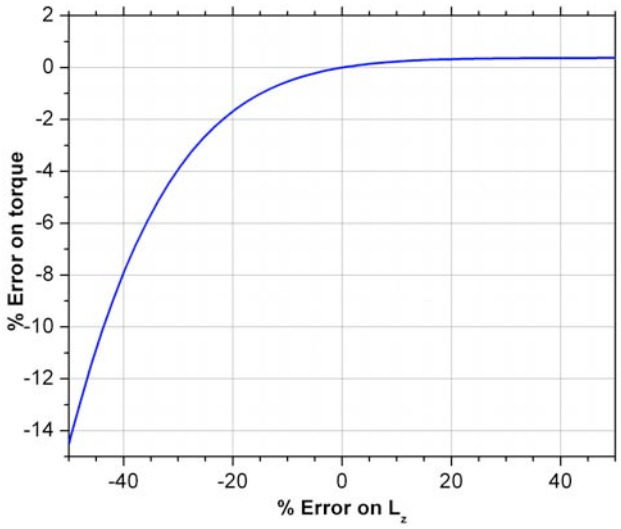

Figure 3.13: Percentage error on the torque for a percentage error on L_z.

3.2.4 Newtonian Torques between masses, supports and micropositioner

In this section I will briefly discuss the Newtonian torques, which are acting on the torsion balance and which are given by the gravitational interaction between all the elements supporting the test masses. I will compare them with the expected peak to peak torque given by the mass density modulation. By using the analytical formula for the Newtonian potential, which is given by a source parallelepiped [55], I found the expression of its force field at a generic point in the space. With Wolfram Mathematica I numerically integrated the resulting torque (given by eq.3.26) over a test parallelepiped, which is attached to the float shell. I therefore calculated the torques for all the different combinations of the elements of the supports and masses. The elements are given by the following list:

1. a lug attached to the torsion balance, which is modelled as a the difference of two copper parallelepipeds. The parallelepipeds are slightly offset such that the central cavity is open on one side (see fig.3.15). This lug is the support for the curved test mass.

2. a support for the flat mass, which is attached to the top of a micropositioner. As for the lug, this part has been modelled as a the difference of two copper parallelepipeds, which are slightly offset to have the resulting cavity open on the bottom side (see fig.3.14). The design of this support had been optimised to minimise the torque it exerts on the lug and on the curved test mass.

3. the top moving part of the micropositioner, which had been modelled as a simple titanium parallelepiped and which is positioned under the support of the flat mass.

4. the source and the test masses had been modelled as simple gold parallelepipeds.

I evaluated the torques, which are given by all the possible combinations of the previous elements versus d_x with $d_y = 15\mu m$ fixed (fig.3.16) and versus d_y with $d_x = 2mm$ (fig 3.17). The result is that, for example, at a distance of $15\mu m$, the Newtonian signal, which is given by the support of the test mass, is 100 times bigger than the expected peak to peak signal due to the density

modulation. This large torque drift will not be a problem during the experiment because it is possible to fit it out of the measured data and it will not influence the signal at the spatial frequency of interest, which is associated with the density modulation. However this Newtonian drift, if not minimised, might force us to increase the dynamic range of the SSTB torque measurements and possibly lose torque sensitivity.

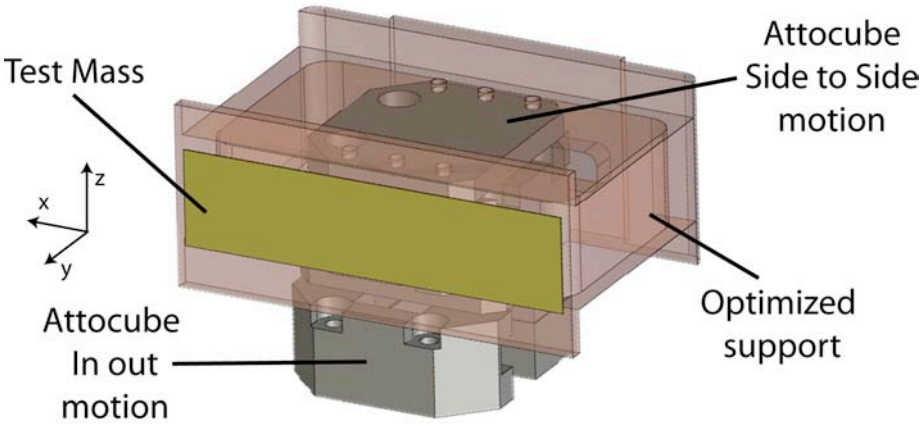

Figure 3.14: Attocubes and support of the flat test mass.

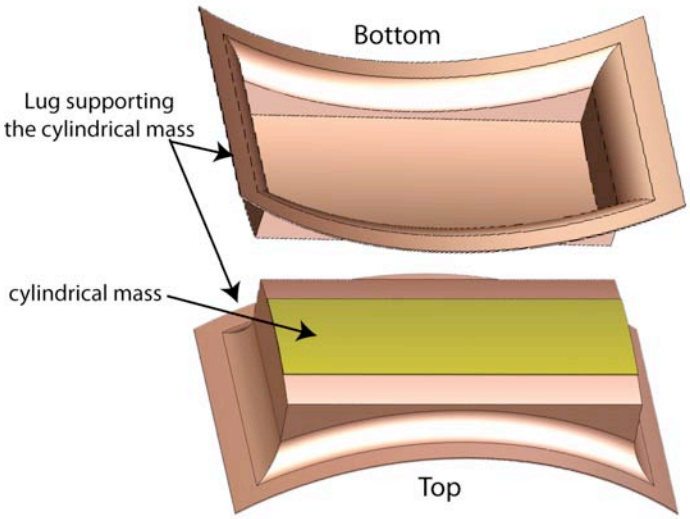

Figure 3.15: Top and bottom view of the curved support for the test mass which has to be attached to the float.

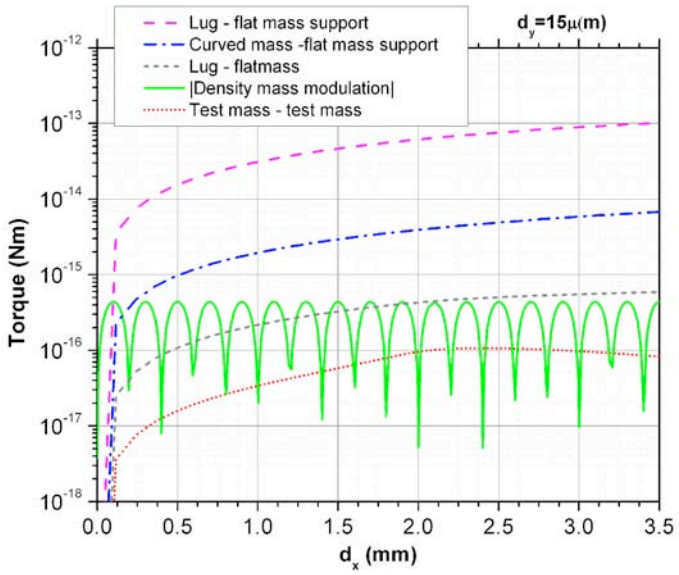

Figure 3.16: Torque versus the distance d_x between the centers of mass of the masses.

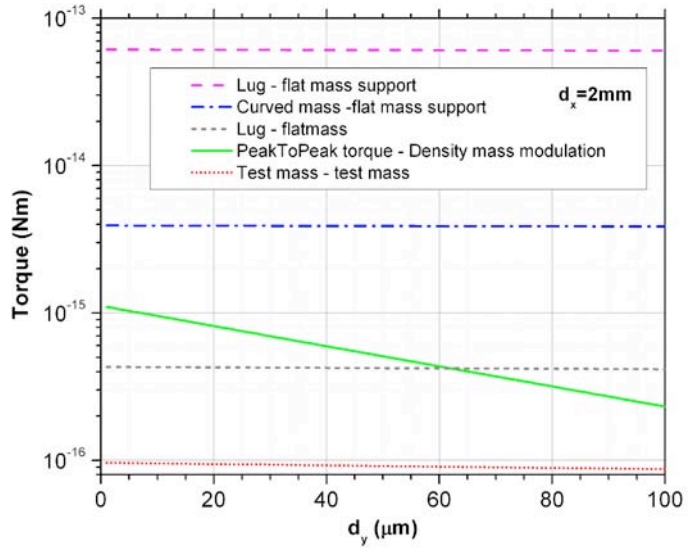

Figure 3.17: Torques of the test masses and supports versus the distance d_y between the surface of the test masses.

3.3 Electrostatic torques

In this section I will analyse some of the possible torques, which might arise between the test masses due to the electrostatic forces. Firstly I will consider the case of the torques, which are induced by periodic perturbations of the topographies of the test masses. Secondly I will model the torques, which are due to periodic surface voltage modulations on the masses in the case of perfect topographies, because contact potentials [45] at the interface between the gold and aluminium stripes are known to induce such voltage modulation. Finally I will model the torques due to the coupling between periodic surface corrugations and potentials.

3.3.1 Torque due to periodic fluctuations of the surface topography

Given a plate and cylinder facing each other, I want to characterise the force due to periodic fluctuations of the topographies of their surfaces. Thanks to the proximity force theorem [12] I model this force as the integral sum over the surface of all the forces associated with infinitesimal cross sections facing each other. I do not take into account the contributions of the forces between cross sections not facing each other. At distances, which are much smaller than the surface dimensions, this approach is considered a reasonable approximation [12]. I start to analyse an infinitesimal cross section of the two surfaces of area dA, whose capacitance is given by:

$$dC = \frac{\epsilon dA}{\bar{d}} \tag{3.34}$$

where $\epsilon = 8.854 \times 10^{-12} F/m$ is the vacuum permittivity and $\bar{d}$ is the average distance between the two infinitesimal plates. $\bar{d}$ is the sum of the average distance, d_0, between the plate and the cylinder on the considered small cross section and the fluctuations, $f_1$and f_2, of the height of the flat and cylindrical surfaces. For small distances z from the symmetry plane of the cylinder, which is perpendicular to the flat mass (see fig.3.3), the distance d_0 can be expressed as:

$$d_0 \approx d_y + \frac{z^2}{2R} \tag{3.35}$$

d_y is the distance between the cylinder and the flat mass and R is the radius of the cylinder. dC is given by the following equation:

$$dC(x,z,d_x) = \frac{\epsilon dA}{d_y + \frac{z^2}{2R} + f_1(x,z) - f_2(x-d_x,z)} \tag{3.36}$$

where (x,z) are the coordinates of the infinitesimal cross sections over the surfaces of the masses and d_x is the displacement of the flat mass with respect to the cylindrical one in the x direction. For simplicity, I name here d_x as ξ and I assume that the fluctuations are smaller than the minimum distance between the plates, $f_1(x) - f_2(x-\xi) \ll d_y$. In this case the previous expression of the capacitance is expressed by the equation:

$$dC(x,z,\xi) \approx \frac{\epsilon dA}{d_y + \frac{z^2}{2R}} \left[1 - \frac{f_1(x,z) - f_2(x-\xi,z)}{d_y + \frac{z^2}{2R}} + \left(\frac{f_1(x,z) - f_2(x-\xi,z)}{d_y + \frac{z^2}{2R}} \right)^2 \right] \tag{3.37}$$

Given the formula for the electrostatic energy between the two capacitor plates, $dE(x,z,\xi) = 1/2V^2 dC(x,z,\xi)$, which is due to a voltage difference V between the masses and the work done by the voltage supply to keep the voltage constant, $dW(x,z,\xi) = -V^2 dC(x,z,\xi)$, the resulting force in the ξ direction is given by the equation [28]:

$$dF(x,z,\xi) = +\frac{1}{2} V^2 \partial_\xi dC(x,z,\xi) \tag{3.38}$$

I substitute now eq.3.37 in eq.3.38 and dA with $dxdz$. I integrate the resulting force dF over the surface of the plate to obtain the total force F:

$$F(\xi) = \int_{-L_z/2}^{L_z/2} \int_{-L_x/2}^{L_x/2} dF(x,z,\xi) dx dz \tag{3.39}$$

where L_z and L_x are the dimensions of the flat test mass. To solve the integral I need to separate it in the two variables of integration, x and z. This is possible if the corrugations are periodic in x and independent from z. Therefore $F(\xi)$ becomes the equation:

$$F(\xi) = \frac{1}{2}V^2\epsilon[\int_{-L_z/2}^{L_z/2} \frac{dz}{\left(d_y + \frac{z^2}{2R}\right)^2}\partial_\xi \int_{-L_x/2}^{L_x/2} f_2(x-\xi)dx + \tag{3.40}$$

$$- 2\int_{-L_z/2}^{L_z/2} \frac{dz}{\left(d_y + \frac{z^2}{2R}\right)^3}\partial_\xi \int_{-L_x/2}^{L_x/2} f_1(x)f_2(x-\xi)dx + \tag{3.41}$$

$$+ \int_{-L_z/2}^{L_z/2} \frac{dz}{\left(d_y + \frac{z^2}{2R}\right)^3}\partial_\xi \int_{-L_x/2}^{L_x/2} f_2(x-\xi)^2dx] \tag{3.42}$$

The first double integral is null because f_2 has null mean. The third one is null too because it is the derivative in ξ of the variance of f_2, which for a periodic function is independent of where it is taken. The second double integral is solved and approximated for $Rd_y \ll L_z$, obtaining:

$$F(\xi) = -V^2\epsilon\frac{3\pi\sqrt{2R}}{8d_y^{5/2}}\partial_\xi corr_{12}(\xi) \tag{3.43}$$

$corr_{12}(\xi)$ is the correlation of f_1 and f_2 over the x direction and is given by the equation:

$$corr_{12}(\xi) = \int_{-L_x/2}^{L_x/2} f_1(x)f_2(x-\xi)dx \tag{3.44}$$

In the case f_1 and f_2 are periodic functions with period Λ and amplitudes $A_1$and $-A_2$ ($f = A\sin(2\pi d_x/\Lambda)$) from eq.3.43 and 3.44. The amplitude of the resulting torque is given by the equation:

$$\Gamma_{cor} = R_{\text{float}}\epsilon V^2\frac{3}{8}\frac{\pi^2\sqrt{2R}}{d_y^{5/2}}\frac{L_x}{\Lambda}A_1A_2\sin(2\pi d_x/\Lambda) \tag{3.45}$$

Assuming a periodic corrugation of $0.5\mu m$ with the same period of the density modulation and a voltage difference of $50mV$, the expected peak to peak torque for our masses at a distance of $15\mu m$ is $5.67 \times 10^{-14}Nm$.

3.3.2 Torque due to periodic fluctuations of the surface potentials

I consider now the case of test masses with perfect topographies ($f_1 = f_2 = 0$) but with periodic voltages across their surfaces, which are due to the contact potentials [49] between the gold and aluminium stripes because of their different

work functions [45]. Because for the aluminium the work function is between 4.06 and $4.26eV$ and for the gold is between 5.47 and $5.31eV$ [49], I expect a contact potential difference within 1 and $\approx 1.4V$ between the two metals. By covering the gold and aluminium surfaces with an uniform gold layer of $1\mu m$ thickness, this periodic fluctuation of the surface potentials is expected to be null. However if the contact potentials are not completely screened by the gold layer, the associated torque might mimic a possible violation of the ISL of gravity. Therefore it is important to model this signal to detect it within the experimental data.

The analytical model

I start to model the torque on the masses given by non-uniform voltages V_1 and V_2 on the flat and cylindrical surfaces. As done in section 3.3.1, I use the proximity force theorem [12] to model the force on an infinitesimal cross section of the two surfaces and I obtain the total force by integrating the result on the surface dimensions, x and z. The infinitesimal capacitance, dC, and its force dF between the two cross-sections are given by the following equations

$$dC(x,z,\xi) \approx \frac{\epsilon dxdz}{d_y + \frac{z^2}{2R}} \tag{3.46}$$

$$dF = \frac{1}{2}(V_1(x,z) - V_2(x-\xi,z))^2 dC(x,z) \tag{3.47}$$

ξ models the translation of one mass with respect to the other one in the x direction and eq.3.47 follows from [77]. The total force is given by the equation:

$$F(\xi) = \int_{-L_z/2}^{L_z/2}\int_{-L_x/2}^{L_x/2} dF(x,z,\xi)dxdz \tag{3.48}$$

As in the case of the varying topography, I suppose that $V_1(x,z)$ and $V_2(x,z)$ are periodic in x with period Λ and independent from z. I separate the integration of eq.3.48 into the product of two integrals in z and x obtaining, for small d_y, the equation:

$$F(\xi) = -\epsilon \frac{2\sqrt{2R}}{\sqrt{d_y}} \arctan\left(\frac{L_z}{2\sqrt{2d_y R}}\right) \partial_\xi corr_{12}(\xi) \quad (3.49)$$

$$\approx -\epsilon \frac{\sqrt{2R}\pi}{\sqrt{d_y}} \partial_\xi corr_{12}(\xi) \quad (3.50)$$

where

$$corr_{12}(\xi) = \int_{-L_x/2}^{L_x/2} V_1(x) V_2(x-\xi) dx \quad (3.51)$$

The eq.3.50 is an approximation of eq.3.49 within $\approx 15\%$, given the numerical value of the parameters for our test masses of table 3.1.

Example of sin function potentials

In the simple case where V_1 and V_2 are sine functions with period Λ and amplitudes V_{10} and V_{20} and supposing that L_x is an integer multiple of Λ, $\partial_\xi corr_{12}(\xi)$ is given by the equation:

$$\partial_\xi corr_{12}(\xi) = -\pi \frac{L_x}{\Lambda} \sin(2\pi/\Lambda\xi) V_{10} V_{20} \quad (3.52)$$

and that:

$$\Gamma \approx -R_{\text{float}} \epsilon \frac{2\sqrt{2R}\pi^2}{\sqrt{d_y}} \frac{L_x}{\Lambda} \sin(2\pi/\Lambda\xi) V_{10} V_{20} \quad (3.53)$$

It is interesting to notice that the predicted torque has opposite phase with respect to the one due to periodic corrugation of eq.3.45 and it differently decays with the distance d_y. It is easy to show that this torque is independent from the the voltage, which is applied between the masses.

Contact potentials

I model here the voltage variations due to the contact potential as square waves V_1 and V_2, which are varying with a period Λ between V_0 and $V_0 + V_c$ and given by the equations:

$$V_1(x) = V_0 + \frac{V_c}{2}\left[\digamma(2\pi x/\Lambda) + 1\right] \tag{3.54}$$

$$V_2(x-\xi) = V_0 + \frac{V_c}{2}\left[\digamma(2\pi (x-\xi)/\Lambda) + 1\right] \tag{3.55}$$

$\digamma(2\pi x/\Lambda)$ is a representation of the square function with period Λ and amplitude between ± 1 and is given by the equation:

$$\digamma(2\pi x/\Lambda) = \left(\frac{4}{\pi}\sum_{k=0}^{N}\frac{\sin\left((2k-1)2\pi x/\Lambda\right)}{2k-1}\right) \tag{3.56}$$

Supposing that L_x is an integer multiple of Λ, the derivate in ξ of the eq.3.51 with V_1 and V_2, which are given by the eq.3.54 and 3.55, is the expression:

$$\partial_\xi corr_{12}(\xi) = -\frac{L_x}{\Lambda}V_c^2\digamma(2\pi x/\Lambda) \tag{3.57}$$

From eq.3.50 the torque due to contact potentials is given by the equation:

$$\Gamma_{cpt} = -R_{\text{float}}\epsilon\frac{2\sqrt{2R}\pi}{\sqrt{d_y}}\frac{L_x}{\Lambda}V_c^2\digamma(2\pi x/\Lambda) \tag{3.58}$$

For example, assuming a voltage difference $V_c = 1V$, which can be due to the contact potentials between the gold and aluminium stripes, the expected peak to peak torque at $15\mu m$ distance is $1.7 \times 10^{-8} Nm$. This signal is much larger than the other expected signals at the spatial frequency of the density modulation. It is absolutely necessary to cover the gold and aluminium stripes with an uniform gold layer, which will null the voltage modulation due to the contact potentials.

3.3.3 Torque due to coupling between periodic corrugations and potentials

I consider now the most general case with both the corrugations and potentials, which are periodically varying across the surfaces of the test masses. The force on the infinitesimal cross section for this case is given by the following expression:

$$dF(x,z,\xi) = \frac{1}{2}\partial_\xi[\frac{\epsilon dA}{d_y + \frac{z^2}{2R}}(V_1(x-\alpha,z) - V_2(x-\alpha-\xi,z) + \Delta V)^2\cdot$$

$$\cdot \left(1 - \frac{f_1(x,z) - f_2(x-\xi,z)}{d_y + \frac{z^2}{2R}} + \left(\frac{f_1(x,z) - f_2(x-\xi,z)}{d_y + \frac{z^2}{2R}} \right)^2 \right)] \tag{3.59}$$

where, to the surface periodic potentials, I also added a voltage difference, ΔV, which is applied between the masses. For simplicity, the phase between the corrugation and potential functions is chosen to be null, $\alpha = 0$, for each mass. By integrating the previous force over the surfaces of the test masses, according to eq.3.48, eq.3.59 becomes the expression:

$$\begin{aligned} F(\xi) &= F_{cor}(\xi) + F_{pt}(\xi) + \\ &+\epsilon \frac{3\pi\sqrt{2R}}{8 d_y^{5/2}} \partial_\xi \int_{-L_x/2}^{L_x/2} (V_1(x) - V_2(x-\xi))^2 (f_1(x) - f_2(x-\xi))^2 dx \\ &+2\Delta V \frac{\sqrt{R}\pi}{d_y^{3/2}\sqrt{2}} \partial_\xi \int_{-L_x/2}^{L_x/2} (V_1(x) f_2(x-\xi) + V_2(x-\xi) f_1(x)) dx \end{aligned} \tag{3.60}$$

with $F_{cor}(\xi)$ and $F_{pt}(\xi)$ given by the eq.3.43 and 3.50. The fourth term has been obtained by solving the integral in z with the equation:

$$\int_{-L_z/2}^{L_z/2} \frac{\epsilon dz}{\left(d_y + \frac{z^2}{2R}\right)^2} \approx \frac{\sqrt{R}\pi}{d_y^{3/2}\sqrt{2}} \tag{3.61}$$

which is a good approximation within 1% for the parameters of our test masses of table 3.1.

I suppose now that V_1, V_2, f_1 and f_2 are sin functions with period Λ and amplitudes V_{01}, V_{02}, A_1 and $-A_2$. From the general expression of the force of eq.3.60 the torque acting of the torsion balance is given by the equation:

$$\Gamma_{el}(\xi) = \Gamma_{cor} + \Gamma_{pt} + \Gamma_{cor+pt} \tag{3.62}$$

with Γ_{cor} and Γ_{pt} given the eq.3.45 and 3.53 while the Γ_{cor+pt} is given by the following sum:

$$\Gamma_{cor+pt} = \Gamma_{k0} + \Gamma_{k1} + \Gamma_{k0+\Delta V} \tag{3.63}$$

with

$$\begin{aligned}\Gamma_{k0} &= R_{\text{float}}\epsilon\frac{9}{16}\frac{\pi^2\sqrt{R}}{d_y^{5/2}\sqrt{2}}\frac{L_x}{\Lambda}\sin(2\pi d_x/\Lambda) \\ &\quad\cdot\left(A_1A_2V_1^2 - A_1^2V_1V_2 - A_2^2V_1V_2 + A_1A_2V_2^2\right)\end{aligned} \tag{3.64}$$

$$\begin{aligned}\Gamma_{k1} &= R_{\text{float}}\epsilon_0\frac{3}{16}\frac{\pi^2\sqrt{R}}{d_y^{5/2}\sqrt{2}}\frac{L_x}{\Lambda}\sin(4\pi d_x/\Lambda) \\ &\quad\cdot\left(A_2^2V_1^2 - 4A_1A_2V_1V_2 + A_1^2V_2^2\right)\end{aligned} \tag{3.65}$$

$$\Gamma_{k0+\Delta V} = R_{\text{float}}\epsilon\frac{\pi^2\sqrt{R}}{\sqrt{2}d_y^{3/2}}\frac{L_x}{\Lambda}\Delta V\sin(2\pi d_x/\Lambda)\left(A_1V_2 - A_2V_1\right) \tag{3.66}$$

The signal Γ_{cor+pt} for a null voltage difference between the masses, $\Delta V = 0$, is characterised by two spectral amplitudes: one, Γ_{k0}, at the spatial frequency of the density modulation, $1/\Lambda$, and the other one, Γ_{k1}, at its second harmonics. If there is a voltage difference between the masses, another additional term, $\Gamma_{k0+\Delta V}$, is added to the main harmonic. This signal, which is given by eq.3.66, linearly changes with the voltage ΔV which is applied to the masses. The signal Γ_{k1} at the second harmonics of the density modulation is instead independent of the applied voltage.

Γ_{el} is given by the three terms of eq.3.62. According to the presence or not of the corrugations and potentials on the test masses, different combinations of the three signals, Γ_{cor}, Γ_{pt} and Γ_{cor+pt}, might be present in the measured torque as shown in table 3.3. Because the test mass C (see chapter 2) is well covered by a screening gold layer but the test mass A is not, the periodic potentials on the first mass are null but they are not on the second one. When using these two test masses we should measure the signal $\Gamma_{cor} + \Gamma_{cor+pt}$ but not the signal Γ_{pt}, because it has to be null according to the eq.3.53.

For example, if the surface potentials on the mass A are not well screened ($V_1 = 1V$), while on the mass C they are null, if the corrugation amplitudes of both masses are $0.5\mu m$ and if the voltage difference is $50mV$, the expected peak to peak torques at $d_y = 15\mu m$ are $\Gamma_{k0} = 1.7\times10^{-11}Nm$, $\Gamma_{k1} = -5.67\times10^{-12}Nm$ and $\Gamma_{k0+\Delta V} = 10^{-9}Nm$.

If a voltage difference is present between the masses, V_0, because for example

Γ_{el}	$V_1 = V_2 = 0$	$(V_1 \text{xor } V_2) = 0$	$V_1 \neq 0$ and $V_2 \neq 0$
$A_1 = A_2 = 0$	0	0	Γ_{pt}
$(A_1 \text{xor } A_2) = 0$	0	Γ_{cor+pt}	$\Gamma_{pt} + \Gamma_{cor+pt}$
$A_1 \neq 0$ and $A_2 \neq 0$	Γ_{cor}	$\Gamma_{cor} + \Gamma_{cor+pt}$	$\Gamma_{cor} + \Gamma_{pt} + \Gamma_{cor+pt}$

Table 3.3: Components of the electrostatic torque which are not null for different combinations of the surface corrugations and potentials.

of contact potentials, when an opposite voltage V_{daq} is applied to them, ΔV is equal to $V_{daq} - V_0$. If there are just the periodic corrugations present on the test masses and not surface potentials, it is possible to measure V_0 by varying the applied V_{daq} until the measured torque Γ_{cor} is minimum (null) at $V_{daq} = V_0$. If the periodic potentials are also present on the masses, the voltage, $V_{\min}$, which will be found to minimise the measured torque, $\Gamma_{cor} + \Gamma_{cor+pt}$, is not anymore V_0 but the following expression:

$$V_{\min} = V_0 - \frac{2d_y V_1}{3A_1} + \frac{2d_y V_2}{3A_2} \tag{3.67}$$

If it is possible to independently measure V_0 (for example by measuring the torque due to the capacitance between the facing the test masses, see chapter 8) and compare it with the $V_{\min}$, which we measure it by minimising the measured torque at the spatial frequency $1/\Lambda$, we will be able to detect the presence of surface potentials over the masses.

3.4 The Casimir torques

The Casimir force is a macroscopic consequence of the quantisation of the electromagnetic field, which predicts that the quantum vacuum is not empty but filled by the ground state of the quantum electromagnetic field. In the presence of metal plates the possible modes of these zero-point electromagnetic fields are reduced in the area between the plates with respect to the all the possible modes in free space. Because it becomes possible to change the electromagnetic zero-point energy, or Casimir energy, associated with these plates by simply modifying their separation y, a force between them arises. This force which was first predicted by Casimir in 1948 [18] and experimentally verified by Lamoreaux in 1997 [47] (for a review of the theoretical and experimental work on the field see [57][13]), has to be taken into account when testing gravity at very short distances, because it

is the dominant force at distances, which are smaller than a few microns. The Casimir energy density for unit area for two parallel plates of infinite conductivity strongly depends on the distance between the plates because it is given by the equation [18]:

$$E = -\frac{\pi^2 \hbar c}{720 y^3} \tag{3.68}$$

with $\hbar = 1.054 \times 10^{-34} J/s$ the reduced Plank constant and $c = 2.997 \times 10^8 m/s$ the vacuum speed of light.

Two possible lateral forces might be present between our test masses, which are associated with the Casimir forces: the lateral Casimir force due to periodic oscillations of the topography of the test masses and the lateral Casimir force due to the modulations of the plasma wavelength of the gold and aluminium stripes.

3.4.1 Lateral torques due to surface corrugations

Following the approach, which was previously adopted in literature for a sphere-plate [21] and a plate-plate [76], I model here the Casimir force between a cylinder and a plane due to sinusoidal corrugations on both surfaces. For perturbations, f_1 and f_2, of the surface topography with the same assumptions of section 3.3.1, the total force is given by the equation:

$$F(\xi) = \partial_\xi \int_{-L_z/2}^{L_z/2} \int_{-L_x/2}^{L_x/2} \frac{\pi^2 \hbar c dx dz}{720 (d_y + \frac{z^2}{2R} + f_1(x) - f_2(x-\xi))^3} \tag{3.69}$$

When solved as in section 3.3.1, the previous integral becomes the equation:

$$F(\xi) = -\frac{7\hbar c \pi^3 \sqrt{R}}{1536\sqrt{2} d_y^{9/2}} \partial_\xi corr_{12}(\xi) \tag{3.70}$$

with $corr_{12}(\xi)$ given by the eq. 3.44

Periodic case

In the case f_1 and f_2 are sine functions of period Λ and amplitudes A_1 and $-A_2$, from eq.3.70 the torque, which is due to the Casimir force, is given by the equation:

$$\Gamma_{\hbar} = R_{\text{float}} \frac{7\hbar c \pi^4 \sqrt{R}}{1536\sqrt{2} d_y^{9/2}} \frac{L_x}{\Lambda} A_1 A_2 \sin(2\pi/\Lambda\xi) \tag{3.71}$$

For example in the case of corrugations with amplitude of $0.5\mu m$, the the peak to peak torque at $15\mu m$ is $5.2 \times 10^{-16} Nm$ while at $5\mu m$ is $7.3 \times 10^{-14} Nm$.

3.4.2 Lateral torques due modulation in conductivity

A more realistic estimate of the Casimir energy for parallel metallic plates has also to take into account the finite conductivity of the metals (see [58] for a review) and the eq.3.68 has to be corrected with terms, which are powers of the metal plasma wavelength λ_p. In the case where the metals on the surface have different plasma wavelengths, like gold ($\lambda_p = 0.14\mu m$) and aluminium ($\lambda_p = 0.11\mu m$), an additional lateral Casimir force will be present between the masses, which is associated with the correlation of the plasma wavelengths [76]. This force might possibly mimic violations of the inverse square law of gravity. It is possible to make this force null by covering the two surfaces with a uniform $1\mu m$ thick gold layer. It has been numerically [46] and experimentally shown [39] that a $30nm$ gold layer is thick enough to shield the variations of the plasma wavelengths.

3.5 The magnetic torques

During the ISL test of gravity magnetic forces will be acting between the masses, which are due to differences in magnetic susceptibilities, $\Delta\chi = \chi_{Au} - \chi_{Al}$, between the gold and aluminium and to the presence of a magnetic field B_0 perpendicular to the mass surface (see fig.3.18). According to [78][74] the resulting torque is given by the following equation (see appendix B):

$$\Gamma_{\Delta\chi} \approx R_{\text{float}} \frac{\left(\Delta\chi B_0\right)^2 L_x}{8\mu_0} \sin\left(2\pi/\Lambda d_x\right) \int_{-Lz/2}^{Lz/2} \frac{dz}{\sinh(2\pi/\Lambda\left(d_y + z^2/(2R)\right))} \tag{3.72}$$

where $\mu_0 = 4\pi \times 10^{-7} H/m$ is the vacuum permeability. For the magnetic susceptibility of aluminium, $\chi_{Al} = 2.2 \times 10^{-5}$, and gold, $\chi_{Au} = -3.7 \times 10^{-5}$, and a magnetic field of $4\mu T$, the expected torque is $10^{-19} Nm$ at $15\mu m$. With respect to the other expected torques, this torque is negligible, however unwanted contaminants during the manufacture process might possibly increase the magnetic susceptibility contrast and the resulting torque above the noise level of the SSTB.

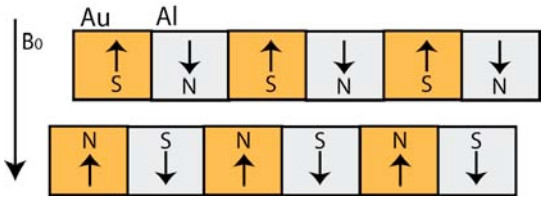

Figure 3.18: Schema illustrating the diamagnetism and paramagnetism properties of the gold and aluminium stripes of the test masses under an incident magnetic field B_0.

3.6 The Yukawa torques

In this section I will consider the possible Yukawa forces which might act between the test masses. I will discuss the numerical model we developed and the method I defined to set upper limits on the allowed Yukawa torques given the geometries of our test masses and the expected sensitivity of the torsion balance.

The classical Newtonian potential solution of the Poisson equation for two point like masses is given by the well known equation:

$$\phi_N(r) = -G\frac{m_1 m_2}{r} \tag{3.73}$$

with G the Newtonian constant. At small ranges there might exist also other forces between the masses, which are mediated by hypothetical bosons of mass m_ϕ (see chapter 1). These forces are governed by the Yukawa potential, which is given by the following equation:

$$\phi_Y(r) = -G\frac{m_1 m_2}{r}\alpha e^{-r/\lambda} \tag{3.74}$$

where α indicates the strength of the interaction and $\lambda = \hbar/(m_\phi c)$ its range.

3.6.1 The numerical model for the Yukawa torques

There are in the literature many analytical models of the possible Yukawa interaction between two masses of different geometries [1] but at present it is not possible to apply any of them to the geometry of our test masses. We developed a numerical model to predict the Yukawa forces between our test masses for any given (α, λ). I start from extending eq.3.74 to the case of two masses of volumes, V_1 and V_2, with mass densities, $\rho_1(x_1, y_1, z_1)$ and $\rho_2(x_2, y_2, z_2)$. The Yukawa com-

ponent of the force in the x direction is given by the following double volume integral:

$$F_x = G \int_{V_1} \rho_1(x_1, y_1, z_1) \frac{d}{dx_2} \left[\int_{V_2} \frac{\rho_2(x_2, y_2, z_2))}{r} \alpha e^{-r/\lambda} dV_1 \right] dV_2 \tag{3.75}$$

with

$$r = \sqrt{(x_1 - x_2)^2 + (y_1 - y_2)^2 + (z_1 - z_2)^2} \tag{3.76}$$

I consider the geometry of our test masses as represented in fig.3.2. I have a flat slab of dimensions $L_x \times L_y \times L_z$ and a section of a hollow cylinder of length L_x, thickness L_y, angular section $\pm\Theta$ and external radius R. The slab and the cylinder are made of two series of alternating gold and aluminum bars or ribs. Each single bar or rib has the same dimensions of the slab or cylinder apart from the extension in the x direction, which is W. Bars and ribs are periodically placed in the x direction with pitch Λ (see fig.3.2). I also include in this numerical model the possibility of rotating one mass with respect to the other one of an angle ϕ_s around the y axis. I want to estimate how much gravitational signal I lose as a function of the misalignment angle ϕ_s between the bars and ribs. The integral of eq.3.75 is the sum of two terms: the Yukawa force between an aluminium slab and an aluminium hollow cylinder of width L_x; the Yukawa force between bars and ribs of width W which have mass density given by $\rho_{Au} - \rho_{Al}$. I will consider just the second term, because it is the only one which depends on the periodicity Λ of the density contrast. The second term is also the only one, which is extracted from the experimental data by spectral analysis. The Yukawa force due to the periodic density contrast in the x direction is given by the equation:

$$F_x\left(d_x, d_y\right) = \alpha G \left(\rho_{Au} - \rho_{Al}\right)^2 \sum_{i=}^{N} \sum_{j=1}^{N} f_{ij}(d_x, d_y) \tag{3.77}$$

$f_{ij}(d_x, d_y)$ is the volume integral between one single bar i and rib j and is given by the equation:

$$f_{ij}(d_x, d_y) = \int_{-L_y/2}^{L_y/2}\int_{-\Theta}^{\Theta}\int_{-W/2}^{W/2}\left(\int_{-L_y/2}^{L_y/2}\int_{-L_z/2}^{L_z/2}\frac{e^{-r_{ij}/\lambda}}{r_{ij}}|_{x_b=-W/2}^{x_b=W/2}dz_b dy_b\right)\cdot \\ \cdot R\cos\theta_r dx_r d\theta_r dy_r \tag{3.78}$$

with the square of r_{ij} given by the following equation:

$$r_{ij}^2 = (x_b - x_r + \Lambda(i-j) + d_x)^2 + (y_b - y_c + d_y + R(1-\cos\theta_r))^2 + \\ + (z_b - R\sin\phi_s)^2 \tag{3.79}$$

The new coordinates (x_b, y_b, z_b) and (x_r, y_r, θ_r) are expressed in the reference systems of each bar and rib (see fig.3.2), N is the total number of bar and ribs and Θ is equal to $\arcsin(L_z/2/R)$. d_x is the distance between the centres of mass of the slab and hollow cylinder projected on the x axis. d_y is the distance in the y direction between the surfaces of the two masses. I also suppose that all the rectangular bars are infinitely long in the z direction. By using the NAG routines [66] and assuming $\alpha = 1$, we numerically integrated eq.3.78. To check the validity of this method and of the numerical integration, I compared the analytical prediction for the Newtonian force of eq.3.24 with the numerical result of the numerical model in the limits $\lambda \to \infty$. Both approaches agree within few parts per thousand.

3.6.2 Setting upper limits on (α, λ)

At the end of the ISL test of gravity at micrometre distances, from the experimental data we would like to set upper limits on the (α, λ) values of the Yukawa forces which are compatible with the measurements. In the next section I will discuss the method I defined to set such upper limits given the torque sensitivity of the torsion balance and the error budget of our Newtonian and Yukawa models. Before deriving them I have to make a small comment about our knowledge of the gravitational constant G.

I implicitly assumed that the value of the gravitational constant is the real one without taking into account the effect of possible long range Yukawa interactions. Under this assumption I will find that an ISL test performed at micrometre

distances constrains also the Yukawa forces with λ as large as desired, which is clearly absurd. To have a method to set upper limits at any λ, I have to also include in the analysis the fact that the knowledge of G is limited at some finite distance. When added together and differentiated with respect to the distance, the Newtonian and the Yukawa potentials of eq.3.73 and 3.74, give a force expressed by the equation:

$$F = -G\frac{m_1 m_2}{r}\left(1 + \alpha\left(1 + r/\lambda\right)e^{-r/\lambda}\right) \tag{3.80}$$

From the previous equation it is clear that the force will be just the Newtonian one only for $r \to \infty$. Only the measurement at this distances can give us the real value of the gravitational constant. Instead from the measurement of the gravitational constant at a finite distance, r_{lab}, in the estimate of the real G I should take into account the possible corrections due to not yet excluded long range Yukawa interactions. The gravitational constant is expressed by the formula:

$$G = \frac{G_{lab}}{(1 + \alpha Y(\lambda))} \tag{3.81}$$

where $Y(\lambda) = (1 + r_{lab}/\lambda)\, e^{-r_{lab}/\lambda}$.

Now given an experimental value for the force $F_{\rm exp}$, I want to set a limit on the possible strength, α, of the Yukawa force with range λ, which is compatible with the measurement. The experimental result is given by the sum of the Newtonian and the Yukawa force:

$$\begin{aligned} F_{\rm exp} &= -G\left(f_N + \alpha f_Y\right) && (3.82)\\ &= -\frac{G_{lab}}{(1 + \alpha Y)}\left(f_N + \alpha f_Y\right) && (3.83) \end{aligned}$$

and α is given by the equation:

$$\begin{aligned} \alpha &= \frac{f_{\rm exp} - f_N}{f_Y(\lambda) - f_{\rm exp} Y} && (3.84)\\ &\approx \frac{f_{\rm exp} - f_N}{f_Y(\lambda)} && (3.85) \end{aligned}$$

Because in the range of interest, $10^{-7} < \lambda < 10^{-3}m$, assuming $r_{lab} \approx 10^{-3}m$, $Y(\lambda)$ can be considered as null. $f_{\rm exp}$ is given by the equation:

$$f_{\rm exp} = -F_{\rm exp}/G_{lab} \tag{3.86}$$

Now if during the experiment we only measure a noise signal, which has null average and standard deviation $\sigma_{F_{\rm exp}}$, the upper limit at the 95% confidence level on the allowed α (averaged for $\alpha > 0$ and $\alpha < 0$) is given by twice the standard deviation on α, σ_α. σ_α is given by the formula:

$$\sigma_\alpha = \sqrt{\left(\frac{\partial\alpha}{\partial f_{\rm exp}}\right)^2 \frac{\sigma^2_{F_{\rm exp}}}{G^2_{lab}} + \left(\frac{\partial\alpha}{\partial f_N}\right)^2 \sigma^2_{f_N} + \left(\frac{\partial\alpha}{\partial f_Y}\right)^2 \sigma^2_{f_Y}} \tag{3.87}$$

where σ_{f_N} and σ_{f_Y} are the standard deviation of our estimates of f_N and f_N. When solved using eq.3.84 the previous equation becomes the following one:

$$\sigma_\alpha = \sqrt{\left(\frac{1}{f_Y}\right)^2 \frac{\sigma^2_{F_{\rm exp}}}{G^2_{lab}} + \left(\frac{f_N}{f_Y}\right)^2 \left(\frac{\sigma_{f_N}}{f_N}\right)^2 + \left(\frac{f_{\rm exp} - f_N}{f_Y}\right)^2 \left(\frac{\sigma_{f_Y}}{f_Y}\right)^2} \tag{3.88}$$

$$= \sqrt{\left(\frac{1}{f_Y}\right)^2 \frac{\sigma^2_{F_{\rm exp}}}{G^2_{lab}} + \left(\frac{f_N}{f_Y}\right)^2 \left[\left(\frac{\sigma_{f_N}}{f_N}\right)^2 + \left(\frac{\sigma_{f_Y}}{f_Y}\right)^2\right]} \tag{3.89}$$

where the last equation is valid for $f_{\rm exp} = 0$. I will assume in the following that the theoretical Newtonian and Yukawa signals are known in total within 10%. It is possible to derive the error budget for the Newtonian signal by the analysis done in section 3.2. It is instead much more complex to derive the error budget for the Yukawa signal, because it implies a set of numerical stochastic simulations to estimate the effect of each parameter on the Yukawa torque. However this Montecarlo analysis is beyond the scope of this PhD thesis and it might be also avoided by developing a substitutive analytical model for the Yukawa torques.

3.6.3 Predictions

I report here some of the results, which I obtained with the numerical simulations for our test masses. The expected Newtonian forces for three different ranges 15, 30 and 50μm versus d_x with $d_y = 15\mu m$ and $\Lambda = 400\mu m$ and assuming $\alpha = 1$ are plotted in fig.3.19. The Yukawa force is rapidly decaying with the range and

it is almost a perfect sinusoid. A spectral analysis of the signals shows that the amplitude at the main spatial frequency ($1/400\mu m^{-1}$) is ten times bigger that its next harmonic at $3/400\mu m^{-1}$. Only the odd harmonics are present in the Yukawa signal.

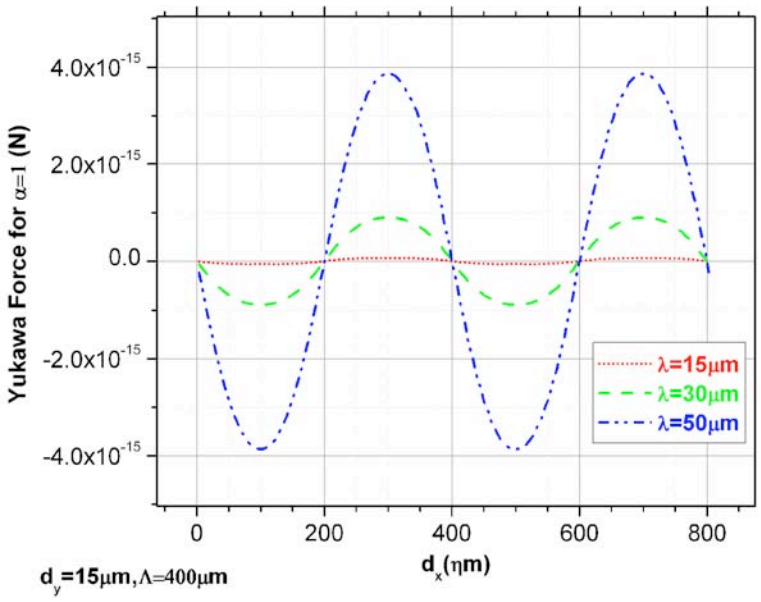

Figure 3.19: Yukawa force for $\alpha = 0$ for different ranges of interaction, λ.

In fig.3.20 I plot how the peak to peak amplitude of the Yukawa force changes versus the range for different pitches of the density contrast ($\Lambda = 400$ and $160\mu m$) and for different distances between the masses ($d_y = 15$ and $5\mu m$). In fig.3.20 the peak to peak Yukawa force for $\lambda \approx 1mm$ is the Newtonian signal, which is expected between the masses. From fig.3.20 it is evident that by reducing the pitch from 400 to $160\mu m$ the Newtonian signal is reduced by almost three orders of magnitude, while the Yukawa signal increases just for ranges, which are smaller than $\approx 2\mu m$. By reducing the distances between the masses from 15 to $5\mu m$ the Newtonian signal decreases by 30%, but the Yukawa peak to peak force increases by a factor of five thousands for $\lambda = 1\mu m$.

In fig.3.21 I plot the peak to peak Yukawa torque versus the separation between the masses for three different values of the force range. I fit them to an exponential decays of the kind, $A + B\exp(y/t_1)$, with A, B and t_1 the fitting constants. For example for a Yukawa range of $\lambda = 15\mu m$, the fitted decaying constant, t_1, is $14.0 \pm 0.4\mu m$ while for bigger ranges, 30 and $50\mu m$, the fitted t_1 are respectively $28.3 \pm 0.3\mu m$ and $40.7 \pm 0.4\mu m$. For ranges shorter than $30\mu m$

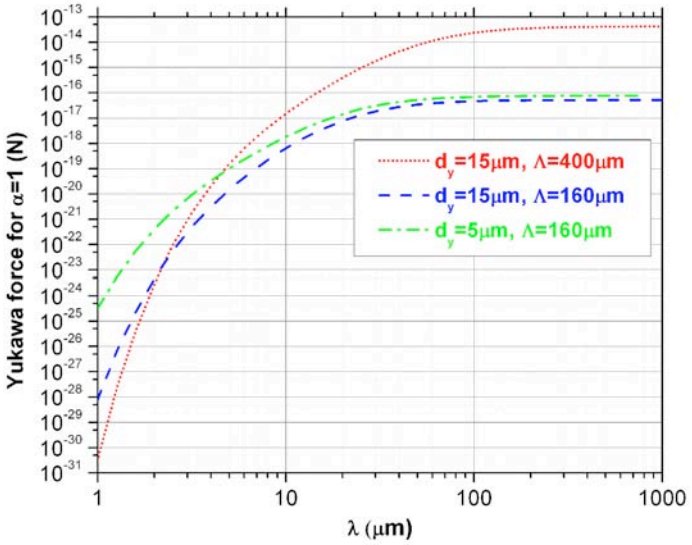

Figure 3.20: Yukawa signals versus range for different pitches and distances between the masses.

the decaying constant t_1 is given by the range of the force. At larger ranges it is possible to numerically evaluate t_1, which is more and more influenced by the decaying constant of the Newtonian force ($t_1 = \Lambda/2/\pi$) obtained for $\lambda \approx 1mm$ (see also section 3.2).

In fig.3.22 I plot the area of the parameters (α, λ), which is possible to explore for different settings of the test masses and torque sensitivities of the torsion balance. With the test masses with pitch $\Lambda = 400\mu m$ at a relative distance of $15\mu m$ and with the torque sensitivity of the MKI SSTB, $7 \times 10^{-14} Nm/\sqrt{Hz}$, [32] we can test the Newtonian gravity within 30% after only one day of integration time and explore new areas of the (α, λ) plot. With a smaller pitch, for example $160\mu m$, we will not be able anymore to directly measure gravity but we will be able to explore a slightly bigger area of the (α, λ) plot for ranges smaller than $10\mu m$. Still in principle with the best possible sensitivity of the SSTB, which is given by its thermal noise, $3.9 \times 10^{-15} Nm/\sqrt{Hz}$, (see chapter 6) and after 100 days of integration time, we will measure gravity within 20% at a distance $d_y = 5\mu m$.

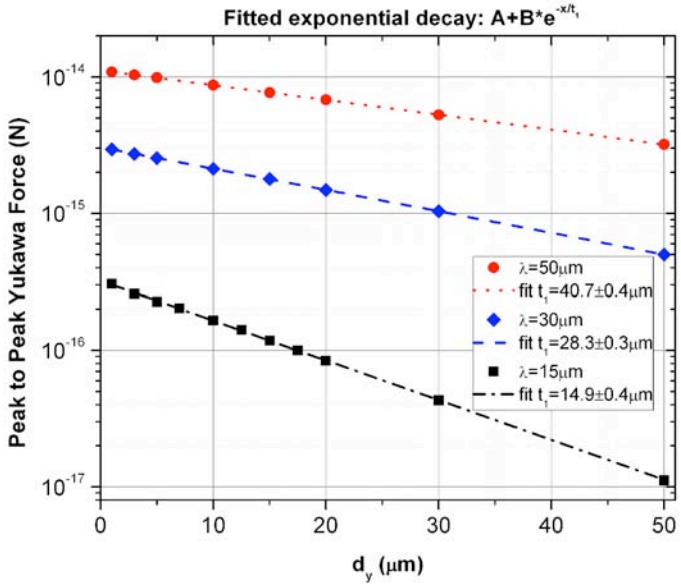

Figure 3.21: Yukawa force for $\alpha = 1$ versus the distance between the masses for different ranges and fit to exponential decays.

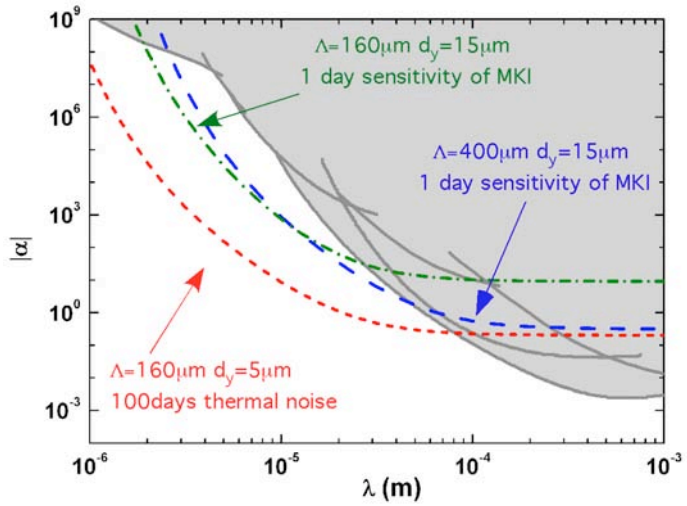

Figure 3.22: Explorable (α, λ) area for different pitches of the mass densities and distance between the masses with different torque sensitivities of the SSTB and integration time.

3.7 Torque summary

In table 3.4 I summarise the properties of all the signals, which I modelled in this chapter, and in fig.3.23 I plotted their expected torque amplitudes versus the distance d_y. For this plot I assumed a voltage difference V_0 of $90mV$, an amplitude of $0.5\mu m$ for the periodic surface corrugations, a background magnetic field perpendicular to the masses of $4\mu T$ and the susceptibility contrast associated with the gold and aluminium stripes, $\Delta\chi = 5.9 \times 10^{-5}$ (see section 3.5). As shown in fig.3.23, the biggest torque, which I expect we will measure, is given by the electrostatic torques due to the surface corrugations of the test masses while the torque due to the difference in magnetic susceptibilities of gold and aluminium stripes is the least relevant. The Casimir torque, which is due to periodic surface corrugations, is expected to dominate the Newtonian torque only at distances smaller than $6\mu m$. I did not plot the torques, which are due to periodic variations of the surface potentials, because they should be screened by the uniform gold layer which covers the top surfaces of the test masses.

During the ISL test of gravity one of this torques, which I name Γ_s, might limit the area of the (α, λ) plot, which is possible to explore. In this case the upper limit at 95%CL on possible Yukawa deviations will be given by the equation:

$$|\alpha| \geq \alpha_{\exp} + 2\sigma_\alpha \tag{3.90}$$

$$\alpha_{\exp} = \frac{\Gamma_s/G_{lab} - f_N}{f_Y(\lambda)} \tag{3.91}$$

where σ_α is given by the eq.3.88

As plotted in fig.3.24 the presence of an electrostatic torque, Γ_{cor}, which is not possible to fit out of the data (because for example of poor statistics), will prevent us from exploring new area of the parameter space of the Yukawa type violations of the ISL of gravity. It is crucial to minimise as much as possible the expected spurious signals or at least to be able to well characterise them. In such a way it will be possible to fit them out of the original data, as it usually done during the Casimir experiments [13].

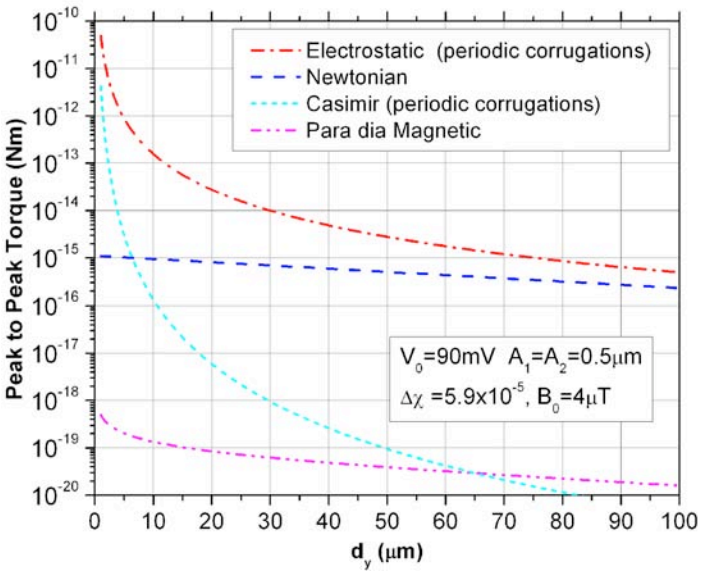

Figure 3.23: The possible peak to peak torques versus distance I expect to find with our test masses.I did not include the electrostatic forces due to contact potentials which should be screened by the top Gold layer.

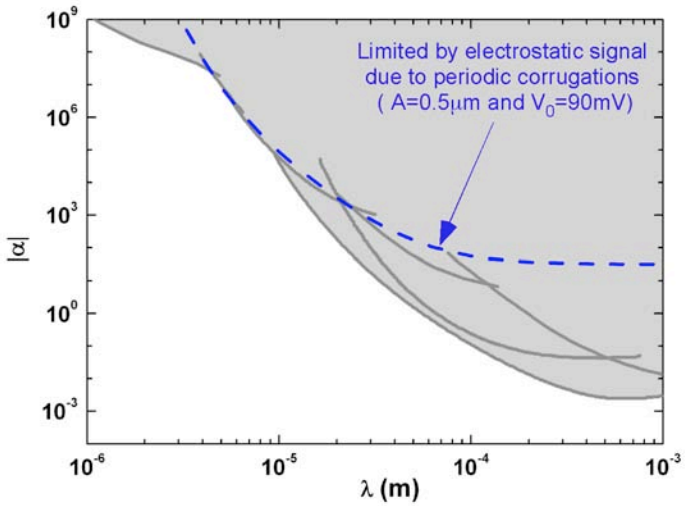

Figure 3.24: The possible (α, λ) upper limits if the measurements are limited only by the electrostatic torques due to periodic corrugations of $0.5\mu m$ and $90mV$ voltage difference. I suppose we cannot fitting them out of the data.

Torque	k_0	k_1	**Dependence on** d_y	**Dependence on other factors**
Γ_{New}	$+$	0	$e^{-\frac{2\pi d_y}{\Lambda}}$	none
Γ_{Yuk}	?	0	$e^{-\frac{d_y}{\lambda}}$ for $d_y << \frac{\Lambda}{2\pi}$	(unknown)
Γ_{cor}	$+$	0	$d_y^{-5/2}$	V_{daq}^2
Γ_{cpt}	$-$	0	$d_y^{-1/2}$	none
Γ_{cor+pt}	$+$	$\pm$	$d_y^{-5/2}$, $d_y^{-3/2}(k_0)$ $d_y^{-5/2}(k_1)$	V_{daq} (only k_0)
$\Gamma_{\Delta\chi}$	$+$	0	numeric (see fig.3.23)	B_0^2
$\Gamma_{\hbar}$	$+$	0	$d_y^{-9/2}$	T

Table 3.4: Properties of all the torques we have modelled in this chapter.

3.8 Conclusion

In this chapter I reviewed and modelled all the possible forces which, to the best of our knowledge, act between the test masses during the ISL experiments. I presented the analytical model, which predicts the Newtonian force due to the mass density contrast of the test masses and which was used to optimise the geometry of the test masses. The model predicts that at a distance of $15\mu m$ the expected peak to peak Newtonian torque is $8.7 \times 10^{-16} Nm$ and it exponentially decays with the distance between the masses. I also discussed the error budget, which is associated with the Newtonian predictions and what is the maximum error is possible to tolerate on each model parameter to measure gravity at micrometre distances within an error of 10%. I also reviewed the background Newtonian signals, which are due to the gravitational interaction between the masses, their supports and the micropositioner. Their maximum torque will be 100 times bigger than the gravitational torque due to the mass density modulation. This signal, because it is not at the spatial frequency of the expected Newtonian or Yukawa torque, does not directly influence our ISL tests. However it has to be minimised because it might reduce the torque sensitivity by requiring an increase of the dynamic range of the torque measurements.

I also discussed the electrostatic forces between the masses due to periodic corrugations of the surfaces. With a distance between the surfaces of $15\mu m$, with a periodic corrugation of $0.5\mu m$ and with same the periodicity of the density contrast, the predicted electrostatic torque, which is given by $50mV$ of voltage difference between the masses, is $5.67 \times 10^{-14} Nm$. These forces are 100 times bigger than the expected Newtonian torques and have to be reduced by manufac-

turing masses with smaller surface corrugations. I also modelled the electrostatic torques, which is due to periodic fluctuations of the surface potential because of unscreened contact potentials between the gold and aluminium stripes. This torque is expected to be $1.7 \times 10^{-8} Nm$ and is clearly very large when compared with the expected Newtonian torque. By covering the surfaces with an uniform $1\mu m$ gold layer, I expect to have it nulled by screening the voltage fluctuations. I also modelled the case where both periodic surface corrugations and potentials are present over the masses. I found that the expected signal has a spectral component also at twice of the spatial frequency, which is associated with the periodic corrugation. Moreover the presence of both periodic surface corrugations and potentials causes a discrepancy between the estimate of voltage difference present between the masses and the voltage, which will minimise the measured torque at the main harmonic. For unscreened voltage potentials of $1V$ on just one of the masses and corrugation of $0.5\mu m$ amplitude, if the voltage difference between the masses is null, the expected torque is $1.7 \times 10^{-11} Nm$ at the main harmonic and is $5.67 \times 10^{-12} Nm$ at the second harmonic. If a voltage difference of $50mV$ is present between the masses, a $10^{-9} Nm$ signal is added to the torque at the main harmonic. I modelled the Casimir lateral forces between our test masses, which are due to periodic corrugations of the surfaces, and found that they are expected to be stronger than the Newtonian signal at distances shorter than $6\mu m$. At $15\mu m$ the Casimir torque due to periodic corrugations of $0.5\mu m$ amplitude is $5.2 \times 10^{-16} Nm$. The torque, which is due to the contrast in the magnetic susceptibilities of gold and aluminium stripes, is also negligible with respect to the other forces. For a incident magnetic field of $4\mu T$ at $15\mu m$ distance it is expected to be $2 \times 10^{-19} Nm$. I presented the numerical model we developed to predict the Yukawa torques for any given range. I discuss the method I defined to set the upper limit on the strength of Yukawa forces for any range given an experimental result and the geometry of our test masses. With the manufactured test masses and reaching a torque sensitivity of the MKI SSTB [32],we will be able to test the Newtonian gravity within 30% at $15\mu m$ distance after one day of integration time. However we will explore new areas of the (α, λ) plot, only if we will be able to reduce or fit out the torques given by the electrostatic forces due to surface corrugations.

Chapter 4

The experimental apparatus

4.1 Introduction

In this chapter I will introduce the experimental apparatus we use to test the inverse square law of gravity at micrometre distances. I will start by describing all the components of the superconducting spherical torsion balance. I will describe the test masses, which are situated inside the experimental chamber and kept under vacuum at a temperature of $4.2K$. I will present all the additional components of the experimental apparatus, which are not specific to the ISL test of gravity as, for example, the subsystems which are used to monitor and control the ambient parameters (temperature, pressure, magnetic field and electric potentials). I will briefly describe the electronic packages which are used to control the torsion balance, measure the applied torques and set the relative position of the test masses. I will leave the detailed analysis of the transfer function of torsion balance between the applied and measured torque to the next chapters, where I will also discuss its expected torque sensitivity.

4.2 The SSTB principles

To test the ISL of gravity at micrometre distances we use a superconducting spherical torsion balance (SSTB), which has been developed over the last ten years by the Birmingham gravitational group. The first version of this balance has been successfully used to improve the constraints on the coupling between the quantum mechanical spin and ordinary matter by many orders of magnitude [34]. The second version (MKII) of the balance is employed to test Newton's law at small

distances and to measure the Casimir forces at $4.2K$ within 1% [33]. The SSTB relies on the magnetic suspension of a superconducting float over the magnetic field created by a superconducting coil. When below a critical temperature, T_c, and a critical magnetic field, H_c, the float becomes superconductive and a perfect diamagnet, it expels all the magnetic flux from itself according to the Meissner effect [45]. All the magnetic field created by the coil (see Fig.4.1) is compressed under the internal surface of the superconducting float. This magnetic pressure generates a vertical lift, which counterbalances the float weight at some height of equilibrium. The lift capacity, which is related to the magnetic pressure ($\sim$ the square of the magnetic field), depends on the square of the current circulating in the superconducting coil. The maximum lift capacity is limited by the maximum magnetic field, that the superconductor can sustain without becoming normal. For this reason for the MKII SSTB, the float, the bearing coil and all the wirings are made of niobium, a type II superconductor, which can sustain high critical magnetic field ($H_c = 1500G$ at $4.2K$) without losing its superconductivity [45].

To measure the torques acting on the torsion balance, the MKII SSTB adopts a servo loop system. The servo keeps the float at a fixed angular position by applying the necessary torque effort, which is eventually the torque measurement. I will discuss in detail the expected transfer function and torque sensitivity of this servo system in the following chapters.

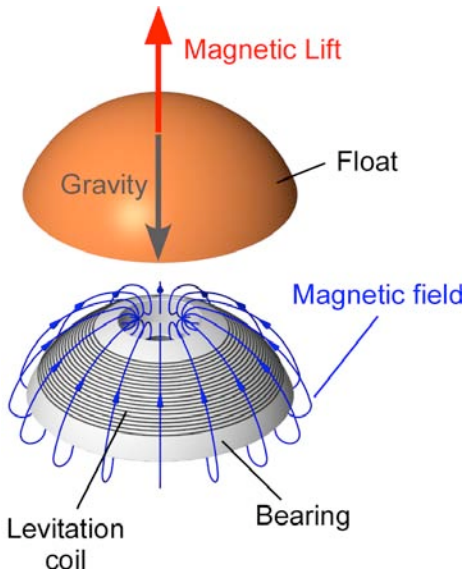

Figure 4.1: Schema of the semispherical float levitated over the magnetic field generated by a bearing coil.

4.3 The experimental vacuum chamber

I will begin the description of the experimental apparatus by introducing all the main elements present inside the experimental vacuum chamber of the SSTB (see fig.4.2). I will discuss the float, the levitation bearing, the capacitive transducer, the source mass with its micropositioners, the damping and the actuator circuits.

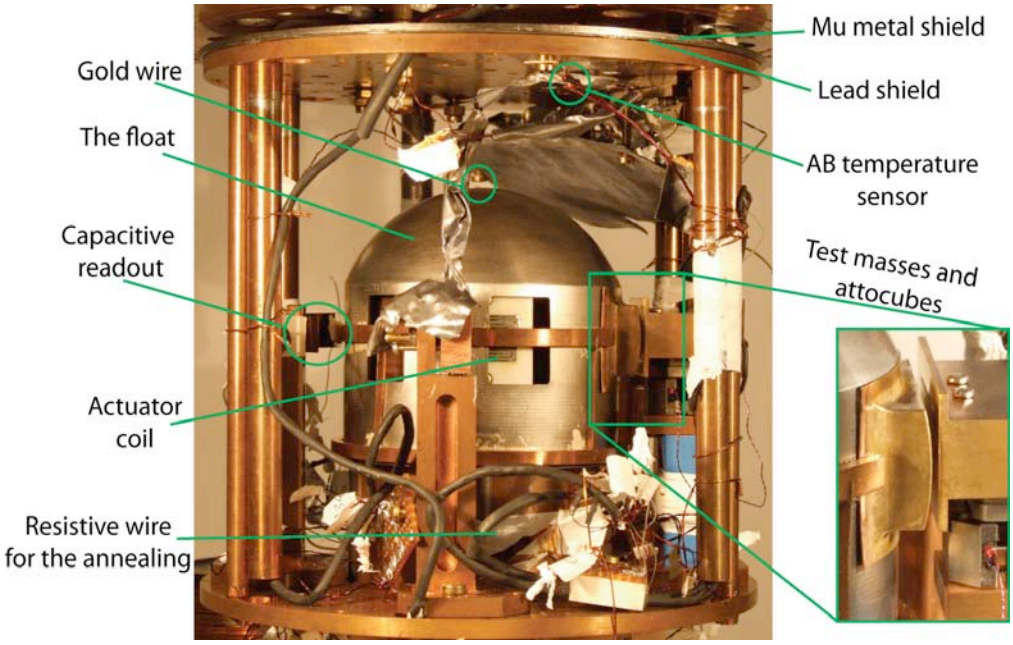

Figure 4.2: Photo of the inside of our experimental chamber. The pillar in the front is used by the Casimir experiment, with which we share the SSTB.

4.3.1 The float

The SSTB float is an almost semi spherical niobium shell, which was obtained by deep drawing from a flat thick metal sheet by Plansee Metals, Austria. Its sphericity is known within $0.2mm$, which was the thickness of the original metal sheet. On the float, which was used for the ISL test, six rectangular windows have been cut away (see fig.4.3) for the feedback control system. The positions of the window cuts have been chosen in such a way that the float moments of inertia, I_{xx} and I_{yy}, are approximately equal (see fig.4.3). We have fitted a double ring structure to the float, which sustains the samples to study and which can be changed according to the needs of different experiments. For the ISL test the support structure has a mirror for the capacitive readout on one side and

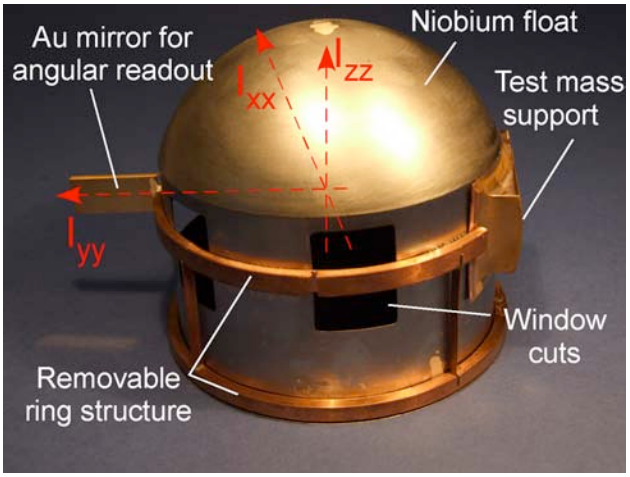

Figure 4.3: Photo of the float for the ISL test: it is visible the Nb float and the double ring structure with the mirror and lug, which are attached to it. The principal axis of inertia are shown in red.

Weight	$100.94g$	Radius	$43mm$
I_{xx}	$1.64 \times 10^{-4} kg \cdot m^2$	Pendulum length	$8.78mm$
I_{yy}	$1.60 \times 10^{-4} kg \cdot m^2$	Nominal height	$0.6mm$
I_{zz}	$1.82 \times 10^{-4} kg \cdot m^2$	Polar angle of the float	$70°$

Table 4.1: Dimensions of the float

the sample mass on the opposite side (see fig.4.3). The mirror was obtained by evaporating titanium and gold layers over a rectangular optical window. Small pieces of copper were glued onto the base of this structure to balance the float in such a way that its bottom rim is parallel to the local horizontal plate, when it is suspended over an air bearing.

The float has the center of buoyancy (CB), which is located at a very small distance ($\approx$ 9 mm) over its center of mass (CM) (see fig.4.4). The float has therefore a pendulum arm length, which is smaller than the usual one of the fibre torsion balance. For these reasons one of the great advantages of the SSTB is the reduced coupling of the float pendulum motion with the horizontal ground noise [35] (see chapter 5). A good sphericity of float top also guarantees a small pendulum stiffness [19], which minimises the coupling of the SSTB torque noise with the ground tilt noise. The float has a copper disk, which is attached on its inside (see fig.4.5) and which is employed to damp down the pendulum oscillations of the float (see Section 4.3.3).

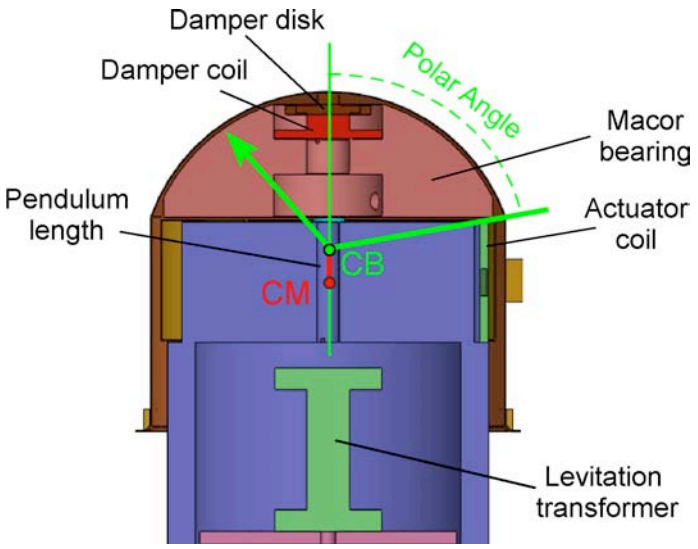

Figure 4.4: Solidworks side section of the float over the pillar, which shows the position of the center of mass (CM) and the center of buoyancy (CB).

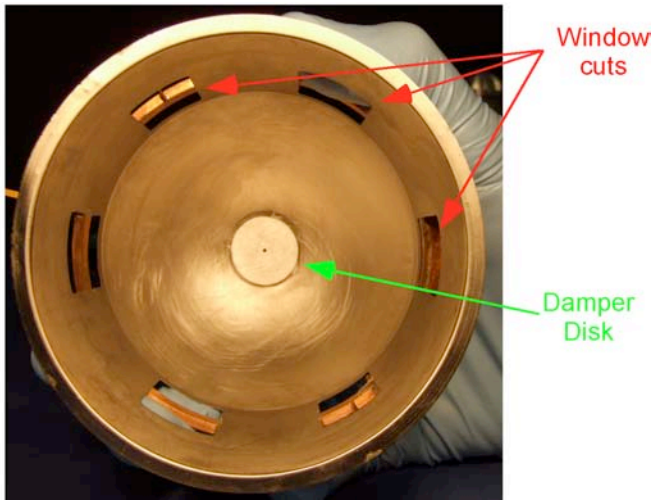

Figure 4.5: Float shell as seen from the bottom: the 6 windows cuts and the damper disk are clearly visible.

4.3.2 The levitation bearing

The bearing generates and maintains the magnetic field, which is necessary to levitate the float. It consists of an almost semi spherical support made of MACOR, which is concentric with the float. Over the bearing a spiraling groove has been machined to host a niobium wire (see fig.4.6). The bearing is made of MACOR because it is very easy to machine, is a good electric insulator and has thermal expansion very similar to niobium. The wire is a hard drawn niobium wire from Supercon of $0.25mm$ diameter, which is able to sustain a maximum critical current of $45A$ at $4.2K$. To maximize the lift capacity and minimising the maximum field which is achievable without losing the superconductivity, the spacing between each wire has previously been optimized by [85] and [35]. The optimal spacing was found to be comparable to the gap between the bearing and the float at its nominal levitation high (i.e. when the two spherical surfaces of the float and of the bearing are concentric). In the centre of the MACOR bearing there is also a cylindrical hole with, at its base. a superconducting coil adopted to generate a magnetic field. This field is used to diminish the pendulum oscillations of the float by eddy current damping in the small copper cylinder, which is attached under the float.

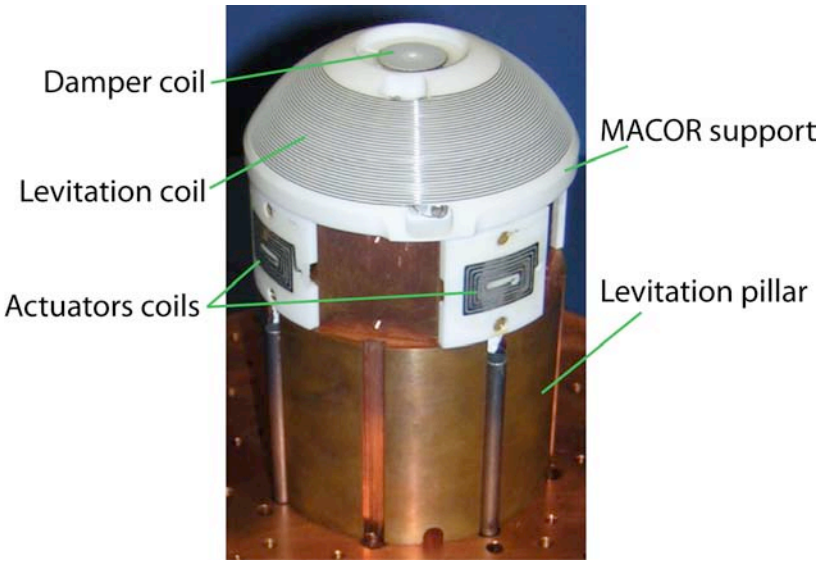

Figure 4.6: Actuator coils on the pillar. The levitation and damper coils are also visible.

Levitation bearing		**Damper coil**	
Number of turns	32	Number of turns	30
Pitch of the winding	$\approx 1mm$	Radius	$20mm$
Initial polar angle	$20°$	Height	$2.5mm$
Final polar angle	$60°$		

Table 4.2: Table with the properties of the levitation and damper bearing.

Setting up the levitation The superconductive properties of niobium are also used in the experiment for the zero resistance, that a superconductor poses to the passage of currents. Thanks to this property we can store a permanent current in a superconducting loop, which consists of the levitation coil and the secondary circuit of a toroidal transformer. Along the superconducting loop there is a heat switch, which is used to warm up the superconductor to normal state when necessary (see Fig.4.7). To store a permanent current in the loop we take advantage of the property of flux conservation over any superconductor loop [65]. We store the current through the following procedure (see fig.4.7):

1. We set a DC current in the heat switch, which has been attached to the secondary loop of the levitation transformer, and we set the current I_p through the charging wires of the primary loop. Because no current is flowing through the secondary loop of the circuit, its total magnetic flux ϕ is given by the equation:
$$\phi = I_p M \tag{4.1}$$
where M is the mutual inductance of the transformer.

2. We turn off the current in the heat switch and wait for a few seconds so that the secondary loop become superconducting. We turn off the charging current I_p. The superconducting loop reacts to conserve the magnetic flux ϕ and generates a permanent current such that:

$$\phi = (L_t + L_c) I_{lev} \tag{4.2}$$

Using the conservation of flux we equate eq.4.2 and eq.4.1:

$$I_{lev} = \frac{M}{L_t + L_c} I_p \tag{4.3}$$

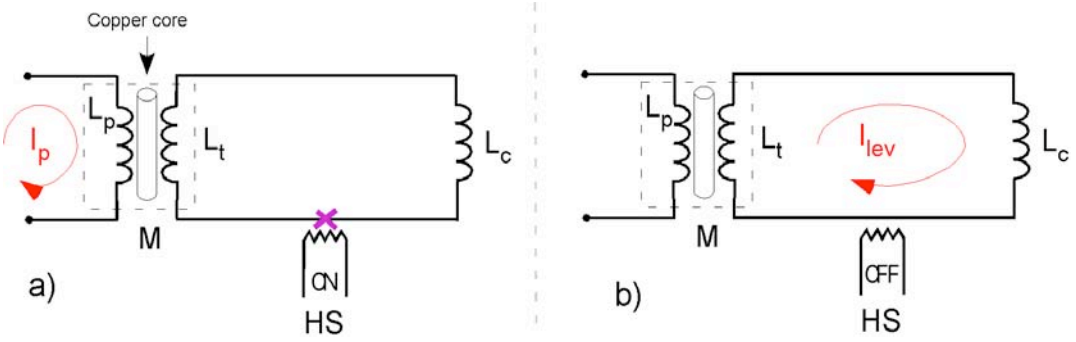

Figure 4.7: Two figures representing the two phases necessary to charge the bearing circuit: a) charging phase; b)stored current. In reality the copper core is a toroid.

Lift Capacity/I_{lev}	$0.3\ g/A^2$
Vertical f_0	$18Hz$
Horizontal f_0	$5Hz$
Pendulum f_0	$1Hz$

Table 4.3: Characteristics of the magnetic suspension [31]

L_t is the inductance of the transformer and L_c is the inductance of the levitation coil. The stored current, I_{lev}, in the superconducting loop will persist unless we heat the secondary loop with the heat switch again or unless the circuit becomes normal. In our case, because we have $L_c \approx 3.6\eta H$ and $M \approx \sqrt{L_p L_t}$, L_p and L_t were chosen such that the transformer ratio is $4:1$. The superconducting transformer is made of a copper toroid with wrapped around it two superconducting wires. The transformer is situated in a cavity inside the levitation pillar (see fig.4.4) whose walls are covered by niobium sheets for magnetic insulation.

The characteristics of the magnetic suspension of the torsion balance have been numerically studied in the past using models of varying levels of complexity [35][73][84][85]. These works predicted the lift capacity of the torsion balance for a given stored current and the horizontal, vertical and tilt stiffness of the float with respect to the bearing [35]. Given the properties of our float and the bearing, we summarize the finding of the numerical results for the SSTB MKII in table 4.3 [31].

4.3.3 The damper circuit

In the MACOR shell also, as previously mentioned, there is the superconducting coil of the damper circuit, which can be made normal using another heat switch. The damper circuit can be charged through the steps shown in fig.4.8. While the heat switch is turned on, we set the current to flow through the superconducting loop. We then turn off the heat switch and trap the current, I_{damp}, which permanently flows around the superconducting loop. In the present version of the torsion balance the parasitic modes of the float are damped down by Eddy current loss in a conductive medium [41]. The pendulum, the horizontal and the vertical oscillations of the float with respect to the bearing are passively damped down by dissipating their energy through Joule heating of a conductive volume. The damping method depends on which oscillations we want to control. The pendulum and horizontal modes are damped down by using the small copper cylinder, which is attached under the float (see Fig.4.5) and which, thanks to the motion of the float, oscillates over the magnetic field created by the damper coil. The magnetic flux, which is coupled with the cylinder, varies in time with the oscillations and generates Eddy currents in the copper by Ampere/Faraday and Ohm's laws [41]. These currents are then dissipated by the Joule heating of copper. We found that $4A$ stored in the damper circuit suffices to critically damp the pendulum mode [33] (see chapter 7). The vertical oscillations of the float are instead damped down by coupling a copper transformer with the bearing circuit. When the float vertically oscillates the inductance of the bearing is modulated inducing a change of the current stored in the superconducting circuit. The magnetic field at the surface of the transformer is proportional to the stored current and exponentially attenuated by the Eddy currents inside the transformer over the distance of the skin depth, δ [23]. The transformer radius has been chosen to be comparable with the skin depth, $\delta \approx 2.2mm$, which is associated with the frequency of the horizontal motion. In such a way we optimise the damping of these modes while keeping the transformer volume minimum.

4.3.4 The source sample and its micropositioners

Inside the experimental chamber - as shown in fig.4.2 and 4.9- in front of the test mass, which is connected to the float, there is the pillar, which supports the source mass. The mass is screwed on the top of two Attocube slip-stick

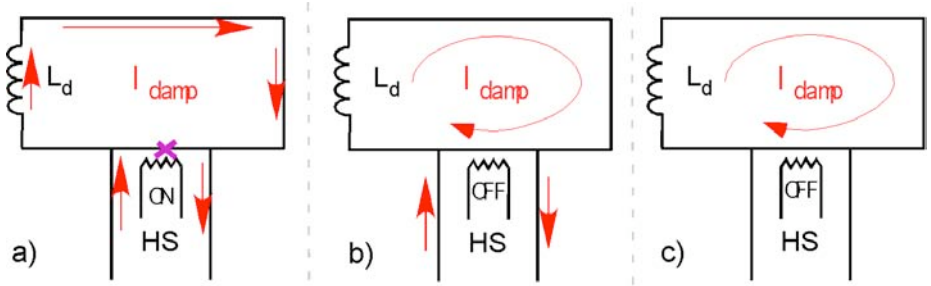

Figure 4.8: Schema of the damping circuit and of the two phases to charge it with a permanent current: a) and b) charging phase; c) stored current.

micropositioners (ANPx100/LT). The support of the flat mass can be moved in the x and y direction up to few millimeters of steps, which are smaller than $100nm$. On the side of the support there is also a capacitive plate which is used to monitor its displacement in the y direction. The head of a Fluxgate magnetometer (Bartington Instruments) is positioned near the source mass (see fig 4.9) and is used to monitor the magnetic field acting on the masses. We can apply a magnetic field to the masses by using a superconducting magnetic coil, which is wrapped around the pillar supporting the micropositioners. We can also control the voltage of the source mass through a wire, which is connected to it. The mass support is electrically insulated from the copper pillar and the experimental chamber because of the Attocubes, whose top section is electrically insulated from the bottom one by design.

4.3.5 The capacitive readout

The capacitive transducer for the angular readout is situated in front of the float on the opposite side with respect to the test masses (fig.4.10). The transducer is made of a gold-coated mirror, which is attached to the float, and two metallic plates on its sides, which are supported by insulating spacers on a copper pillar. The transducer transforms angular displacements of the float in capacitance differences between the previous plates. The float, through a very thin gold wire, and the two plates are electrically connected to the outside of the cryostat with coaxial cables. The capacitive transducer is part of a capacitive bridge circuit and transforms the capacitance differences in a voltage output. I will analyse in detail the expected transfer function and sensitivity of the capacitive sensor in

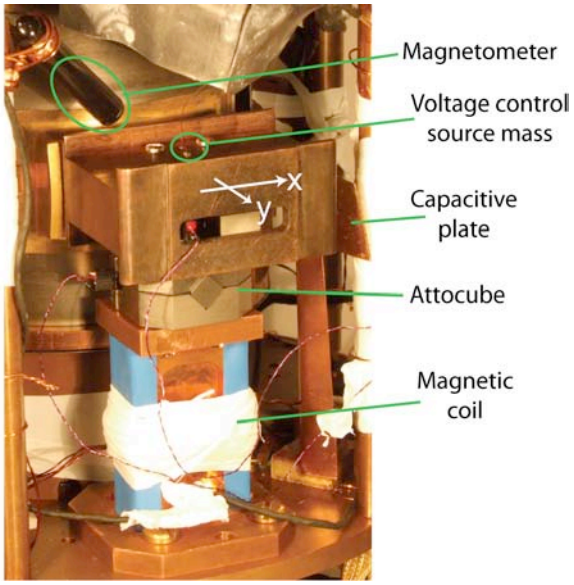

Figure 4.9: Photo of the pillar with the Attocube and the source mass. Additional sensors are shown too.

chapter 6.

4.3.6 The magnetic actuator circuit

To apply a torque to the float we use a set of four superconducting coils (fig.4.6), which are partially shielded by the float shell (see fig.4.2). The float, when it rotates, modifies their inductances. The coils are connected to a superconducting circuit, where we store permanent currents and add a variable current offset by using two superconducting transformers and two heat switches (see chapter 6). By modifying the currents flowing in the coils, we can change the magnetic fields applied to the float and rotate it in any chosen direction and/or give it a natural stiffness. I will analyse the magnetic actuation as the capacitive transducer in detail in the following chapters. I will model its transfer function and magnetic stiffness versus the currents which are stored in the superconducting circuitry (see chapter 6).

While the levitation transformer is inside the levitation pillar, the superconductive circuitry of the magnetic actuator is instead located under the base plate of the experimental chamber (see fig.4.11) almost completely inside a niobium sheet box, which is used for magnetic shielding. Outside the box there are all the heat switches, the actuator transformers and the joints between all the supercon-

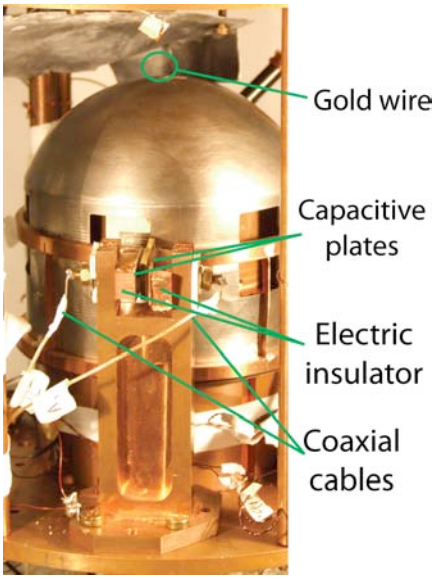

Figure 4.10: Photo showing the current capacitive readout and the thin gold wire attached to the float top.

ductive wires.

4.3.7 Temperature sensors and magnetic shields

Inside the vacuum chamber there are also a few temperature sensors made of Allen Bradley carbon resistors [90]: one on the top of the vacuum chamber (visible in fig.4.2), one on its base and one inside the levitation pillar. The resistance of these temperature sensors increases with the decrease of the temperature as shown in the example data of fig.4.12. By measuring their resistances we can directly monitor the temperature inside the chamber down to a few Kelvin. A high resistance wire is also wrapped around the levitation pillar, which can be used to anneal the float, the levitation coil and transformer when necessary.

To minimise the magnetic fields, which are acting on the test masses and on the float, a mu-metal and a superconducting lead box encloses the experimental chamber (see fig.4.2 and 4.13). The chamber is electrically insulated from the copper can by a set of MACOR spacers on its top and a plastic foil on its walls and base. The electric potential of the chamber is controlled through a coaxial wire, which is connected to the bottom copper plate under the levitation pillar.

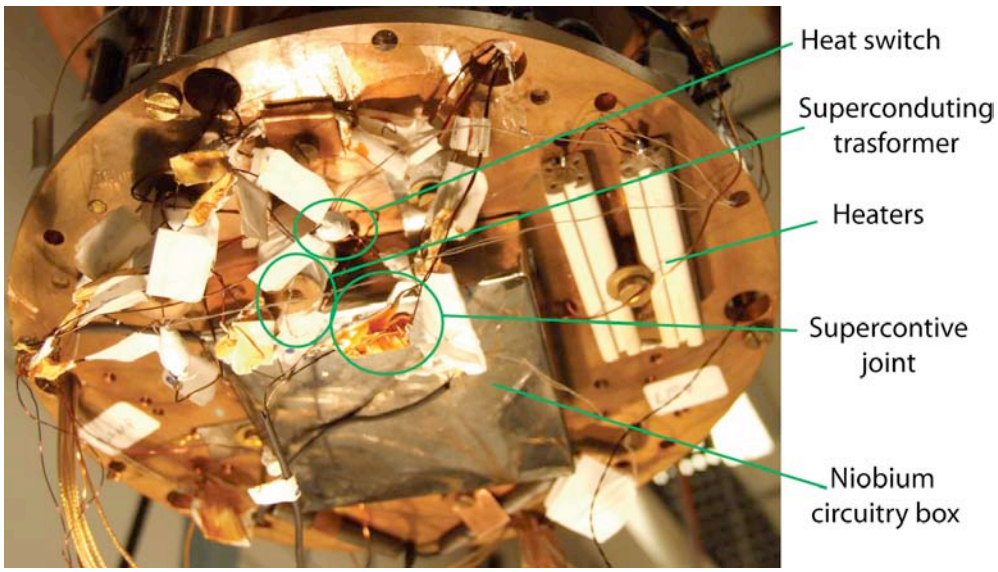

Figure 4.11: Superconductive circuitry under the base plate of the experimental chamber.

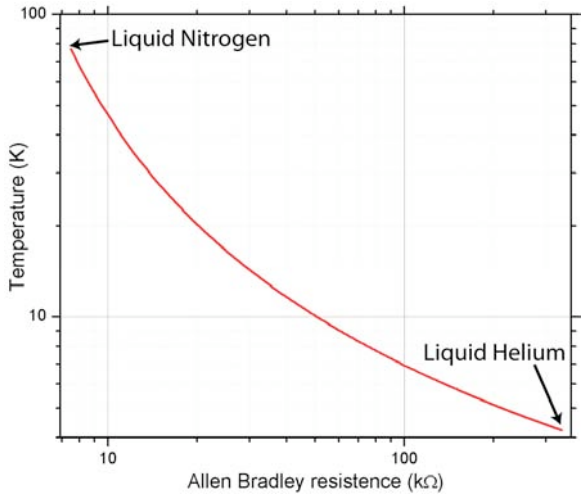

Figure 4.12: Temperature versus the Allen Bradley resistence.

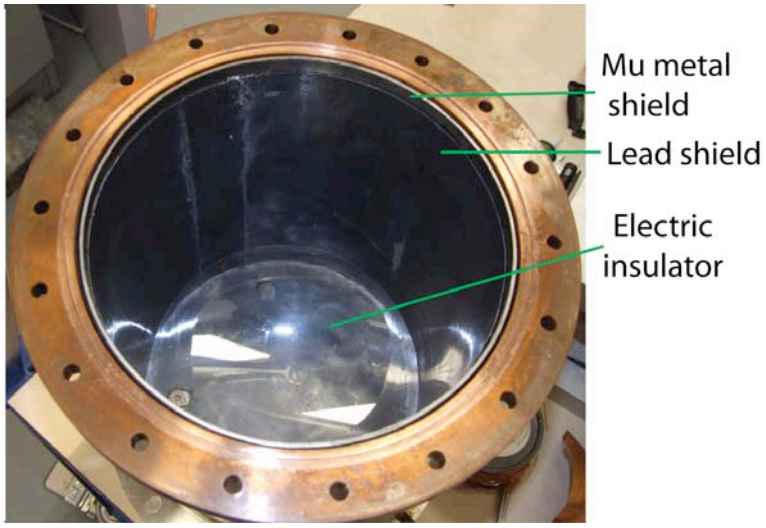

Figure 4.13: Photo of the vacuum can showing all the magnetic shields.

4.4 The cryostat and the cryogenic insert

On the outside of the experimental chamber, on its top and bottom, there are two additional Allen Bradley resistors which are used to measure the Helium level inside the cryostat. On the stainless steel plate, which is connected under the vacuum can, there are the heaters which are employed to boil off any residual liquid nitrogen or helium, when it is necessary. The copper can is suspended from the top plate of the cryogenic insert (see fig.4.14) by a stainless steel cable, which sustains all the load. The three vacuum pipes, which are connected to the can through three springy bellows, do not sustain the can weight. In this way when the cryogenic insert is inside the Janis cryostat, the vacuum can is sitting on its base plate, releasing the tension of the stainless wire. The cryostat is positioned on a concrete block, which is separated from the surrounding building by rubber cylinders to further reduce its coupling with the seismic noise. Between the Janis cylinder and the ground there is a simple tilt stage (see fig.4.15), which is made of three adjustable feet and by which it is possible to tilt the dewar in three directions. Coaxial and manganin/copper wires connect the experimental chamber with the outside of the cryostat, whose number, section and material has been chosen to minimise the heat leaking from the external environment to the vacuum can. There are also a pressure gauge and a gas gate, which are connected to the vacuum pipes on the outside of the cryostat. The latter is used to introduce the helium exchange gas in the vacuum chamber in a controlled

manner by alternatively opening and closing each of its two valves.

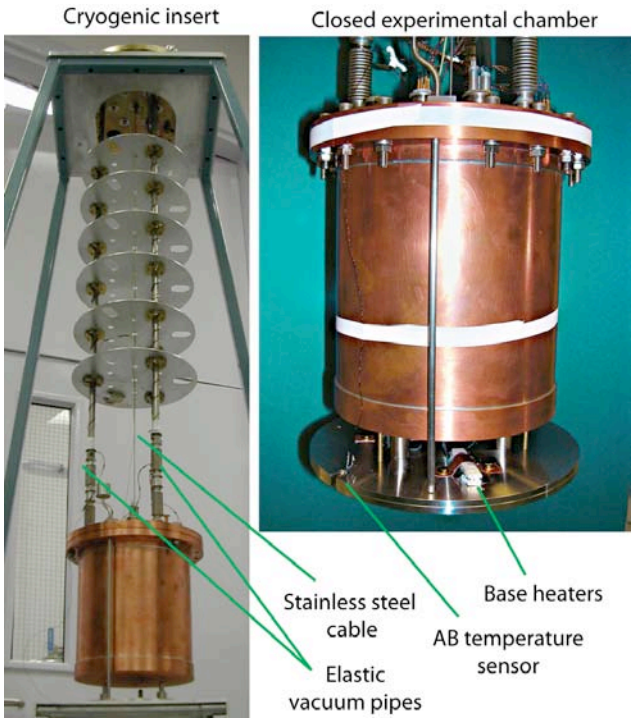

Figure 4.14: Photos showing the cryogenic insert and the closed experimental chamber.

4.5 External hardware and software

Near the cryostat on two racks which are situated outside of the seismic isolation block, are all the electronics which are used to control the torsion balance, to measure the torque servo effort and to move the Attocube micropositioners (see fig 4.16). An Andeen-Hagerling ultra-precision capacitance bridge (model AH 2550A) is adopted to measure all the capacitances involved in the experiment, such as the one which measures the Attocube displacement in the x direction or the capacitance between the source and the test mass. An Agilent function generator (model 33120A) gives the AC signal, which drives the SSTB capacitor bridge and transforms the angular displacement of the float in a voltage signal (see chapter 6 for details) by mean of a FEMTO phase lock-in amplifier (model LIA-BVD-150-H). This voltage output is digitised by a 16 bit digital to analogue cards (Measurement Computing model PCI-DAS6035), which is connected to the PCI bus of a PC and elaborated by a digital servo program. The program was

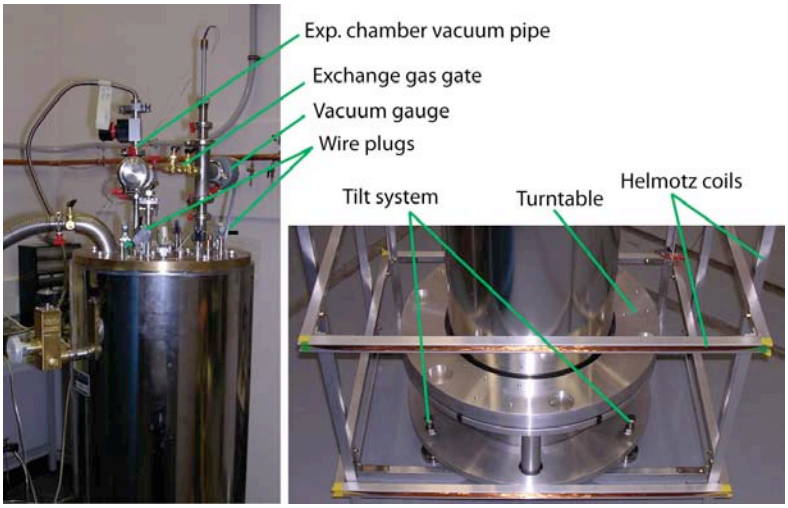

Figure 4.15: Photos showing the Janis dewar with the vacuum pipe and feed-through on the top and the levelling tilt system on its base. The Helmotz coils have not been used for the ISL tests.

developed in Agilent Vee on Windows XP. The servo output is transformed back to an analogue signal by a 16-bit digital to analogue card and a summing amplifier (see chapter 6 for details). The output voltage controls a current source, whose output is sent back to the magnetic actuator circuit of the SSTB and is monitored through a resistor by a Keithley 2000 digital multimeter. The multimeter readout is recorded as an ASCII file by a PC Vee program through the GPIB bus connection. On the same rack of the previous electronics there is also a Thurlby Thandar Instruments power supply (model TSX-820), which is employed to store the currents in the levitation and the actuator circuits. On the rack is the control box of a Fluxgate magnetometer (MAG-01), which measures the magnetic field in the experimental chamber near the test masses. Because of the large numbers of wires which are grouped within four 15-pin connectors, and the coaxial cables coming from the Janis dewar an interface panel has been developed and mounted on the rack to simplify and facilitate the electrical connections (see fig.4.16). A relay box on the same rack, which is controlled by the PCI digital cards, and the Attocube control unit on a second rack are used to automatically move the Attocubes in the x and y direction according to instructions given by a Vee program. The vacuum in the experimental chamber is created at first with a Edwards Rotary vane vacuum pump (model RV5) down to $10^{-1} - 10^{-2} mBar$ and with a Variant turbo molecular pump (model V70) down to lower pressures.

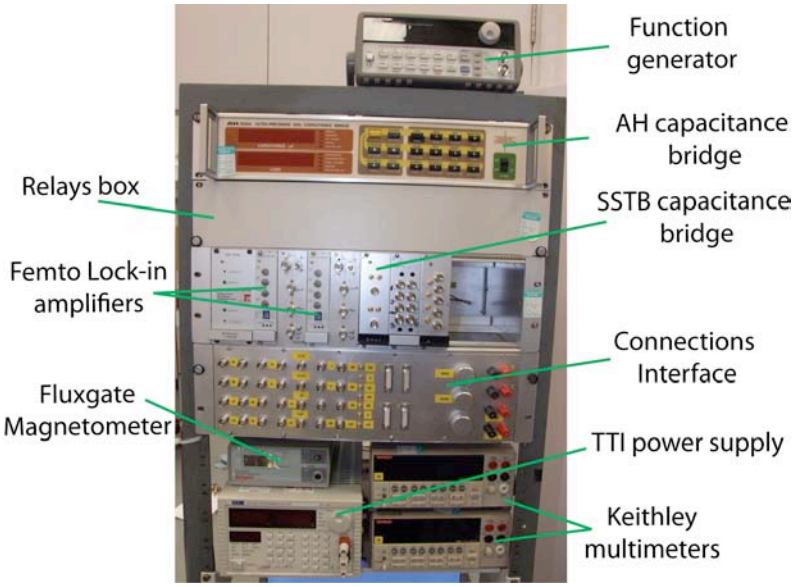

Figure 4.16: Electronics to monitor and control the SSTB for the ISL test of gravity.

4.6 Conclusion

In this chapter I have reviewed all the components of the experimental apparatus, which we are using to test the ISL of gravity at micrometre distances. I have discussed the principles of the MKII SSTB, which is based on the magnetic levitation of a superconducting float at $4.2K$. The current version of the SSTB adopts a servo loop system to keep the float at a constant angular position. The float angle is monitored by a capacitive sensor as a temporary solution. The feedback torque is applied to the float through a system of superconducting circuits, coils and an opening on the float shell. The same circuitry is used to give a tunable, natural stiffness to the torsion balance. By design, the spurious oscillations of the float are reduced by Eddy current damping in the copper core of the levitation transformer, and in the copper cylinder, which is attached under the float. In front of the curved mass, which is connected to the float, the flat mass is supported by a set of two micropositioners, which can move it in the x and y directions up to a distance of a few millimetres by steps smaller than $100nm$. The torsion balance, the test masses and the whole experimental chamber are enclosed in a magnetic shield box and are electrically isolated from the vacuum can. Their temperature and magnetic field are monitored by a few sensors. The torsion balance has also its coupling with the seismic noise reduced by the con-

crete block over which the cryostat is positioned and which is isolated from the main building by rubber spacers. With this experimental apparatus we plan to verify Newton's law of gravity down to micrometre distances. In the following chapters I will discuss the expected and measured torque sensitivity of the torsion balance and the transfer function between the applied and measured torque. I will also present the experimental results that we obtained during the first tests of the ISL of gravity at micrometre distances.

Chapter 5

The float dynamics and the seismic torque noise

5.1 Introduction

In this chapter, I will study the dynamics of the torsion balance with two goals in mind: first to determine the transfer function of the float between the applied torque and the float angle; second, to estimate the influence of the ground seismic noise on the torque noise to which the float is subjected. There are already some simplified models, which describe the dynamics of the torsion balance and the seismic coupling [35] [75]. These models are based on the representation of the torsion balance as a simple point mass which is attached at the end of a pendulum arm and which has two possible angular degrees of freedom. These models did not explicitly consider the effect of the three moments of inertia of the float on its dynamics. Even if, in these works, the coupling of the float with the seismic noise was separately analysed with other dedicated models, the direct coupling with the horizontal and tilt seismic noise was not directly taken into account. In the following chapter I will present a new model of the float dynamics, which I have developed. This model, given the three moment of inertia of the float and some measured parameters (such as the elastic and damping coefficients) predicts the transfer function of the float between the applied torque and the float angle. The model also describes the effect of the horizontal, vertical and tilt seismic noise on the torque, to which the float is subjected. This model will predict new contributions to the torque noise, which have not previously been considered and which may explain the torque noise level we measured during our ISL tests.

5.2 3D dynamics of the SSTB

I will begin by presenting the new model of the torsion balance, which is a pendulum of mass m, pendulum arm l and with the three moment of inertia I_{xx}, I_{yy}, I_{zz}, around the three principal axes of inertia x^p, y^p and z^p (see fig.5.3). In the following analysis I will consider two possible motions of the float, a pendulum one associated with the angle θ and a torsional motion associated with the angle ϕ. I will also include the stiffness acting on these two angular degrees of freedom and also the effect of the ground vibrations and tilt. I will not include the stiffness associated with the horizontal and vertical oscillations of the float. These spurious oscillations have respectively resonant frequencies of 5 and $18Hz$. Because the float rigidly moves with the laboratory ground at the low frequency of interest between a few mHz to approximately $1Hz$, this omission can be considered as a valid approximation.

5.2.1 Coordinate changes

To model the dynamic of the torsion balance I follow an approach based on Euler's angles similar to [36], and I use a set of coordinate changes to represent the effect of the seismic noise, the float angular free motions (pendulum and torsional) and the tilt of its center of mass with respect to the gravity direction. In fig.5.1 I summarise the sequence of all the coordinate changes discussed in the following paragraphs.

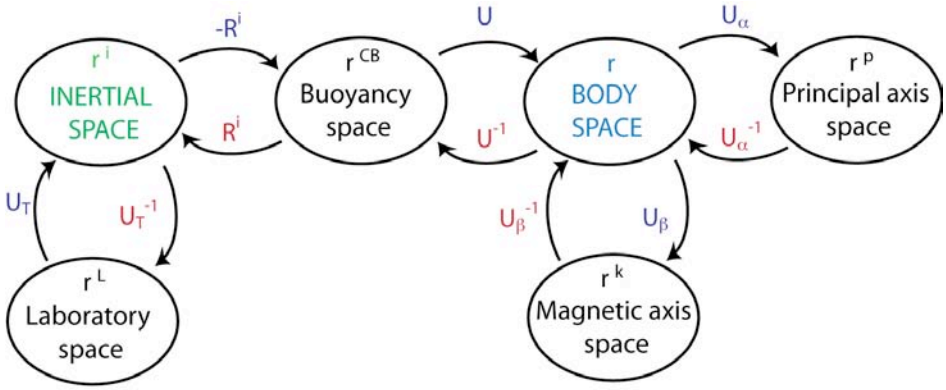

Figure 5.1: Schema illustrating the different changes of coordinate, which I used to model the SSTB dynamics.

From laboratory space to inertial space

I will begin with the coordinates associated with the "laboratory space", $r^L = (x^L, y^L, z^L)$. Such space is subjected to a tilt rotation as a function of time with respect to an inertial coordinate frame, which is given by $r^i = (x^i, y^i, z^i)$. I represent the coordinates change from the laboratory space to the inertial one with the following matrices (see fig.5.2):

$$r^i = U_T.r^L \tag{5.1}$$

$$U_T = U_{\phi_T} U_{\theta_T} \tag{5.2}$$

$$U_{\theta_T} = \begin{pmatrix} \cos\theta_T(t) & 0 & -\sin\theta_T(t) \\ 0 & 1 & 0 \\ \sin\theta_T(t) & 0 & \cos\theta_T(t) \end{pmatrix} \tag{5.3}$$

$$U_{\phi_T} = \begin{pmatrix} \cos\phi_T & \sin\phi_T & 0 \\ -\sin\phi_T & \cos\phi_T & 0 \\ 0 & 0 & 1 \end{pmatrix} \tag{5.4}$$

U_{θ_T} is a rotation around the axis y^L of an angle $\theta_T(t)$ and U_{ϕ_T} is a rotation around the axis $U_{\theta_T} z^L$ of an angle ϕ_T.

From the inertial space to the buoyancy space

I am now in what I call the "inertial space", if I do not consider the effect of the Earth's rotation. In this reference frame the gravitational force is directed along the axis z^i and the float is a rigid body, whose rotations about its centre of buoyancy (CB) are described by two angles, θ and ϕ. The centre of buoyancy of the float is at a distance R^i from the axis origin (see fig.5.2). The distance R^i is defined by the equation:

$$R^i = U_T.R^L \tag{5.5}$$

$$R^L = \begin{pmatrix} X \\ Y \\ Z \end{pmatrix} \tag{5.6}$$

R^L describes the position of CB in the laboratory space and is used to model the effect of the horizontal and vertical seismic vibrations on the float. I move now to the reference frame - called the "buoyancy space" - which is centered on float CB, with the transformation:

$$r^{CB} = r^i - R^i \tag{5.7}$$

Because $\ddot{R}^i$ might be different from zero, the CB space is generally not an inertial coordinate system.

From the buoyancy space to the body space

The free motions of the float around CB are represented by the following transformations from the CB coordinates, r^{CB}, to the one I name the "body coordinates", r:

$$r = U.r^{CB} \tag{5.8}$$

$$U = U_\phi U_\theta \tag{5.9}$$

$$U_\theta = \begin{pmatrix} \cos\theta(t) & 0 & -\sin\theta(t) \\ 0 & 1 & 0 \\ \sin\theta(t) & 0 & \cos\theta(t) \end{pmatrix} \tag{5.10}$$

$$U_\phi = \begin{pmatrix} \cos\phi(t) & \sin\phi(t) & 0 \\ -\sin\phi(t) & \cos\phi(t) & 0 \\ 0 & 0 & 1 \end{pmatrix} \tag{5.11}$$

I associate the pitch angle θ with the rotation of the float along the y_i axis and the yaw angle ϕ with the rotation around the $U_\theta z_i$ axis. I call r the "body coordinates" space because, with respect to them, the float position is fixed.

From the body space to the principal axis space

The starting equilibrium position of the float may not be the one with its centre of mass (CM) located under its centre of buoyancy on the z axis but a position slightly rotated. A restoring torque can act on the float due to the elastic constant k_θ (associated with the pendulum oscillations of the float) and the angle between the magnetic symmetry axis of the levitation bearing, z^L, and the symmetry axis

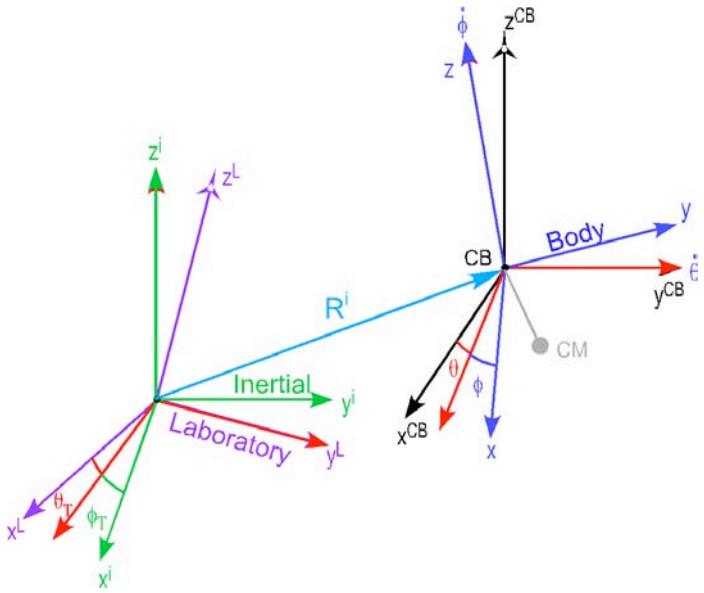

Figure 5.2: Schema showing the coordinate changes used to model the dynamic of the torsion balance and the seismic noise.

of the float, z^k. This torque might possibly change the initial equilibrium position of the float. If the centre of mass of the float is not along the z^k axis (see fig.5.3) but along a different axis, z^p, which is tilted with an angle θ_0 with respect to z^k, the float then rotates by an angle β. The rotation stops when the elastic torque is balanced by the gravitational torque acting on the centre of mass which is tilted at an angle α with respect to z. Mass asymmetry of the float might cause the displacement of CM off the z^k axis [35]. For θ, ϕ, θ_T and ϕ_T null, the balancing of the two previous torques at the equilibrium position is expressed by the following condition (see fig.5.3):

$$-\beta k_\theta + mgl\sin(\alpha) = 0 \tag{5.12}$$

The passage from the body coordinate space to the space, which I call the "principal axis space", $r^p = (x^p, y^p, z^p)$ (defined by the principal axis of inertia of the float), is given by the following equations:

$$r^p = U_\alpha . r \tag{5.13}$$

$$U_\alpha = \begin{pmatrix} 1 & 0 & 0 \\ 0 & \cos\alpha & \sin\alpha \\ 0 & -\sin\alpha & \cos\alpha \end{pmatrix} \tag{5.14}$$

U_α is a rotation of an angle α around the x axis as shown in fig.5.3.

In this coordinate frame the moments of inertia of the float at its centre of buoyancy are given by the matrix:

$$I = \begin{pmatrix} I_{xx} + ml^2 & 0 & 0 \\ 0 & I_{yy} + ml^2 & 0 \\ 0 & 0 & I_{zz} \end{pmatrix} \tag{5.15}$$

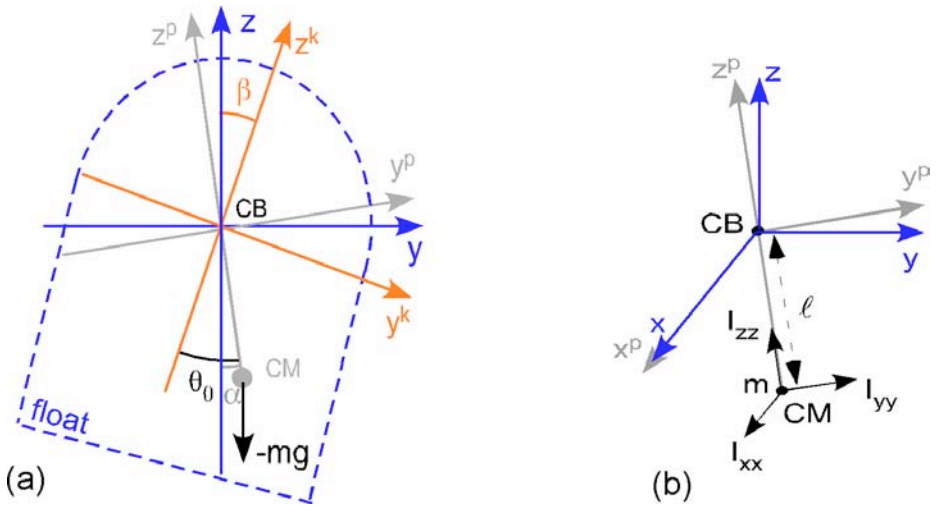

Figure 5.3: Schema showing the coordinate space associated with the principal axis of inertia (x^p, y^p, z^p) and the magnetic axis, z^k. Here $\theta = \phi = \theta_T = 0$.

From the body space to the z^k axis space

It is also useful to define the coordinate change from the body space to the one associated with the z^k axis. Under ideal conditions the z^k axis coincides with the revolution symmetry axis of the float shell [35], but it is possible that trapped magnetic flux or asphericity of the float shell might move z^k to a different angular position. The coordinate change from r to r^k is given by the equation:

$$r^k = U_\beta . r \tag{5.16}$$

$$U_\beta = \begin{pmatrix} 1 & 0 & 0 \\ 0 & \cos\beta & \sin\beta \\ 0 & -\sin\beta & \cos\beta \end{pmatrix} \tag{5.17}$$

5.2.2 Kinetic energy

I will proceed now to write down the kinetic energy of the float in the inertial space. I can decompose the float into a series of small masses, m_j, whose positions in the inertial coordinate system are given by the equation:

$$d_j^i = R^i + U^{-1} . d_j \tag{5.18}$$

where d_j are expressed in the body reference system and U^{-1} is the inverse matrix of U. We should remember that, as the rotations preserve the vector lengths, the matrix U is an orthogonal matrix and its inverse matrix is simply equal to its transposed:

$$U^{-1} = U^T \tag{5.19}$$

Because I suppose the float to be a rigid body, i.e. the derivative with respect to the time of d_j is null ($\dot{d}_j = 0$), the velocity in the inertial system of the j^{th} mass is given by the following equation:

$$\dot{d}_j^i = \dot{R}^i + \dot{U}^{-1} . U . U^{-1} . d_j \tag{5.20}$$

$$= \dot{R}^i + \omega^{CB} \times d_j^{CB} \tag{5.21}$$

ω^B is the instantaneous angular velocity of the rigid body expressed in the CB coordinate system such that [36]:

$$\omega^{CB} = \begin{pmatrix} \omega_x^{CB} \\ \omega_y^{CB} \\ \omega_z^{CB} \end{pmatrix} \tag{5.22}$$

$$\left(\omega^{CB}\times\right) = \begin{pmatrix} 0 & -\omega_z^{CB} & \omega_y^{CB} \\ \omega_z^{CB} & 0 & -\omega_x^{CB} \\ -\omega_y^{CB} & \omega_x^{CB} & 0 \end{pmatrix} = \dot{U}^{-1}.U \tag{5.23}$$

where $\dot{U}^{-1}$ is the derivative matrix with respect to the time of the inverse matrix of U. It can be shown that the total kinetic energy of the whole body is given by the following equation [36]:

$$T = \frac{1}{2}\sum_j m_j \left(\dot{d}_j^i\right)^2 \tag{5.24}$$

$$= \frac{1}{2}m\left(\dot{R}^i\right)^2 + m\left(\dot{R}^i\right)^T \cdot \omega^{CB} \times r_{cm}^{CB} + \frac{1}{2}\left(\omega^{CB}\right)^T .I^{CB}.\omega^{CB} \tag{5.25}$$

with I^{CB} the moments of inertia of the float and r_{cm}^{CB} the position of its centre of mass, both expressed in the CB coordinate system. I call the third term of eq.5.25, T_{rot}, which is the kinetic energy associated with the rotations of the rigid body around CB.

After some simple linear algebra from eq.5.23, 5.9 and 5.19, I find that:

$$\omega^{CB} = \begin{pmatrix} \dot{\phi}\sin\theta \\ \dot{\theta} \\ \dot{\phi}\cos\theta \end{pmatrix} \tag{5.26}$$

which is easily verified by inspection of fig.5.2.

The matrix of the moments of inertia I^{CB} is instead given by the equation:

$$I^{CB} = U.U_\alpha.I.U_\alpha^{-1}.U^{-1} \tag{5.27}$$

with U_α^{-1} the inverse matrix of U_α.

The velocity of the float centre of buoyancy, $\dot{R}^i$, as seen in the inertial coordinate system, is equal to:

$$\dot{R}^i = U_T.U_T^{-1}\dot{U}_T.R^L + U_T\dot{R}^L \tag{5.28}$$
$$= U_T(\omega_T^L \times R^L + \dot{R}^L) \tag{5.29}$$

ω_T^L is the instantaneous angular velocity of the laboratory coordinate system, which is expressed in the laboratory reference system and defined as $(\omega_T^L\times) = U_T^{-1}\dot{U}_T$ [36]. Now if I assume that X and Y are very small, ≈ 0, and that Z is equal to $Z_0 + Z_1(t)$ with Z_0 a time independent constant, it is possible to show that, to the first order in X, Y, θ_T and $\dot{\theta}_T$, the previous equation is equal to the following one:

$$\dot{R}^i \approx U_T. \begin{pmatrix} \dot{X} - Z_0\dot{\theta}_T \\ \dot{Y} \\ \dot{Z} \end{pmatrix} \tag{5.30}$$

If Z_0 is not null, which means that the center of buoyancy of the float is not at the pivot point of the ground tilt, the ground tilt noise will act on the float CB as an equivalent horizontal seismic noise, when it is expressed in a inertial coordinate system. In the following analysis I suppose $Z_0 \approx 0$ and that:

$$\dot{R}^i \approx U_T\dot{R}^L \tag{5.31}$$

The centre of mass position, r_{cm}^{CB}, in the CB coordinate system is simply given by the expression:

$$r_{cm}^{CB} = U^{-1}.U_\alpha^{-1}. \begin{pmatrix} 0 \\ 0 \\ -l \end{pmatrix} \tag{5.32}$$
$$= l \begin{pmatrix} -\cos(\alpha)\sin(\theta) + \cos(\theta)\sin(\alpha)\sin(\phi) \\ \cos(\phi)\sin(\alpha) \\ -\cos(\alpha)\cos(\theta) + \sin(\alpha)\sin(\theta)\sin(\phi) \end{pmatrix} \tag{5.33}$$

I proceed now to evaluate the third term of eq.5.25, that I name the rotational kinetic energy of the float, T_{rot}. After some linear algebra, having approximated for small angle α and removed all terms with order higher than three, T_{rot} is given

by the following expression:

$$
\begin{aligned}
T_{rot} &= \frac{1}{2}\left(\omega^{CB}\right)^{T}.I^{CB}.\omega^{CB} \\
&\approx \frac{1}{2}(\left(\left(I_{yy}+ml^2\right)\cos\left(\phi\right)^2+\left(I_{xx}+ml^2\right)\sin\left(\phi\right)^2\right)\dot{\theta}^2+ \qquad (5.34)\\
&\quad \left(I_{yy}-I_{zz}+ml^2\right)\cos\left(\phi\right)2\alpha\dot{\theta}\dot{\phi}+I_{zz}\dot{\phi}^2) \qquad (5.35)
\end{aligned}
$$

The second term of eq.5.25, T_{disp}, after approximating for small angles, α and θ_T, and after excluding all terms with order higher than three, is the following expression:

$$
\begin{aligned}
T_{disp} &= m\left(\dot{R}^i\right)^{T}\cdot\omega^{CB}\times r_{cm}^{CB} \qquad (5.36)\\
&\approx -lm(-\dot{Z}\left(\theta+\theta_T\cos\phi_T+\alpha\sin\phi\right)\dot{\theta} \qquad (5.37)\\
&\quad +\dot{X}\left(\dot{\theta}\cos\phi_T+\alpha\cos(\phi+\phi_T)\dot{\phi}\right) \qquad (5.38)\\
&\quad +\dot{Y}\left(\dot{\theta}\sin\phi_T+\alpha\sin(\phi+\phi_T)\dot{\phi}\right)) \qquad (5.39)
\end{aligned}
$$

Because the first term of eq.5.25 does not depend on any of the two degrees of freedom, ϕ and θ, which govern the dynamics of the torsion balance, it is not necessary to include it in the calculus of the total kinetic energy of the system to evaluate the Euler-Lagrange equations in ϕ and θ.

5.2.3 Potential energy

Now I examine the three potential energies associated with the float dynamics: the gravitational potential associated with the float CB, V_g, the elastic potential associated with the pendulum motion, V_θ, and the elastic potential associated with the torsional motion, V_ϕ.

Gravitational potential energy

I start with the gravitational potential of the centre of mass of the float, which can be written as:

$$V_g = mg\begin{pmatrix}0 & 0 & 1\end{pmatrix}.r_{cm}^{I} \tag{5.40}$$

$$= mg\begin{pmatrix}0 & 0 & 1\end{pmatrix}.(R^i + r_{cm}^{CB}) \tag{5.41}$$

Because R^i does not depend on the variables, ϕ and θ, I do not include it in the calculus of the potential energy as I have previously done for the kinetic energy. For small α and θ, V_g is given by the following equation:

$$V_g \approx -mgl\left(1 - \frac{\alpha^2}{2} - \frac{\theta^2}{2} - \alpha\theta\sin(\phi)\right) \tag{5.42}$$

Pendulum elastic potential energy

The potential energy, which is due to the restoring torque given by the elastic constant k_θ and the angle, θ_k, between the float axis z^k and the magnetic axis of the levitation bearing, z^L, is:

$$V_\theta = \frac{1}{2}k_\theta\theta_k^2 \tag{5.43}$$

where θ_k is given by the expression:

$$\theta_k = \arctan\left(\sqrt{\frac{((e_z^k)^L.e_x^L)^2 + \left((e_z^k)^L.e_y^L\right)^2}{((e_z^k)^L.e_z^L)^2}}\right) \tag{5.44}$$

$$(e_z^k)^L = U_{\theta_T}^{-1}.U^{-1}.U_\beta^{-1}.\begin{pmatrix}0\\0\\1\end{pmatrix} \tag{5.45}$$

$(e_z^k)^L$ is the unit vector associated with the z^k direction and represented in the laboratory coordinate system which has (e_x^L, e_y^L, e_z^L) as reference unit vectors. For small angles, θ, β and θ_T, excluding all the third order terms, θ_k^2 is given by the following equation (see in fig.5.4 for the simple case with $\theta = 0$):

$$\theta_k^2 \approx \theta^2 + \beta^2 + \theta_{\theta_T}^2 + 2\theta\theta_T\cos(\phi_T) - 2\theta\beta\sin(\phi) + 2\beta\theta_T\sin(\phi + \phi_T) \tag{5.46}$$

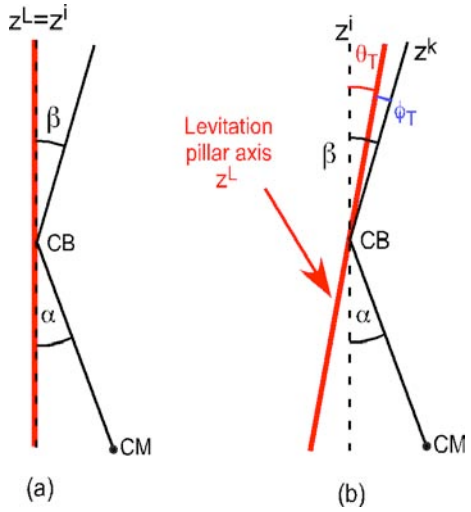

Figure 5.4: Schema indicating the tilt angle of the levitation pillar axis, z^L, with respect to the magnetic axis of the float for $\theta = 0$: a) untilted case ($\theta_T = 0$) and b) tilted case.

Torsional elastic potential energy

For small angles, θ and θ_T, I can reasonably assume that the potential energy due to the stiffness k_ϕ is given by the equation:

$$V_\phi = \frac{1}{2} k_\phi \left(\phi - \phi_1\right)^2 \tag{5.47}$$

with ϕ_1 a constant reference angle.

5.2.4 Euler-Lagrange differential equations

I compose the Lagrangian for our torsion balance which is given by the following sum:

$$L = T_{rot} + T_{disp} - V_g - V_\theta - V_\phi \tag{5.48}$$

I proceed to evaluate the Euler-Lagrange equations governing the motion of the float for the variables, ϕ and θ.

General equations in ϕ

From eq.5.48 I evaluate the differential equation associated with ϕ, which is given by:

$$\frac{\partial L}{\partial \phi} - \frac{d}{dt}\left(\frac{\partial L}{\partial \dot{\phi}}\right) = 0 \tag{5.49}$$

In the previous expression I substitute ϕ with $\phi' + \phi_0$ to consider different possible orientations of the pendulum motion with respect to the one given by U_α. After removing all the third order terms, adding the damping term $b_\phi \dot{\phi}'$ and the applied external torque Γ_0, I find the equation:

$$I_{zz}\ddot{\phi} + b_\phi \dot{\phi} + k_\phi \phi = \Gamma_0 + \Gamma_n \tag{5.50}$$

with

$$\Gamma_n = -\left(I_{yy} - I_{zz} + ml^2\right)\cos\left(\phi_0\right)\alpha\ddot{\theta} \tag{5.51}$$

$$+\frac{1}{2}\left(I_{xx} - I_{yy}\right)\sin\left(2\phi_0\right)\dot{\theta}^2 \tag{5.52}$$

$$+k_\theta \beta \theta_T \cos(\phi_0 + \phi_T) \tag{5.53}$$

$$+lm\alpha(\cos(\phi_0 + \phi_T)\ddot{X} + \sin(\phi_0 + \phi_T)\ddot{Y}) \tag{5.54}$$

where for simplicity I also supposed that $\phi_1 = \phi_0$ and dropped the index of ϕ', writing only ϕ. The input spurious torque, Γ_n, is composed by the following terms:

1. A term proportional to $\ddot{\theta}$, which I name the *pendulum acceleration term*. This term is maximum when the pendulum rotation θ is perpendicular to the tilt rotation α for $\phi_0 = 0$.

2. A term proportional to $\dot{\theta}^2$, which I call the *inertia asymmetry term,* and which derives from Euler's equations [36] [75]. It non linearly couples the velocity of pendulum mode $\dot{\theta}$ into the torsional mode and is null for $I_{xx} = I_{yy}$ or $\phi_0 = 0$.

3. A term proportional to θ_T, which I name the *direct tilt term* and which is due to the direct effect of the tilt oscillations of the laboratory ground. It is not null $k_\theta \beta \neq 0$.

4. A term proportional to $\ddot{X}$ and $\ddot{Y}$, which I call the *direct horizontal term* and which is due to the direct effect of horizontal seismic vibrations.

Only the first two terms have previously been found [35] but they are here expressed in terms of the moment of inertia which I can directly measure or derive from the CAD drawings of the float. To further evaluate the effect of these first two terms on the dynamic of the torsion balance, it is necessary to estimate $\ddot{\theta}$ and $\dot{\theta}$.

Simplified equations in θ

From the Lagrangian of eq.5.48 I can also write the Euler-Lagrangian equation in θ:

$$\frac{\partial L}{\partial \theta} - \frac{d}{dt}\left(\frac{\partial L}{\partial \dot{\theta}}\right) = 0 \tag{5.55}$$

If I assume $I_{xx} = I_{yy}$ and keep just the first order terms in θ, θ_T, $\dot{\theta}_T$, α and $\ddot{R}$, the previous equation becomes the following expression:

$$\left(I_{yy} + ml^2\right)\ddot{\theta} + b_\theta\dot{\theta} + (k_\theta + glm)\,\theta = \Gamma_p \tag{5.56}$$

with

$$\Gamma_p = lm\left(\ddot{X}\cos\phi_T + \ddot{Y}\sin\phi_T\right) - k_\theta\theta_T\cos\phi_T \tag{5.57}$$

where I added the damping term $b_\theta\dot{\theta}$ into eq.5.56. At first order the dynamic of the pendulum motion of the float is only influenced by the horizontal and tilt vibrations of the laboratory reference system with respect to the inertial frame.

5.3 SSTB transfer functions and input noise

In the following sections, given the differential equations governing the pendulum and torsional motions of the float, I will present the resulting transfer functions between the external applied torques and the angles, ϕ and θ.

I will evaluate the input torque noises acting on the float due to the horizontal and tilt seismic noises. For comparison, I will also estimate the torque noise, which is given by the thermal noise.

5.3.1 SSTB transfer function

I start from eq.5.50, from which I derive the transfer function, $T\left(\Gamma_{ext}, \phi\right)$, between the applied torque, $\Gamma_{ext} = \Gamma_0 + \Gamma_n$, and the resulting float angle, ϕ. Under the initial conditions:

$$\dot{\phi}(t=0) = \ddot{\phi}(t=0) = 0 \tag{5.58}$$

I write eq.5.50 as the following one:

$$\left(I_{zz}s^2 + b_\phi s + k_\phi\right) Y\left(s\right) = R\left(s\right) \tag{5.59}$$

$Y\left(s\right)$ and $R\left(s\right)$ are respectively the Laplace transforms of $\phi\left(t\right)$ and $\Gamma_{ext}(t)$ [5]. The transfer function $G_{\text{float}} = T\left(\Gamma_{ext}, \phi\right)$ is defined as:

$$G_{\text{float}}(s) = \frac{Y(s)}{R(s)} \tag{5.60}$$

$$= \frac{1}{I_{zz}s^2 + b_\phi s + k_\phi} \tag{5.61}$$

If the previous equation is expressed in the Fourier domain by setting $s = i\omega$, the amplitude of the transfer function is given by the expression:

$$\left|T\left(\Gamma_{ext}, \phi\right)\left(\omega\right)\right| = \frac{1}{I_{zz}\sqrt{(\omega_\phi^2 - \omega^2)^2 + (2\gamma_\phi\omega)^2}} \tag{5.62}$$

with $\gamma_\phi = b_\phi/(2I_{zz})$ and $\omega_\phi^2 = k_\phi/I_{zz}$.

5.3.2 Pendulum transfer function

The transfer function between the applied torque Γ_p of eq.5.57 and the pendulum angle, θ, is expressed instead by the equation:

$$T\left(\Gamma_p, \theta\right) = \frac{1}{I_\theta s^2 + b_\theta s + (k_\theta + glm)} \tag{5.63}$$

with $I_\theta = I_{yy} + ml^2$. In the Fourier domain for $\gamma_\theta = b_\theta/(2I_\theta)$ and $\omega_\theta^2 = \left(k_\theta + glm\right)/I_\theta$, the amplitude of the previous transfer function is given by the expression:

$$\left|T\left(\Gamma_p, \theta\right)\left(\omega\right)\right| = \frac{1}{I_\theta\sqrt{(\omega_\theta^2 - \omega^2)^2 + (2\gamma_\theta\omega)^2}} \tag{5.64}$$

5.3.3 Input seismic noise

Now, given the amplitude spectrum densities of the seismic horizontal acceleration and tilt noise, $S_{\ddot{X}}^{1/2} = S_{\ddot{Y}}^{1/2}$ and $S_{\theta_T}^{1/2}$ (which I suppose not to be correlated), I present the spectra of the input torque noises, $S_{\Gamma_{\ddot{\theta}}}^{1/2}$, $S_{\Gamma_{\theta_T}}^{1/2}$, $S_{\Gamma_{\ddot{X}}}^{1/2}$ and $S_{\Gamma_{\dot{\theta}^2}}^{1/2}$, which are associated respectively with eq.5.51, 5.52, 5.53 and 5.54.

Pendulum noise spectra

To evaluate the power spectra, $S_{\Gamma_{\ddot{\theta}}}$ and $S_{\Gamma_{\dot{\theta}^2}}$, I need first to know the power spectrum density, S_θ, of the pendulum oscillations, which are excited by the seismic noise. Thanks to eqs.5.57 and 5.63, S_θ can be written as the following equation [61]:

$$S_\theta = T\left(\Gamma_p, \theta\right)^2 \left(l^2 m^2 S_{\ddot{X}} + k_\theta^2 S_{\theta_T}\right) \tag{5.65}$$

From S_θ, I simply obtain the power spectrum density of the pendulum acceleration with the equation:

$$\begin{aligned} S_{\ddot{\theta}} &= \omega^4 S_\theta & (5.66)\\ &= \omega^4 T\left(\Gamma_p, \theta\right)^2 \left(l^2 m^2 S_{\ddot{X}} + k_\theta^2 S_{\theta_T}\right) & (5.67) \end{aligned}$$

The spectrum of $\dot{\theta}^2$, $S_{\dot{\theta}^2}$, is instead less straightforward to evaluate. $S_{\dot{\theta}^2}^{1/2}$ had been shown by [75] and [35] to be equal to:

$$S_{\dot{\theta}^2}^{1/2} = \omega_\theta^2 \sqrt{\tau_\theta}\left\langle \theta^2 \right\rangle \tag{5.68}$$

with $\tau_\theta = 1/\gamma_\theta$. $\left\langle \theta^2 \right\rangle$ is the standard deviation of the pendulum angle and is given by the equation:

$$\begin{aligned} \left\langle \theta^2 \right\rangle &= \int_0^\infty S_\theta d\omega & (5.69)\\ &= \int_0^\infty \left(l^2 m^2 S_{\ddot{X}} + k_\theta^2 S_{\theta_T}\right) T\left(\Gamma_p, \theta\right)^2 d\omega & (5.70) \end{aligned}$$

Torque noise due to the asymmetry of the moment of inertia

The power spectrum density, $S_{\Gamma_{\dot{\theta}^2}}$, of the torque noise, which is associated with the inertia asymmetry term of eq.5.52, is given by the following equation:

$$S_{\Gamma_{\dot{\theta}^2}} = \frac{1}{4}\left(I_{xx} - I_{yy}\right)^2 S_{\dot{\theta}^2} \tag{5.71}$$

where I have considered the worst case for $|\sin 2\phi_0| = 1$.

Torque noise due to the pendulum acceleration

The power spectrum density, $S_{\Gamma_{\ddot{\theta}}}$, of the torque due to the pendulum acceleration of eq.5.51, is given in the worst case by the following equation:

$$S_{\Gamma_{\ddot{\theta}}} = \left(I_{yy} - I_{zz} + ml^2\right)^2 \alpha^2\omega^4 T\left(\Gamma_p, \theta\right)^2 \left(l^2 m^2 S_{\ddot{X}} + k_\theta^2 S_{\theta_T}\right) \tag{5.72}$$

with $T\left(\Gamma_p, \theta\right)$ given by eq.5.63.

Torque noise from the direct coupling with the seismic noise

The power spectrum densities of the torque noises, which are given by the direct coupling of the float angle with the seismic noise, are given in the worst cases by the following equations:

$$S_{\Gamma_{\theta_T}} = k_\theta^2 \beta^2 S_{\theta_T} \tag{5.73}$$

$$S_{\Gamma_{\ddot{X}}} = l^2 m^2 \alpha^2 S_{\ddot{X}} \tag{5.74}$$

5.3.4 Input thermal noise

For comparison I have also calculated the expected amplitude spectrum density of the input thermal torque noise, $S^{1/2}_{\Gamma_{Th}}$, which is supposed to be white and given by the fluctuation dissipation theorem [48]. For a system, which is characterized by damping coefficient b_ϕ and which is at temperature T, $S^{1/2}_{\Gamma_{Th}}$ is given by the following equation:

$$S^{1/2}_{\Gamma_{Th}} = \sqrt{4 b_\phi K_B T} \tag{5.75}$$

with $K_B = 1.38 \times 10^{-23} J/K$ the Boltzman constant.

5.4 Model parameters and predictions

Before presenting all the expected input torque noise levels given by the seismic noise, it is necessary for me to provide a numerical estimate of all the defined parameters.

5.4.1 Seismic noise spectra

I will begin by describing the seismic noise, which is represented by three components: the vertical, the horizontal and the tilt seismic noise. I directly measured the vertical seismic noise down to $1Hz$ with a geophone, HS-10, from Geo Space LP, USA, on the isolation block where the cryostat is positioned. At $1Hz$ I found $S_{\ddot{Z}}^{1/2} = 10^{-5} ms^{-2}/\sqrt{Hz}$ which is in agreement with the previous estimate [35]. Because I know that $S_{\ddot{X}}^{1/2} = 2S_{\ddot{Z}}^{1/2}$ [9], I assumed $S_{\ddot{X}}^{1/2} = 2. \times 10^{-5} ms^{-2} Hz^{1/2}$ for frequencies bigger than $1Hz$. For frequencies, f, which are instead between $10mHz$ and $1Hz$, I have modelled the horizontal seismic noise with $S_{\ddot{X}}^{1/2} = 2. \times 10^{-5}/f^2 ms^{-2} Hz^{3/2}$ to include the observed drop of the seismic noise at such frequencies (see for example [11] and [56] about the Earth ambient noise spectrum at low frequencies). In my seismic model I have not included the microseismic peak, which is observed at $\approx 0.15Hz$ and which has no effect at frequencies of the torque measurements smaller than $20mHz$. Because I do not have any measured data about the seismic tilt of our laboratory, I assume an amplitude spectrum density, $S_{\theta_T}^{1/2}$, equal to $10^{-4}\mathrm{rad}/\sqrt{\mathrm{Hz}}$ and constant at all the frequencies [53] as it was assumed in the previous study of our SSTB [35].

5.4.2 Torsion balance

I present here the parameters, which describe the torsion balance and its dynamics:

- the torsion balance for the ISL test has a mass of $m = 100g$ and moments of inertia along the axis x, y, z $(I_{xx}, I_{yy}, I_{zz}) = (1.60, 1.64, 1.82) \times 10^{-4} kg \times m^2$. The moments of inertia are derived from the 3D Solidworks drawing of the float (with the test masses), which is used for ISL experiment.

- the pendulum mode is characterized by a pendulum arm $l = 8.78mm$. With such a pendulum arm length, the compound pendulum frequency f_θ

corresponds to the measured one of $1.1Hz$:

$$f_\theta = \frac{1}{2\pi}\sqrt{\frac{k_\theta + mgl}{ml^2 + I_{xx}}} \tag{5.76}$$

The damping factor of the pendulum mode for $4A$ in the damper circuit is $\gamma_\theta = 0.18\ s^{-1}$ (or equivalently $b_\theta \approx 6 \times 10^{-5} kg \cdot m^2/s$ or $Q \approx 19$), while the tilt stiffness has been numerically estimated [35] to be $k_\theta = 2.9 \times 10^{-7} Nm/rad$. A tilt stiffness k_θ, which is even two orders of magnitude higher cannot be excluded. Trapped magnetic flux in the float shell or magnetic impurities in the damper disk, which might couple with the levitation magnetic field, or deformations of the shape of the float shell [19] might possibly boost k_θ to larger values.

- The torsional mode, when the current is stored in the actuator superconducting circuits, has $k_\phi = 4.5 \times 10^{-6} Nm/rad$ (for period of $\approx 40s$) and $\gamma_\phi \approx 1.85 \times 10^{-4} s^{-1}$ (or equivalently $b_\phi = 6.73 \times 10^{-8} kg \cdot m^2/s$ or $Q \approx 420$).

- The tilt angle, β, is assumed to be no larger than $1°$, which implies an extremely small $\alpha \approx 5.5 \times 10^{-7} rad$ as given by eq.5.12.

5.4.3 Expected transfer functions and torque noises

Given the numerical values from the previous paragraph, in fig.5.5 I plot the amplitude of the transfer functions $|T(\Gamma_{ext}, \phi)|$ and $|T(\Gamma_p, \theta)|$, multiplied respectively by the torsional and the pendulum stiffness, k_ϕ and k_θ. In table 5.1 I give instead the expected torque noise at a frequency of $20mHz$ for all the noise terms I have so far modelled.

Source	$Nm/\sqrt{Hz}$	Source	$Nm/\sqrt{Hz}$
$S^{1/2}_{\Gamma_{\theta_T}}$	2.5×10^{-13}	$S^{1/2}_{\Gamma_{\ddot{X}}}$	2.2×10^{-18}
$S^{1/2}_{\Gamma_{\dot{\theta}^2}}$	2.9×10^{-14}	$S^{1/2}_{\Gamma_{\ddot{\theta}}}$	3.2×10^{-22}
$S^{1/2}_{\Gamma_{Th}}$	3.9×10^{-15}		

Table 5.1: Different components of the expected torque noise, which are due to the seismic and the thermal noise at 20mHz.

The smallness of the expected α implies that the acceleration term due to eq.5.72 has a torque noise spectrum, $S^{1/2}_{\Gamma_{\ddot{\theta}}}$, which is negligible at $20mHz$ with

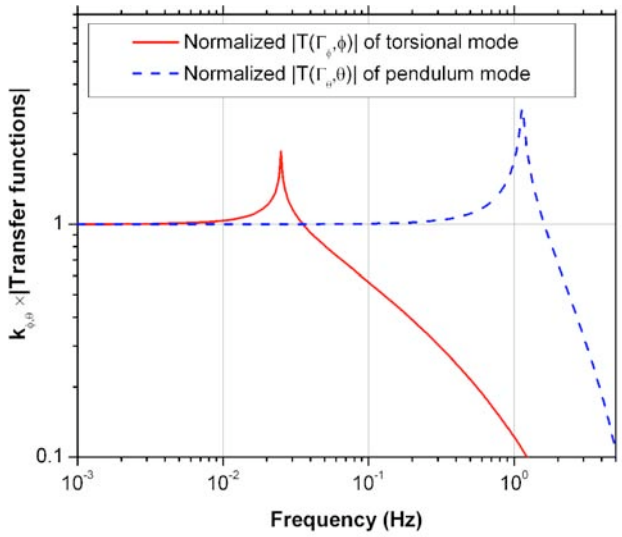

Figure 5.5: Amplitudes of the transfer functions $|T(\Gamma_{ext}, \phi)|$ and $|T(\Gamma_p, \theta)|$ multiplied respectively by the associated stiffness k_ϕ and k_θ.

respect to the other noise terms, being of the order of $3.2 \times 10^{-22} Nm/\sqrt{Hz}$. At these frequencies the term, which is given by the direct coupling of the horizontal seismic oscillations to the torque (eq.5.74), gives a torque noise spectrum, $S^{1/2}_{\Gamma_{\ddot{X}}} = 2.2 \times 10^{-18} Nm/\sqrt{Hz}$ which still is smaller than the expected thermal noise, $S^{1/2}_{\Gamma_{Th}} = 3.9 \times 10^{-15}$, for a temperature of $4.2K$.

The torque noise, which is given by the difference of the moment of inertia I_{xx} and I_{yy} and which is given by eq.5.71, has noise spectrum $S^{1/2}_{\Gamma_{\dot{\theta}^2}} = 2.9 \times 10^{-14} Nm/\sqrt{Hz}$, a few times larger than the thermal noise. As is clear from table 5.1 and fig.5.6, the biggest contribution to the torque noise is given by the direct coupling between the tilt seismic noise and the torsional angle ϕ: the expected torque spectrum $S^{1/2}_{\Gamma_{\theta_T}}$ is $2.5 \times 10^{-13} Nm/\sqrt{Hz}$ - which, I notice, is also the typical noise level which was achieved during the spin coupling experiment with the MKI SSTB [34]. As expressed by eq.5.73, this contribution to the torque noise is independent of the mass and moment of inertia of the float and depends only on the ground tilt noise level, $S^{1/2}_{\theta_T}$, on the tilt stiffness, k_θ, and the observed tilt, β, of the float. Because the values of these parameters are similar to the ones used [35] for the MKI SSTB, I expect that my prediction for $S^{1/2}_{\Gamma_{\theta_T}}$ also applies to the previous version of torsion balance.

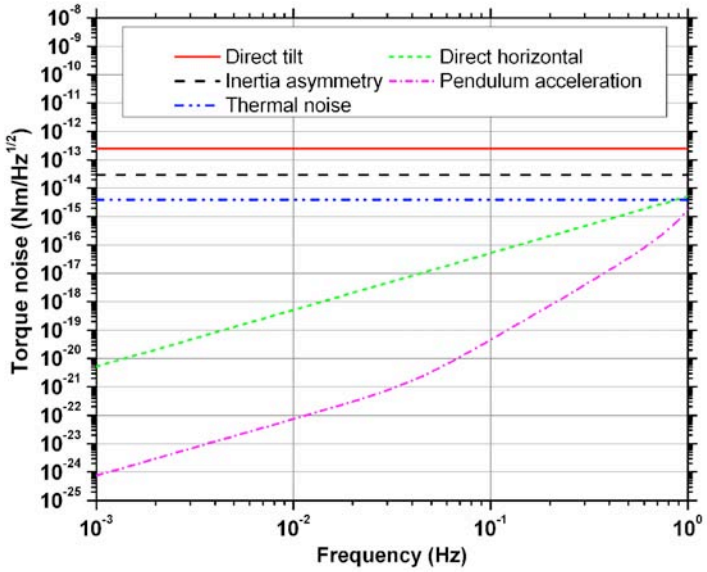

Figure 5.6: Amplitude spectrum densities of the torque noise, which are given by different seismic noise terms between $1mHz$ and $1Hz$.

5.5 Conclusion

In this chapter I have discussed the model of the torsion balance that, given the moments of inertia of the float and its elastic and damping coefficients, predicts the differential equations governing the dynamics of the float. I have used this analytical model to evaluate the transfer function between the applied torque and the float angle ϕ and to estimate the effect of the seismic noise on the torque, to which the float is subjected. The new model, compared with previous work, predicts new contributions to the torque noise, which are due to seismic noise. These new terms are due to the difference of moment of inertia, I_{xx} and I_{yy}, or to the direct coupling of tilt seismic oscillations with the float angle ϕ. For our SSTB the contribution of the former is expected to be $2.9 \times 10^{-14} Nm/\sqrt{Hz}$ at a frequency of $20mHz$. The contribution of the latter is instead predicted to be around $2.5 \times 10^{-13} Nm/\sqrt{Hz}$, for a tilt coupling $d\Gamma/d\theta_T = 2.5 \times 10^{-9} Nm/rad$ and a ground tilt noise of $10^{-4}\mathrm{rad}/\sqrt{\mathrm{Hz}}$. However, the effect of the tilt noise might be larger by a few orders of magnitude, if the tilt coupling is boosted to higher values by asymmetries of the shape of the float shell or by magnetic flux trapped inside it. The expected thermal noise for the MKII SSTB is $3.9 \times 10^{-15} Nm/\sqrt{Hz}$.

Chapter 6

The servo loop and the expected torque sensitivity

6.1 Introduction

The mechanism of the torque measurement of the torsion balance is based on a servo loop principle: when the torsion balance is subjected to a torque, Γ_{ext}, spurious or the one we want to study, what we measure is the torque necessary to keep the balance at a constant angular position, Γ_{ext}. The torsion balance, when it is subjected to an input torque, rotates in one direction by an angle which is defined by the transfer function of the float, G_{float} (see eq.5.61). Instead of letting the float freely rotate, by using the servo system of fig.6.1, we automatically apply a torque to the float with the opposite sign with respect to the input torque. In this way the balance is kept at a constant angle. This chapter is dedicated to the analysis of all the elements of the servo loop in order to reach the following two goals:

1. To define the closed loop transfer function between the input torque and the servo effort, we consider to be our torque measurement.

2. To characterise all the noise sources which contribute to the noise of the measured torque.

I will analyse the capacitive sensor, which was adopted to read the float angle during the preliminary test of the inverse square law of gravity. I will predict and measure its transfer function, G_{CS}, and its noise level. I will discuss the

digital compensator and, through numerical simulation, I will define its open loop transfer function, H_{PII^2D}. I will present the transfer function, H_{MA}, and the noise level of the magnetic actuator adopted to feed back torque to the float and to control its angle. After having described all the subsystems, I will analyse the servo loop as a whole system and I will predict the closed loop transfer function between the applied and the measured torque. Thanks to the developed analytical model of the servo system I will briefly study the angular stability of the torsion balance. I will conclude our analysis of the SSTB by modelling the contribution of all the different noise sources to the output torque noise.

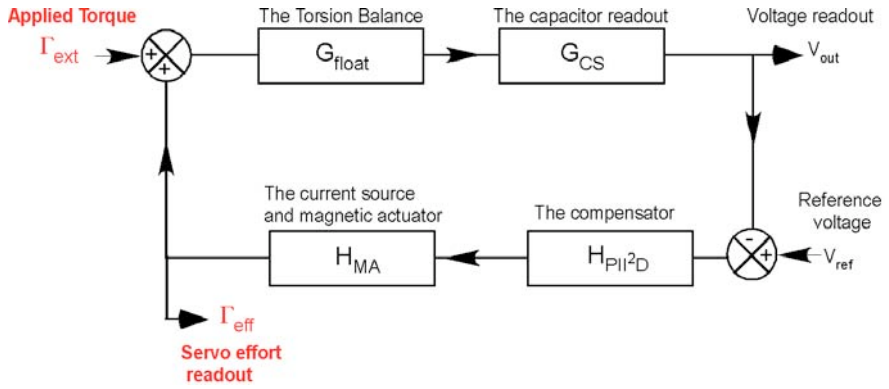

Figure 6.1: Global schema of the SSTB servo system

6.2 The capacitive readout

In the final design of the MKII SSTB we will use a homodyne low temperature interferometer [62] to read out the angular position of the float. However because this device is currently being developed, we used a capacitive sensor readout for the preliminary tests of the SSTB and of the ISL of gravity. This angular readout system, even though a temporary solution, has enough angular sensitivity for the preliminary tests of the ISL of gravity. The following section is dedicated to the analysis of the capacitive sensor, which converts the angular position of the torsion balance to a voltage output. Because the signal we are looking for is a low frequency one, to avoid the $1/f$ noise of the electronics, we use a lock-in technique which boosts the signal at high frequency in the detection chain and recover it at its end by using a lock-in amplifier. Our capacitive readout is composed of the following subsystems:

- 1. a capacitive transducer, which transforms the angular displacement of the float in the change of two capacitances.
  2. a capacitance bridge with its preamplifier, which, given a high frequency AC voltage signal as input, transforms the difference of the previous capacitances into an amplitude modulation of the AC voltage output.
  3. a lock-in amplifier which recovers the voltage modulation from the high frequency carrier.

6.2.1 Capacitive transducer

The capacitive transducer is the first step of our readout system and transforms angular displacements of the float, $\Delta\phi$, in variations of the two capacitances, C_1 and C_2, between a common a gold coated mirror connected to the float, and two metal plates on its sides. The plates are connected through insulating spacers to a pillar facing the float (see fig.6.2). The capacitance between two plates of area A and separated by a distance d is given by the equation:

$$C\left(d\right) \approx \epsilon_0 \frac{A}{d} \tag{6.1}$$

where $\epsilon_0 = 8.85pF/m$ is the permittivity of vacuum. For the capacitive transducer of the SSTB the two capacitances, C_1 and C_2, are associated with the distances, d_1 and d_2, between the two side plates and the central one (see fig.6.2). d_1 and d_2 are given by the expressions:

$$d_1 = \frac{(D-t)}{2} + (h+R)\phi \tag{6.2}$$

$$d_2 = \frac{(D-t)}{2} - (h+R)\phi \tag{6.3}$$

where D is the measured distance between the two plates, t is the thickness of the gold coated mirror, R is the radius of the float and h is the distance of the plates from the float shell (see fig.6.2 and table 6.1).

The difference of two capacitances is given by the formula:

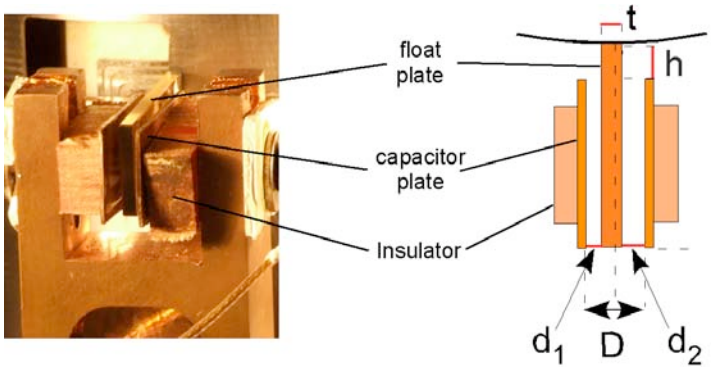

Figure 6.2: Picture and schema of the capacitive plates and the float.

A	$2.57cm^2$	h	$7mm$
D	$3.5mm$	t	$1.8mm$
R	$46.86mm$		

Table 6.1: Parameters of the capacitive transducer. A is an average value.

$$\Delta C(\phi) = \epsilon_0 \frac{8A(h+R)\phi}{(D-t)^2 - 4(h+R)^2\phi^2} \tag{6.4}$$

$$\approx \epsilon_0 \frac{8A(h+R)}{(D-t)^2}\phi \tag{6.5}$$

$$= (3.4 \times 10^{-10} F/rad)\phi \tag{6.6}$$

Eq.6.5 had been derived in case of small angular displacement and it is a good approximation within 1% for angles smaller than $\approx 5 \times 10^{-4} rad$. Because the capacitive transducer is not linear for large angles ($|\phi| \gtrsim 5mrad$), we have to try to set the float working position as near as possible to the null angular position of the capacitive bridge.

6.2.2 The capacitance bridge

The second stage of the angular readout is the capacitive bridge and its preamplifier, which transform the previous $\Delta C(\phi)$ in the amplitude modulation of an high frequency AC voltage signal. During the experiment we used two different configurations of the capacitance bridge: the first one was adopted when we had to calibrate the torque effort of the SSTB and the Attocube motion; the second one was used when we were taking the torque measurements necessary for the

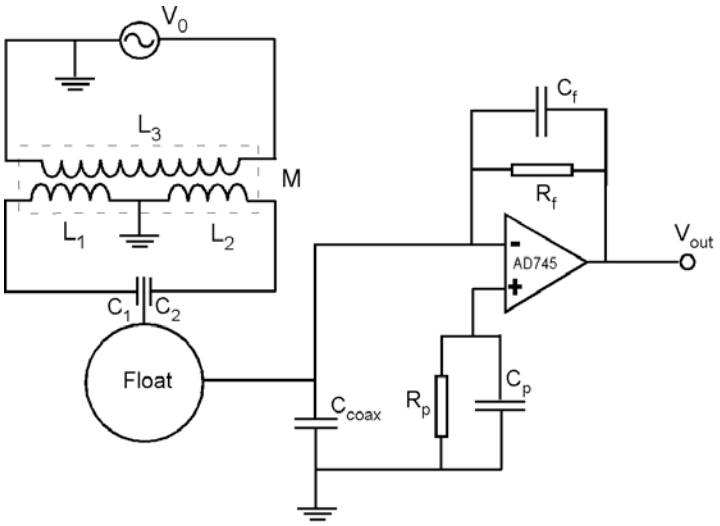

Figure 6.3: Schema of the capacitor bridge, which was used during the torque measurements.

ISL tests of gravity. The two configurations mainly differ in terms of where the AC reference voltage is applied to the system.

Measurement configuration

This configuration uses a transformer and a reference AC signal to apply two current signals to the capacitive plates facing the float. The change in the difference of the capacitance ΔC modulates the current signal coming out from the float through the thin gold wire, which is attached to its top. Outside the cryostat a current pre-amplifier transforms and amplifies the previous current signal in a voltage output, V_{out}, which will be read by the digital servo compensator. For a detailed analysis of the transfer function and expected output noise of such a capacitive bridge I refer to the appendix C. This configuration has the advantage that the float is set to virtual ground through the op-amp, and that the electrostatic forces between the ISL test masses are reduced with respect to the other configuration of the capacitive bridge, where we apply the reference AC voltage to the float.

From our theoretical model of the capacitive bridge and the pre amplifier I expect (see appendix C):

$$\left|\frac{dV_{out}}{d\Delta C}\right|_{meas.} = \frac{R_f}{\sqrt{1+\omega_0^2 R_f^2 C_f^2}}\omega_0 V_0 \tag{6.7}$$

where ω_0 and V_0 are the frequency and the amplitude of the reference AC

Capacitive bridge (measurement mode)			
R_f	$1.5M\Omega$	R_p	$1.5M\Omega$
C_f	$10pF$	C_p	$0.33nF$
C_{coax}	$400pF$	$L = M$	$20mH$
ω_0	$2\pi \times 70kHz$	V_0	$0.5 \times \sqrt{2}V$

Table 6.2: Numerical values of all the components of the capacitive bridge used during the torque measurements

Capacitive bridge (calibration mode)			
R_f	$10k\Omega$	R_i	200Ω
C_f	$4.7pF$	$L = M$	$20mH$
C_{coax}	$400pF$		
ω_0	$2\pi \times 70kHz$	V_0	$\sqrt{2}V$

Table 6.3: Numerical values of all the components of the capacitive bridge used during the calibration of the torque effort

signal. Assuming the value of table 6.2 I expect $|dV_{out}/d\Delta C|_{meas.} = 69.8mV/pF$ while from room temperature measurements we found instead $|dV_{out}/d\Delta C|_{meas.} = 71.53 \pm 0.05mV/pF$.

From the analysis of all the different noise sources of the op-amp (see appendix C), the noise level predicted for the amplifier output, is around $0.12\mu V/\sqrt{Hz}$. This noise level is mainly given by the voltage noise of the op-amp which is amplified by the high capacitance to ground of the coaxial cable, C_{coax}, bringing the current from the float to the pre-amplifier input. The measured noise at the output of the amplifier was $\approx 15\mu V/\sqrt{Hz}$, which was attributed to pick-up noise inside the vacuum can. Improved shielding inside the vacuum can may remove this extra noise source for future experiments.

Calibration configuration

This configuration was used during the calibration of the torque effort and of the Attocube displacement, where an accurate knowledge of various capacitances is necessary. As shown in fig.6.4, the capacitive sensor is made of two parts: firstly the capacitive bridge which applies the reference AC voltage signal to the float. It transforms the difference of capacitances ΔC to a voltage signal V_{ab} between the output terminal a and b of a transformer. Secondly, the pre-amplifier which amplifies the signal V_{ab} to V_{out}.

As shown in fig.6.4 with this configuration of the capacitance bridge we apply two AC signals added together to the float: one is used for the capacitive sensor

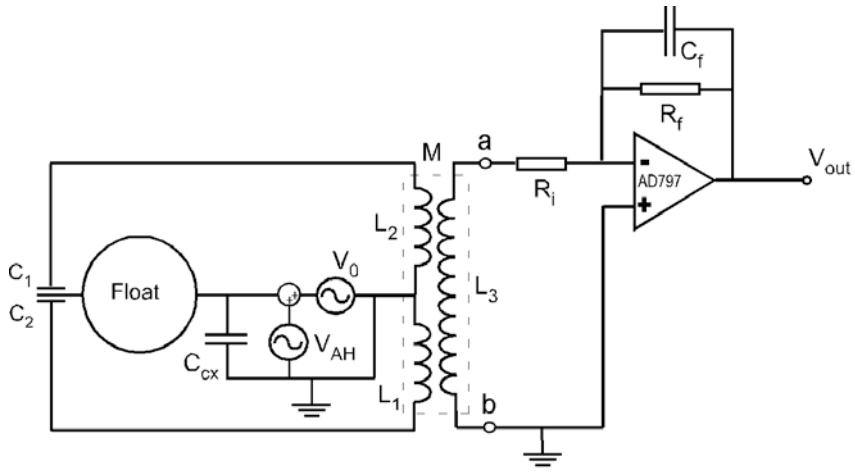

Figure 6.4: The schema of the capacitive bridge, which was used during the calibration of the SSTB.

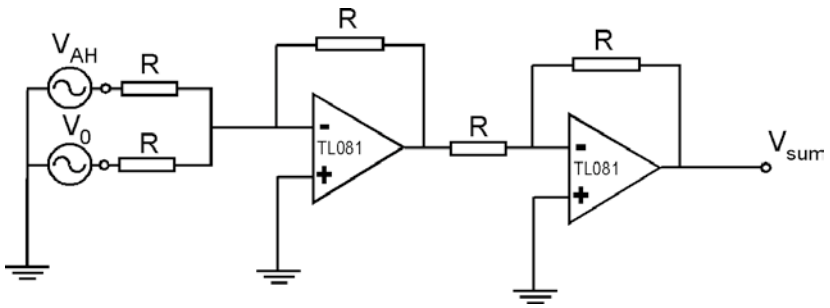

Figure 6.5: Summing amplifier, which is used to add the drive signals together of the Andeen-Hagerling and of our capacitive bridge.

and the other one for the Andeen-Hagerling ultra precision capacitance bridge (see chapter 4). The two signals are added together thanks to the summing amplifier circuit showed in fig.6.5. We employ the Andeen-Hagerling capacitance bridge to perform the necessary capacitance measurements while at the same time servo controlling the torsion balance. We could not have taken these measurements with the capacitive bridge adopted for the torque measurements. This configuration of the capacitive bridge does not suit the torque measurements necessary for the ISL test of gravity, because of the large voltages, which are applied to the float, and because of the large electrostatic forces, which are therefore induced between the test masses.

I do not discuss here an analytical model for this capacitive bridge and its preamplifier, because it is beyond the scope of this work, and furthermore unne-

cessary to predict the torque noise spectrum of the SSTB. From room temperature measurements (see 6.2.3) I found that:

$$\left|\frac{dV_{out}}{d\Delta C}\right|_{calib.} \approx 3mV/pF \tag{6.8}$$

For this capacitive bridge, the output voltage noise of the preamplifier was measured to be $80nV/\sqrt{Hz}$.

6.2.3 The lock in amplifier

A FEMTO LIA-BVD-150-H phase lock-in amplifier is used to extract the low frequency signal, which is associated with the angular motion of the float from the AC high frequency voltage signal at the output of the capacitive bridges. For the capacitive bridge of the torque measurements, the lock-in sensitivity was $100mV$, which corresponded to a measured transfer function of $TF_{lockin}(100mV) = 60$. When we used the capacitive bridge for the calibration of the SSTB, the lock-in sensitivity was $30mV$, which corresponded to a measured transfer function of $TF_{lockin}(30mV) = 200$. For the capacitive bridge of the torque measurements, combining the results from the theoretical estimation of the $d\Delta C/d\phi$ and the previous experimental estimate of $|dV_{out}/d\Delta C|_{meas.}$, I find that:

$$\left|\frac{dV_{out}}{d\phi}\right|_{meas.} \approx 1460V/rad \tag{6.9}$$

During the low temperature experimental run we measured $|dV_{out}/d\phi|_{meas.} = 1500 \pm 157V/rad$ (see chapter 7). For the capacitive bridge of the torque calibration, the transfer function is expected to be:

$$\left|\frac{dV_{out}}{d\phi}\right|_{calib} \approx 208V/rad \tag{6.10}$$

During the low temperature experimental run we measured $|dV_{out}/d\phi|_{calib.} = 11 \pm 38V/rad$ (see chapter 7).

The measured input voltage noise of the lock-in amplifier is $\approx 200nV/\sqrt{Hz}$. This noise level is smaller than the output voltage noise of the capacitive bridge of the torque measurements but is larger than the output voltage noise of the capacitive bridge of the torque calibrations. An intermediate additional amplifier is therefore necessary to make the noise from the pre-amplifier the dominant noise

for the capacitive bridge of the torque calibrations [87].

6.3 The digital servo compensator

In this section I will discuss the core of the servo system of our torsion balance: the digital servo compensator. This subsystem has as input the voltage signal associated with the angular position of the float, and as output the signal controlling the feedback torque, which is applied back to the float. If the float is subjected to an external torque, the digital compensator applies an opposite feedback torque to it which, at least at low frequency, cancels it perfectly. I can divide the digital compensator into three stages: the digitalisation of the analogue voltage, the digital PII^2D compensator (see the following) and the passage from digital to analogue output. Because we want to sample the analogue signal at $50Hz$, firstly we filter this signal with an anti-aliasing low pass filter, which is characterised by a cutoff frequency of $25Hz$. The signal is digitalised by 16-BIT analogue to digital converter (Measurement Computing PCI-DAS6035), which is running on the PCI bus of a PC. The digital signal is given as input to the digital compensator program developed with HP Vee.

The digital compensator has a proportional (P), a differential (D), a integral (I) and a double integral (I^2) term (see fig.6.6). If $V_e = V_{in} - V_{ref}$ is the error voltage signal with respect to a reference signal, V_{ref}, setting the angular position of the float the four previous terms are represented by the following equations:

$$V_P = K_P V_e \tag{6.11}$$

$$V_D = K_D \frac{\partial V_e}{\partial t} \tag{6.12}$$

$$V_I = K_I \int_o^t V_e d\acute{t} \tag{6.13}$$

$$V_{I^2} = K_{I^2} \iint_0^t V_e d\acute{t} \tag{6.14}$$

K_P, K_I, K_{I^2} and K_D are the proportionality constants for each term. The output voltage of the PII^2D compensator, V_{out}, is given by the sum of the four terms. In the Fourier space the transfer function of the compensator, TF_{PII^2D}, is represented by the following equation:

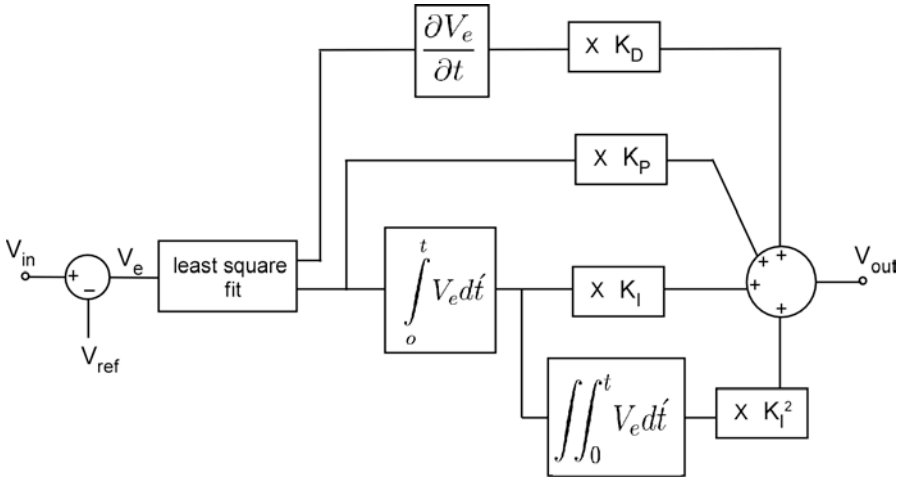

Figure 6.6: Schema of the digital compensator developed in HP-VEE.

$$TF_{PII^2D} = \frac{\tilde{V}_{out}}{\tilde{V}_e} = K_P + i\omega K_D - i\frac{K_I}{\omega} - \frac{K_{I^2}}{\omega^2} \tag{6.15}$$

with $\tilde{V}_{out}$ and $\tilde{V}_e$ the Fourier transforms of V_{out} and V_e.

In order to reduce the effect of the noise at high frequencies, a Savitzky–Golay smoothing filter [69] is applied to the error voltage input, V_e, which is least-square fitted to a straight line. Using this procedure we obtain a more accurate estimate of the error voltage input and of its derivative [33]. To avoid having a loop execution time of the program, τ_{exe} , which is too long and introduces an unwanted large phase shift of the voltage output, the buffer size n of the fitted data set has been chosen such that $\tau_{exe} \leq 15ms$. The loop execution time also fixes the sampling rate of the data acquisition, which is now around at $66Hz$.

In fig.6.7 and fig.6.8 I plot the amplitude and phase of the open loop transfer functions for each term of the digital compensator. The transfer function was obtained by injecting simulated data into the compensator input and by assuming

$$(K_P, K_I, K_{I^2}, K_D)_{set} = (1, 1, 1, 1) \tag{6.16}$$

It is clear from fig.6.7 and fig.6.8 that at up to $0.1Hz$, the PII^2D transfer functions follow the expected theoretical behavior. At higher frequencies they are greatly reduced by the low pass Savitzky–Golay smoothing filter within the Vee program. However I had not included any low pass filter in the analytical model I had developed. I found that for frequencies smaller than $\approx 0.1Hz$, the total

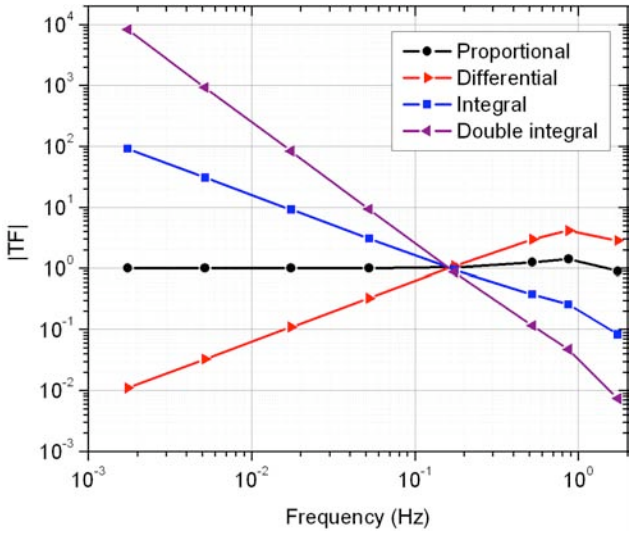

Figure 6.7: Amplitude of the transfer functions for the different terms of the compensator for unity input parameters.

transfer function, which fits to the data, is given by the following equation:

$$\begin{aligned} TF_{PII^2D}(f) &= -[K_P + iK_D f \times (5.69 \pm 0.09) \\ &\quad -i\frac{K_I}{f \times (6.29 \pm 0.01)} - \frac{K_{I^2}}{f^2 \times (39.51 \pm 0.05)}] \qquad (6.17) \\ &\approx -[K_P + i\omega \times K_D\,(0.9 \pm 0.01) - i\frac{K_I}{\omega} - \frac{K_{I^2}}{\omega^2}] \qquad (6.18) \end{aligned}$$

with $\omega = 2\pi f$ and where I introduced the minus sign to guarantee the stability of the servo system. Only the proportional term, K_D, which is given as input parameter to the Vee program, has to be corrected by 10% to obtain the correct parameter for the analytical model.

During the test of the ISL of gravity we used the optimal parameters:

$$(K_P, K_I, K_{I^2}, K_D)_{set} = (2, 1.2 \times 0.9, 10^{-2}, 10) \qquad (6.19)$$

which guaranteed that the servo effort exactly cancelled the applied torque at low frequencies (see chapter 7).

The digital signal from the compensator is transformed to an analogue signal via a PC based PCI bus 16-BIT digital-to-analogue converter card.

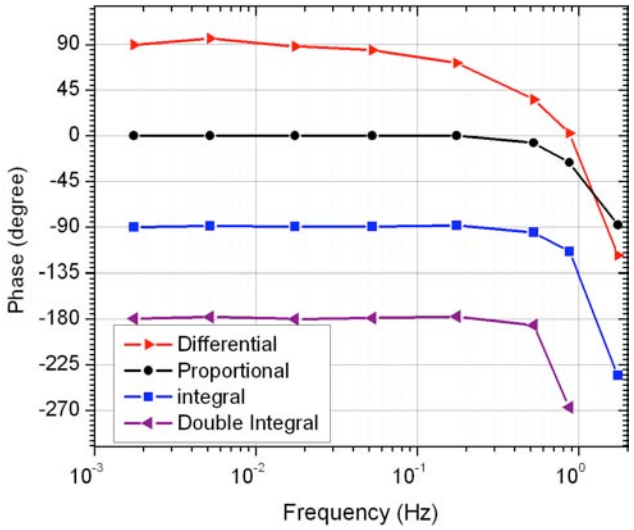

Figure 6.8: Phase of the transfer function of the different terms of the compensator for unity imput parameters.

6.4 The magnetic actuator

In this section, I will present the actuator system of the torsion balance by which we give a natural stiffness to the float and counter balance the applied torque. In principle the torsion balance will have the best torque sensitivity with a null or very small torsional stiffness (see section 6.6.1). During the tests of the ISL of gravity we found that it was necessary to set a minimum stiffness corresponding to a period of $\approx 30-40sec$ to balance an unwanted spurious torques acting on the SSTB. This spurious torque might be due to an asphericity of the float shell or to magnetic flux, which was trapped within the shell itself. Without this added large natural stiffness, the torsion balance stuck on one of the two capacitive plates, making any torque measurements impossible.

The basic idea of the magnetic actuator is the conservation of the magnetic flux in a superconducting circuit and the modulation of the inductances of such circuit as function of the angular position of the float. The inductances are the ones associated with the four superconducting rectangular coils (see fig.4.6), which are connected together in pairs as shown in fig.6.11. Because the coils are facing four rectangular windows cut out of the float shell (see fig.6.9 and fig.4.5), when the float rotates in one direction, two of the float windows overlap more over the respective coils while the other pair overlaps less (see fig.6.10). In this way the inductances of the four coils are modulated by the rotation of the

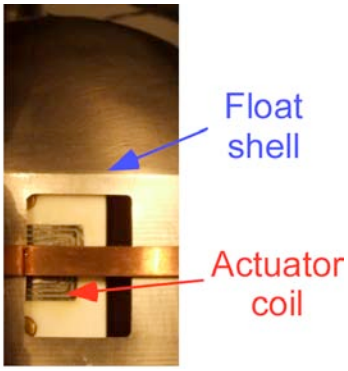

Figure 6.9: Photo of the superconductive coil, when it is partially covered by the niobium shell of the torsion balance

float: the inductances of the first pair of coils are decreased, while the ones of the second pair are increased, when the float angle is increased. Because of the conservation of the magnetic flux in a superconducting loop, this modulation of the inductances changes the currents flowing in the superconductive circuits and the total stored energy as a function of the float rotation. As a consequence, a torque is exerted back to the float, giving it a natural restoring stiffness. Thanks to a flux transformer coupled with the two superconducting circuits (FT_s see fig.6.11), we can change the magnetic fluxes, which are stored in each of them. By adding magnetic flux to one circuit and subtracting it from the other one, it is possible to modify the total stored energy and to apply a torque back to the balance. The following section is divided into two parts: firstly, the discussion and modelling of the superconducting actuator circuits; secondly, the description of the current source, which modulates the magnetic fluxes within the circuits and which applies a variable torque to the balance.

6.4.1 The superconducting transducer circuit

By looking at the circuit of fig.6.11 we can write the equations for the system using a method similar to the Maxwell mesh method which, when applied to the two superconducting circuits, has to satisfy the conservation of their magnetic fluxes, Φ_1 and Φ_2. For our circuits, Φ_1 and Φ_2 are given by the following system [33],[35] [34]:

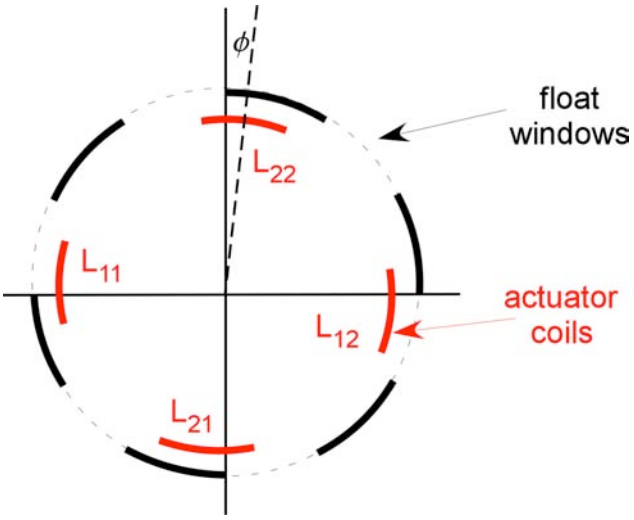

Figure 6.10: Schema of the float and of the four niobium coils, whose inductances are modulated by the float rotation.

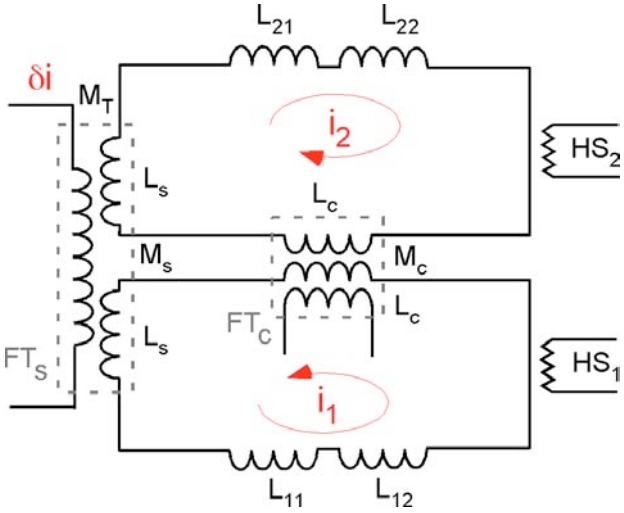

Figure 6.11: Schema of the superconducting circuit, which is used to apply a torque (or restoring stiffness) back to the torsion balance.

$$\begin{aligned} \Phi_1 &= i_1(L_1 + L_c + L_s) - i_2(M_c + M_s) \\ \Phi_2 &= i_2(L_2 + L_c + L_s) - i_1(M_c + M_s) \end{aligned} \tag{6.20}$$

where

$$\begin{aligned} L_1 &= L_{11} + L_{12} \\ L_2 &= L_{22} + L_{21} \end{aligned} \tag{6.21}$$

are the sum of the inductances of the superconducting coils connected in pairs. i_1 and i_2 are the currents stored in the two superconducting loops by means of the superconducting transformer FT_c (see fig.6.11) and the heat switches (HS_1 and HS_2). The procedure for storing i_1 and i_2 is similar to the one we employed to store the levitation current (see chapter 4). M_c and M_s are the mutual inductances between the two superconducting loops due to the associated flux transformers, which we employ respectively to store the initial currents in the circuits and to modify them with a variable offset current, δi. L_c and L_s are the inductances of the secondary circuits of the two transformers. The eq.6.20 can be rewritten as:

$$\Phi = \Psi i \tag{6.22}$$

with

$$\Psi = \begin{pmatrix} L_1 + L_c + L_s & -(M_c + M_s) \\ -(M_c + M_s) & L_2 + L_c + L_s \end{pmatrix} \tag{6.23}$$

$$\Phi = \begin{pmatrix} \Phi_1 \\ \Phi_2 \end{pmatrix} \tag{6.24}$$

$$i = \begin{pmatrix} i_1 \\ i_2 \end{pmatrix} \tag{6.25}$$

The total energy stored in the superconducting circuits is given by the equation:

$$E = \frac{1}{2}\Phi_0^T \Psi^{-1} \Phi_0 \tag{6.26}$$

with

$$\Psi^{-1} = \frac{1}{\varkappa} \begin{pmatrix} L_1 + L_c + L_s & M_c + M_s \\ M_c + M_s & L_2 + L_c + L_s \end{pmatrix} \tag{6.27}$$

and

$$\varkappa = (L_1 + L_c + L_s)(L_2 + L_c + L_s) - (M_c + M_s)^2 \tag{6.28}$$

If i_{10} and i_{20} are the initial stored currents in the two superconducting loops, for $L_1 \approx L_2 \gg M_c + M_s$ the initial stored magnetic flux is:

$$\Phi_0 = L \begin{pmatrix} i_{10} \\ i_{20} \end{pmatrix} \tag{6.29}$$

We approximate the inductances L_1 and L_2 for small angles ϕ with the following equations:

$$L_1 = L + \alpha\phi - \beta\phi^2 \tag{6.30}$$

$$L_2 = L - \alpha\phi - \beta\phi^2 \tag{6.31}$$

By assuming that

$$L_c = M_c \quad , \quad L_s = M_s \tag{6.32}$$

we find that

$$\Psi^{-1} = \frac{1}{\xi} \begin{pmatrix} L + M_c + M_s - \phi(\alpha + \beta\phi) & M_c + M_s \\ M_c + M_s & L + M_c + M_s + \phi(\alpha - \beta\phi) \end{pmatrix} \tag{6.33}$$

with

$$\xi = L(L + 2(M_c + M_s)) - (\alpha^2 + 2(L + M_c + M_s)\beta)\phi^2 + \beta^2\phi^4 \tag{6.34}$$

From the previous equation, eq.6.26, from eq.6.29 and assuming

$$i_{10} = i_0 + \Delta i \tag{6.35}$$

$$i_{20} = i_0 - \Delta i \tag{6.36}$$

for $\phi = 0$ the torque acting on the float is given by the equation:

$$\Gamma = -\left(\frac{\partial E(\phi)}{\partial \phi}\right)_{\phi=0} = \frac{2 i_0 \Delta i \alpha L}{L + 2(M_c + M_s)} \tag{6.37}$$

The resulting natural torsional stiffness, k_ϕ, is instead given by the expression:

$$\begin{aligned} k_\phi &= \left(-\frac{\partial E(\phi)}{\partial \phi^2}\right)_{\phi=0} \qquad (6.38)\\ &= -2\frac{\Delta i^2\left(\alpha^2 + L\beta\right) + i_0^2\left(L + 2(M_c + M_s)\right)\left(\alpha^2 + \left(L + 2(M_c + M_s)\right)\beta\right)}{\left(L + 2(M_c + M_s)\right)^2} \end{aligned}$$

k_ϕ for $L >> M_c + M_s$ is approximated by the equation:

$$k_\phi \approx -2\left(\Delta i^2 + i_0^2\right)\left(\frac{\alpha^2}{L} + \beta\right) \tag{6.39}$$

By storing two different currents, i_{10} and i_{20}, in the two circuits, it is possible to create an extra torque Γ at $\phi = 0$ (see eq.6.37) to counterbalance any spurious torque acting on the float. The natural stiffness k_ϕ is employed to make the float oscillate around an equilibrium position, before servo controlling it to a fixed angular position.

Applying an extra torque to the float

By setting an external current δi through the flux transformer FT_s, it is possible to couple an additional torque to the float. Because the flux transformer is wound in such a way that it subtracts flux from the first circuit and adds flux to the second one, the extra flux coupled to the system is given by the equation:

$$\delta\Phi = M_t \begin{pmatrix} -\delta i \\ \delta i \end{pmatrix} \tag{6.40}$$

The stored energy becomes the equation:

$$E = \frac{1}{2}\left(\Phi_0 + \delta\Phi\right)^T \Psi^{-1}\left(\Phi_0 + \delta\Phi\right) \tag{6.41}$$

	Value	Error	Units
L	5.733×10^{-7}	10^{-10}	H
α	9.21×10^{-7}	4×10^{-9}	H/rad
β	8×10^{-7}	10^{-7}	H/rad^2

Table 6.4: Inductance values for the couples of coils L_1 and L_2.

	Inductance (H)
M_t	5×10^{-6}
M_s	$1 - 2 \times 10^{-6}$
M_c	4×10^{-6}

Table 6.5: Inductances of the flux transformers.

At $\phi = 0$ the extra applied torque added to Γ of eq.6.37 is given by the equation:

$$\Gamma_{extra} = -2i_0\alpha\frac{M_t}{L + 2(M_c + M_s)}\delta i \tag{6.42}$$

$$= -\left(i_1 + i_2\right)\alpha\frac{M_t}{L + 2(M_c + M_s)}\delta i \tag{6.43}$$

which for $i_1 = i_2$ is equivalent to the expression found in [33]. To the stiffness of the system, which is given by the eq.6.38, we add an extra term which for $L >> M_c + M_s$ is given by the equation:

$$k_{extra} \approx 2\left(\alpha^2 + L\beta\right)\frac{2\Delta i L M_t \delta i - M_t^2 \delta i^2}{L^3} \tag{6.44}$$

Model parameters and expected results

From room temperature measurements based on a copper reproduction of the niobium coils we adopted for the SSTB, I found that the change of the inductance of a coil pair is characterised by the parameters of table 6.4.

The values of all the other inductances of the actuator circuits are shown in table 6.5 and had been chosen in such a way as to have a 1 to 1 transformation ratio in both the flux transformers. The predicted natural stiffness is

$$k_\phi \approx -4.56 \times 10^{-6}\left(\Delta i^2 + i_0^2\right) Nm/rad \tag{6.45}$$

while the expected servo torque is given by the formula:

$$\Gamma_{extra} = 3.66 \times 10^{-7}\left(i_1 + i_2\right)\delta i Nm \tag{6.46}$$

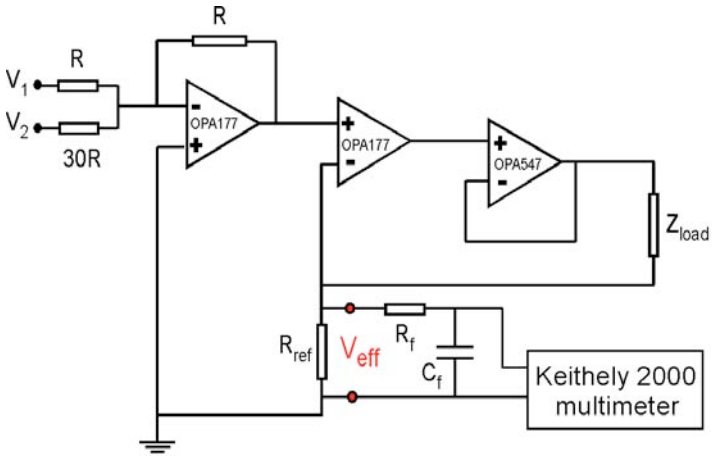

Figure 6.12: Schema of the current source, which is used to actuate the torsion balance

6.4.2 The current source

To apply the external torque given by the eq.6.37, a current δi is generated by a computer controlled current source [33], whose output is monitored by a Keithley 2000 digital multimeter (see fig.6.12). For the configuration of the current source (see fig.6.12) the voltage read by the multimeter is equal to the voltage controlling the current source. Because the resolution of the input voltage of the multimeter is $10\mu V$ within a range of $\pm 10V$ and the voltage output of the digital card has a resolution of $150\mu V$, it was found necessary to use a summing amplifier circuit to improve the resolution of the signal controlling the current source. The output voltage of the servo system is split into two signals, V_1 and V_2, where the first is the requested voltage driven at 16-bit and the second one is 30 times the difference between the desired output and V_1. The two signals are summed through a voltage summing amplifier such that $V_{tot} = V_1 + V_2/30$ (see fig.6.12), which has a quasi 21-bit resolution of $5\mu V$. V_{tot} is given as input to a voltage follower circuit composed by a high precision op-amp and controlling a high power current source. Such current source generates the current δi through the unknown Z_{load} of the actuator circuit (typically a few Ohm). The maximum generated current is set by $R_{ref} = 40\Omega$ to be $250mA$. R_{ref} also sets the conversion between the readout voltage and current, now $25mA/V$. A low pass filter is positioned between V_{eff} and the multimeter to exclude all the high frequencies, which are not of interest.

From the noise measurements shown in fig.6.13, the current noise of the current source follows an $1/f$ behavior at low frequencies. The amplitude spectrum

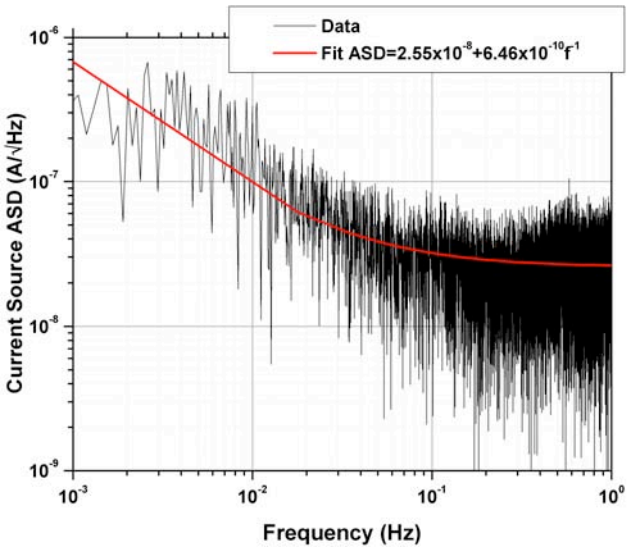

Figure 6.13: The amplitude spectrum density of the output current noise of the current source.

density (ASD) of the current noise, $S_{CS}^{1/2}$, fits the following function with a 1% error on the parameters:

$$S_{CS}^{1/2}(f) = 2.55 \times 10^{-8} A/\sqrt{Hz} + \frac{6.46 \times 10^{-10}}{f} A\sqrt{Hz} \tag{6.47}$$

6.5 The servo system

So far I have described all the single subsystems of the torsion balance whose open loop transfer functions I have individually analysed. To understand the torsion balance as a servo system it is necessary also to study the closed loop transfer functions between the torque input and the readout torque.

It can be shown that, given a system of N subsystems connected in a servo loop as in fig.6.14, the closed loop transfer function, $T_{CL}(i,j)$, from any input point i to any output point j can be written as the following equation (see Appendix D):

$$T_{CL}(i,j) = \frac{\prod_{i<n\leq j} H_n}{1 - \prod_{all} H_n} \tag{6.48}$$

H_n, is the transfer function of each single subsystem and $i < n \leq j$ stands for

$(i < n \leq N)\&(1 \leq n \leq j)$. The previous formula makes it possible to evaluate the transfer function between the torque signal, to which the float is subjected, and the torque servo readout, which we actually measure. Thanks to eq.6.48, it is possible to predict the effect of all the noise sources to the final torque measurement.

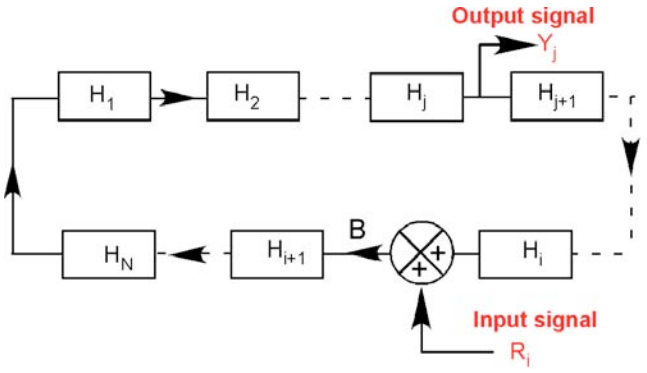

Figure 6.14: Block diagram of a general servo system with N blocks and the input and output: R_i and Y_j.

In fig.6.1 I provided a simplified block diagram of the servo system controlling the MKII SSTB: Γ_{ext} is the torque which is applied to the float by mean of the masses, Γ_{eff} is the torque which we actually measure and V_{ref} is the constant reference voltage which sets the equilibrium position of the torsion balance. For the sake of simplicity I assume V_{ref} to be null ($\phi = 0$). In the Laplace space I can write the transfer functions of each term of fig.6.1 as the following equations:

$$G_{\text{float}} = \frac{1}{I_{zz}s^2 + b_\phi s + k_\phi} \tag{6.49}$$

$$G_{CS} = \frac{dV_{out}}{d\phi} = 1460V/rad \tag{6.50}$$

$$H_{PII^2D} = -\frac{s^3K_D + s^2K_P + sK_I + K_{I^2}}{s^2} \tag{6.51}$$

$$H_{MA} = \frac{d\Gamma}{dV} = 1.8 \times 10^{-8}Nm/V \tag{6.52}$$

G_{float}, G_{CS}, H_{PII^2D} and H_{MA} are respectively the transfer functions of the float, the capacitive angular readout of the measurement configuration, the digital compensator and the magnetic actuator (assuming $i_1 + i_2 = 2A$). For sake of simplicity in eq.6.50 and 6.52 I did not consider any phase shift due to

the capacitive readout or the magnetic actuation. For this analysis I assumed $I_{zz} = 1.82 \times 10^{-4} kg \cdot m^2$, $b_\phi = 2.16 \times 10^{-7} kg \cdot m^2/s$ and $k_\phi = 4.5 \times 10^{-6} Nm/rad$ (for period of $\approx 40s$) (see also chapter 5). For the analytical model, I assumed the parameters, which define the PII^2D compensator, as equal to the ones of eq.6.19.

The open loop transfer function, T_{OL}, is given by the equation:

$$T_{OL} = G_{\text{float}} \cdot G_{CS} \cdot H_{PII^2D} \cdot H_{MA} \tag{6.53}$$

$$= \frac{dV}{d\phi}\frac{d\Gamma}{dV}\frac{s^3K_D + s^2K_P + sK_I + K_{I^2}}{s^2\left(I_{zz}s^2 + b_\phi s + k_\phi\right)} \tag{6.54}$$

According to eq.6.48 and fig.6.1, the transfer function between the input torque and the readout torque is given by the expression:

$$T(\Gamma_{ext}, \Gamma_{eff}) = \frac{T_{OL}}{1 - T_{OL}} \tag{6.55}$$

$$= -\frac{(s^3K_D + s^2K_P + sK_I + K_{I^2})\frac{dV}{d\phi}\frac{d\Gamma}{dV}}{s^2\left(I_{zz}s^2 + b_\phi s + k_\phi\right) + (s^3K_D + s^2K_P + sK_I + K_{I^2})\frac{dV}{d\phi}\frac{d\Gamma}{dV}} \tag{6.56}$$

Because, if $s = i\omega$, for $\omega \to 0$ the previous equation has -1 as limit, the servo effort at very low frequencies has the opposite phase with respect to the applied torque but it has the same amplitude. The expected amplitude and phase of $T(\Gamma_{ext}, \Gamma_{eff})$, for $\omega > 0$, are presented in fig.6.15 and 6.16. The effect of the differential gain on the closed loop transfer function at high frequencies is clear. The analytical model predicts that the phase of the $T(\Gamma_{ext}, \Gamma_{eff})$ is $\pi/2$ for sufficient high frequencies, because the effect of the differential gain dominates the output of the compensator. As will be shown in chapter 7, this result does not agree with the measured $T(\Gamma_{ext}, \Gamma_{eff})$, because the analytical model does not include yet the effects of the low pass filters, which are present in the servo system and which effectively reduce the gain of the differential term at high frequencies.

To study now the stability of readout output of the torsion balance or equivalently its angular stability, it is necessary to look at the transfer function between the voltage reference, V_{ref}, and the voltage angular readout, V_{out}, of the torsion balance. Again thanks to eq.6.48, it can be shown that:

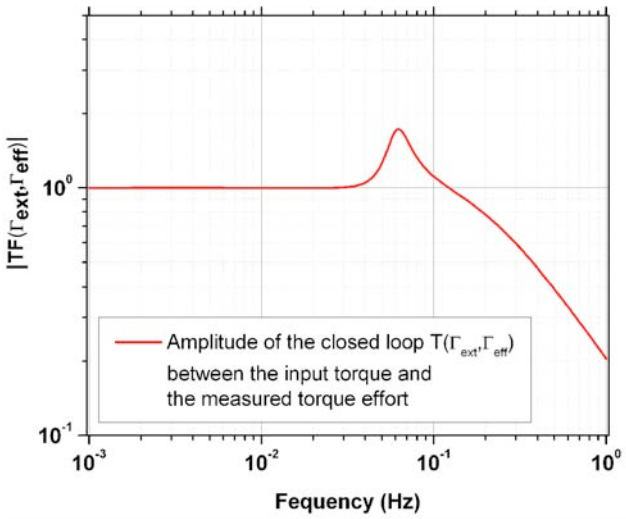

Figure 6.15: Amplitude of the transfer function, $T(\Gamma_{ext}, \Gamma_{eff})$, between the applied torque and the servo effort output.

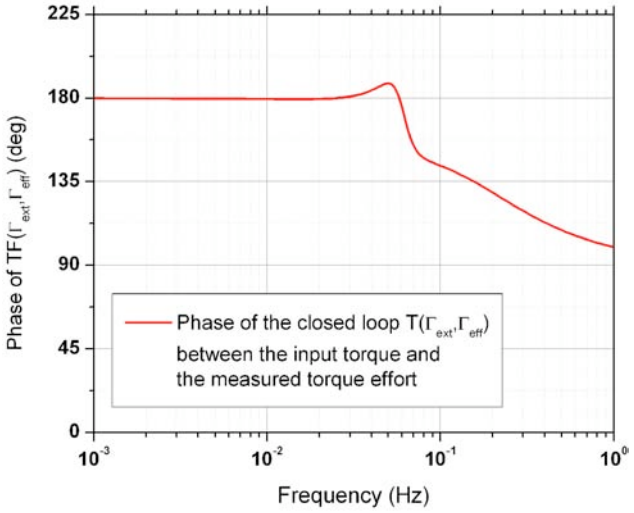

Figure 6.16: Phase of the trasfer function, $T(\Gamma_{ext}, \Gamma_{eff})$, between the applied torque and the servo effort output.

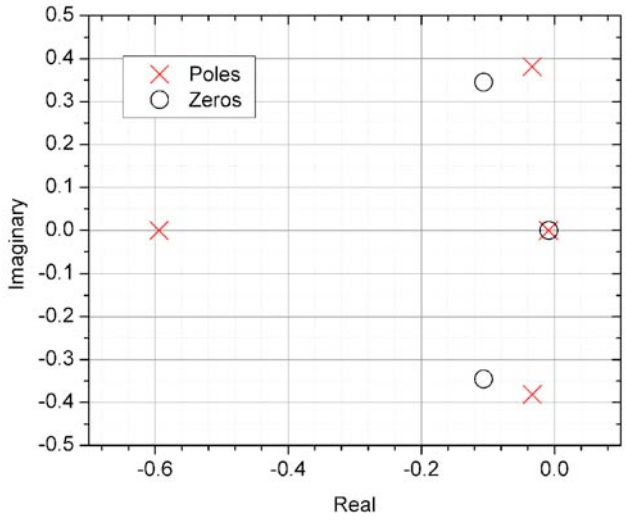

Figure 6.17: Poles and zeros of the transfer function $T(V_{ref}, V_{out})$.

$$T(V_{ref}, V_{out}) = T(\Gamma_{ext}, \Gamma_{eff}) \tag{6.57}$$

To study the stability of the system I look at the poles of the transfer function which, as presented in fig.6.17, are all left half-plane poles. The system is therefore asymptotically stable [81].

In the time domain (see fig.6.18) I plot the step response function of the voltage readout, V_{out}, of the torsion balance, given a $1V$ change in the reference voltage V_{ref}: the step response time has a overshoot of 48% (for the definition see fig.6.18 and [81]); the settling time (time to reach the final value within $\pm 5\%$) is only 11 sec, which is smaller than the assumed natural period of the float ($\approx 40s$).

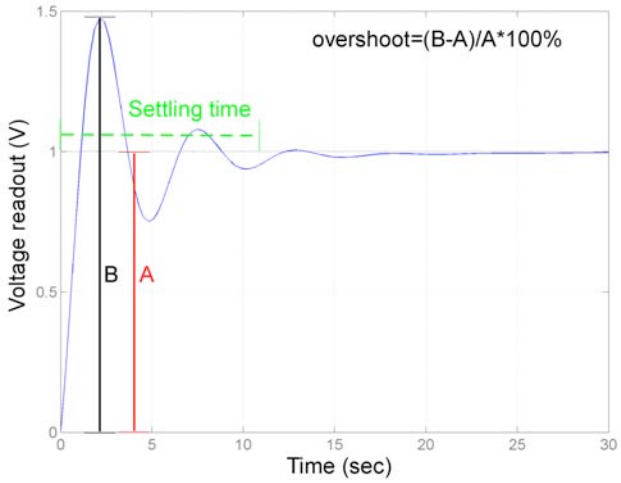

Figure 6.18: Step response function of the angular position of the torsion balance.

6.6 Noise budget

To predict the expected angular and torque effort noise of the torsion balance, I will use this section to analyse how all the noise sources propagate through the servo system and effect the measured torque noise. For the sake of simplicity I group here the transfer functions of the float, G_{float}, and of the capacitor readout, G_{GS}, into the transfer function G and the transfer functions of the compensator, H_{PII^2D}, current source and magnetic actuator, H_{MA}, into H (see fig.6.19).

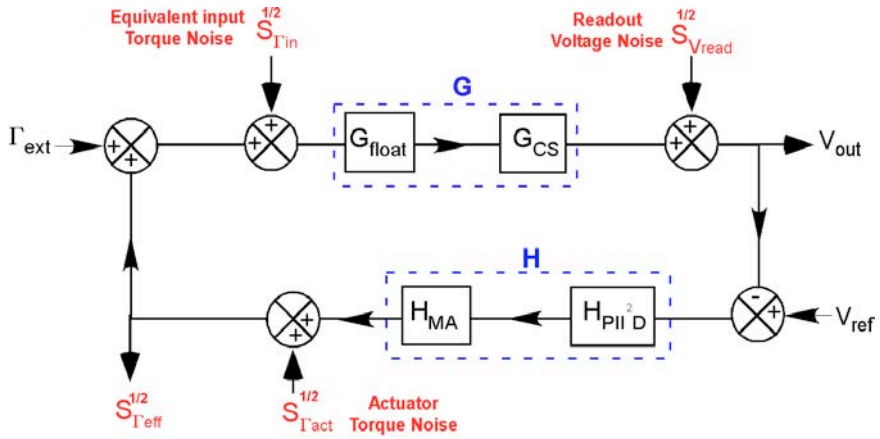

Figure 6.19: Schema of the servo system of the SSTB and all the main noise sources entering the servo loop.

The noise sources, whose effect I want to model, can be divided into three

groups depending on where they enter the servo loop:

1. *Equivalent input torque noise*, $S_{\Gamma in}^{1/2}$: all the noise sources, which can be modelled as an equivalent torque noise acting on the torsion balance (for example the seismic and the thermal noise).

2. *Readout output noise*, $S_{Vread}^{1/2}$: the voltage noise, which is at the output of the capacitor readout.

3. *Actuator torque noise,* $S_{\Gamma act}^{1/2}$: the equivalent torque noise of the actuator, which is given by the current noise of the current source. In the servo loop it is just before the torque readout.

$S_{\Gamma in}^{1/2}$, $S_{Vread}^{1/2}$, and $S_{\Gamma act}^{1/2}$ are defined here as the amplitude spectrum densities [61] of the considered noise sources and in general are functions of ω. To model the effect of these noise sources on the measured torque noise, I need to evaluate the transfer functions between each noise source and the desired output. If there is a linear system with transfer function $T(i\omega)$ between an input $\tilde{X}(\omega)$ and an output $\tilde{Y}(\omega)$, a stochastic process with amplitude spectrum density at the input $S_{xx}^{1/2}(i\omega)$ produces an output noise, which is characterised by an amplitude spectrum density $S_{yy}^{1/2}(i\omega)$ given by the following equation [61]:

$$S_{yy}^{1/2}(i\omega) = |T(i\omega)| S_{xx}^{1/2}(i\omega) \tag{6.58}$$

Supposing here that all the noise sources are independent, I will sum in quadrature the contributions of each noise source to obtain the total noise.

6.6.1 Servo effort torque noise

Firstly, I evaluate the analytical models of all the transfer functions between the three different groups of noise sources and the servo effort readout, plotting them under the assumptions of the previous section.

Transfer function of the equivalent input torque noise

From fig.6.19 and from eq.6.48, I can write the transfer function between the equivalent input torque noise, $S_{\Gamma in}^{1/2}$, and the measured torque effort noise, $S_{\Gamma eff}^{1/2}$:

$$|T(S_{\Gamma in}^{1/2}, S_{\Gamma eff}^{1/2})| = |\frac{GH}{1-GH}| \tag{6.59}$$

which is equivalent to $|T(\Gamma_{ext}, \Gamma_{eff})|$ given by 6.56 and plotted in fig.6.15. As found in the previous section, for $s = i\omega$ and in the limit of low frequencies I find that

$$\lim_{\omega \to 0} |T(S_{\Gamma in}^{1/2}, S_{\Gamma eff}^{1/2})| = 1 \tag{6.60}$$

Transfer function of the readout noise

The transfer function between the readout noise, S_{Vread}, and the measured torque effort noise is given by the equation:

$$|T(S_{Vread}^{1/2}, S_{\Gamma eff}^{1/2})| = |\frac{H}{1 - GH}| \tag{6.61}$$

which is plotted in fig.6.20. In the limit of small frequencies the previous equation becomes:

$$\lim_{\omega \to 0} |T(S_{Vread}^{1/2}, S_{\Gamma eff}^{1/2})| = \lim_{\omega \to 0} |\frac{1}{G}| = k_\phi \frac{d\phi}{dV} \tag{6.62}$$

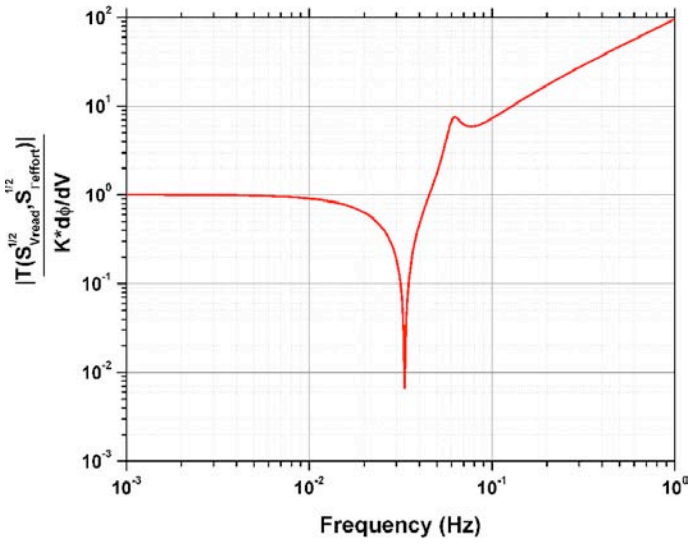

Figure 6.20: Transfer function, $|T(S_{Vread}^{1/2}, S_{\Gamma eff}^{1/2})|$, between the readout noise and the torque effort normalized to unit at low frequencies.

Transfer function of the actuator torque noise

The transfer function between the actuator torque noise, $S_{\Gamma act}^{1/2}$, and the torque effort noise is given by the equation:

$$|T(S^{1/2}_{\Gamma act}, S^{1/2}_{\Gamma eff})| = |\frac{1}{1-GH}| = \tag{6.63}$$

$$= \left| \frac{s^2\left(I_{eff}s^2 + b_\phi s + k_\phi\right)}{s^2\left(I_{eff}s^2 + b_\phi s + k_\phi\right) + \left(s^3K_D + s^2K_P + sK_I + K_{I^2}\right)\frac{dV}{d\phi}\frac{d\Gamma}{dV}} \right| \tag{6.64}$$

which is presented in fig.6.21. In the limit of small frequencies, the previous equation becomes the expression:

$$\lim_{\omega\to 0}|T(S^{1/2}_{\Gamma act}, S^{1/2}_{\Gamma eff})| = \left| \frac{\omega^2 k_\phi}{K_{I^2}\frac{dV}{d\phi}\frac{d\Gamma}{dV}} \right| \tag{6.65}$$

The previous equation is null for $\omega = 0$, which means that at extremely low frequencies the noise of the current source has no effect on the measured torque. The torque noise generated by the current source is cancelled at low frequencies by the output of the PII^2D compensator, because of the large gain of the integrator and double integrator at these frequencies. This theoretical result was also independently verified through MATLAB Simulink numerical simulations, by measuring the torque effort and using a white noise source in place of the current source. As shown in fig.6.22, the simulated torque effort has an amplitude spectrum density which at $10mHz$ is reduced by a few orders of magnitude with respect to the input torque noise due to the current source.

This reduction of the contribution of actuator torque noise to the torque effort at low frequencies was indirectly proved with experimental measurements as I will show in chapter 7.

Total noise and predictions

Because I assume that all the different noise sources are independent and not correlated, the total noise budget for the torque effort is given by the equation:

$$S^{1/2}_{\Gamma eff} = |\frac{GH}{1-GH}|\sqrt{S_{\Gamma inTh} + S_{\Gamma inSm} + \left(|\frac{1}{G}|\right)^2 S_{Vread} + \left(|\frac{1}{GH}|\right)^2 S_{\Gamma act}} \tag{6.66}$$

$S^{1/2}_{\Gamma inTh}$ and $S^{1/2}_{\Gamma inSm}$ are the amplitude spectrum densities of the thermal and

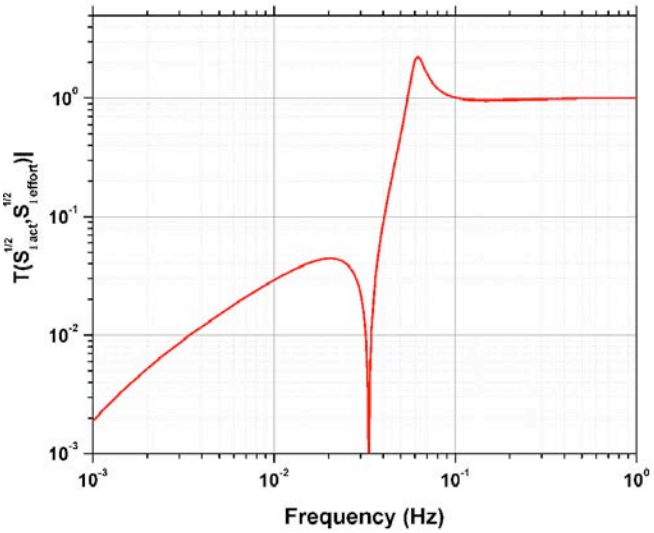

Figure 6.21: Transfer function, $|T(S^{1/2}_{\Gamma act}, S^{1/2}_{\Gamma eff})|$, between the actuator noise and the torque effort.

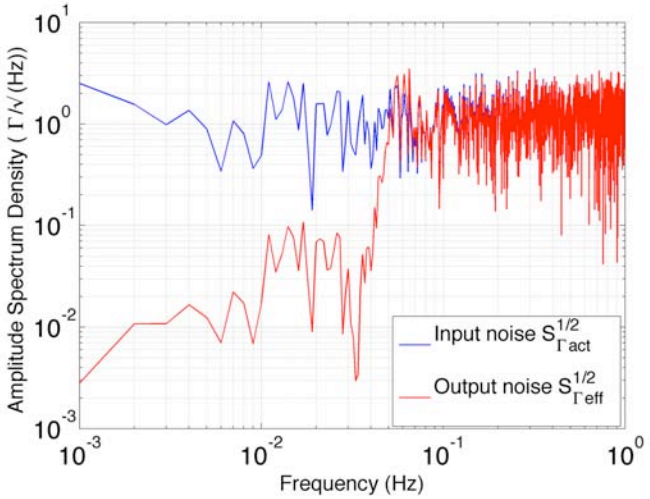

Figure 6.22: Actuator and servo effort noise based on a MATLAB simulink simulation.

Source	**ASD at** $10mHz$ $(Nm/\sqrt{Hz})$
Readout	$5\times\ 10^{-12}$
Seismic (tilt)	2.5×10^{-13}
Thermal	3.9×10^{-15}
Actuator	1×10^{-15}

Table 6.6: Amplitude spectrum densities at $10mHz$ of the different torque noise sources.

seismic noise given respectively by eq.5.75 and 5.73. $S_{\Gamma in}^{1/2}$ is the sum in quadrature of these two components. At very low frequencies the previous equation becomes the equation:

$$\lim_{\omega\to 0} S_{\Gamma eff}^{1/2} = \sqrt{S_{\Gamma inTh} + S_{\Gamma inSm} + S_{Vread}\left(k_\phi \frac{d\phi}{dV}\right)^2} \tag{6.67}$$

It is clear that by reducing the natural stiffness of the instrument it is possible to lower the contribution of the readout noise to the servo effort noise. The amplitude spectrum densities of each noise source at $10mHz$ is summarised in table 6.6 and plotted for different frequencies in fig.6.23. In practice we will not see the increase in the torque effort noise at high frequencies due to the readout noise as shown in fig.6.23, because we included in the servo loop and PII^2D compensator a few low pass filters, which effectively reduce the noise at these frequencies. The effect of the low pass filters were not included in the analytical model of the servo system of the SSTB.

By decreasing the k_ϕ, from eq.6.67, it is clear that it is possible to decrease the contribution of the readout noise to the servo effort noise. For example, with a period of $T \approx 150sec$, the contribution from the readout noise equals the contribution from the seismic noise. A higher level of torque effort noise due to the seismic noise might be also possible if the elastic pendulum stiffness k_θ or $k_\theta\beta$ are greater than expected (see eq.5.73).

6.7 Conclusion

This chapter has been dedicated to the analysis of the servo loop of the torsion balance and of all its subsystems. The scope of this analysis has been to define the transfer function between the applied and the measured torque and to indicate the noise sources which contribute to the output torque noise. I have discussed

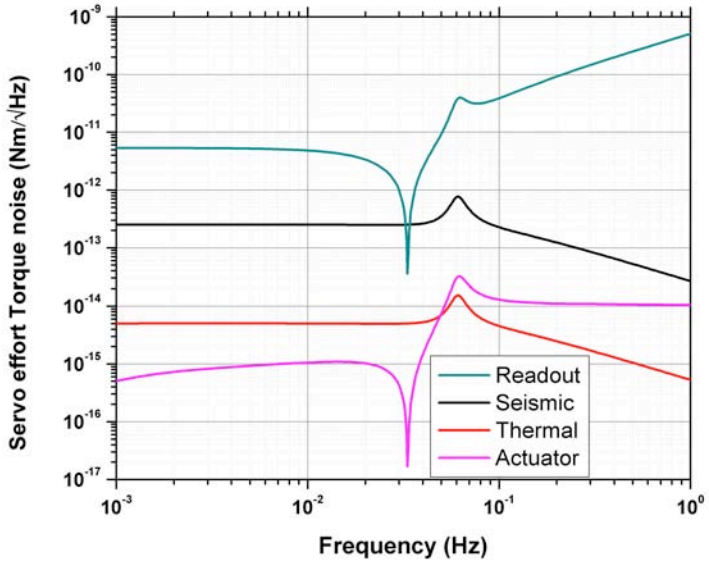

Figure 6.23: Predicted torque effort noise spectrum for the different noise sources.

the capacitive sensor, which we adopted during the preliminary test of the ISL of gravity to monitor the angular position of the float. This sensor was developed in two configurations: the first configuration was used during the calibrations of the SSTB; the second one was used during the torque measurements. The latter configuration was characterised by a transfer function of $(dV_{out}/d\phi)_{meas} \approx 1460V/rad$ and was limited by pick up noise in the vacuum can. By a using numerical simulation I have analysed the open loop transfer function of the PII^2D digital compensator. We have modelled the magnetic actuator and its superconducting circuit predicting the natural stiffness, which we can give to the torsion balance. We have also modelled the torque which is applied to the float versus the current, δi, which is generated by an external current source. I have estimated the closed loop transfer function of the servo system between the applied and the measured torque, which, for the choice of the servo parameters adopted during the ISL experiments, has unity gain and phase shift of 180° at low frequency. For the same choice of the servo parameters, the angular position of the float has been proved asymptotically stable. The step response associated with the change of $1V$ of the reference voltage, V_{ref} (used to set the angular position of the float), has settling time of just $11s$, which is much shorter than the assumed natural period of the torsion balance ($\approx 40s$). I have analysed the contribution of each noise source to the measured torque noise. With a typical natural period of the torsion balance

of $40s$, the largest contribution to the torque noise is expected to be given by the readout noise. At low frequencies, this noise limit is $5 \times 10^{-12} Nm/\sqrt{Hz}$. However, this torque noise is strongly dependent on the chosen natural stiffness. Just an increase in the natural period of merely a few times is enough to decrease the readout torque noise below the expected torque noise given by the seismic noise, $2.5 \times 10^{-13} Nm/\sqrt{Hz}$. The contribution of the seismic noise could also be much larger, if the tilt coupling of the float was to be larger than expected, as is described in chapter 5. In the next chapter I will discuss the SSTB performances, we actually measured during the low temperature tests of the ISL of gravity at micrometre distances.

Chapter 7

Experimental performance of the MKII SSTB

7.1 Introduction

In this chapter I will present the low temperature performances of the MKII SSTB, we obtained during the preliminary tests of the ISL of gravity. I will present the experimental procedure, we adopted to cool down the torsion balance to $4.2K$, setup its levitation and control it. I will define the method, we employed to calibrate the torque measurements. I will discuss the results about the calibration of the magnetic actuator system and compare them with the theoretical expectations. I will analyse the experimental performances of the damping systems, which we built to reduce the spurious oscillations of the torsion balance by dissipation of eddy currents. We will characterise the closed loop transfer function of the servo system between the applied and measured torque and compare it with the theoretical estimate. I will also give an indirect experimental proof of the reduction of the actuator torque noise at low frequencies, which is due to the servo feedback as predicted in chapter 6. I will present the amplitude spectrum density of the torque, we measured with the MKII SSTB during the ISL tests of gravity. I will discuss some preliminary measurements of the coupling factor between the ground tilt and the torque, which is applied to the float. This coupling factor might explain the measured torque noise of the SSTB. To conclude I will discuss the possible modifications of MKII SSTB, which are necessary to improve its performance.

7.2 Set up procedure

In this section I will briefly describe the procedure, which was required to set the torsion balance ready to take the torque measurements. Firstly we reached the cryogenic temperatures, which are necessary to make the niobium and the lead superconducting; secondly we stored the currents in the levitation, damper and actuator circuits to levitate the float and make it oscillate around an equilibrium position.

7.2.1 The vacuum and cooling process

The cooling of the experimental vacuum chamber to $4.2K$ consisted of the following steps (see fig.7.1):

1. After having hermetically closed the experimental vacuum chamber and the cryostat, we evacuated the atmospheric gas inside the experimental room and we introduced $1mBar$ of He gas.

2. We evacuated the cryostat and filled it up with $\approx$ 40 liters of liquid nitrogen, which, during approximately 48 hours, cooled down the vacuum chamber and the cryogenic insert to $77.2K$. We monitored the temperature by measuring the Allen Bradley resistances as described in chapter 4.

3. We expelled all the liquifed nitrogen left in the cryostat, firstly by blowing it out with pressurised nitrogen gas and then by boiling off, what was left, thanks of resistive heaters at the bottom of the cryostat (see chapter 4).

4. We slowly introduced the cold He gas and the liquid He until a level detector indicated that the liquid had almost reached the first baffle of the cryostat insert.

5. We waited for a period of approximately thirty minutes after which the vacuum chamber was uniformly at $4.2K$ and the He gas pressure was measured to be around $2 \times 10^{-2} mBar$ at the vacuum gauge.

Because the torque sensitivity of the torsion balance was not limited by the thermal noise associated with the gas damping (see chapter 6), it was not necessary to further reduce the pressure inside the vacuum chamber. Usually a He fill was enough to keep the experiment cold for a period between 4 to 5 days. After

this period the temperature inside the vacuum chamber started to increase above $4.2K$ and it was necessary to repeat the last two points of the cooling process. The refilling and cooling took up to a few hours to be completed, during which any experiment had to be stopped.

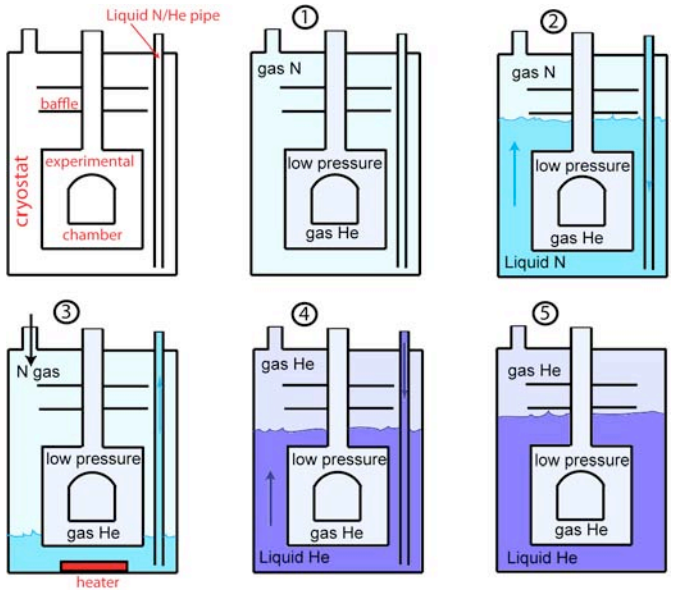

Figure 7.1: Simplified shema illustrating the cooldown of the SSTB.

7.2.2 Establishing the levitation and the servo control

After the cooling down to $4.2K$, we stored $4.51A$ in the primary of the transformer of the levitation circuit and we levitated the float over the bearing pillar (see chapter 4). Because the float turned in one preferred direction until its capacitive plate touched one of the two plates on its sides, we had to store at least a total current of $1.5A$ in the actuator circuits (see section 6.4) to make the float freely oscillate with a period of $\approx 40s$. We stored $4A$ in the damper circuit to damp down the $1Hz$ pendulum oscillations (see chapter 4) and we turned on the digital servo compensator to control the float to the desired position (see section 6.3).

7.3 The calibration protocol

To calibrate the torsion balance, we had to estimate the following constants:

1. $dV_{out}/d\phi$, which is the conversion factor between the angular displacement, ϕ, of the torsion balance and the voltage output, V_{out}, of the capacitive bridge.

2. $d\Gamma_{eff}/dV_{eff}$, which is the conversion factor between the voltage readout, V_{eff}, of the current source controlling the magnetic actuator (see section 6.4) and the torque applied to the float, Γ_{eff}.

As I will see, these two calibration factors are related to the calibration of the displacement of one single step of the Attocubes, which we used to modify the position of the test masses in the x and y directions (see fig.7.2).

7.3.1 Calibration of the Attocubes

The first step of the calibration protocol was the calibration of the one step displacement of the two Attocubes at $4.2K$. As introduced in chapter 4, we monitored the x and y position of the support of the flat mass with respect the float by measuring two capacitances (see fig.7.2 and chapter 4):

C_x is the capacitance between the support of the flat mass and a dedicated capacitive plate on its side. It was used to monitor the movement of the flat mass in the x direction.

C_y is the capacitance between the support of the flat mass and the float. It was used to monitor the movement of the flat mass in the y direction

The calibrations of the Attocube displacement for a given number of steps in the x and y directions followed two different procedures. Because the results about the Attocube calibration are slightly different at each cool down of the torsion balance, I report here the calibrations we measured during the two tests of the ISL of gravity (see chapter 8) named "I run" and "II run". For all the calibrations the voltage signal, which was controlling the Attocube, had an amplitude of $20V$.

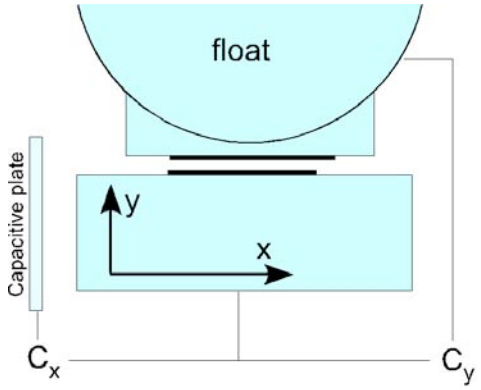

Figure 7.2: Schema of the capacitances monitoring the x and y displacements of the flat mass.

Motion in the x direction

The calibration of the step motion in the x direction, $(dx/dn)_+$, was done by measuring the total number of steps, n_{tot}, which were necessary at $4.2K$ to fully displace the Attocube between its two extreme positions. The distance between the two positions, $L_{\max}$, was measured with a caliper at room temperature and found to be $7 \pm 0.02mm$. By monitoring the capacitance C_x versus the number of steps, n, the two extreme positions was identified where the gradient dC_x/dn became null. The calibration of the step motion in the opposite direction, $(dx/dn)_-$, was done by comparing the measurements of C_x versus n for both directions (see fig.7.3). We scaled $(dx/dn)_-$ in such a way that the two measurements overlapped. The results for $(dx/dn)_+$ and $(dx/dn)_-$ for both experimental runs are reported in table 7.1. The value of $(dx/dn)_-$ was found to be 2% smaller than the value of $(dx/dn)_+$.

Motion in the y direction

Because it was not possible to displace the Attocube in the y direction for its full motion, we needed to calibrate its step motion, dy/dn, using a different procedure with respect to dx/dn. We firstly calibrated $(dy/dn)_-$ at room temperature by measuring with a caliper the displacement of the Attocube for a chosen number of steps. We found $(dy/dn)_- = 0.556 \pm 0.02\mu m/step$. I fitted the measured value of C_y versus the number of steps, n, with the expected capacitance of a cylinder facing an infinite plate. This capacitance is given by the following equation [72] :

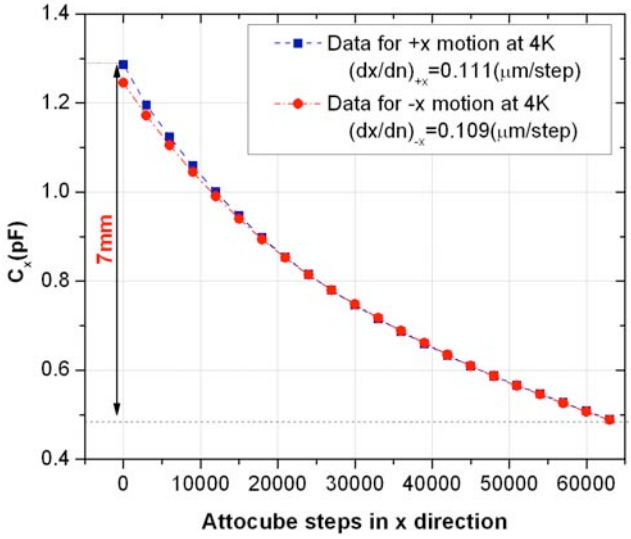

Figure 7.3: Calibration of the Attocube step motion in the positive and negative x directions.

$$C_y(h) = 2\pi\epsilon_0 \frac{L\alpha}{\text{arccosh}(h/R)} \tag{7.1}$$

with L the length of the cylinder ($L = 4cm$) and R its radius ($R = 46mm$). α is a scaling factor, which models the fact that the curved support is not a full cylinder. h is the distance between the plate and the cylinder axis, and it is given by the sum:

$$h = n\left(\frac{dy}{dn}\right)_{-} + h_0 + R \tag{7.2}$$

where h_0 is an unknown distance offset. Assuming the measured value for $(dy/dn)_-$ at room temperature and by least square fitting the function of eq.7.1 to the room temperature data (see fig.7.4) I found the value for the correction factor $\alpha = 0.572 \pm 0.006$ for our capacitances. I used this value to fit the measurements of C_y versus n taken at $4.2K$ and obtained the associated $(dy/dn)_-$ (see table 7.1). By directly comparing the capacitance measurements for the Attocube displacement in the two y directions I found that the two calibration constants $(dy/dn)_+$ and $(dy/dn)_-$ still differed of only a 2% (see table 7.1).

	I **run** (μm)	II **run** (μm)
$(dy/dn)_+$	0.156 ± 0.006	0.159 ± 0.006
$(dy/dn)_-$	0.159 ± 0.006	0.156 ± 0.006
$(dx/dn)_+$	0.111 ± 0.002	0.108 ± 0.002
$(dx/dn)_-$	0.109 ± 0.002	0.106 ± 0.002

Table 7.1: Calibration constants for the possible movements of the two Attocubes for the two low temperature runs of this work. The control voltage of the Attocube was set to $20V$.

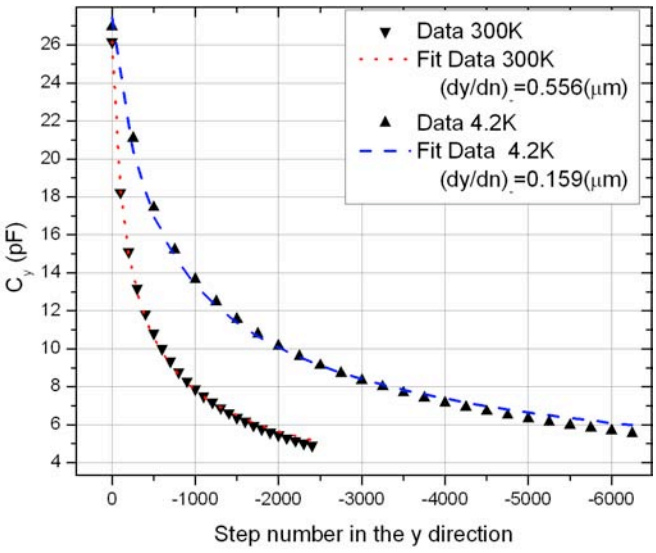

Figure 7.4: C_y versus the attocube motion in the y direction at 300 and 4.2K and the fits performed on the two data sets.

7.3.2 Capacitive bridge calibration

The second part of the calibration protocol was to determine the factor, $dV_{out}/d\phi$, which transforms the angular motion of the torsion balance, ϕ, to the voltage output of the capacitive bridges, V_{out}. For this calibration we measured the change of the angular motion of the torsion balance versus the y displacement of the test mass. I compared the voltage results with the expected angular value and obtain $dV_{out}/d\phi$.

Because of the presence of the flat mass in front of the cylindrical support, the motion of the float was constrained between two angular values. These positions corresponded to two voltage outputs of the capacitive sensor I named $V_{\min}$ and $V_{\max}$. As shown in fig.7.5 the difference between these two values linearly decreases as the flat mass approaches the cylindrical one. I linearly fitted $V_{\min}$ and $V_{\max}$ versus the step number n of the Attocube and obtained the gradients $dV_{\min}/dn$ and $dV_{\max}/dn$.

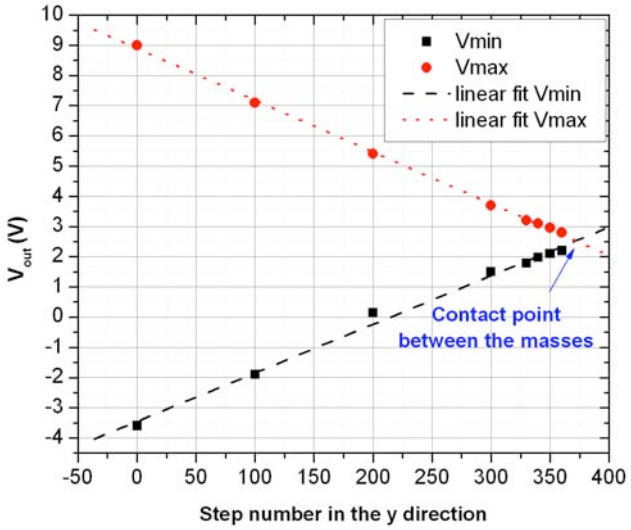

Figure 7.5: Example plot of the minimum and maximum voltage outputs of the capacitive bridge versus the displacement of the support.

From a theoretical approach I expect that, for example, the change, $\Delta\phi_{\min}$, of the minimum angle reached by the torsion balance versus the change, Δy, in the y position of the support is governed by the following equation:

$$\frac{\Delta\phi_{\min}}{\Delta y} = \frac{\phi_1 - \phi_2}{d_1 - d_2} = \frac{2}{D} \tag{7.3}$$

$V_{out} = A + B \cdot n$	A (V)	B $(V/step)$
$V_{\min}$	8.89 ± 0.06	$0.0161 \pm 5 \times 10^{-4}$
$V_{\max}$	-3.4 ± 0.15	$-0.0171 \pm 2 \times 10^{-4}$

Table 7.2: Results of the linear fits of fig.7.5

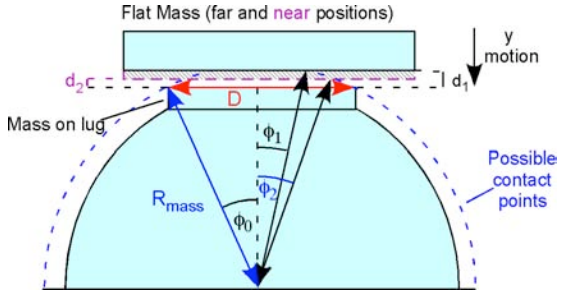

Figure 7.6: Schema of the flat test mass approaching the lug. The possible minimum angles of the torsion balance, ϕ_1 and ϕ_2, depend on the distances, d_1 and d_2, between the test masses according to eq.7.3.

where D is the length in the x direction of the shortest test mass ($D = 24.98mm$ for the mass A, see chapter 2) and d_1 and d_2 are the distances between the masses, which corresponded to the minimum possible angles, ϕ_1 and ϕ_2 (see fig 7.6 and 7.7). The same result is valid also for $\Delta\phi_{\max}/\Delta y$.

The calibration factor $dV_{out}/d\phi$ is given by the equation:

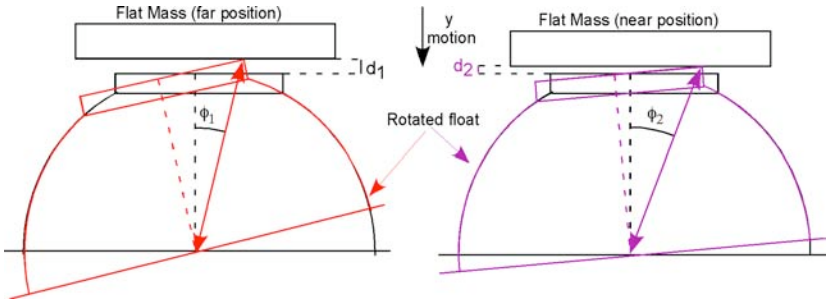

Figure 7.7: Schema of the flat test mass approaching the lug for two different distances between the flat support and the float and showing the change in the minimum angles, ϕ_1 and ϕ_2.

$$\frac{dV_{out}}{d\phi} = \frac{dV_{\min}}{dn}\left(\frac{dy}{dn}\frac{\Delta\phi}{\Delta y}\right)^{-1} \tag{7.4}$$

$$= \frac{dV_{\min}}{dn}\frac{D}{2}\left(\frac{dy}{dn}\right)^{-1} \tag{7.5}$$

I followed the same procedure for $V_{\max}$ and found the respective calibration factor $dV_{out}/d\phi$. This value was averaged with the value obtained from $dV_{\min}/dn$. For example from the linear fits to the $V_{\min}$ and $V_{\max}$ data of fig.7.5 and presented in table 7.2, assuming the $(dy/dn)_+$ of table 7.1 (data from the "II run"), I found $dV_{out}/d\phi$=1304 $\pm$ 40V/rad. We often found very convenient to move the flat mass on one side and estimate $dV_{out}/d\phi$ only from the measurements of $V_{\max}$ or $V_{\min}$ versus the number of Attocube steps. In this way the calibration of the capacitive sensor was performed, just before the procedure of torque calibration of the SSTB, which I will explain in the next section. Because of the non-perfect cylindrical and flat geometries of the test masses, the previous procedure was repeated many times during the experiment and all the estimates of $dV_{out}/d\phi$ were then averaged together.

For the capacitive bridge of the measurement mode with a PSD sensitivity of $100mV$, with a drive signal of amplitude $V_0 = 0.5\sqrt{2}V$ and frequency of $70kHz$ I obtained on average:

$$\left|\frac{dV_{out}}{d\phi}\right|_{meas.} = 1500 \pm 157V/rad \tag{7.6}$$

which is in agreement with the expected value of $1460V/rad$ (see chapter 6, eq.6.9). For the capacitive bridge, we adopted during the torque calibration of the SSTB with a PSD sensitivity of $30mV$, with a drive signal of amplitude $V_0 = \sqrt{2}V$ and frequency of $70kHz$, by following a similar analysis, on average I found:

$$\left|\frac{dV_{out}}{d\phi}\right|_{calib.} = 211 \pm 38V/rad \tag{7.7}$$

while from room temperature measurements I expected $208V/rad$ (see chapter 6, eq.6.10).

Fit to $C_y = A + B \cdot V_{ref} + C \cdot V_{ref}^2$			
A	$18.71 \pm 0.03pF$	C	$0.76 \pm 0.05pF/V^2$
B	$1.51 \pm 0.03pF/V$		

Table 7.3: Results of the polynomial fit of fig.7.8

7.3.3 Actuator calibration

The third step of the calibration protocol was the calibration of the torque actuator. We needed to estimate the calibration of the conversion factor $d\Gamma/dV_{eff}$ between the voltage signal, which was read from the current source, V_{eff}, and the torque, which was applied to the torsion balance, Γ_{eff}. For this scope we applied a voltage difference, V_{daq}, between the torsion balance and the support of the test masses .We measured the voltage effort V_{eff}, which was necessary to keep the float at a constant angular position versus the applied voltage V_{daq}. The calibration factor $d\Gamma_{eff}/dV_{eff}$ was obtained by comparing the results with the theoretical prediction, which is given by the following equation:

$$\Gamma = \frac{1}{2}\frac{dC_y}{d\phi}(V_{daq} - V_0)^2 \tag{7.8}$$

V_0 is any residual voltage difference, which was present between the float and the flat test mass even when we did not apply any voltage to it.

Firstly we measured the capacitive C_y versus the set voltage, V_{ref}. We fitted the results with a second order polynomial and obtained dC_y/dV_{ref} around a chosen set point (see fig.7.8 and table 7.3). We obtained $dC_y/d\phi$ thanks of the following equation:

$$\frac{dC_y}{d\phi} = \frac{dC_y}{dV_{ref}}\left|\frac{dV_{out}}{d\phi}\right|_{calib.} \tag{7.9}$$

For these measurements it was necessary to use the capacitive bridge of the calibration mode, which allowed the use of the AH capacitive bridge (to measure the investigated capacitances) while we recorded the angular position of the float. For a correct calibration it was important to measure dC_y/dV_{ref} around a set point which was within the limit of linear output of the capacitive sensor. Otherwise the calibration factor might be found a few times smaller than the true value. The actuator calibration was performed when the flat mass support was completely moved to one side. In this way we maximised dC_y/dV_{ref} and minimised the error on the torque calibration.

Secondly we moved the float to a predetermined angular position and meas-

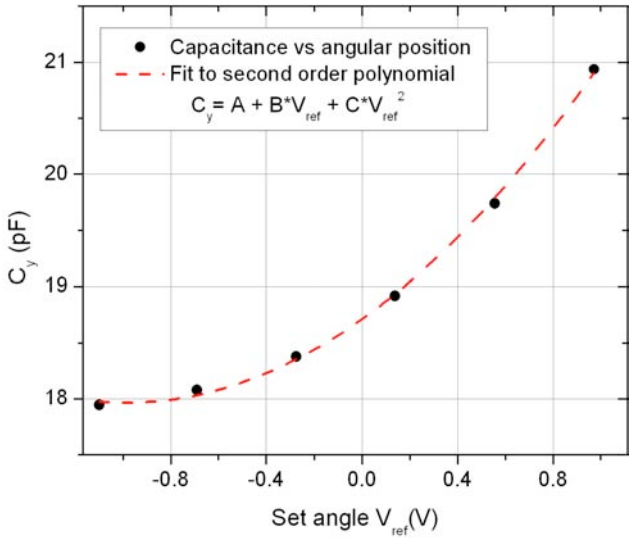

Figure 7.8: Plot of the capacitance C_y between the float and the test mass support versus the set point.

Fit to $V_{eff} = \beta(V_{daq} - V_0)^2 + V_1$			
β	$0.00372 \pm 10^{-5} V^{-1}$	V_0	$0.15 \pm 0.01 V$
V_1	$0.2731 \pm 8 \times 10^{-4} V$		

Table 7.4: Results of the polynomial fit of fig.7.9

ured the servo voltage effort, V_{eff}, which was necessary to keep the torsion balance at that position for any applied voltage, V_{daq}. We fitted the results with the function:

$$V_{eff} = \beta(V_{daq} - V_0)^2 + V_1 \tag{7.10}$$

V_1 is the voltage effort, which was necessary to balance the spurious torques acting on the float, when the voltage difference between the masses, $V_{daq} - V_0$, was null.

From the eq.7.8, 7.9 and 7.10 we found that:

$$\frac{d\Gamma}{dV_{eff}} = \frac{1}{2}\frac{dC_y}{dV_{ref}}\left|\frac{dV_{out}}{d\phi}\right|_{calib}\frac{1}{\beta} \tag{7.11}$$

For example for the capacitive data of fig.7.8 and table 7.3 and for the voltage effort data of fig.7.9 and table 7.4 (taken for $V_{ref} = 0V$) I found:

$$\frac{d\Gamma_{eff}}{dV_{eff}} = 4.28 \times 10^{-8} \pm 7.7 \times 10^{-9} Nm/V \tag{7.12}$$

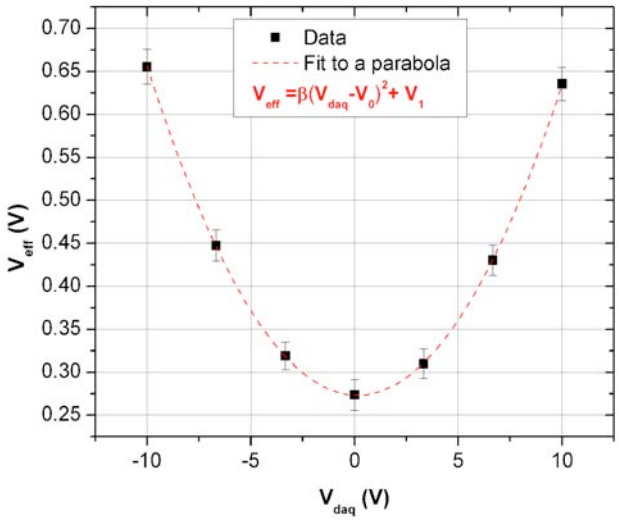

Figure 7.9: Plot of the voltage, V_{eff}, monitoring the output the current source required to keep the torsion balance at a constant position versus the voltage difference applied between the float and test mass support.

where we stored 1.6 and $0.54A$ in the actuator circuits.

7.4 Characterisation of the SSTB

At this point we had the torsion balance levitated and ready to take torque measurements. This section is dedicated to the further analysis of the SSTB and to understand the limits and the validity of the previous analytical description of its expected performances. I will firstly proceed to analyse how the torque calibration constant changed versus the currents, which were stored in the actuator circuits. I will show that even if we correctly predicted the change of the calibration constant versus the stored currents, the calibration constant is not null when there is not any current stored. This result indicated a possible coupling of the actuator coils with the levitation current. The natural stiffness, which is given by the actuator circuits, will be shown to be in agreement with the theoretical predictions. I will characterise the performance of the eddy current damper, showing that $4A$ in the damper circuit was sufficient to quickly damp down any $1Hz$ pendulum oscillation of the torsion balance. The $5Hz$ horizontal oscillation were damped down even without any current stored in the damper, presumably because of the levitation field. We will characterise the transfer function of the servo system between the applied and the measured torque. We will show that

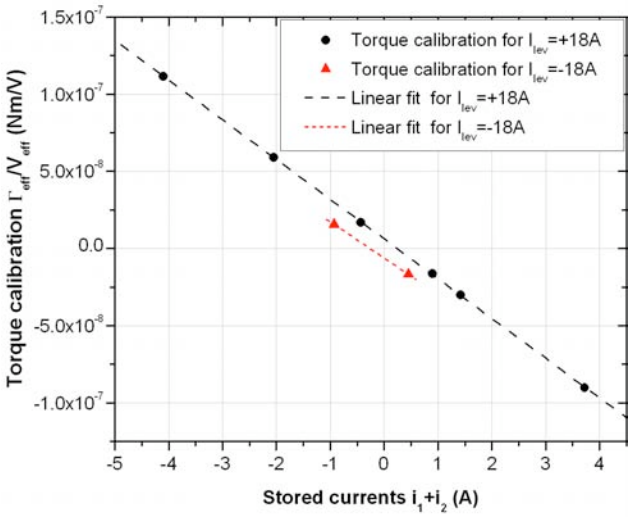

Figure 7.10: Measured calibration constants $d\Gamma_{eff}/dV_{eff}$ versus the sum of the current stored in the detector coil and the corresponding linear fit (see table 7.5).

at low frequencies the torque servo effort had the same amplitude but 180° phase shift with respect to the torque acting on the torsion balance. I will show how the torque noise level we reached during the ISL tests was around $2\times10^{-10}Nm/\sqrt{Hz}$. This noise level corresponded to an angular noise of $\approx 4.5\times10^{-5}rad/\sqrt{Hz}$. This torque noise level was more than one order of magnitude higher than the torque noise level we reached during previous Casimir experiments [33]. I will show that the most probable origin of this noise level was a large coupling of the torsion balance with the ground tilt noise. Preliminary measurements of the coupling constant between tilt angle and servo torque seemed to confirm this hypothesis.

7.4.1 Torque calibration versus stored currents

To characterise the magnetic actuator of the MKII SSTB, we repeated the procedure of the actuator calibration (see 7.3.3) for different values of the currents, i_1 and i_2, which were stored in the actuator circuits and for opposite polarities of the current, I_{lev}, which was stored in the levitation circuit. In fig.7.10 I plot the values of the calibration factors $d\Gamma_{eff}/dV_{eff}$ versus the sum of the stored currents. Their respective linear fits are presented in table 7.5.

The calibration factor $d\Gamma_{eff}/dV_{eff}$ was governed by a couple of linear equations, which had compatible gradients but different offsets. These offsets depended on the polarities of the levitation current (see table 7.5). From eq.6.46

Fit to $d\Gamma_{eff}/dV_{eff} = A + B\,(i_1 + i_2)$		
I_{lev}	$A\ (Nm/V)$	$B\ (Nm/V/A)$
$+18A$	$6.1 \times 10^{-9} \pm 10^{-9}$	$-2.58 \times 10^{-8} \pm 4.6 \times 10^{-9}$
$-18A$	$-6.2 \times 10^{-9} \pm 10^{-9}$	$-2.34 \times 10^{-8} \pm 4.2 \times 10^{-9}$

Table 7.5: Results of the linear fits of fig. 7.10

and knowing that $V_{eff} = 40\Omega * \delta i$ (see section 6.4), we expected the gradient $|d\Gamma_{eff}/(dV_{eff}d\,(i_1 + i_2))|$ to be $3.38 \times 10^{-8} Nm/V/A$. This estimate was near but not compatible within 2σ with the average of the measured values:

$$\left|\frac{d\Gamma_{eff}}{dV_{eff}d\,(i_1 + i_2)}\right| = 2.46 \times 10^{-8} \pm 3.1 \times 10^{-9} Nm/V/A \tag{7.13}$$

From the experimental data we found a correlation between the polarity of the levitation current and the offset of the linear fits. This result indicates a possible coupling between the levitation current and the actuator circuit. This coupling might be due different possible reasons. The rectangular windows cut into the niobium shell might store some magnetic flux, which couple with the magnetic field generated by the actuator coils and modify the torque calibration. Moreover the actuator coils might be directly coupled with the magnetic field of the levitation bearing.

7.4.2 Measured moment of inertia

We were able to measure the moment of inertia of the float by measuring the change of the torque effort, which was necessary to keep the torsion balance at different angular positions. For these measurements we used the capacitive sensor of the calibration mode. By comparing the resulting torsional stiffness, k_ϕ, with the measured natural period of the float I derived the moment of inertia I_{zz}. For example as shown in fig.7.11 we changed the position of the float by modifying the reference voltage, V_{ref}, while we kept measuring the corresponding servo effort, V_{eff}. From the measured gradient dV_{eff}/dV_{ref} (see table 7.6) and from the associated calibration constants of eq.7.12 and of eq.7.7, the resulting torsional stiffness is given by the equation:

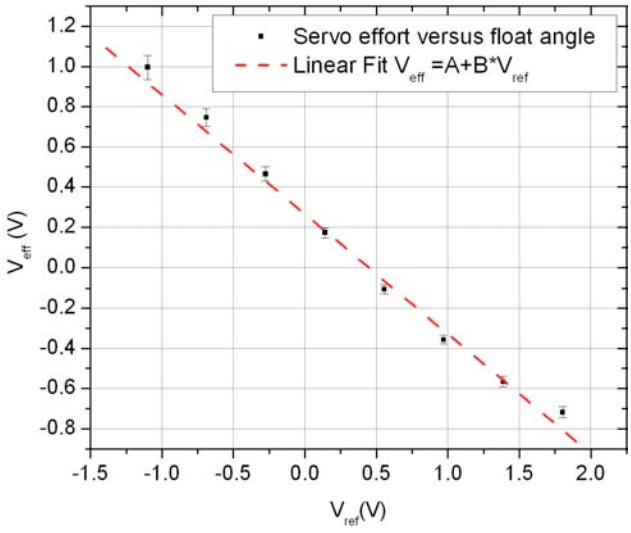

Figure 7.11: Plot of the measured torque effort versus the voltage set point.

$$k_\phi = \frac{d\Gamma_{eff}}{dV_{eff}} \frac{dV_{eff}}{dV_{ref}} \left| \frac{dV_{out}}{d\phi} \right|_{calib} \tag{7.14}$$

$$= 5.37 \times 10^{-6} \pm 9.6 \times 10^{-7} Nm/rad \tag{7.15}$$

Knowing the natural period of the torsion balance was $T = 36.6s$, the moment of inertia is given by the following formula:

$$I_{zz} = \frac{k_\phi}{(2\pi/T)^2} = 1.8 \times 10^{-4} \pm 6 \times 10^{-5} kg \cdot m^2. \tag{7.16}$$

This experimental value is compatible with the expected value, which was given by the CAD drawings, $I_{zz} = 1.82 \times 10^{-4} kgm^2$.

The fact that the measured moment of inertia of the float was compatible with the expected value confirmed the correctness of the calibration constant of the capacitive sensor of the calibration mode.

Fit to $V_{eff} = A + B \cdot V_{ref}$	
$A\ (V)$	B
0.266 ± 0.01	-0.594 ± 0.01

Table 7.6: Results of the linear fits of fig. 7.11

7.4.3 Natural stiffness versus stored currents

From eq.6.45 I expect the natural torsional stiffness, k_ϕ, of the torsion balance to be linear versus the sum of the square of the currents, which are stored in the actuator coils. Assuming $I_{zz} = 1.82 \times 10^{-4} kg \cdot m^2$, I plotted k_ϕ versus $(i_1^2 + i_2^2)$ and linearly fitted the results (fig.7.12). The fitted gradient $dk_\phi/d(i_1^2 + i_2^2)$ given in table 7.7 is compatible with the expected theoretical value of $dk_\phi/d(i_1^2 + i_2^2) = 2.279 \times 10^{-6} Nm/rad/A^2$. This value was derived within the theoretical analysis of the actuator circuits (see section 6.4) thanks to eq.6.45.

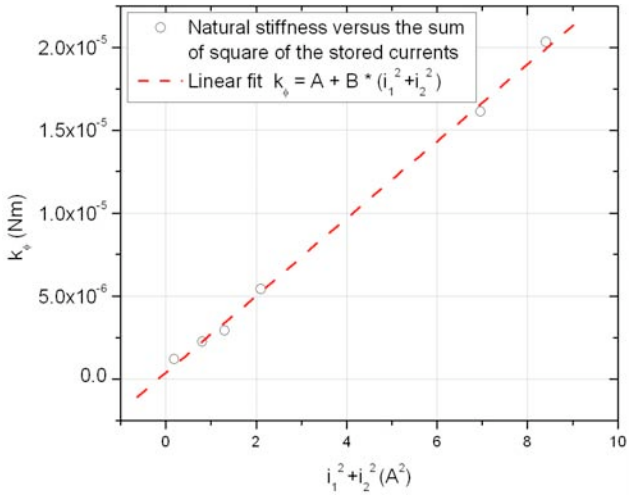

Figure 7.12: Natural stiffness of the torsion balance versus the sum of the square of the currents, which were stored in the actuator circuit.

Fit to $k_\phi = A + B(i_1^2 + i_2^2)$	
$A\ (Nm/rad)$	$B\ (Nm/rad/A^2)$
$3.8 \times 10^{-7} \pm 2.5 \times 10^{-7}$	$2.325 \times 10^{-6} \pm 5.5 \times 10^{-8}$.

Table 7.7: Results of the linear fits of fig. 7.12

7.4.4 Damping of the parasitic modes

In this section I will analyse the experimental performance of the damper mechanism of the MKII SSTB, which was adopted to damp down its parasitic oscillations. The pendulum and horizontal oscillations were monitored by measuring the capacitance between the float and a temporary copper plate positioned on its side.

I briefly discuss here the method I used to measure the quality factor of the damping of the parasitic modes. If we impulsively excite the pendulum mode at $t = 0$, the solution of eq.5.56 governing the dynamic of the pendulum motion is the function [5]:

$$\theta(t) = \frac{A}{I\omega_1} e^{-\gamma t} \sin(\omega_1 t + \phi_1) \tag{7.17}$$

with

$$\gamma = \frac{b_\theta}{2I_\theta}, \quad \omega_1 = \sqrt{\frac{k_\theta + glm}{I_\theta} - \frac{b_\theta^2}{4I_\theta}} \tag{7.18}$$

I_θ is the moment of inertial of the float relative to axis of the pendulum mode, b_θ is the damping coefficient and k_θ is the restoring stiffness.

From the fit of the pendulum angle, or of the equivalent voltage readout of the capacitive sensor, to the eq.7.17 it is possible to measure the quality factor Q which is defined by the equation [42]:

$$Q = \frac{2\pi E}{\Delta E} \tag{7.19}$$

E is the energy stored in the oscillations and ΔE is the energy loss per period. The previous equation, given eq.7.17, for $\omega_1 \gg \gamma$ is approximated by $Q \approx \omega_1/2\gamma$.

In practice, given a data set of the voltage readout of the capacitive sensor, I extracted the subset, which I was interested in. I fitted it with a general polynomial and subtracted the result from the original data set to remove any low frequency drift. I fitted the resulting data set with the function:

$$y(t) = A \sin(2Q\gamma t + \phi) e^{-\gamma t} \tag{7.20}$$

and estimated the coefficients A , Q, γ and ϕ by using the least square method within the MATLAB statistics toolbox .

Damping of the pendulum mode

For no stored current in the damper circuit the measured quality factor Q was ≈ 4000 (or $\tau \approx 1000s$) due to viscous He gas damping and to the magnetic field of the levitation bearing, which was acting on the copper damper. For a current of $4A$, which was stored in the damper circuit, I found $Q = 19 \pm 3$, which was associated with a decay time τ of $5.4 \pm 1.5s$. This stored current was sufficient to quickly damp down the $\approx 1Hz$ pendulum oscillations. The Q values associated with other stored currents, I_{damp}, are plotted in fig.7.13 and fitted to a rational polynomial of second order. The results of the fit are presented in table 7.8. I obtained that the measured Q value were inversely proportional to the square of the current, which was stored in the damper circuit. This result is in agreement with the fact that the power loss per second of the pendulum mode is expected to be proportional to the square of the magnetic field present in the copper damper [23] and therefore to the square of the current, I_{damp}, which is stored in the damper coil and which is generating such magnetic field.

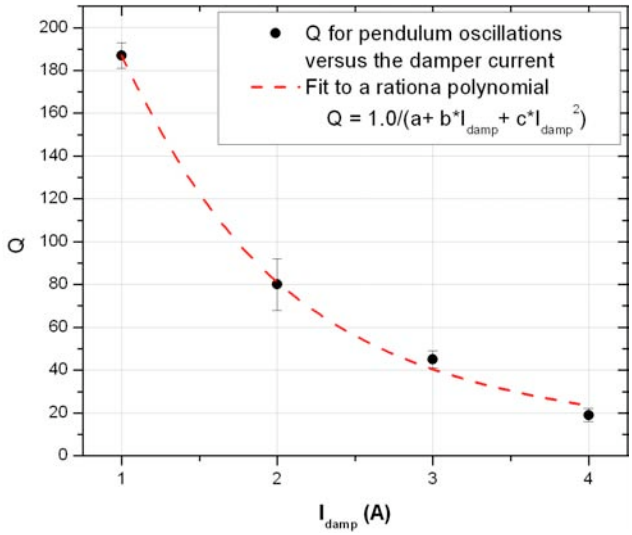

Figure 7.13: Q for the pendulum oscillations versus the current stored in the damper circuit and fit to a rational polynomial.

Fit to $Q = (a + b \cdot I_{damp} + c \cdot I_{damp}^2)^{-1}$		
a	$b\ (A)$	$c\ (A^{-2})$
0.004 ± 0.004	-0.001 ± 0.005	0.0027 ± 0.0016

Table 7.8: Results of the fits to a rational polynomial of fig. 7.13

Damping of the horizontal mode and of the vertical mode

I measured the Q of the horizontal parasitic oscillations from a data set, which showed the $5Hz$ oscillations together with the $1Hz$ ones due to the pendulum mode. I found that the horizontal oscillations were damped down with a $Q = 74 \pm 8$ or $\tau = 5 \pm 1s$. Because no current was stored in the damper circuit, the damping of these oscillations were due to a mechanism which was independent from the current stored in the damper coil. Their damping might have been related to the eddy currents, which were generated in the damper by the magnetic field of the levitation bearing. By monitoring the capacitance between the float and a temporary plate, which was positioned over its top, we tried to also characterise the damping of the $30Hz$ vertical oscillations of the balance. Because I found no evidence of the vertical oscillation, I conclude that the eddy current damping in the levitation transformer was working effectively [33].

7.4.5 Servo System closed loop transfer function

To further characterise the performances of the MKII SSTB we had to measure the closed loop transfer function, $T(\Gamma_{ext}, \Gamma_{eff})$, between the input torque, Γ_{ext}, which was acting on the float, and the torque effort, Γ_{eff} (see eq.6.55), which was applied to the float by the magnetic actuator to keep it at a constant angular position. Instead of applying an external torque to the float and measuring the servo effort Γ_{eff} to derive $T(\Gamma_{ext}, \Gamma_{eff})$, we summed an additional voltage, V_{cur}, to the input of the current source and measured the voltage output, V_{PII^2D}, of the digital compensator (see fig.7.14). We obtained the transfer function between V_{cur} and V_{PII^2D}, $T(V_{cur}, V_{PII^2D})$, which is equivalent to $T(\Gamma_{ext}, \Gamma_{eff})$.

We measured the phase and amplitude of $T(V_{cur}, V_{PII^2D})$ by comparing the phase and amplitudes of V_{cur} and V_{PII^2D}, where V_{cur} is an AC modulated signal. By repeating the procedure for different frequencies we obtained figure 7.15 [33]. In the same figure, for comparison I also plotted the theoretical prediction for $T(\Gamma_{ext}, \Gamma_{effort})$, which was obtained by assuming a natural period of the torsion balance of $T = 38s$. The theoretical model is consistent with the experimental results at low frequencies, $f \lesssim 0.1 - 0.5Hz$, within the limit of validity of the developed analytical model (see chapter 6). The analytical model in fact does not take into account the low pass filters, which were present in the servo loop.

The result of fig.7.15 is also an indirect proof of the reduction of the actuator

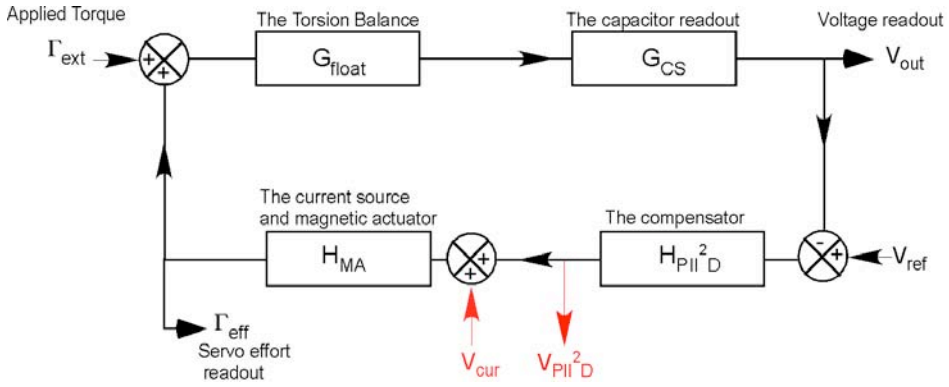

Figure 7.14: Schema of the servo loop indicating the input, V_{cur}, and the output voltage, V_{PII^2D}, used to measure the closed loop transfer function $T(\Gamma_{ext}, \Gamma_{effort})$.

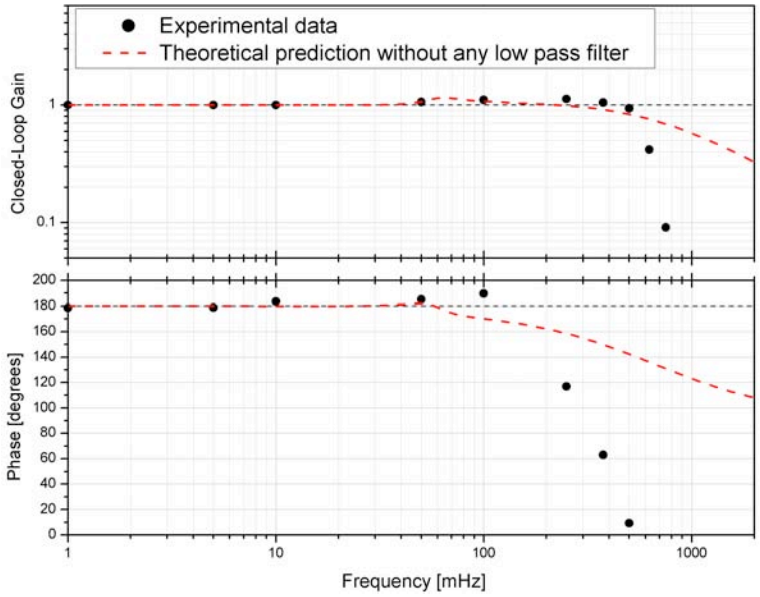

Figure 7.15: Measured closed loop transfer function $T(V_{cur}, V_{PID})$ equivalent to $T(\Gamma_{ext}, \Gamma_{effort})$ for a $PII^2D = (2, 1.2, 0.01, 10)$.

noise at low frequencies, that I predicted in chapter 6. The torque noise, which is applied to the float by the current source and magnetic actuator, can be considered as equivalent voltage noise at the input of the current source. We have just verified that the transfer function between the input of the current source and the output of the digital compensator at low frequencies is $T(V_{cur}, V_{PID}) \approx -1$. This result means that any low frequency component of the equivalent input voltage noise of the current source is almost completely cancelled by the voltage output of the digital compensator. This cancellation of the voltage noise of the current source results in the reduction at low frequency of the actuator noise which is applied to the float, as expected from chapter 6.

7.4.6 Torque noise spectrum

Ultimately the performance of the torsion balance is defined by the amplitude spectral density of the torque noise, which for a given time interval defines the torque sensitivity of the torsion balance. During the ISL tests of gravity we found that in average the amplitude torque spectrum density was $2 \times 10^{-10} Nm/\sqrt{Hz}$ at low frequencies (see fig.7.16) which corresponded to a displacement noise of $\approx 4.5 \times 10^{-5} rad/\sqrt{Hz}$. In fig.7.16 I also plot the equivalent torque noise given by the readout circuit, which we measured when the float was not levitated. This voltage noise is transformed into angular noise and multiplied by the natural stiffness of the torsion balance to obtain an equivalent torque spectrum. The torque noise level, which was given by the readout system, was at least one order of magnitude lower than the one, which was obtained when the float was levitated and servo controlled. This result indicates that the limiting torque noise was not due to the readout noise but instead to other noise sources, like the seismic noise. In previous experiments with the MKII SSTB, during Casimir measurements, we obtained a lower noise level, $\approx 10^{-11} Nm/\sqrt{Hz}$ [33], which was near the noise limit given by the readout circuit.

7.4.7 Tilt coupling

To further investigate the origin of the measured torque noise we did some preliminary measurements of the coupling constant, $k_\theta \beta$, between the ground tilt and the torque, which was acting on the float (see eq.5.73 in chapter 5). From chapter 5 I theoretically know that for a tilt angle θ_T in a direction ϕ_T, the torsion

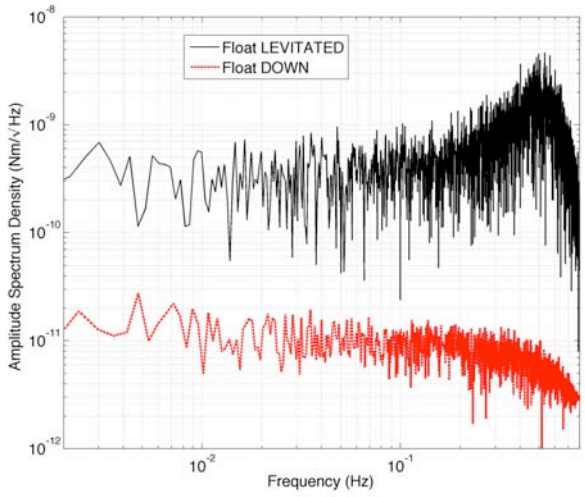

Figure 7.16: Amplitude spectrum density of the torque effort necessary to keep the torsion balance at a constant position: black is the torque noise level obtained when the float was levitated and servo controlled, the red one is the equivalent torque noise level obtained from the readout sensor which was measured when the float was not levitated.

balance is subjected to a torque, which is given by the eq.5.53. By measuring $d\Gamma_{eff}/d\theta_T$ for different values of ϕ_T I can derive $k_\theta\beta$. By acting on the three tilt stages of the cryostat base (see section 4.4), we measured the torque, Γ_{eff}, versus the tilt angle, θ_T, for three values of ϕ_T and linearly fitted the results (see fig.7.17 and table 7.9). The measured gradients $d\Gamma_{eff}/d\theta_T$ were fitted themselves to a sinusoidal function in ϕ_T with a period of 2π (see fig.7.18 and table 7.10). I found that:

$$k_\theta\beta = 8.77 \times 10^{-7} \pm 1.7 \times 10^{-8} Nm/rad \tag{7.21}$$

These results about the tilt coupling are given by preliminary measurements and need to be confirmed by further experimental investigations. They predict a torque noise level, which is associated with the tilt ground noise, of the same order of magnitude of the one we measured during the ISL runs. In fact by supposing a tilt ground noise of $10^{-4} rad/\sqrt{Hz}$ (see chapter 5) and given the coupling constant of eq.7.21, from eq.5.73 the expected torque noise level is $\approx 9 \times 10^{-11} Nm/\sqrt{Hz}$.

A few reasons can explain the large coupling between the measured torque and the ground tilt. One reason is that, because during the ISL runs we were not able to anneal the float due to a broken connection, some magnetic flux might have been trapped in the float shell. Trapped magnetic flux can interact with the

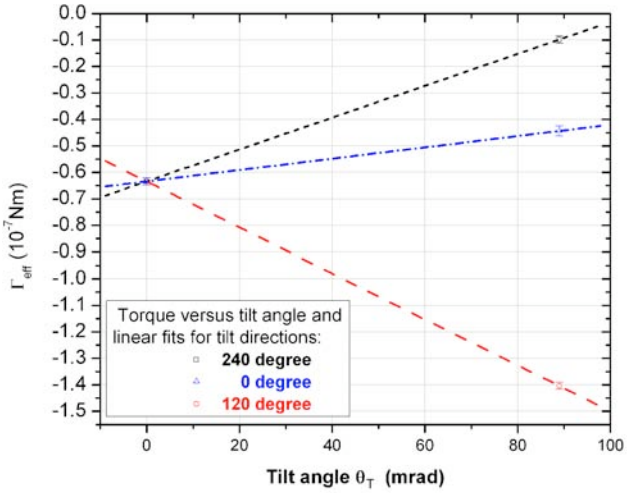

Figure 7.17: Torque servo effort necessary to keep the float at a constant position versus tilt angle in three possible tilt directions.

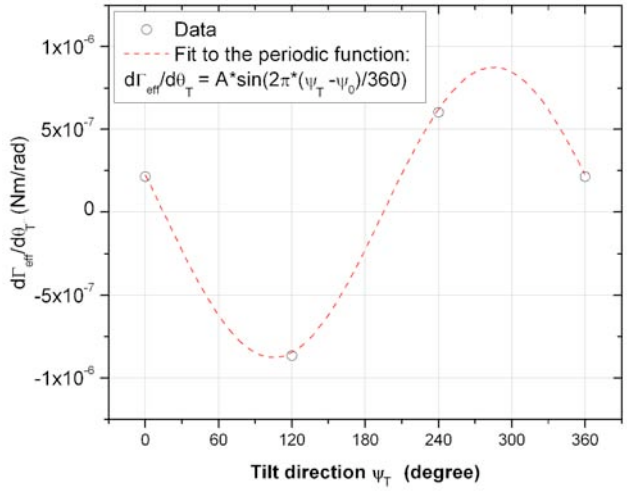

Figure 7.18: Torque change per radiant tilt versus tilt direction angle. The data relative to 0° and 360° are assumed to be the same.

Fit to $\Gamma_{eff} = A + B \cdot \theta_T$		
ϕ_T (deg)	$A\ (Nm)$	$B\ (Nm/rad)$
0	-6.34×10^{-8}	2.14×10^{-7}
120°	-6.34×10^{-8}	-8.65×10^{-7}
240°	-6.34×10^{-8}	6.02×10^{-7}

Table 7.9: Results of the linear fits of fig. 7.17

Fit to $d\Gamma_{eff}/d\theta_T = A \cdot \sin(2\pi(\phi_T - \phi_0)/360)$	
ϕ_0 (deg)	A (Nm/rad)
194.8 ± 0.9	$8.77 \times 10^{-7} \pm 1.7 \times 10^{-8}$

Table 7.10: Results of the linear fits of fig. 7.18

magnetic field of the levitation bearing and increase the expected tilt coupling of the float. Another reason is that during the ISL we substituted the damper cylinder, which was attached underside the float, with a new one. The new damper might have contained some magnetic impurities, which coupled with the levitation field increasing the tilt coupling. Moreover asymmetries of the shape of the float shell, which can couple with the levitation magnetic field, might have increased the tilt coupling too [19].

7.5 Possible improvements

In this section I discuss the possible modifications that can be applied to the SSTB to improve its performance given the experimental results, which were presented in this chapter.

In order to reduce the influence of the tilt seismic noise, which is most probably the limiting noise source of the SSTB, we have to install an active vibration isolation on a base of the cryostat. Otherwise we can reduce the tilt coupling constant, $k_\theta\beta$, by many possible approaches:

- We can insert a lifting device under the float in the levitation pillar. In this way it will be possible to position the float at the nominal height, before activating the levitation field. This choice will minimise the creation of magnetic fluxes, which couple the float with the bearing.

- In the legs of the lifting device we can insert some heaters, to thermally cycle the float and eliminate any residual trapped magnetic flux.

- We can fabricate a new float by using an electro formed copper shell, as we did for the MKI float, and have niobium sputtered in its inside. In this way we will have a float with much better sphericity and smaller residual torque, which is given by the coupling with the bearing.

- We can use a new float without any window cut on it. In this way we will avoid any magnetic flux trapped inside the float windows. We will

have to apply the torque to the float otherwise, for example by using a superconducting insert or with superconducting plates attached outside the float.

The possibility to have a float with smaller residual torsional torque, which a electro formed float better guarantees, can also lead to a much smaller minimum natural stiffness and a smaller contribution of the readout noise to the torque noise.

The capacitive readout system is just a temporary solution and it has to be substituted with the optical readout, which is under development within our group [62]. An optical readout of the float angle will bring many advantages. The SSTB will have a much better angular sensitivity than now. It will permit a much easier and more precise calibration of the torque effort versus the voltage effort. It will let us use only one readout system even when we need to apply voltages to the float to measure the capacitances with a capacitive bridge and to keep controlling the float position. Moreover the optical readout will lead to a much simpler and less time consuming calibration protocol.

To further improve the duty-cycle another possible solution is to install a permanent cryocooler to keep the torsion balance almost indefinitely at $4.2K$. This solution will improve the duty cycle of the SSTB and it will increase its torque sensitivity.

7.6 Conclusions

In this chapter I presented the experimental performances of the MKII SSTB, we obtained during the preliminary tests of the ISL of gravity at micrometre distances. I discussed the protocol, we defined to calibrate the torque effort of the torsion balance. We found that most of the behavior of the torsion balance followed the theoretical predictions. The damping of the parasitic pendulum oscillations was found to be proportional to the square of the current, which was stored in the damper circuit. A current of $4A$ in this circuit was shown to be sufficient to damp down such oscillations within few seconds. The closed loop transfer function of the servo system between the applied and measured torque was measured and, at low frequencies, found to be in agreement with the analytical model of chapter 6 I gave indirect experimental evidence of the reduction of the torque noise from the current source thanks of the feedback loop. The gradient of the torque calibration constant versus the sum of the currents, which were stored in the actuator circuits, $|d\Gamma_{eff}/(dV_{eff}d\left(i_1+i_2\right))|$, was found $2.46\times10^{-8}\pm3.1\times10^{-9}Nm/V/A$. This value is near its theoretical estimate of section 6.4, but it was not fully compatible with it within 2σ. The torque calibration constant, $d\Gamma_{eff}/dV_{eff}$, was found not null even when no current was stored in the actuator circuits. The sign of this offset of the torque calibration constant depended on the polarity of the current, which was stored in the levitation circuit. These results are evidence of a magnetic coupling between the levitation and the actuator circuits, which might be due to the pick up of the levitation magnetic field by the actuator coils.

The torsion balance during the ISL tests was characterised by an unexpected large torque noise spectrum. The torque noise level was $2\times10^{-10}Nm/\sqrt{Hz}$ at $30mHz$ and it was more than one order of magnitude larger than the one we measured during the previous Casimir experiments [33]. From preliminary measurements I suspect that the origin of this torque noise is a large coupling constant between the ground tilt and the measured torque. This constant, $d\Gamma/d\theta_T$, was estimated to be around $8.77\times10^{-7}Nm/rad$. A possible cause of the measured $d\Gamma/d\theta_T$ might be some magnetic flux, which might be trapped in the float shell and coupling with the levitation field. Another reason might be the presence of magnetic impurities in the damper cylinder or asymmetries of the float shell, which can couple with the levitation magnetic field from the bearing coil.

Many solutions to decrease the contribution of the tilt noise to the torque noise of the SSTB are possible. We can thermally cycle the float and reduce the magnetic flux, which might be trapped in its shell. We can install a new seismic active insulation system at the base of the cryostat, which will reduce the tilt noise acting on the float. By using a new electro formed copper float, which will have sputtered niobium on its inside, we can reduce the contributions of both the seismic and the readout noise to the measured torque noise. The new and improved float can lead to a smaller coupling with the ground tilt and it will require a small natural stiffness to be able to freely oscillate around an equilibrium position. The reduced natural stiffness of the torsion balance will decrease the contribution of the readout noise to the measured torque noise. To decrease the readout noise and to simplify the calibration procedure, a solution is to adopt a optical readout system, which is now under development [62] and which is expected to have a better angular sensitivity than the current capacitive readout. The installation of a cryocooler will reduce the time spent to cool down and calibrate the torsion balance with respect to the total time, which is available for the torque measurements. This increase of the duty cycle of the SSTB will lead to an enhancement of its torque sensitivity.

Chapter 8

First tests of the ISL of gravity at micrometre distances

8.1 Introduction

In this chapter I will present the first results, which we obtained with the tests of the ISL of gravity at micrometre distances. I will review all the preliminary procedures, which are necessary to have the test masses ready for the torque measurements. I will discuss the alignment of the masses, the calibration of their relative distance, the cancellation of the voltage difference between them and the measurement of the misalignment angle, Ω, between the x motion of the flat mass and its surface. I will describe the method, by which we took the torque measurements for the ISL tests of gravity and describe the procedure, which we adopted to increase the signal to noise ratio of possible coherent signals. The experimental results about the tests of the ISL of gravity will be divided in two groups: the "I run" will include all the torque measurement, which were taken using the test masses A and C (see chapter 2); the "II run" will include the torque measurements, which we obtained using the mass C and the improved curved mass B (see chapter 2). I will present the periodic signals, which we measured during both experimental runs above the noise level of the SSTB. I will study the dependence of the spectral components of these signals on the distance between the masses, on the voltage and on the magnetic field, which we applied to them. The signal, which we measured during the II run with the improved mass B, is smaller than the one found during the I run. In the next chapter I will interpret the signals, which we measured, according to the analytical models of

the possible forces, which, to the best of our knowledge, are acting between the masses.

8.2 Setting up for the ISL test

In this first section I will present all the preliminary work that has to be completed before taking any torque measurements for the ISL test. I will discuss the alignment of the test masses, the calibration of the absolute distance between them, the measurement of the misalignment angle of the Attocube motion, Ω, with respect to its nominal x direction and the minimisation of the voltage difference between the masses.

In the following sections, D_x is the displacement of the Attocube in the x direction with respect to the zero position which is when the support of the flat mass positioned all on one side of the torsion balance (see fig.8.1). D_y is instead the measured distance between the surfaces of the test masses. With respect to the variables I used for the analytical models of chapter 3, d_x and d_y, D_x is equal to $d_x - 3.5mm$ while D_y is equal to $d_y - 2t_{Au} - h_1 - h_2$. t_{Au} is the thickness of the Gold layer covering the density mass modulation and $h_1$and h_2 are the average depths of the long range routhness of the surfaces of the masses (see table 2.1).

8.2.1 Test mass alignment

For a correct ISL test we need that the cylindrical surface of the mass on the float is parallel to the planar surface of the other mass. To guarantee this parallel condition we performed a first rough alignment of the masses at room temperature and then a more accurate one at $4.2K$. At room temperature we moved the flat mass in the central position for $D_x \approx 3.5mm$ and then we rotated the copper pillar around its central vertical axis. By doing this we minimised the capacitance between the flat and the curved mass, that we measured with the AH capacitive bridge (see chapter 4). Once this position was found, we fixed the support on the underlying base plate by fastening its base screws. At $4.2K$, after the float was levitated, the optimal parallel position between the masses was found by taking the average position between the minimum and the maximum voltage output of the capacitive readout, $(V_{\min}, V_{\max})$. These voltages are obtained by rotating the float to the two extreme angular positions, where the curved mass touched

the flat mass. We found that the parallel position, defined by this procedure, is independent of the distance between the test masses, D_y, (see for example fig.7.5 of chapter 7). With this technique, for example given the data of fig.7.5 and table 7.2, we estimated the angular position, which satisfies the parallel condition given by $(V_{\min}, V_{\max})$, within $\sigma_\phi = 2.3 \times 10^{-4} rad$.

8.2.2 Calibration of the absolute distance between the masses

The data about $(V_{\min}, V_{\max})$ versus the number of the Attocube steps in the y direction, as the one of fig.7.5, was used to measure the distance D_y between the surfaces of the two test masses. Because we found that D_y changes as a function of D_x, such distance measurements had been usually performed with the flat mass, which was moved to the position with $D_x = 0$. Because at this position the distance D_y was measured to be minimum. Given the value of $(V_{\min}, V_{\max})$ versus the step number of the Attocube motion, n, the position, n_0, for which the masses are touching each other, is defined by the condition $V_{\min} = V_{\max}$. n_0 is give by the following equation:

$$n_0 = -\frac{A_{\min} - A_{\max}}{B_{\min} - B_{\max}} - n_{last} \tag{8.1}$$

$A_{\min}$, $A_{\max}$, $B_{\min}$ and $B_{\max}$ are the parameters of the linear fit performed over $V_{\min}$ and $V_{\max}$ versus n (for example $V_{\min} = A_{\min} + B_{\min} \cdot n$). n_{last} is the step number of the last voltage measurement, which was taken while the masses were approaching. For example from the data of fig.7.5 and table 7.2 we found $n_0 = 12 \pm 6 steps$. Given the calibration of the Attocube displacement for a single step in the y direction, $(dy/dn)_+$ (see table 7.1), the found n_0 implies that the last measurements of $V_{\min}$ and $V_{\max}$ were taken at a distance $D_y \approx 2 \pm 1 \mu m$. At this distance however, as soon as we moved the flat mass in the x direction, the two masses touched at some point and we could not complete the torque measurements. On average the error on the distance between the test masses was found to be $\approx 1 \mu m$.

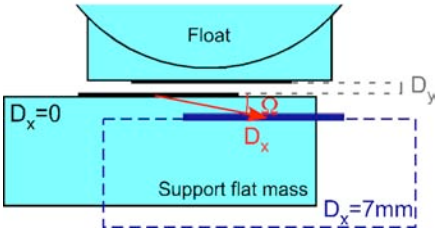

Figure 8.1: Schema illustrating the misaligment angle, Ω, between the x motion of the support of the flat mass and the surface of the mass as seen from the top.

8.2.3 Tilt angle of the Attocube motion

As previously mentioned, during the ISL tests we found that the direction of the Attocube displacement in the x direction was not parallel to the flat surface of the mass by an angle Ω (see fig. 8.1). By measuring the capacitance C_y between the float and the support of the flat mass with the AH capacitive bridge (see chapter 4) versus the Attocube position D_x (see fig.8.2), we found that the function $C_y(D_x)$ is not symmetric with respect to the central position ($D_x = 3.5mm$) as we would expect given the symmetry of the problem for $\Omega = 0$. To estimate this tilt angle Ω we measured the distance, ΔD_y, we moved the support in the y direction to keep the two masses at a constant distance, D_{y0}, while we progressively increase D_x. D_{y0} was identified by the associated $(V_{\min}, V_{\max})_0$. The measured misalignment angle, Ω, was $0.15° \pm 0.01°$ for the I run (see fig.8.3 and fit results in table 8.1) and $0.3° \pm 0.02°$ for II run.

Fit to $\Delta D_y = A + B \cdot D_x$		
A	B	$\Omega = \arctan(B)$ (deg)
$0.1 \pm 0.7\mu m$	$2.7 \times 10^{-3} \pm 2 \times 10^{-4}$	$0.15° \pm 0.01°$

Table 8.1: Results of the linear fit of fig. 8.3. Here D_x and D_y are given in meters.

8.2.4 Voltage cancellation between the masses

Before starting the ISL torque measurement, it was also necessary to minimise the possible voltage difference between the masses, V_0, which could give origin to spurious electrostatic torques (see chapter 3). We cancel V_0 by applying a DC voltage of the opportune sign to the flat mass. To measure V_0 we used the same technique, which I described in the section 7.3.3 for the torque calibration of the voltage servo effort of the SSTB. Firstly we moved the support of the flat mass

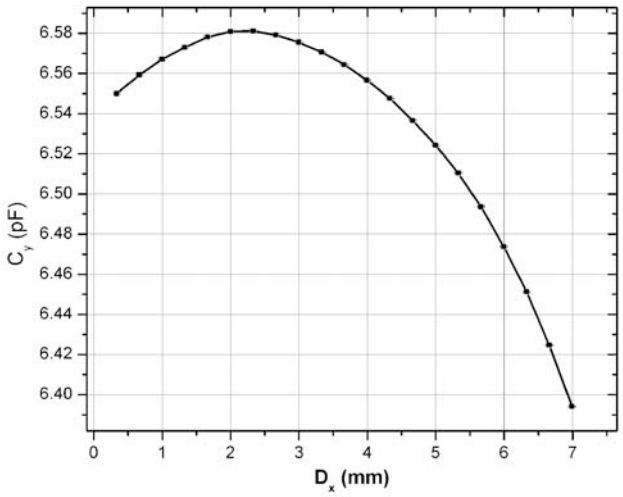

Figure 8.2: Capacitance between the float and the support of the flat mass, C_y, versus its position in the x direction, D_x.

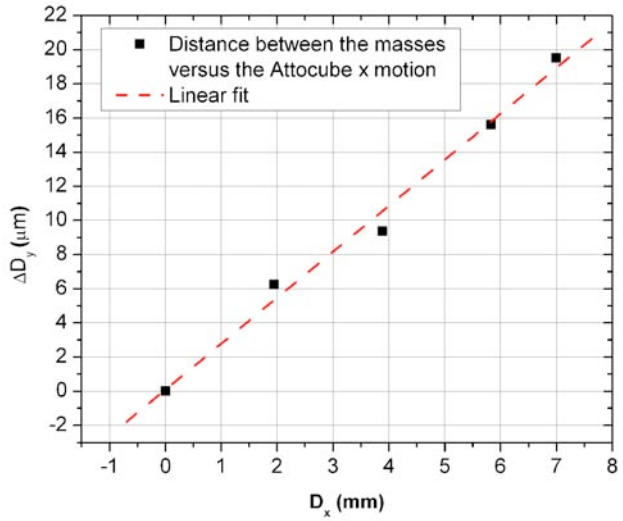

Figure 8.3: Correction of the y position of the flat mass, ΔD_y, necessary to keep the masses at a constant distance, D_{y0}, while increasing D_x.

at the x position (usually for $D_x = 0$ or $D_x = 7mm$) where the gradient of C_y versus the float angle ϕ, $dC_y/d\phi$, was the biggest. In this position the torque, which was applied to the float for a given voltage difference (see eq.7.8), was the biggest. WIth the flat mass in the chosen position we measured the voltage effort, V_{eff}, which was necessary to keep the torsion balance at a fixed angular position while we applied a set of voltages, V_{daq}, to the flat mass. By fitting the measured (V_{daq}, V_{eff}) with the expected second order polynomial of eq.7.10, we derived the voltage difference between the test masses V_0. We applied a DC voltage with amplitude $-V_0$ to the flat mass and canceled the measured voltage difference within the error of its estimate.

During the ISL experimental runs we measured a weighted average $\bar{V}_0 = 147.9 \pm 0.5mV$ with an average error of $\approx 15mV$ on the single estimate.

8.3 Method measuring the torques

I describe here the method, by which we took the torque measurements to study possible violations of the inverse square law of gravity at micrometre distances. We placed the support at the x position, $D_x = 0mm$, which corresponded to the minimum distance, D_y, between the masses. We slowly moved the flat mass in the x direction and continuously measured the torque effort versus the D_x position. The speed of such torque scan, dD_x/dt, was chosen in such a way that the frequency of a possible signal, which was coming from the $1/400^{-1}\mu m$ periodicity associated with the mass density modulation, was much smaller than the natural frequency of the torsion balance, which is typically $f_0 \approx 25mHz$. In our tests we sent a control signal to the Attocubes with frequency of $20Hz$ and amplitude of $20V$. This settings, given the Attocube calibration constant $(dx/dn)_+$of table 7.1, corresponded in a scan speed of $dD_x/dt \approx 2.2\mu m/s$ or to a signal frequency of $\approx 5.5mHz$. A full scan in the x direction from $D_x = 0$ to $D_x = 7mm$ took around 50 minutes to be completed. Afterwards we quickly moved the support in the reverse direction back to its original position without recording any torque measurement. If necessary the torque scan was repeated. The described process for the torque measurements was automated and run for days without interruptions. If desired, every fixed number of torque scans in the x direction, the y position of the test mass and the voltage applied to the masses was automatically changed. Therefore we obtained the torque effort measurements,

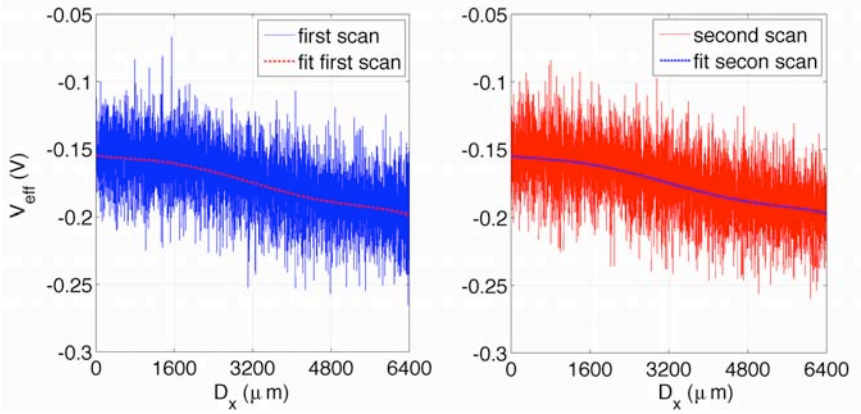

Figure 8.4: Example of two servo effort measurements versus the x position of the test mass and the their relative polynomial fits.

V_{eff}, versus the position D_x of the test mass as shown in fig.8.4.

A drift in the signal might be present because of a possible voltage difference between the masses and the change of the distance D_y between them during the x scan (see section 8.2.3). From the original dataset I selected a subset whose length was a fixed integer multiple of $400\mu m$, because I wanted to consistently extract the spectral information around $k_0 = 1/400\mu m^{-1}$ from different samples. I removed the low frequency drift by fitting the measured signal with a 5th order polynomial (see section 8.2.3) and by subtracting the fitted function from the original signal. By using numerical simulations I checked that this procedure does not modify the signal at the spatial frequency we are interested in. An example of the final result is shown in fig.8.5.

8.3.1 Coherently averaged amplitude spectrum

From each of the measured torque scans I evaluated the associated fast discrete Fourier transform with the MATLAB function "*fft*". I obtained a real and an imaginary amplitude, (R, I), versus the spatial frequency, k. At each k I averaged the (R, I) of all the torque scans and obtained $(\bar{R}, \bar{I})$. From this value I evaluated the one-sided amplitude spectrum of the torque scans with the equation [83]:

$$AS(k) = \left|(\bar{R}, \bar{I},)\right| \frac{2}{n_{tot}} \tag{8.2}$$

where n_{tot} is the total number of torque measurements of each scan. The amplitude spectrum spans from the minimum spatial frequency $1/L$ to the maximum

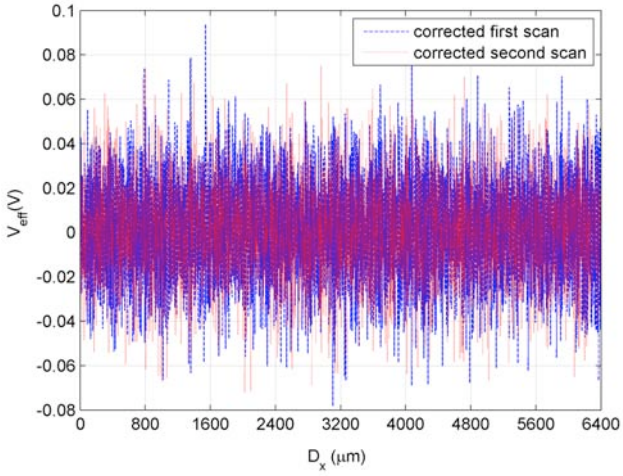

Figure 8.5: Torque servo effort signal after having removed the long range drift with the polinomial fit.

one $k_s/2$, where L is the total length of the scan in micrometers and $k_s = n_{tot}/L$ is the sampling spatial frequency. The amplitude spectrum, which is defined by the eq.8.2, is such that for a sin wave signal of amplitude A and frequency k_0, its amplitude spectrum at k_0 is exactly A. By coherently averaging the torque scans, the amplitude of any periodic signal remains constant while the amplitude of any stochastic signal decays as $1/\sqrt{m}$, where m is the number of scans. The error of the spectral amplitude at the frequency of interest was simply chosen as the average of the amplitude spectrum over the nearby frequencies where the possible expected signals are know no to have harmonic components (for example see fig.8.6).

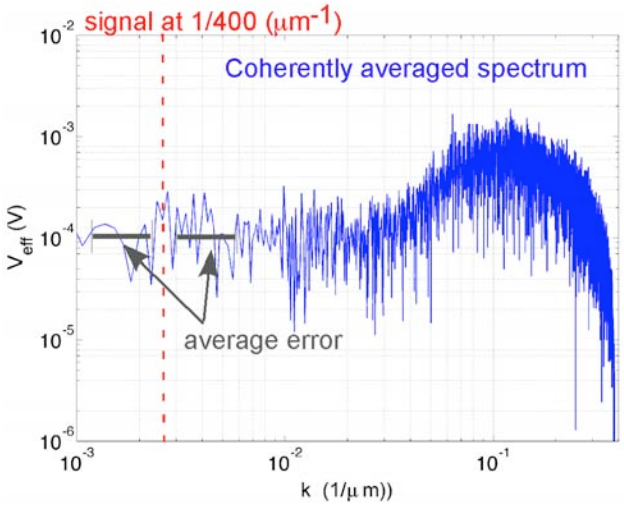

Figure 8.6: Coherently averaged amplitude spectrum of the samples of fig.8.5

8.4 Torque results from the I run

In this section I will present the experimental results relative to the torque scans for the ISL tests of gravity at micrometre distances, which were obtained with the test masses A and B (see chapter 2) and which I grouped under the label of "*I* run". I acknowledge that the quality of the surface of the curved mass A was not ideal to test gravity at short distances because it was not fully covered by a gold layer but just partially by a silver paint as shown in chapter 2 and fig.2.3. However I should discuss here the torque results obtained with these masses, because they let us test some of the expected torques, which were modelled in chapter 3. The torque measurements of the *I* run will give us some indications about the possible origins of the torque we measured during the "*II* run" with the improved mass C. The results of the "*I* run" also taught us some unexpected lessons on how to further improve our experimental set up to investigate the ISL of gravity at micrometre distances. With these preliminary masses we succeed in performing torque scans down to a minimum distance, D_y of $13\mu m$ (without taking into account the roughness of test masses and the thickness of their gold/silver paint layers). To our knowledge torque measurements at such short distance had never been measured without an electrostatic screen positioned between the samples during a dedicated test of the ISL of gravity.

As I will show, with these masses we measured a periodic signal which had spectral components at even and odd harmonics of the spatial frequency associ-

ated with the periodicity of the density modulation ($k = 1/400\mu m^{-1}$, $2/400\mu m^{-1}$, $3/400\mu m^{-1}$ and $4/400\mu m^{-1}$). The amplitudes of these spectral components decreased with the increase of the distance, D_y, between the masses. I will show that we minimised but not cancelled the measured periodic signal by modifying the voltage applied to the flat mass. While the $1/400\mu m^{-1}$ and $3/400\mu m^{-1}$ spectral amplitudes changed according to a parabola in the applied voltage, the spectral amplitude associated with $k = 1/200\mu m^{-1}$ showed instead a linear dependence on the voltage. I will also present the measured linear dependence of the spectral amplitudes at $k = 1/400\mu m^{-1}$, $3/400\mu m^{-1}$ and $4/400\mu m^{-1}$ on the sum of the currents, which were stored in the actuator circuits (see section 6.4). This result indicates that the measured torques are coupled with the magnetic field generated by the actuator coils. At $D_y = 13\mu m$ the spectral amplitude at $k_0 = 1/400\mu m^{-1}$ was $8.4 \times 10^{-11} \pm 1.5 \times 10^{-11} Nm$.

As previously mentioned, I will leave the physical interpretation of these signals to the next chapter.

8.4.1 Torques versus distance

Firstly we checked the dependence of the torque signals on the distance, D_y, between the masses. With a complete automatic procedure we performed two torque scans for each distance from a minimum distance D_y of $13\mu m$ up to a maximum one of $35\mu m$ (see fig. 8.7). The periodic signals we measured were clearly above the torque noise level of the SSTB and decreased as D_y was increased. I performed the average spectral analysis of each couple of scans, as described in the previous section. The results are presented in fig.8.8. The main spectral components of the measured signals were at four spatial frequencies ($k = 1/400\mu m^{-1}$, $2/400\mu m^{-1}$, $3/400\mu m^{-1}$ and $4/400\mu m^{-1}$) which are even and odd harmonics of the main spatial frequency associated with the periodicity of the density modulation ($k_0 = 1/400\mu m^{-1}$). In fig.8.9 I plot the found spectral amplitudes at these frequencies as a function of the distance D_y between the masses. In the next chapter I will discuss which equations best fit their measured decays.

8.4.2 Torques versus applied voltage

We also checked the dependence of the measured signals on the voltage, which was applied to the flat mass , V_{daq}. With a complete automatic procedure we

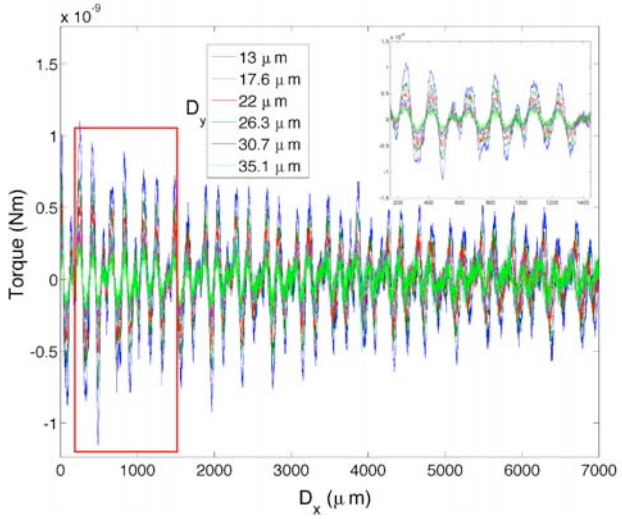

Figure 8.7: I run: measured torque versus the D_x position of the flat mass at different distances, D_y, between the masses. The torque was detrended as explained in section 8.3

changed V_{daq} every 4 scans which were performed at a distance of $\approx 24\mu m$. The torque results are shown in fig.8.10 and their amplitude spectra in fig.8.11.

In fig.8.12 I plot the spectral amplitude of the signal for the different harmonics of k_0 versus the voltage, which was applied to the flat mass. I found that the amplitudes of the modes at $1/400\mu m^{-1}$, $3/400\mu m^{-1}$ and $4/400\mu m^{-1}$ followed a parabola, whose minima were not null and happen at three different values of the applied voltage, V_0, respectively $-3.5 \pm 0.5V$, $7 \pm 1V$ and $2 \pm 0.6V$ (see table 8.2). We expected instead $V_0 = 0.37 \pm 0.01V$ by performing direct voltage measurements as described in section 8.2.4. The spectral amplitude at $k = 2/400\mu m^{-1}$ linearly depended on the applied voltage (as fig.8.13 and table 8.3).

Fit to $\Gamma_{eff} = A + B\,(V_{daq} - V_0)^2$			
k (μm^{-1})	A (Nm)	B (Nm/V^2)	V_0 (V)
$1/400$	$1.29 \times 10^{-10} \pm 8 \times 10^{-13}$	$2.9 \times 10^{-13} \pm 3 \times 10^{-14}$	-3.5 ± 0.5
$3/400$	$8.85 \times 10^{-10} \pm 9 \times 10^{-12}$	$1.1 \times 10^{-12} \pm 1 \times 10^{-13}$	7 ± 1
$4/400$	$3.05 \times 10^{-10} \pm 4 \times 10^{-12}$	$3.8 \times 10^{-13} \pm 7 \times 10^{-14}$	2 ± 0.6

Table 8.2: Result of fit to a second order polynomial of fig.8.12 and 8.13

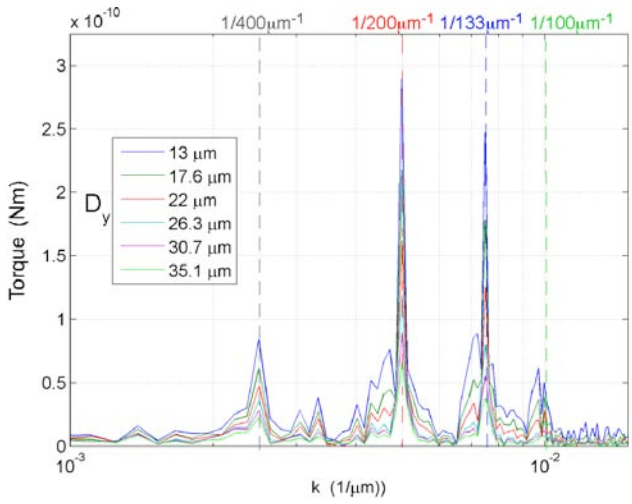

Figure 8.8: I run: spectral amplitudes of the measured signals at the different distances, D_y, between the masses.

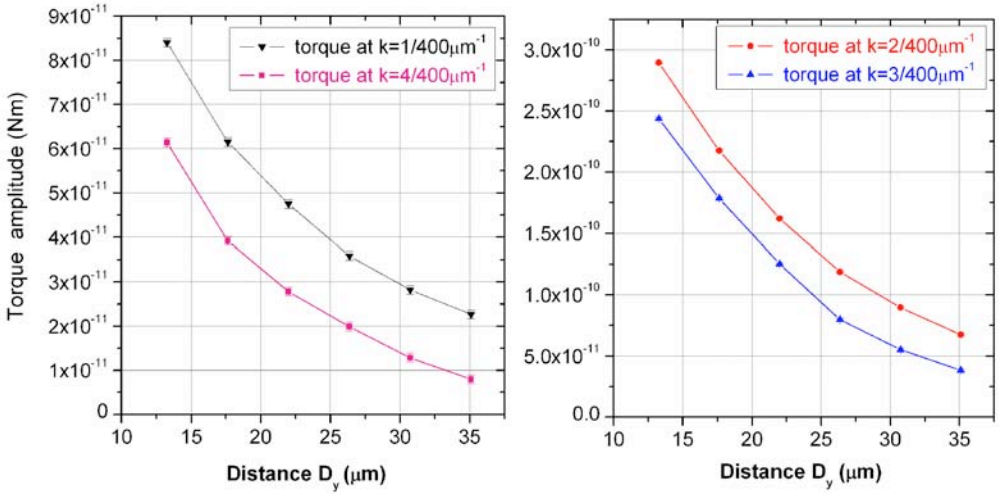

Figure 8.9: I run: spectral components versus the distance between the masses and relative exponential fits for the January run.

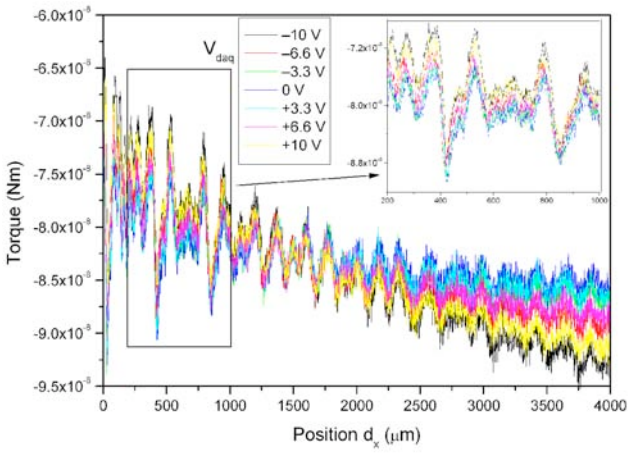

Figure 8.10: I run: torque versus side to side position for different values of the voltage applied to the flat mass, V_{daq}.

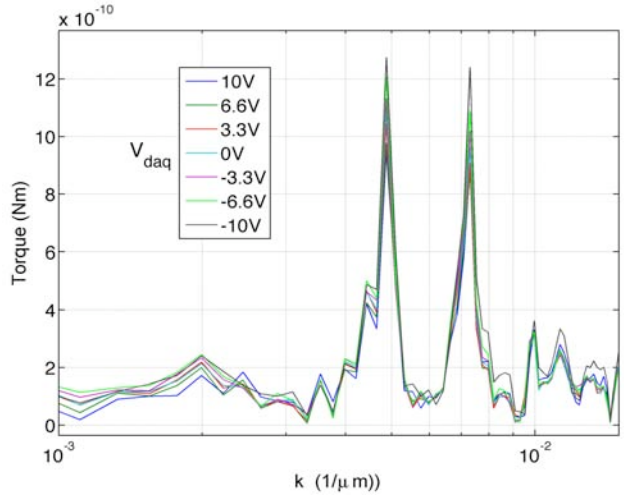

Figure 8.11: I run: amplitude spectra of the torque scans performed with different voltages, V_{daq}, applied to the flat mass.

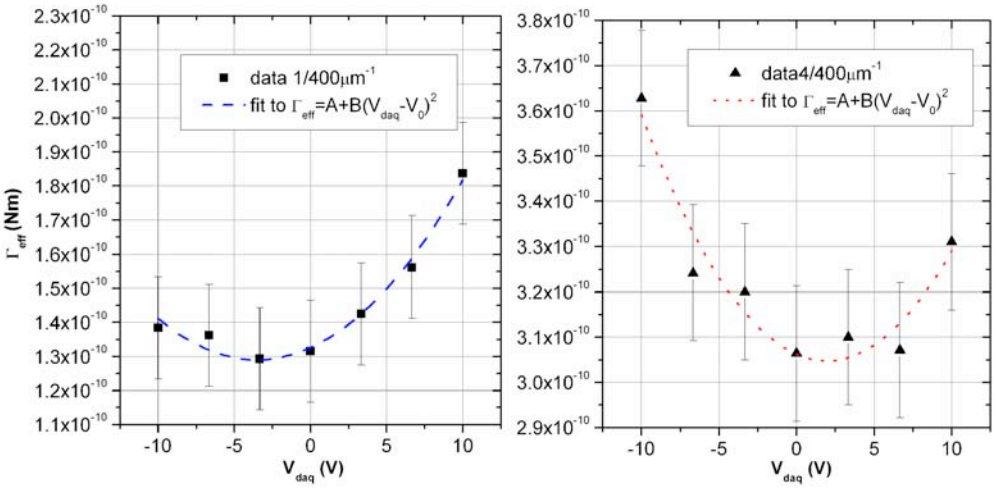

Figure 8.12: *I* run: spectral amplitude at $1/400\mu m^{-1}$ and $4/400\mu m^{-1}$ versus the voltage applied to the flat mass.

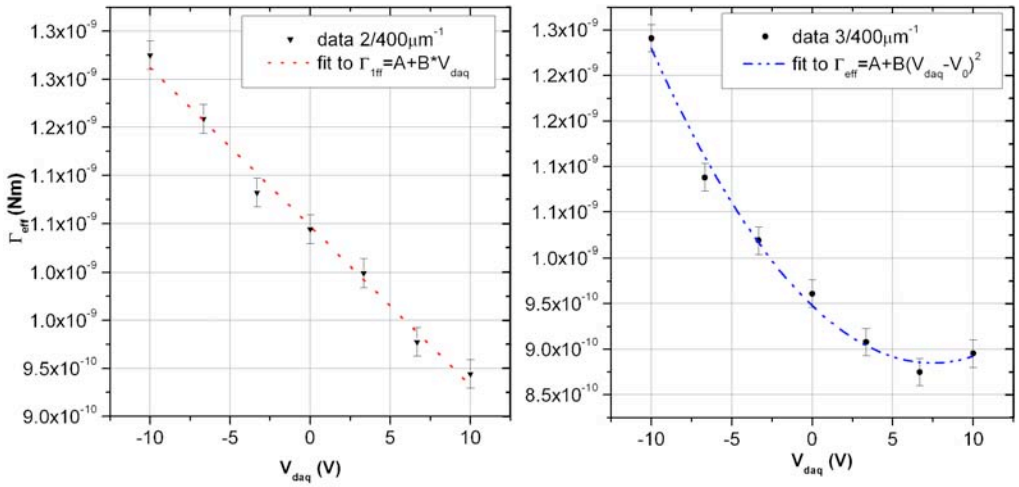

Figure 8.13: *I* run: spectral amplitude at $2/400\mu m^{-1}$ and $3/400\mu m^{-1}$ versus the voltage applied to the flat mass.

Fit to $\Gamma_{eff} = A + BV_{daq}$		
$k\ (\mu m^{-1})$	$A\ (Nm)$	$B\ (Nm/V)$
2/400	$10^{-9} \pm 5 \times 10^{-12}$	$-1.64 \times 10^{-11} \pm 7.4 \times 10^{-13}$

Table 8.3: Result of the linear fit to the $2k_0$ data of fig.8.13

8.4.3 Torques versus the actuator currents

We also changed the current stored in the actuator circuit to modify the magnetic field, which was indirectly applied to the masses though the actuator coils. In fact through one of the window cuts on the Niobium shell, which was behind the support of the curved mass, the magnetic field, which was generated by the actuator coils and the levitation bearing, reached the mass from the back of the support. As shown in fig.8.14 and table 8.4 I found that the spectral amplitudes at the spatial frequencies $k = 1/400\mu m^{-1}$, $3/400\mu m^{-1}$ and $4/400\mu m^{-1}$ linearly changed with the sum of the stored currents, $i_1 + i_2$ (see section 6.4). This result indicates a possible magnetic origin of these spectral components as I will further discuss in the next chapter. The gradient of the spectral component at $k = 2/400\mu m^{-1}$ versus $i_1 + i_2$ was instead compatible with zero within 2σ.

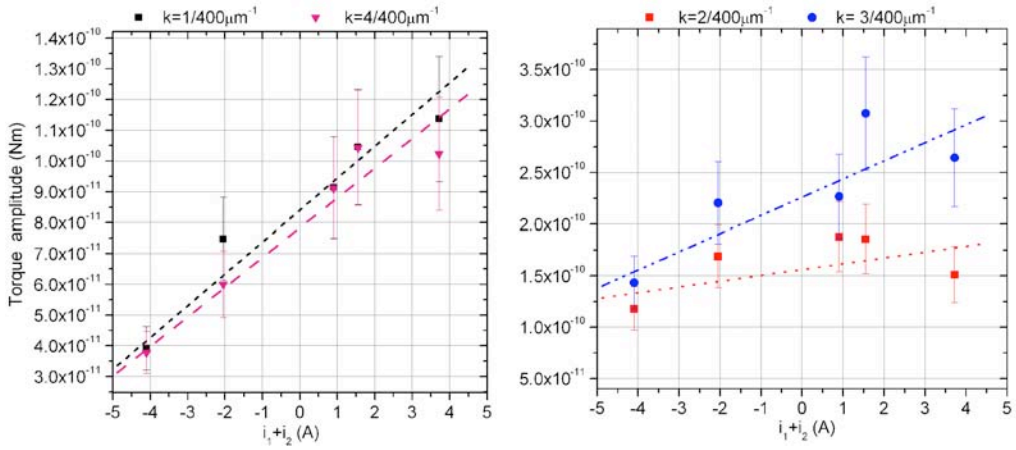

Figure 8.14: *I* run: spectral amplitudes at different k versus the change of the sum of the actuator currents and their relative linear fit.

Fit to $\Gamma_{eff} = A + B\,(i_1 + i_2)$		
k (μm^{-1})	A $(10^{-12} Nm)$	B $(10^{-12} Nm/A)$
1/400	84 ± 7	10 ± 2
2/400	160 ± 10	5.6 ± 4
3/400	226 ± 20	18 ± 6
4/400	78 ± 6.6	9.6 ± 2

Table 8.4: Result of a linear fits of fig.8.14

8.5 Torque results of the II run

In this section I will present the results relative to the ISL tests of gravity at micrometre distances, which we obtained with the flat mass C and the new curved mass B (see chapter 2) during the "II run". The mass B with respect to the mass A of the "I run" had a surface quality, which had been greatly improved with respect to the previous one. It was successfully polished and covered by the gold layer.

I will see how with these test masses we performed torque scans down to a minimum distance D_y of $3\mu m$ without considering the surface roughness of the masses. With these masses we found a torque signal above the noise level which showed a spectral component just at the spatial frequency $k_0 = 1/400\mu m^{-1}$. I will show how this signal was smaller than the one measured during the I run because its largest k_0 spectral amplitude was equal to $1.91 \times 10^{-11} \pm 4.7 \times 10^{-12} Nm$ at a distance of $D_y = 5.4\mu m$. Because the torque noise of the SSTB was the same during both runs, it took longer time to integrate the signal above the noise level during the II run with respect to the previous run and it was much more difficult and time consuming to fully characterise it. I will show that even though we had a reduced number of torque measurements, we were still able to measure a possible dependence of the signal on the distance, D_y. I will also discuss how we were able to modify but not cancel the signal spectral amplitude by changing the voltage applied to the flat mass. We had not found any clear dependence of the measured signal on the magnetic field, B_0, which was directly applied to the masses through a dedicated coil (see chapter 4).

8.5.1 Torques versus distance

Even if during the II run the signal was close to the noise level such that it was not clearly visible in the space domain (see for example in fig.8.15), we studied the

possible dependence of the spectral amplitude at $k_0 = 1/400\mu m^{-1}$ versus the distance D_y between the masses. We performed a number of scans at each distance, respectively 8, 11, 17 and 23 scans for the distances 4.5, 5.4, 7.3 and $10.4\mu m$. I coherently averaged the torque measurements for each distance (see fig.8.16). During these scans the voltage difference between the masses was cancelled up to few mV. By plotting the k_0 spectral amplitude versus D_y (fig.8.17), we had not found a clear trend of the data. The signal increased with the decrease of the distance D_y down to $D_y = 5.4\mu m$ where it was $1.91\times10^{-11}\pm4.7\times10^{-12}Nm$. It became smaller at a shorter distance, because it was $8.8\times10^{-12}\pm4.6\times10^{-12}Nm$ at a distance of $4.5\mu m$. During the II run we were also able to take three torque scans at the distance of $3\mu m$ finding a torque amplitude of $1.28\times10^{-11}\pm4.3\times10^{-12}Nm$. During these torque scans at $D_y = 3\mu m$ the voltage difference between the masses was not fully cancelled but was $0.148V$. Further investigation of the found signals are necessary once the torque sensitivity of torsion balance is improved.

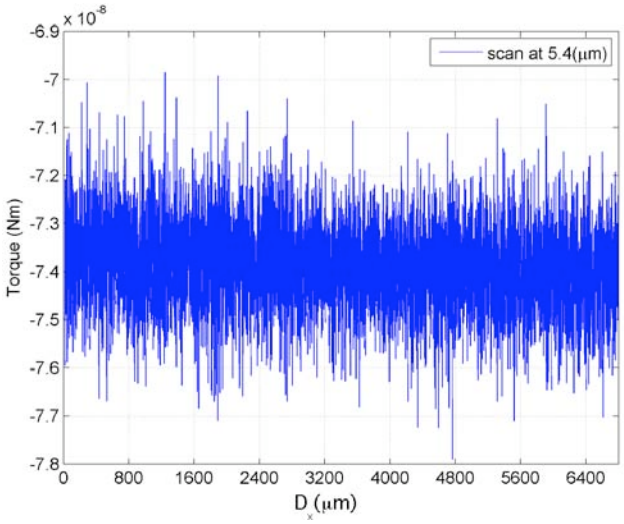

Figure 8.15: Example of the measured torque versus the D_x position of the flat mass at the distance $D_y = 5.4\mu m$.

8.5.2 Torque versus applied voltage

At the distance D_y of $6\mu m$ we took a series of torque scans versus the voltage, V_{daq}, that we applied to the flat mass: 16 scans with $0.153V$, 9 scans with $0V$ and 11 scans with $-0.3V$. After these scans, the superconducting circuits of the SSTB became normal and we had to refill the cryostat of the liquid helium and

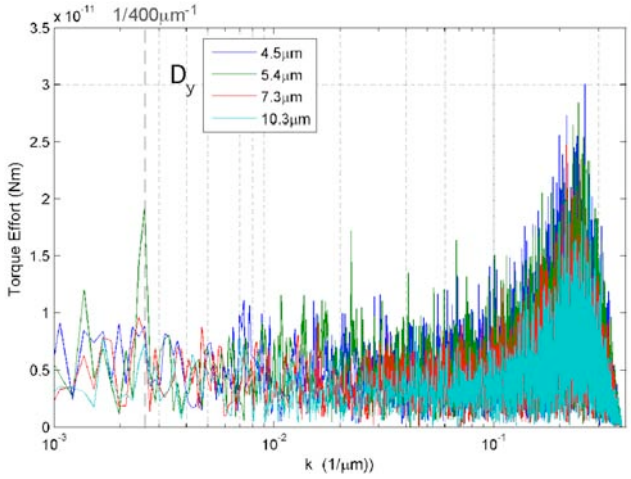

Figure 8.16: II run: amplitude spectrum of the measured signal versus the distance D_y between the masses.

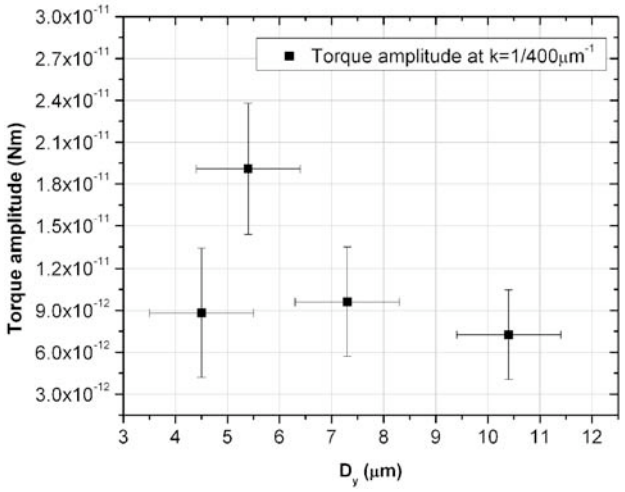

Figure 8.17: II run: spectral amplitude at $k = 1/400\mu m^{-1}$ versus the distance D_y between the masses.

restore the actuator and levitation currents. We could not take other torque measurements with higher applied voltages to be directly compared with the one we had already measured. Because of the lost of the levitation we could not complete the torque calibration of the servo effort for the taken torque scans, which I present as Volts and not Nm. I analysed the averaged spectrum of these scans as plotted in fig.8.18 and plotted their spectral amplitudes at $k_0 = 1/400\mu m^{-1}$ versus V_{daq} in fig.8.19. I fit the amplitudes with second order polynomials (see table 8.5). I found that even though we were able to modify the signal amplitude by applying a voltage to the flat mass we could not cancel it. The voltage offset, $V_0 = 147mV$, which minimised the k_0 spectral amplitude, was found compatible with the voltage difference, $V_0 = 151 \pm 6mV$, we measured between the masses according to the procedure described in section 8.2.

In another data set, which after the He fill was calibrated in Nm and which was taken at a similar distance with respect to the previous scans, we found that with $V_{daq} = -3V$ the measured spectral amplitude at k_0 was $3.1 \times 10^{-11} \pm 7.4 \times 10^{-12} Nm$. With $V_{daq} = 0.144V$ the k_0 amplitude was $3.9 \times 10^{-12} \pm 4 \times 10^{-12} Nm$ which was within the measured torque noise of the SSTB. I will discuss in the next chapter which are the implications of these torque measurements under the assumptions of the expected electrostatic forces I modelled in section 3.3

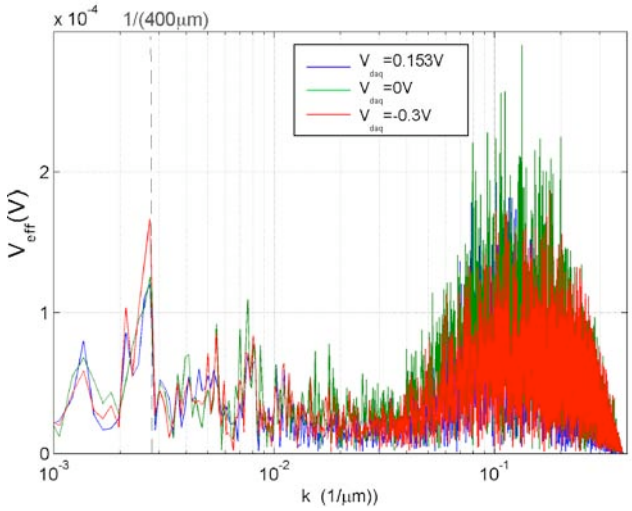

Figure 8.18: II run: amplitude spectrum of the servo effort versus the voltage V_{daq} applied to the flat mass

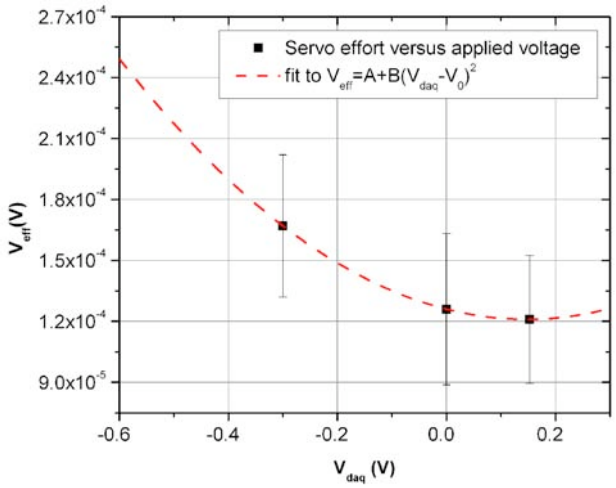

Figure 8.19: II run: torque effort spectral amplitude at $k = 1/400\mu m^{-1}$ versus the voltage applied to the flat mass.

Fit to $V_{eff} = A + B\,(V_{daq} - V_0)^2$			
$k\ (\mu m^{-1})$	$A\ (V)$	$B\ (V^{-1})$	$V_0\ (mV)$
$1/400$	1.2×10^{-4}	2.3×10^{-3}	147

Table 8.5: Result of fit to a second order polynomial of fig.8.19

8.5.3 Torques versus applied magnetic field

We performed a few sets of torque scans versus the magnetic field, B_0, which we applied to the surfaces of the masses by using a superconducting coil wounded around the support of the flat mass as described in chapter 4. The scans were performed at a distance of $D_y = 6.2\mu m$. The voltage difference between them was cancelled up to a few mV. In fig.8.20 I plotted the torque spectral amplitude at k_0 versus the magnetic field B_0, which was varied between 0 and $8.4\mu T$. As shown in table 8.6 the fitted gradient of the measured torque versus the applied magnetic field had been found compatible with zero. In the following chapter I will compare this result with the one, which were obtained during the I run.

Fit to $\Gamma_{eff} = a + c \cdot B_0$		
$k\ (\mu m^{-1})$	$a\ (Nm)$	$c\ (Nm/\mu T)$
$1/400$	$3.9 \times 10^{-12} \pm 3.6 \times 10^{-12}$	$4 \times 10^{-13} \pm 6.7 \times 10^{-13}$

Table 8.6: Result of the linear fit of fig.8.20

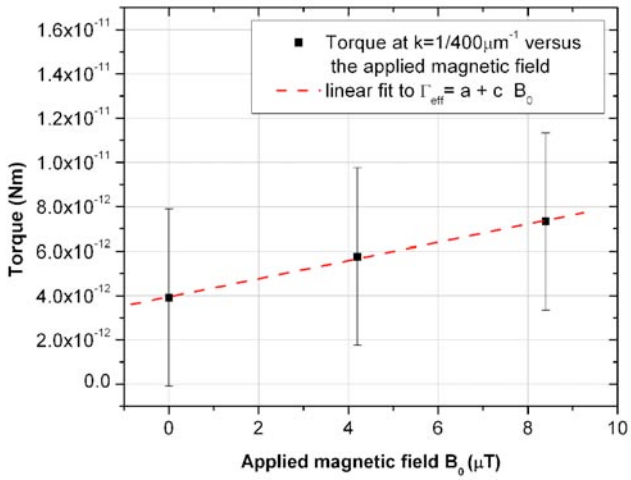

Figure 8.20: II run: spectral amplitude at $k = 1/400\mu m^{-1}$ versus the magnetic field, which was applied to the surface of the test mass.

8.6 Conclusion

In this chapter I presented all the experimental results, which we obtained during our first tests of the ISL of gravity at micrometre distances with our prototypes of the test masses. I reviewed all the procedures, which we defined to set up the instrument before the torque measurements. I discussed the alignment of the test masses, the calibration of the absolute distance between them, the cancellation of their voltage difference and the measurement of the misalignment angle, Ω, between the x motion of the flat mass and its surface. We aligned the test masses within an error of few tenth of $mrad$, estimated the distance between them with an average error of $1\mu m$ and cancelled the voltage difference between them within few tens of mV. The misalignment angle, Ω, was found to be on average $0.22°$. In this chapter I presented the torque results, which we took during two separate runs of the ISL tests of gravity. During both runs we used the same flat mass, but during the I run we used the curved mass A, while during the II run we used the much improved test mass B. During these experimental runs to test the ISL of gravity at micrometre distances, we measured periodic signals above the noise level of the SSTB. During the I run the measured signal was characterised by spectral amplitudes above the noise level at four spatial frequencies, which were even and odd harmonics of $1/400\mu m^{-1}$. The signal, which we measured during the II run, had only one spectral component above the noise at $k_0 = 1/400\mu m^{-1}$.

The signal of the I run had a k_0 spectral amplitude, which was $8.4 \times 10^{-11} \pm$

$1.5 \times 10^{-11} Nm$ at the distance D_y between the masses of $13 \mu m$, while the signal of the II run had a k_0 amplitude of $1.91 \times 10^{-11} \pm 4.7 \times 10^{-12} Nm$ at the distance $D_y = 5.4 \mu m$. During the II run we took torque measurements down to a minimum distance between the masses of $D_y = 3 \mu m$. However this distance D_y does not include the roughness of the surfaces of the test masses, which have standard deviations between 4 and $14 \mu m$. The spectral amplitudes of the signal, which we found during the I run, decreased with the increase of the distance between the masses. Such decay was not fully confirmed for the small signal of the II run.

During both runs we increased the signal amplitude by applying a voltage difference, V_{daq}, between the masses. The induced variation of almost all the spectral amplitudes of the signal of the I run followed a second order polynomial in the applied voltage. However the amplitude of the II harmonics at $2/400 \mu m^{-1}$ of the I run showed a linear dependence on V_{daq}.

During the I run we also found a correlation between the signal spectral amplitudes and the sum of the currents, which were stored in the actuator circuits. This result indicates a coupling between the measured torque and the magnetic field, which was generated by the actuator coils. In the II run we applied a magnetic field directly to the test masses but, within the errors of the torque measurements, we did not confirm the result of the I run. Because the signal found during the II run had low SNR, further experimental investigations are necessary to better characterise such signal, once the torque sensitivity of the SSTB will be improved.

The interpretation of the measured signals according to our theoretical models of the torques, which are acting between the test masses, will be discussed in the next chapter.

Chapter 9

Analysis of the results of the ISL tests

9.1 Introduction

In this chapter I will compare the torque results of our first experimental tests of the ISL of gravity with the models, which I developed to describe the expected torques acting between our masses (see chapter 3). By doing this I will try to understand the origins of the measured torques. In fact even though the measured torque sensitivity of the torsion balance did not let us explore new Yukawa type deviations from the ISL of gravity, we were able to characterise the torques, which were acting between the masses. We experimentally discriminated between the different components of the measured torques (electrostatic or magnetic) with the scope to further reduce them or at least to confidently fit them out of the original data. I will also show how the electrostatic torques, which were due to periodic surface corrugations, had been very useful during the ISL test, because they make possible to estimate the phase of all the measured signals. I will also show how the upper limits on the Yukawa type deviations, which were set by the results of the I run, were better than the ones given by the results of the II run. This difference in the upper limits was due to the high SNR of the signals of the I run.

9.2 Possible origins of the measured torques

I proceed now to analyse the torque results we obtained during our first experimental runs with the prototypes of test masses A, B and C (see chapter 2). I will show how test mass A, which was not uniformly covered by a gold layer but instead by a silver paint, let us investigate which forces acted between the masses and which strategies we should adopt to reduce them. Because I am interested here more in the study of the measured torques than in setting a rigorous upper limit on the Yukawa forces (which have already been excluded - see chapter 1), in the following section, I will make some simplifications about the test mass geometries and their relative motion. A complete analysis of the measured torques should also take into account the non-ideal topographies of the test masses (see chapter 2) and the change of the distance D_y as a function of the lateral motion D_x. However I will consider the test masses as ideally flat and cylindrical and at a constant relative distance, which I will estimate from the torque signals and/or from the performed CMM measurements (see chapter 2). Even though in the previous chapter I made a full spectral analysis of the torque measurements, estimating all their spectral harmonics, in the following analysis I will primarily study the amplitude of the main harmonic at the spatial frequency - $k_0 = 1/400\mu m^{-1}$- of the density modulation.

9.2.1 Torques from the I run

I will start by looking at the torque results, which were obtained with the mass prototypes A and C during the "I run".

Dependence on the distance D_y

To investigate the origin of the measured k_0 amplitudes I analysed how the torque signal changes versus the distance D_y between the masses. It was possible to fit many possible functions to the experimental data of fig.8.9 (see table 3.4): the exponential decay associated with Yukawa type forces, the decay due to the contrast in magnetic susceptibility, the decays associated with the electrostatic forces due to an uniform potential difference, periodic surface potentials and/or corrugations (see chapter 3 table 3.4). However only the fit, which was associated with the $1/D_y^{5/2}$ decay, predicts a distance offset D_{y0} between the masses (see

fig.9.1 and table 9.1) which is consistent with their measured topographies (see section 2.3 and table 2.1). The estimated D_{y0} from the $1/D_y^{5/2}$ fit is $\approx -23 \pm 2\mu m$ while the average distance between the masses, which is expected from the CMM measurements and which is given by the sum of their average depths (see chapter 2 and table 2.1), is $29 \pm 14\mu m$.

From the theoretical models of chapter 3, I know that the k_0 torque, which is associated with the $1/D_y^{5/2}$ decay, is related to the presence of periodic surface corrugations and a voltage difference between the masses and/or to the coupling between unscreened contact potentials and surface corrugations. By applying a voltage difference between the masses we were able to discriminate between these two kinds of torques, because it is possible to cancel only the first torque by applying the appropriate voltage (see chapter 3). During the I run we were not able to cancel the measured torque signal by applying a voltage difference, so I deduced that unscreened contact potentials were present at least on one of the masses. I assume that the measured k_0 corrugation amplitude of the flat mass is $0.6\mu m$ (see section 2.3) and that there are unscreened contact potentials only on the curved mass. From the gradient α of table 9.1 and from eq.3.64, the theoretical model predicts that the amplitude of the contact potentials is $\pm 6.8V$. This voltage value is large with respect to the contact potential expected between gold and aluminium ($\approx 1.5V$ see section 3.3). Therefore other electrostatic forces, which I had not yet modelled, must be present and influencing the result.

The presence of an uncomprehended electrostatic force is also suggested by the second harmonic of the torque signal, k_1. Its amplitude decays with distance as $1/D_y^{5/2}$ (see fig.9.2 and table 9.1) as expected from eq.3.65. If I assume that a periodic contact potential is present only on the surface of the curved mass, it is possible to estimate its voltage amplitude from eq.3.65 and from the parameter A of the fit of the k_1 amplitude versus the distance between the masses (see table 9.1). The theoretical model predicts that this voltage amplitude is $\approx \pm 40V$ which is too large for a contact potential.

Even the electrostatic torque associated with the $1/D_y^{5/2}$ decay can not fully explain the magnitude of the k_0 measured torque, because of the fitted torque offset, $-4.5 \times 10^{-12} Nm$ (B in the table 9.1). In the following sections I will see that this torque offset may have a magnetic origin. I will consider this residual torque as the limiting torque for the I run when I will estimate the upper limits on the Yukawa forces (see section 9.3).

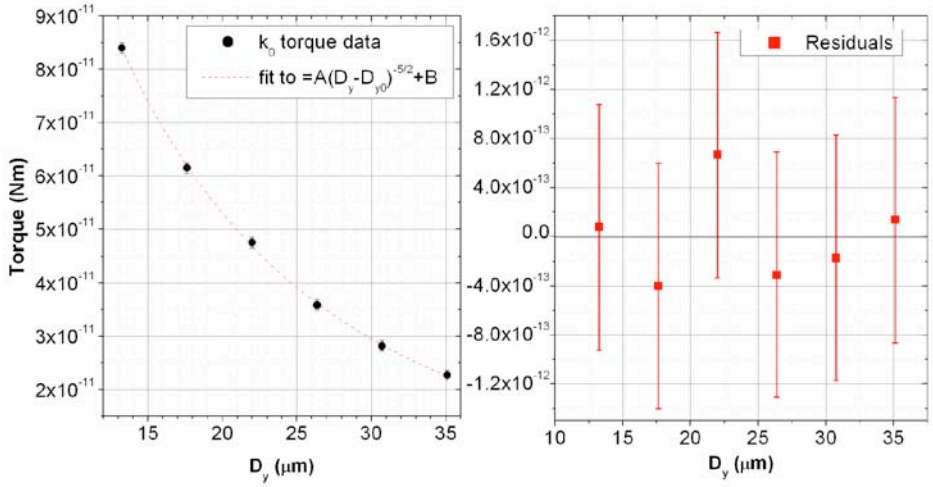

Figure 9.1: I run: torque amplitude of the $1/400\mu m^{-1}$ signal versus the measured distance between the masses and fit to the $D_y^{-5/2}$ decay. On the right the residuals of the fit.

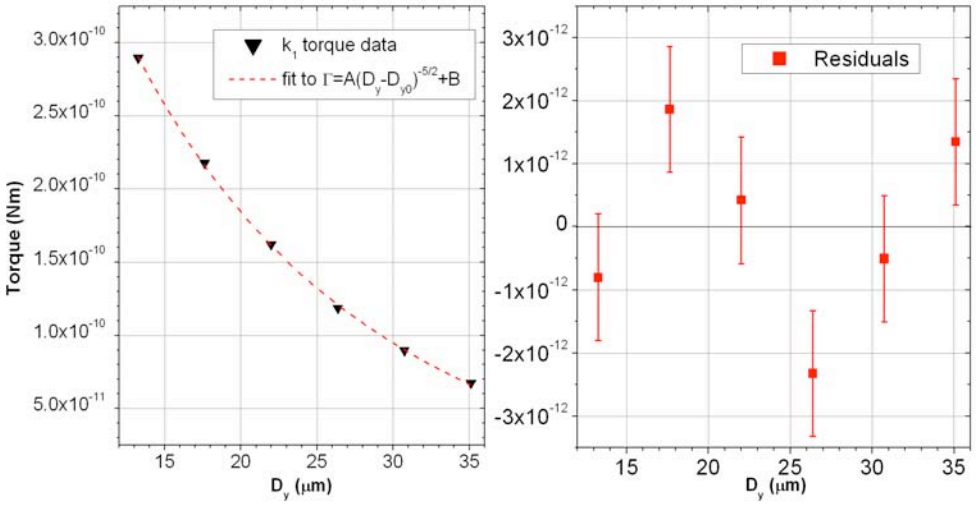

Figure 9.2: I run: torque amplitude of the $2/400\mu m^{-1}$ signal versus the measured distance between the masses and fit to the $D_y^{-5/2}$ decay. On the right the residuals of the fit.

Fitted function: $\Gamma_{eff} = A(D_y - D_{y0})^{-5/2} + B$			
	D_{y0} (μm)	A $(Nm \times \mu m^{5/2})$	B (Nm)
k_0	-22.7 ± 1.8	$6.8 \times 10^{-7} \pm 10^{-7}$	$-4.5 \times 10^{-12} \pm 2.2 \times 10^{-12}$
k_1	-30.2 ± 2.7	$4.4 \times 10^{-6} \pm 8 \times 10^{-7}$	$-6.0 \times 10^{-11} \pm 1.2 \times 10^{-11}$

Table 9.1: I run: fit results of fig.9.1 and 9.2

Dependence on the applied voltage

The presence of surface corrugations on the test masses was further confirmed by the measurements of the torque signal versus the voltage which was applied to the masses, V_{daq}. The k_0 torque amplitude is well fitted by a second order polynomial in V_{daq} (see fig.8.12) as expected from eq.3.45 (section 3.3). From the coefficient $d\Gamma_{eff}/dV_{daq}^2 = 2.9 \times 10^{-13} Nm/V^2$ of the fit (see table 8.2) and assuming an estimated distance, d_y, between the masses of $52.7 \pm 14\mu m$ ($D_y = 24\mu m$ plus the estimated offset $D_{y0} = 28.7 \pm 14\mu m$ from table 2.1) I found an average corrugation amplitude of $0.3 \pm 0.1\mu m$. From the CMM measurements I expected a geometric average of $0.6\mu m$ (see section 2.3).

During the tests with the applied voltages, V_{daq}, the k_0 torque was minimised for $V_{daq} = -3.5V$ while we independently estimated (see section 8.2.4) that the voltage difference between the masses, V_0, was $-0.16V$. According to eq.3.67 of section 3.3 this discrepancy between the voltage estimates is associated to the presence, on the surface of one mass, of periodic contact potentials, which were coupled with periodic corrugations of the surface of the other one. In this case, according to eq.3.67 and given the measured k_0 amplitude of the surface corrugations of the mass C (see section 2.3 and table 2.1), the theoretical model predicts that voltage amplitude of the contact potentials on the curved mass A is $\pm 85mV$.

The torque measurements versus the applied voltages also pose a number of problems: firstly we found that the measured amplitude of the second harmonic, k_1, linearly changed with the applied voltage, suggesting the presence of an additional uncomprehended electrostatic force. Secondly the torque measurements associated with the applied voltages, which we took at the beginning of the I run, showed larger amplitudes than the torque measurements, which were taken in the subsequent phases of the experiment after a few He fills. However it seems that all these issues were associated with test mass A, because they were not present in the data of II run during which the said mass was substituted with the improved mass B (see chapter 2).

Dependence on applied magnetic field

I now consider the dependence of the measured torque on the magnetic field, which was incident on the test masses. In fig.8.14 I showed that it was possible to

fit the k_0 amplitude by a linear function on the sum of the currents i_1 and i_2 which were stored in the actuator circuit. This change of the torque amplitude could not be attributed to an error associated with a multiplicative constant on the torque calibration: in that case the calibrated torque would have differed from the real one just by a multiplicative factor, which was independent from the stored currents. Therefore the change of the amplitude torque, which was associated with k_0, versus $i_1 + i_2$ is a real effect. I can say that the test masses are mostly influenced by the magnetic field produced by one coil only. The magnetic field of this coil directly leaked to the back of the support of the curved mass through a window cut of the float shell. Because at this stage of the analysis I do not know which coil was responsible for the field reaching the test masses, in fig.9.3 I plotted the k_0 amplitude versus each of the currents stored in the actuator circuits and fitted the data with second order polynomials. Because, from the results of table 9.2, the measured torques versus the current i_1 showed the best fit with the expected function, I assume that the magnetic field reaching the test masses is simply the one from the coil associated with this current. Fig.9.3 and table 9.2 show that the torque amplitude depended on the square of the applied magnetic field as expected from eq.3.72. However I cannot attribute this torque change to the torque, which is due by the contrast in magnetic susceptibilities of chapter 3, because its sign (see C of table 9.2) is opposite to what is expected. Eq.3.72 shows that the para/diamagnetic torque has the same phase of the electrostatic torque, which is due to the surface corrugations and a voltage difference applied between the masses. If it is possible to increase the torque signal by applying a voltage to the masses because of the electrostatic forces due to the corrugations, in the case the magnetic torque is due to the para/diamagnetism, it should also be possible to increase the torque by applying a magnetic field to the masses. However, this result is the opposite of what we actually measured (see table 9.2 and fig.9.3).

The fitted torque also had the same sign of the residual torque of fig.9.1 and table 9.1, which suggests a possible common magnetic origin. Ferromagnetic impurities left by the manufacturing process over the gold/aluminium stripes can in principle cause a torque, which is dependent on the applied magnetic field. However a dedicated analysis of this magnetic torque has yet to be developed in order to confirm or either exclude this hypothesis against the measurement.

A conservative estimate of the magnetic field versus the current, which is

$\Gamma_{eff} = A + C(I - I_0)^2$			
	$A\ (10^{-10}Nm)$	$C\ (10^{-12}Nm/A^2)$	$I_0\ (A)$
i_1	1.14 ± 0.05	-3.9 ± 0.9	2.23 ± 0.6
i_2	1.1 ± 0.2	-2.7 ± 2.7	3.2 ± 3.3

Table 9.2: I run: table showing the results of the fit to a second order polynomial of fig.9.3

stored in one actuator coil, is $dB_0/di \approx 20 - 40\mu T/A$ (I obtained this result by modelling the coil as a classic solenoid). From the fit associated with i_1 of table 9.2 , I derived that $d\Gamma_{eff}/di_1 = 1.7 \times 10^{-11} Nm/A$ at $i_1 = 0$. Therefore, from the previous estimate of dB_0/di, I obtained the gradient:

$$d\Gamma_{eff}/dB_0 \approx 4 - 9 \times 10^{-13} Nm/\mu T \tag{9.1}$$

This value is the gradient of the measured torque versus the magnetic field, which was applied to the masses, at $B_0 = 0$.

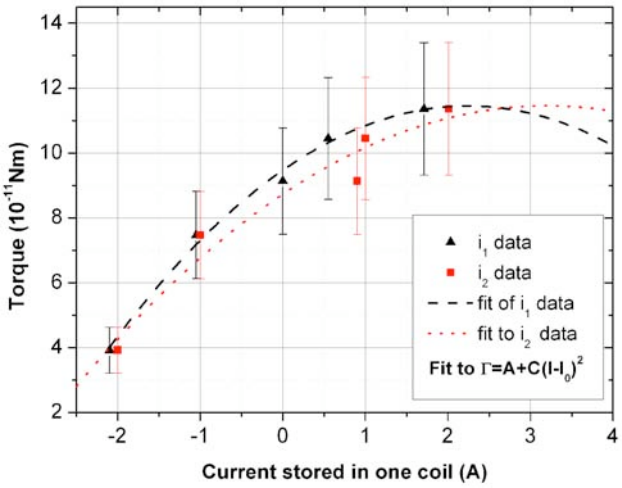

Figure 9.3: I run: torque amplitude of the $1/400\mu m^{-1}$signal versus each of the current, which were stored in the actuator circuit.

9.2.2 Torques from the II run

The torque measurements of the II run, which were performed with masses B and C showed a great reduction of the signal measured at the spatial frequency k_0. Moreover all the higher harmonics of k_0 were absent above the noise level. However, because the torque signal had a low signal-to-noise ratio, it was very

difficult and time-consuming to measure and characterise it. A measurement of the torque amplitude that in the I run took only one hour to be completed, during the II run took between the 10 and 20 hours depending on the distance d_y between the masses. The necessary helium fills and the associated setting-up procedures were present between different torque measurements, and made more difficult to compare their results than during the I run. Eventually to further investigate the origin of the measured torques with these masses, additional tests will be required once the torque sensitivity of the torsion balance has been improved.

Dependence on distance D_y

Due to the small number of the torque measurements versus the distance, D_y, of fig.8.17 I cannot fit any possible decay to the data set and thus measure the offset distance between the masses, D_{y0}, which was due to the surface roughness, as done for the I run. From the CMM measurements of chapter 2 I assume an average distance offset between the masses of $25 \pm 10\mu m$.

Dependence on applied voltage

As in the previous run, we were able to modify but not cancel out the measured torque by applying a voltage difference between the masses (see fig.8.19). The possible dependence of the induced torque on the square of the applied voltage suggests the presence of the electrostatic torque due to periodic surface corrugations on the test masses. In this case the measured increase of the torque, which was obtained by applying $3V$ on the test masses, implies the presence of a corrugation amplitudes of $0.4 \pm 0.2\mu m$. From the CMM measurements I expected $0.46\mu m$. Moreover, the voltage which minimised the torque amplitude, $V_{daq} = 147mV$, was compatible with the weighted average, $151 \pm 7mV$, of all the voltage difference estimates, which were performed during the II run (see section 8.2.4).

Dependence on applied magnetic field

During the II run, we directly applied a magnetic field up to $8.4\mu T$ to the surfaces of test masses through a dedicated coil (see chapter 4). We found that the dependence of the measured torque to the magnetic field was compatible with zero within the errors, being $d\Gamma_{eff}/dB_0 = 4 \times 10^{-13} \pm 7 \times 10^{-13} Nm/\mu T$ (see table

8.6). By comparing this result with the one of the I run of eq.9.1, I found that the null result of the II run did not completely exclude the magnetic torque, we measured during the I run. Both measurements of $d\Gamma_{eff}/dB_0$ are compatible within the errors.

9.2.3 Torque summary

In the following section I will summarise which torque signals I think we observed during the first two experimental runs with the SSTB, and the prototypes of the masses to test the ISL of gravity at micrometre distances.

Electrostatic torque due to periodic surface corrugations

This torque, which in tables 9.3 and 9.4 I called Γ_{cor}, is due to the electrostatic forces acting between the masses because of the periodic surface corrugations and an applied voltage difference. During the I run Γ_{cor} was present in the raw torque measurements, because, as shown in table 9.3, we were able to change the k_0 torque amplitude by applying a voltage difference between the masses, V_{daq}. The induced change was found to be proportional to V_{daq}^2 as I expected from eq.3.45. From the results of the I run, the estimated average amplitude corrugation was $0.3 \pm 0.1 \mu m$, half the expected value from the CMM measurements. The experimental data of the II run, even though it bears a reduced significance due to the low SNR, confirms the presence of this electrostatic torque. The estimate of the corrugation amplitude obtained during the II run, $0.4 \pm 0.2 \mu m$, is compatible with the CMM measurements of table 2.1.

Electrostatic torques due to periodic surface potentials on both masses

This torque, which in tables 9.3 and 9.4 I call Γ_{cpt}, is given by the electrostatic forces due to periodic contact potentials on the surface of both test masses (see section 3.3). During the I and II runs we did not find any evidence of Γ_{cpt} because the typical $D_y^{-1/2}$ decay of its k_0 amplitude was not measured.

Electrostatic torques due to periodic surface corrugations and at least one periodic surface potential

This torque, which in tables 9.3 and 9.4 I call Γ_{cor+pt}, is associated with the presence of both periodic surface potentials and periodic surface corrugations on

the surface of the masses. There is some evidence to suggest the presence of this kind of torque in the data, which was collected during the I run. Firstly the k_0 torque amplitude decayed with distance as $1/D_y^{5/2}$ as expected from eq.3.64 and it was not possible to cancel it by applying a voltage, V_{daq}, to the masses. Secondly by modifying the voltage - V_{daq} - applied to the masses, the k_0 torque was minimised at a voltage which was larger than the direct estimate of voltage difference between the masses. This discrepancy is predicted in the presence of both periodic corrugations and contact potentials over the masses by eq.3.67. However, assuming that the periodic potentials were on only one mass, the two estimates of the amplitudes of the contact potentials obtained from eq.3.64 and 3.67 are not in agreement, being respectively $68mV$ and $6.8V$. The presence of another electrostatic torque, for example due to trapped charges, may be the cause of this discrepancy.

There is no evidence that this kind of torque was present during the II run because the second harmonic at the spatial frequency $k_1 = 1/200\mu m^{-1}$ was absent above the noise level.

Magnetic torques due to contrast in magnetic susceptibilities

I named this kind of torque $\Gamma_{\Delta\chi}$ in table 9.3 and 9.4 and it is associated with the presence of a contrast in the magnetic susceptibilities of the gold and aluminium stripes. During the I run we found a dependence of the measured torque on the applied magnetic field as expected from eq.3.72 but the sign of this magnetic torque was opposite to what it is expected from its analytical model (see section 3.5). Therefore the torque due to a periodic contrast in the magnetic susceptibilities was not the origin of the measured magnetic component of the torque.

During the II run we found no evidence of any dependence of the measured signal on the applied magnetic field. However, due to the smaller magnetic fields, which was applied to the mass, with respect to the I test, this null result does not rule out the presence of the magnetic torque we previously found.

Other torques

Other electrostatic torques, which I had not yet modelled, were present in the torque measurements of the I run. These uncomprehended torques are respons-

ible for the linear dependence of the k_1 signal on the applied voltage V_{daq}, and for the change of the k_0 amplitude during the different measurements of the I run. These spurious torques, which may be related to trapped charges, must to be attributed to the particular conditions of test mass A, which was covered by a silver conductive paint and not by a gold layer. There is no evidence of the presence of such electrostatic signal within the torque measurements, which were taken during the II run and which were obtained with the improved test mass B.

An unexpected magnetic torque was measured during the I run and was not fully excluded by the measurements of the II run. It may be related to ferromagnetic impurities which might have been deposited within the gold/aluminium stripes during the manufacturing process. However, this hypothesis has still to be fully studied and verified against the measurements.

I **run**	Γ_{cor}	Γ_{cpt}	Γ_{cor+pt}	$\Gamma_{\Delta\chi}$
k_0	$+$	$(-)$	$+$ YES $(+)$	$-$ NO $(+)$
k_1	(0)	(0)	?$(\pm)$	(0)
$\mathbf{f}(d_y)$	YES $(d_y^{-5/2})$	NO $(d_y^{-1/2})$	YES $(d_y^{-5/2}\ k_0)$ YES $(d_y^{-5/2}\ k_1)$	? (≈constant)
$\mathbf{f}(V_{daq})$	YES (V_{daq}^2)	(no)	YES (V_{daq})	(no)
$\mathbf{f}(B_0^2)$	(no)	(no)	(no)	YES (B_0^2)
Conclusion	found	not found	found?	not found

Table 9.3: Comparison of the measured torques of the I run with the modelled signals, whose expected properties are shown in parentheses.

II **run**	Γ_{cor}	Γ_{cpt}	Γ_{cor+pt}	$\Gamma_{\Delta\chi}$
k_0	$+$	$(-)$	$(\pm)$	NO $(+)$
k_1	0 (0)	0 (0)	NO $(\pm)$	0 (0)
$\mathbf{f}(d_y)$	? $(d_y^{-5/2})$	? $(d_y^{-1/2})$	? $(d_y^{-5/2}\ k_0)$ NO$(d_y^{-5/2}\ k_1)$	? (≈constant)
$\mathbf{f}(V_{daq})$	YES (V_{daq}^2)	(no)	NO (V_{daq})	(no)
$\mathbf{f}(B_0^2)$	(no)	(no)	(no)	NO (B_0^2)
Conclusion	found	not found	not found	not found

Table 9.4: Comparison of the measured torques of the II run with the modelled signals, whose expected properties are shown in parentheses.

9.3 Explored strengths for Yukawa type forces

Following the approach, which was defined in section 3.6, I now set upper limits on the possible (or already excluded) Yukawa type deviations to the ISL of gravity. Again, this analysis has more a propaedeutic goal than the scope of setting the most rigorous upper limits possible. While a rigorous analysis should take into account the particular topographies of the test masses and the change of d_y versus d_x, for the sake of simplicity I here consider the masses to be perfectly flat or cylindrical and at a constant relative distance. In fig.9.4 I plot the upper limits on (α, λ) for three different scenarios:

1. The upper limit, which is given by the I run after I subtracted the $1/d_y^{5/2}$ decay from the measured data. I assumed that the measurements were limited by the torque offset of $-4.5\times10^{-12}\pm2.2\times10^{-12}Nm$ at the minimum total distance $d_y = 42 \pm 14\mu m$.

2. The possible upper limit given by the measured signal during the II run $1.9 \times 10^{-11} \pm 5 \times 10^{-12}Nm$ at the total distance $d_y = 31 \pm 10\mu m$.

3. The potential upper limit I will be able set on (α, λ) plot, given the present torque sensitivity of the torsion balance, $2 \times 10^{-10}Nm/\sqrt{Hz}$, at the minimum reached total distance, $d_y \approx 30\mu m$ and for a nominal integration time of 1 day. For example during the II run we took torque measurements for a total of ≈ 4.7 days of integration time.

From the third upper limit it is clear that to be able to explore not yet excluded regions of the possible Yukawa type deviations of the ISL we have to improve the torque sensitivity of the torsion balance and/or increase its duty cycle. However it is interesting to note that in principle with the prototypes of test masses of the I run I was able to set stronger upper limit than with the improved ones of the II run. Even though during the first ISL test we measured large signals above the noise level, because they had such a good SNR, I was able to effectively characterise their possible origins and to fit them out of the original data set. The standard deviations, which describe the surface roughness of the test masses, is currently larger than the minimum distance D_y which was reached between the masses. To increase the parameter region of the Yukawa type deviations, which we would like to explore during an ISL test, we would have to

reduce the long period corrugations of the test masses, which are responsible for the large standard deviations of the surface roughness.

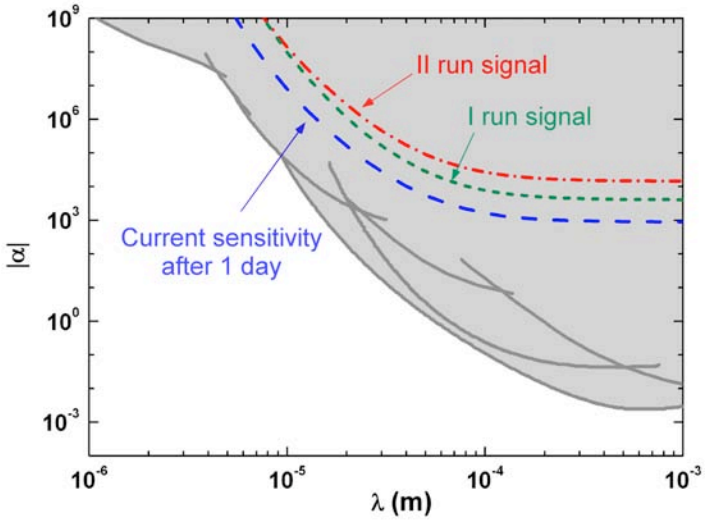

Figure 9.4: Upper limits to Yukawa type forces given the two experimental runs and the possible upper limit at 95% confidence level with the present torque sensitivity of the SSTB, after a nominal integration time of 1 day.

9.4 Conclusions

In this chapter I discussed the possible origins of the torque signals we measured during the first experimental tests of the ISL of gravity, which we performed with three prototypes of our test masses.

I showed that for the I run the torque signal at the spatial frequency of the density modulation was given by the sum of many different signals. The strongest component was given by the electrostatic torque, which was due to the coupling of periodic surface corrugations of one mass with periodic electrostatic potential on the surface of the other. The surface of mass A, because it was not well covered by an uniform layer of gold, presented the periodic surface potentials, which are given by the contact potentials of the gold and aluminium stripes. The torque, which was due to the coupling of the corrugations on both masses and the presence of a voltage difference between them, was also used to estimate the average amplitude of the corrugations. It was further adopted as a reference signal to establish the phase of the other measured signals. From the results of the I run the estimated average amplitude corrugation $\approx 0.3 \pm 0.1 \mu m$ was half the expected value from the CMM measurements of chapter 2. The decay, with the distance D_y, of the electrostatic torque at the main spatial frequency $1/400 \mu m^{-1}$ was used to fit a minimum distance - D_{y0}- between the masses, which was due to their surface roughness. From the data of the I run the fitted $D_{y0} \approx -23 \mu m$ was found to be compatible with the CMM measurements, which predicted $D_{y0} \approx -29 \pm 14 \mu m$.

During the I run we found evidence of the dependence of the measured torque on the magnetic field, which was applied to the masses by the actuator coils through a window cut in the float shell. However, the phase of the measured magnetic signal excludes the para/diamagnetic origin, which is related to the periodic contrast of the magnetic susceptibilities and which we modelled in chapter 3. The measured magnetic torque may be related to ferromagnetic impurities left by the manufacturing process over the masses, but this hypothesis has still to be fully investigated and verified.

The linear dependence of the second harmonic of the measured signal on the voltage, which was applied to the masses, also indicated the presence of another kind of electrostatic torque. However this signal, which has still to be fully understood, must be associated with the particular conditions of the test mass A. The presence of signal at the k_1 harmonic and its linear dependence on the

applied voltage was not found during the II run when we substituted the mass A with the improved mass B.

During the II run it was much more difficult and time consuming to characterise the torque measurements with respect to the I run, because the measured k_0 signal was weaker and had smaller SNR (the SSTB torque noise level was in fact unchanged). Because during the II run, at the second harmonic of the density modulation, $k_1 = 2/400\mu m^{-1}$, there was no signal above the noise level, I deduced that the surface contact potentials of test mass B were better screened with respect to mass A and that their associated torque was reduced below the SSTB noise level.

During the II run, by applying a voltage difference to the masses we confirmed the presence of periodic surface corrugations whose amplitude was $0.4 \pm 0.2\mu m$ and compatible with the CMM estimates. However, during the II run I could not fit the torque measurement versus the distance and therefore obtain the offset distance between the masses, D_{y0}. The associated CMM estimate was $-25 \pm 10\mu m$.

During the II test we found no evidence of the dependence of the measured torque on the applied magnetic field but, because of the smaller applied magnetic field with respect to the I run, I cannot exclude the presence of the magnetic signal which was detected during the I run.

Because the torque signal of the I run was stronger than the one measured during the II run, I was able to better characterised it and subtracted the electrostatic signal, which was decaying as $D_y^{-5/2}$, from the original data-set. The upper limit on the Yukawa violations of the ISL of gravity which was obtained from the data of the I run, was therefore better than the one given by the data of the II run. However both upper limits were in the already excluded area of the Yukawa type violations. An improvement of torque sensitivity of the torsion balance is necessary to further characterise the torques, which were measured with the improved masses B and C, and to explore new possible violations of Newton's law of gravity.

Chapter 10

Overall conclusions

In the last few years many theories related to quantum gravity hypothesised new violations of the ISL of gravity at sub millimetre distances. In this PhD thesis I presented the experimental test of Newton's law of gravity at micrometre distances that we are developing at the School of Physics and Astronomy of the University of Birmingham. Our approach is based on a novel design of the sample masses and on the use of the spherical superconducting torsion balance (SSTB), which is magnetically levitated at $4.2K$ and which is currently in its second version. Another novel feature of our experimental approach is the lack of any electrostatic shield between the masses.

As shown in this thesis, during the last few years we studied, manufactured and characterised the first prototypes of the test masses for our ISL tests of gravity. To optimise the design of the geometry of these masses, I developed the analytical models of the gravitational and electromagnetic forces, which are acting between them. The Newtonian torque, which is due to the mass density modulations associated with the gold and aluminium stripes constituting the masses, is expected to be $8.7 \times 10^{-16} Nm$ at a distance of $15\mu m$ between the masses. For comparison the thermal noise of the torsion balance is $3.9 \times 10^{-15} Nm/\sqrt{Hz}$. I created the analytical models which describe the electrostatic forces due to possible periodic corrugations and/or unscreened contact potentials over the surface of the test masses. I found that, in the case where the contact potentials are properly screened by a uniform gold layer over the test masses, the electrostatic torques, which are due to periodic surface corrugations, will be the strongest signal we will measure. This signal is expected to be $5.67 \times 10^{-14} Nm$ for $50mV$ of voltage difference between the masses, an average corrugation amplitude of

$0.5\mu m$ and at a distance between the masses of $15\mu m$. I also presented the models for the weak torque due to the Casimir force, which are given by the periodic surface corrugations, and the torque due to the magnetic force, which is given by the periodic contrast of magnetic susceptibilities of the gold and aluminium stripes. I completed the modelling of expected torques by presenting the numerical models of the possible Yukawa forces which might violate the ISL of gravity at submillimetre distances.

This thesis was also dedicated to the analysis of the MKII SSTB, which was developed during the last few years to measure the Casimir force at $4.2K$ and to test the ISL of gravity at micrometre distances. A lot of work was dedicated toward the goal of defining an overall analytical model of the SSTB. This model predicts the expected torque sensitivity of the balance given all the known noise sources and help us to identify the necessary modifications to improve the instrument. I developed a full 3D model of the dynamics of the torsion balance, which, given the metrology of the float (for example its moments of inertia or its natural torsional stiffness), predicts the coupling of the float with all the components of the seismic noise (horizontal, vertical and tilt). I expect that the dominant contribution to the input torque noise, to which the float is subjected, is given by the direct coupling of the float with the tilt noise. This model predicts that, given some assumptions on the tilt seismic spectrum and on the tilt coupling of the float, the torque noise, which is given by the ground oscillations, is around $2.5 \times 10^{-13} Nm/\sqrt{Hz}$.

The MKII SSTB, with respect to its previous version, is based on a servo system which is adopted to keep the float at a constant angular position. To predict the transfer function between the torque, which is externally applied to float, and the feedback torque, which we measure, and to quantify the expected measured torque noise level, it was necessary to analyse the servo loop of the SSTB. I presented the analytical models of all the subsystems of the servo loop, like the capacitive readout, the digital PII^2D compensator and the magnetic actuator system. I characterised their open loop transfer functions and measured their noise spectra. I predicted the closed loop transfer function of the SSTB between the applied and measured torque and I found that, for $30 - 40s$ natural period of the torsion balance, the expected dominant torque noise is $5 \times 10^{-12} Nm/\sqrt{Hz}$. This theoretical noise limit is given by the the readout noise of the capacitive bridge. I found that if we are able to increase the natural period by a factor of

a few, we will easily reduce this noise contribution below the expected seismic torque noise. Thanks to the analytical model of the servo loop, I showed that the torque noise given by the current source is also greatly reduced by the feedback loop of the torsion balance.

The second part of this PhD thesis was dedicated to the presentation and discussion of the low temperature results we achieved with the SSTB and with the sample masses during the first tests of Newton's law of gravity.

I discussed the torque calibration protocol of the SSTB, which we defined during the ISL tests of gravity. I compared the measured performances of the SSTB with the associated theoretical predictions. We are able to damp down the parasitic modes of the SSTB by Eddy current dissipation as it was planned and to change the natural stiffness of the balance by modifying the current, which were stored in the actuator circuits as it was theoretically expected. We also measured the closed loop transfer function of the SSTB between the applied and measured torque, which at low frequencies is in agreement with the analytical model. I had indirect evidence of the reduction at low frequencies of the torque noise, which is given by the current source and which was cancelled out by the feedback loop. We also measured the additional torque offset, which was acting on the float and which we had to counterbalance by storing the appropriate currents in the actuator circuits. Because of these currents the maximum period of the torsion balance was limited to $\approx 30-40s$. This extra torque, which was also found during the Casimir tests, might be related to asymmetries of the float shell which couple with the levitation magnetic field. The torque noise level, we measured during the ISL tests, was $2 \times 10^{-10} Nm/\sqrt{Hz}$ at $30mHz$ and higher than the expected value. After some preliminary tests we found a large coupling of the measured torque with the ground tilt, $d\Gamma/d\theta_T = 8.77 \times 10^{-7} Nm/rad$, which may explain the origin of the torque noise. This tilt coupling might be due to magnetic flux trapped within the float, to asymmetries of the float shell itself or to magnetic impurities in the damper cylinder of the float.

In this PhD thesis I also discussed the first preliminary tests of Newton's law of gravity at micrometre distances, that we performed with the manufactured prototypes of the test masses. I discussed the procedures, we defined during these experiments, to set up the alignment of the masses within a few tenths of $mrad$, to calibrate their relative y distance within $1\mu m$ and to cancel the voltage difference between the masses within a few tens of mV. We measured

an unexpected misalignment angle between the x motion of the micropositioner and the surface of the test masses, which was found to be on average $0.22°$. As a consequence the D_y distance between the masses linearly varied with the D_x position of the flat mass. During these first ISL tests, we also found that we were able to take torque measurements down to a minimum distance between the masses of $D_y = 3\mu m$. This distance does not include the roughness of the surfaces of the masses, which had standard deviations between ≈ 4 and $\approx 10\mu m$. This minimum distance, which was reached thanks to the lack of any electrostatic screen between the masses and to the angular stability of the torsion balance ($4.4 \times 10^{-5} rad/\sqrt{Hz}$ at $30mHz$ for $40s$ natural period), is, to our knowledge, the smallest distance between masses, which had been reached during a test of the ISL of gravity.

The ISL tests with the prototypes of the test masses were very useful to check most of the expected torques acting between them and reveal new possible ones which might limit the sensitivity to violations of Newton's law. We successfully performed two experimental runs, which I called the I and II run, during which we measured periodic signals at the spatial frequency of the density modulation, k_0, (but not exclusively) with two combinations of the test masses. During the I run we used the flat mass C and the curved mass A, which was the first one to be manufactured, and which was not well covered by the gold layer but partially by a Silver paint. During the II run we substituted the mass A with the improved mass B, which was well covered by an uniform gold layer. The signal we measured during the I run was found to have a bigger amplitude and richer spectral components of the signal of the II run. While the signal of the first run had k_0 spectral component $8.4 \times 10^{-11} \pm 1.5 \times 10^{-11} Nm$ at the distance of $D_y = 13\mu m$, the signal of the II run was a few times smaller, being $1.91 \times 10^{-11} \pm 4.7 \times 10^{-12} Nm$ at the distance of $D_y = 5.4\mu m$. The signal of the I run had also other spectral components at higher harmonics of k_0, as $2k_0$, $3k_0$ and $4k_0$, which were above the noise level, while the signal of the II run had none.

It was possible to properly characterise the signal of the I run because of its high SNR. The measured torque was found to decrease with the increase of the distance D_y and to increase with the voltage, which was applied to the masses. We also measured a correlation between the measured torque and the currents, which were stored in the actuator circuits. This correlations indicates a coupling of the measured signal with the magnetic field of the actuator coils. In fact the

magnetic field from at least one coil was able to reach the masses through the windows cut in the float shell behind the support of the curved mass.

A improved torque sensitivity is instead necessary to fully characterise the signals we measured during the II run, which had lower SNR with respect to the ones of the I run.

Given the experimental evidence and the theoretical models of the expected torques, I think that the signal, we measured during the I run, is made of the sum of a few signals of different origins. The main component is the electrostatic torque, which is due to the coupling of the surface corrugations on the flat mass with the periodic contact potentials on the surface of the curved mass A because this mass was not well covered by the top gold layer. As expected from the theoretical model of this electrostatic torque, the k_0 signal was found to decrease with the distance D_y between the masses as $D_y^{-5/2}$ and we were not able to cancel it by applying a voltage difference to the masses.

We also found that we were able to excite the torque, which is due to the surface corrugations, by applying a voltage difference to the masses. We were able to use this signal as a reference to determine the phase of the other measured torques. A signal of magnetic origin was detected, because of its dependence on the applied magnetic field. This magnetic torque was not due to the contrast of magnetic susceptibilities, because of its opposite sign with respect to our analytical estimate. Perhaps ferromagnetic impurities left by the manufacture or by the polishing process on the masses might be the cause of this magnetic signal but further theoretical and experimental investigation is necessary to both confirm or either exclude such this hypothesis. During the I run we also measured a linear dependence of the second harmonic ($k_1 = 2k_0$) of the signal to the voltage, which was applied to the masses. The k_1 amplitude was also found to decrease with the distance D_y as $D_y^{-5/2}$. Probably another electrostatic torque, which I have not yet understood and modelled but which is maybe due to trapped charges, is responsible of the measured characteristics of the k_1 amplitude. This signal was specifically associated with test mass A because the k_1 amplitude was not detected above the noise level during the II run, when we substituted mass A with the improved mass B. With the II run we proved that we were able to effectively reduce the size of the spurious signals by improving the quality of the test masses. However the reduced signals were more difficult to characterise as they approached the torque noise level. During the II run we were still able

to excite the electrostatic torque due to the surface periodic corrugations. The amplitude of the corrugation was $\approx 0.4\mu m$. We did not confirm the presence of the magnetic torque, which was found during the I run, or clearly established the dependence of the measured signals on the distance, D_y, between the masses.

Given the measured spurious signals and torque noise of the SSTB, which were measured during this preliminary tests of the ISL of gravity, we did not explore new parameter areas describing possible Yukawa type deviations of Newton's law. However these preliminary tests and the theoretical analysis of the expected forces were extremely useful. Thanks to them I can establish which are the improvements to the masses and to the balance, which are necessary to explore the expected ISL violations of gravity at micrometre distances with future experiments. The first improvement which has to be addressed is the enhancement of the torque sensitivity of the SSTB. We need a reduction of the torque noise level of the SSTB to properly characterise the torque signals from the masses B and C and, if possible, to fit them out of the data as done for the I run.

The biggest gain will come from a new electroformed copper float with niobium sputtered on its inside. The new float would reduce both the coupling with the ground tilt noise and the residual torque acting on the float. Therefore with the new float we would be able to choose a longer natural period for the SSTB and decrease the effect of the readout noise on the torque noise. The new float has to be left untouched without any windows and it should be magnetically actuated otherwise with a superconducting insert or with external superconducting plates. The lack of any window cuts on the float shell will isolate the test masses from the magnetic fields of the levitation and actuation coils.

A low frequency tilt meter can be used to characterise the tilt spectrum of laboratory ground and to confirm the tilt seismic noise as the actual noise source which limits the torque sensitivity of the SSTB. Moreover the tilt meter should be included in an active isolation system to actively reduce the ground tilt which is acting on the float.

To reduce magnetic fluxes, which might be trapped within the float shell, a lifting and heating device based on a Attocube can be used to lift the float and thermally cycle it before activating the levitation field.

The optical interferometric readout, which we are developing within our group [62], should be used in place of the capacitive readout to further reduce the readout noise and the associated torque noise. The optical readout will also

greatly simplify the calibration protocol of the SSTB, because we will be able to apply voltages to the float while in the same time accurately read out its angular position.

It will be also very useful to adopt a cryocooler to increase the duty cycle of the SSTB and reduce the time spent for its calibration with respect to the time dedicated to the torque measurement. To reduce the spurious forces, we measured, we have to ensure that no magnetic tools are used during the manufacture and polishing process of the test masses. An additional Attocube micropositioner has to be adopted to compensate for the misalignment angle between the direction of motion of the flat mass and its surface.

We will have to adopt a non contact procedure (like optical) to characterise the topographies of the masses and to improve the polishing process of the surfaces such that the standard deviation of their roughness is reduced below a few microns. It is however important to leave some periodic surface corrugations on the masses. Such periodic corrugations had been proven to be very useful to estimate the phase of the signals which cannot be measured otherwise. The torque, which is given by the periodic corrugation, and a voltage applied to the masses can also be used to measure the distance between the masses, without letting them to touch.

It will be very useful to study a new manufacturing process and produce new masses with much smaller pitch, down to tens of microns or even less. These new masses will let us explore possible Yukawa violations of Newton's law at even smaller ranges with respect to the masses we manufactured so far.

Bibliography

[1] Adelberger, E. G. and B. R. Heckel. "Test of the gravitational inverse-square law," *Annu. Rev. Nucl. Part. Sci*, *53*:77–121 (2003).

[2] Adelberger, E. G., et al. "Particle-physics implications of a recent test of the gravitational inverse-square law," *Physical Review Letters*, *98*(13) (2007). 131104.

[3] Aitchison, I. J. R. and Anthony J. G. Hey. *Gauge theories in particle physics. : From Relativistic Quantum Mechanics to QED* (3rd Edition). Graduate student series in physics, Bristol: IoP, 2003.

[4] Antoniadis, I., et al. "New dimensions at a millimeter to a fermi and superstrings at a TeV," *Physics Letters B*, *436*(3-4):257–263 (1998).

[5] Arfken, G. B. and H. J. Weber. *Methematical methods for physicists* (5th Edition). London: Academic Press, 2001.

[6] Arkani-Hamed, N., et al. "The hierarchy problem and new dimensions at a millimeter," *Physics Letters B*, *429*(3-4):263–272 (1998).

[7] Arkani-Hamed, N., et al. "Large new dimensions and quantum gravity around the corner," *Comptes Rendus Physique*, *4*(3):347–354 (2003).

[8] Beane, S. R. "On the importance of testing gravity at distances less that 1cm," *General Relativity and Gravitation*, *29*(8):945–951 (1997).

[9] Beccaria, M., et al. "Relevance of Newtonian seismic noise for the VIRGO interferometer sensitivity," *Classical and Quantum Gravity*, *15*(11):3339–3362 (1998).

[10] Bennett, C. L., et al. "First-year Wilkinson Microwave Anisotropy Probe (WMAP) observations: Preliminary maps and basic results," *Astrophysical Journal Supplement Series*, *148*(1):1–27 (2003).

[11] Berger, J., et al. "Ambient Earth noise: A survey of the Global Seismographic Network," *Journal of Geophysical Research-Solid Earth*, *109*(B11) (2004). B11307.

[12] Blocki, J., et al. "Proximity Forces," *Annals of Physics*, *105*(2):427–462 (1977).

[13] Bordag, M., et al. "New developments in the Casimir effect," *Physics Reports-Review Section of Physics Letters*, *353*(1-3):1–205 (2001).

[14] Burgess, C. P. "Towards a natural theory of dark energy: Supersymmetric large extra dimensions." *New Cosmology 743*. Aip Conference Proceedings, edited by R. E. Allen, et al., 417–449, 2004. Conference on Strings and Cosmology MAR 14-17, 2004 Coll Stn, TX.

[15] Carroll, S. M., et al. "The Cosmological Constant," *Annual Review of Astronomy and Astrophysics*, *30*:499–542 (1992).

[16] Carroll, Sean M. "The Cosmological Constant," *Living Reviews in Relativity*, *4*(1) (2001).

[17] Carusotto, I., et al. "Sensitive measurement of forces at the micron scale using bloch oscillations of ultracold atoms," *Physical Review Letters*, *95*(9) (2005). 093202.

[18] Casimir, H.B.G. "On the attraction between two perfectly conducting plates," *Proc. Kon. Ned. Akad.*, *51*:793Ð795 (1948).

[19] C.C.Speake, "Ellipticity of float and torques due to horizontal ground vibrations," 2007. Internal note.

[20] Chang, C.C. *Development of an accelerpmeter for a space-born gravitational wave detector*. PhD dissertation, University of Birmingham, 2002.

[21] Chen, F., et al. "Demonstration of the lateral Casimir force," *Physical Review Letters*, *88*(10) (2002). 101801.

[22] Chiaverini, J., et al. "New experimental constraints on non-Newtonian forces below 100 microns," *Physical Review Letters*, *90*(15) (2003). 151101.

[23] Craik, D. *Magnetism: Principles and Applications*. John Wiley and Sons, 1997.

[24] Dimopoulos, S. and G. F. Giudice. "Macroscopic forces from supersymmetry," *Physics Letters B*, *379*(1-4):105–114 (1996).

[25] Dimopoulos, Savas and Andrew A. Geraci. "Probing submicron forces by interferometry of Bose-Einstein condensed atoms," *Physical Review D*, *68*(12):124021 (2003).

[26] Ferrari, G., et al. "Long-lived Bloch oscillations with bosonic Sr atoms and application to gravity measurement at the micrometer scale," *Physical Review Letters*, *97*(6) (2006).

[27] Giudice, G. F., et al. "Quantum gravity and extra dimensions at high-energy colliders," *Nuclear Physics B*, *544*(1-2):3–38 (1999).

[28] Grant, I. S. and W. R. Phillips. *Electromagnetism*. The Manchester physics series, Chichester: Wiley, 1991.

[29] Haiberger, L., et al. "Highly sensitive silicon crystal torque sensor operating at the thermal noise limit," *Review of Scientific Instruments*, *78*(2) (2007). 025101.

[30] Haiberger, L., et al. "An Experiment to Detect Gravity at Sub-mm Scale with High-Q Mechanical Oscillators." *The Tenth Marcel Grossmann Meeting. On recent developments in theoretical and experimental general relativity, gravitation and relativistic field theories*, edited by M. Novello, et al. 2005.

[31] Hammond, G. D., 2007. Private communication.

[32] Hammond, G. D., et al. "Novel torsion balance based on a spherical superconducting suspension," *Review of Scientific Instruments*, *75*(4):955–961 (2004).

[33] Hammond, G. D., et al. "Development of a second generation torsion balance based on a spherical superconducting suspension," *Review of Scientific Instruments*, *79*(2) (2008). 025103.

[34] Hammond, G. D., et al. "New constraints on short-range forces coupling mass to intrinsic spin," *Physical Review Letters*, *98*(8) (2007).

[35] Hammond, G.D. *Development of a spherical superconducting torsion balance for weak force physics*. PhD Thesis, University of Birmingham, 1999.

[36] Hand, Louis N. and Janet D. Finch. *Analytical Mechanics*. Cambridge University Press, 1998.

[37] Hannestad, S. and G. G. Raffelt. "Stringent neutron-star limits on large extra dimensions," *Physical Review Letters*, *88*(7) (2002). 071301.

[38] Harber, D. M., et al. "Measurement of the Casimir-Polder force through center-of-mass oscillations of a Bose-Einstein condensate," *Physical Review A*, *72*(3) (2005). 033610.

[39] Harris, BW, et al. "Precision measurement of the Casimir force using gold surfaces," *Physical Review A*, *62*(5) (2000). 052109.

[40] Hoyle, C. D., et al. "Submillimeter tests of the gravitational inverse-square law," *Physical Review D*, *70*(4) (2004). 042004.

[41] Jackson, J. D. *Classical Electrodynamics*. John Wiley and Sons, 1998.

[42] Jackson, R. G. *Novel sensors and sensing*. Sensors series, Bristol: Institute of Physics Pub., 2004.

[43] Kapner, D. J., et al. "Tests of the gravitational inverse-square law below the dark-energy length scale," *Physical Review Letters*, *98*(2) (2007). 021101.

[44] Kehagias, A. and K. Sfetsos. "Deviations from the 1/r(2) Newton law due to extra dimensions," *Physics Letters B*, *472*(1-2):39–44 (2000).

[45] Kittel, C. *Introduction to solid state physics* (8th Edition). John Wiley and Sons, 2005.

[46] Klimchitskaya, G. L., et al. "Casimir and van der Waals forces between two plates or a sphere (lens) above a plate made of real metals," *Physical Review A*, *6106*(6) (2000). 062107.

[47] Lamoreaux, S. K. "Demonstration of the casimir force in the 0.6 to 6 microns range," *Physical Review Letters*, *78*(1):5–8 (1997).

[48] Landau, L. D., et al. *Statistical physics* (3rd Edition). Oxford: Butterworth-Heinemann, 1980.

[49] Lide, David R. *CRC handbook of chemistry and physics : a ready-reference book of chemical and phyical data* (85th Edition). Boca Raton, Fla. ; London: CRC Press, 2004. p2209.

[50] Long, J. C., et al., "New Experimental limits on Macroscopic Forces below 100 Microns," 11 Mar 2003.

[51] Long, J. C., et al. "Upper limits to submillimetre-range forces from extra space-time dimensions," *Nature*, *421*(6926):922–925 (2003).

[52] Long, J. C. and J. C. Price. "Current short-range tests of the gravitational inverse square law," *Comptes Rendus Physique*, *4*(3):337–346 (2003).

[53] Luiten, A. N., et al. "Ground tilt seismic spectrum measured with a new high sensitivity rotational accelerometer," *Review of Scientific Instruments*, *68*(4):1889–1893 (1997).

[54] Lykken, J. D. "Weak scale superstrings," *Physical Review D*, *54*(6):R3693–R3697 (1996).

[55] Macmillan, W. D. *Theory of the Potential*. Dover Books, 1958.

[56] McNamara, D. E. and R. P. Buland. "Ambient noise levels in the continental United States," *Bulletin of the Seismological Society of America*, *94*(4):1517–1527 (2004).

[57] Milonni, Peter W. *The quantum vacuum : an introduction to quantum electrodynamics*. Boston, Mass. ; London: Academic Press, 1994.

[58] Mostepanenko, Vladimir Mikhaiĭălovich and N. N. Trunov. *Casimir effect and its applications*. Oxford science publications., Oxford: Clarendon, 1997. Translated from the Russian.

[59] Mota, D. F. and D. J. Shaw. "Strongly coupled chameleon fields: New horizons in scalar field theory," *Physical Review Letters*, *97*(15) (2006). 151102.

[60] Paik, H. J., et al. "Short-range inverse-square law experiment in space," *General Relativity and Gravitation*, *36*(3):523–537 (2004).

[61] Peebles, P.Z.Jr. *Probability, random variables and random signal principles* (2nd Edition). electrical engineering, communication and information theory, McGraw Hill, 1987.

[62] Pena-Arellano, Fabian. *Characterization of homodyne polarization interferometers*. PhD dissertation, University of Birmingham, 2008.

[63] Perlmutter, S., et al. "Measurements of Omega and Lambda from 42 high-redshift supernovae," *Astrophysical Journal*, *517*(2):565–586 (1999). Part 1.

[64] Riess, A. G., et al. "Observational evidence from supernovae for an accelerating universe and a cosmological constant," *Astronomical Journal*, *116*(3):1009–1038 (1998).

[65] Rose-Innes, A. C. *Introduction to superconductivity*, *vol.6*. International series in solid state physics. Pergamon, 1978.

[66] routines, NAG Fortran, "http://www.nag.co.uk."

[67] Rovelli, Carlo. *Quantum gravity*. Cambridge monographs on mathematical physics, Cambridge: Cambridge University Press, 2007.

[68] Sarkar, S. "Is the evidence for dark energy secure?," *General Relativity and Gravitation*, *40*(2-3):269–284 (2008).

[69] Savitzky, A. and M. J. E. Golay. "Smoothing + Differentiation of Data by Simplified Least Squares Procedures," *Analytical Chemistry*, *36*(8):1627 (1964).

[70] Schwarz, John H., "Introduction to Superstring Theory," 2000. Lectures presented at the St. Croix NATO Advanced Study Institute on Techniques and Concepts of High Energy Physics.

[71] Smullin, S. J., et al. "Constraints on Yukawa-type deviations from Newtonian gravity at 20 microns," *Physical Review D*, *72*(12) (2005). 122001.

[72] Smythe, W.R. *Static and dynamic electricity* (3rd Edition). International series in pure and applied physics, New York Toronto London: McGraw Hill Book Company Inc., 1968.

[73] Speake, C. C., "Calculation of the caracteristics of a sperical superconducting magnet bearing," 1993.

[74] Speake, C. C., "Forces due to magnetic susceptibility," 2007. Internal note.

[75] Speake, C. C. and G. T. Gillies. "Why Is G the Least Precisely Known Physical Constant," *Zeitschrift Fur Naturforschung Section a-a Journal of Physical Sciences*, *42*(7):663–669 (1987).

[76] Speake, C. C., et al. "The feasibility of testing the inverse square law of gravitation at Newtonian strength and at mass separations of 1 microns," *General Relativity and Gravitation*, *36*(3):503–521 (2004).

[77] Speake, C. C. and C. Trenkel. "Forces between conducting surfaces due to spatial variations of surface potential," *Physical Review Letters*, *90*(16) (2003).

[78] Speake, C. C., et al. "Force and force gradients due to trapped-flux in superconducting accelerometers," *Advances in Space Research*, *32*(7):1345–1350 (2003).

[79] Spergel, D. N., et al. "Three-year Wilkinson Microwave Anisotropy Probe (WMAP) observations: Implications for cosmology," *Astrophysical Journal Supplement Series*, *170*(2):377–408 (2007).

[80] Spergel, D. N., et al. "First-year Wilkinson Microwave Anisotropy Probe (WMAP) observations: Determination of cosmological parameters," *Astrophysical Journal Supplement Series*, *148*(1):175–194 (2003).

[81] Stefani, R.T., et al. *Design of feedback control systems* (4th Edition). The Oxford series in electrical and computer engineering, Oxford: Oxford University Press, 2002.

[82] Sundrum, R. "Fat gravitons, the cosmological constant and submillimeter tests," *Physical Review D*, *69*(4) (2004). 044014.

[83] Tan, Li and Jean Jiang. *Fundamentals of Analog and Digital Signal Processing*. Authorhouse, 2007. pag. 203.

[84] Trenkel, C. *Development of a superconducting torsion balance designed to search for a new short-range force coupling quantum mechanical spin and matter.*. PhD Thesis, University of Birmingham, 1997.

[85] Trenkel, C. and C. C. Speake. "Geometrical optimization of superconducting levitation systems based on the complete Meissner effect," *Classical and Quantum Gravity*, *13*(11A):A299–A309 (1996). Suppl. S.

[86] Tu, L. C., et al. "Null test of Newtonian inverse-square law at submillimeter range with a dual-modulation torsion pendulum," *Physical Review Letters*, *98*(20) (2007). 201101.

[87] Vasilescu, Gabriel. *Electronic noise and interfering signals : principles and applications*. Signals and communications technology, Springer, 2004.

[88] Webster, John G. *The measurement, instrumentation, and sensors handbook*. The electrical engineering handbook series, Boca Raton, Fla.: CRC Press, 1999.

[89] Weinberg, S. "The Cosmological Constant Problem," *Reviews of Modern Physics*, *61*(1):1–22 (1989).

[90] White, Guy K. and Philip J. Meeson. *Experimental techniques in low-temperature physics* (4th Edition). Monographs on the physics and chemistry of materials, Oxford: Clarendon, 2002.

[91] Will, M. Clifford. "The Confrontation between General Relativity and Experiment," *Living Reviews in Relativity*, *9*(3) (2006).

[92] Wolf, P., et al. "From optical lattice clocks to the measurement of forces in the Casimir regime," *Physical Review A*, *75*(6) (2007). 063608.

[93] Yao, W. M., et al. "Review of particle physics," *Journal of Physics G-Nuclear and Particle Physics*, *33*(1) (2006).

Appendix A

Integration of the Newtonian potential

In this appendix I gives some more details about the integration of eq.3.21 to obtain eq.3.22 describing the gravitational potential between the curved and flat test mass. I here rewrite eq.3.21 as:

$$\Phi(d_x,d_y)=-2\pi G(\rho_1-\rho_2)\int_{-W/2}^{W/2}\int_{-\Theta}^{\Theta}\int_{\frac{R\theta^2}{2}}^{L_y+\frac{R\theta^2}{2}}\int_{0}^{L_y}R\cos\theta[-\frac{W}{\Lambda}(d_y+y_b+y_r)+$$

$$+\frac{\Lambda}{\pi^2}\sum_{n=1}^{K}\frac{\sin(\frac{n\pi W}{\Lambda})}{n^2}\cos(\frac{2n\pi}{\Lambda}(x_r+d_x))e^{-\frac{2n\pi}{\Lambda}(d_y+y_b+y_r)}]dy_b dy_r d\theta_r dx_r \qquad (A.1)$$

where y_b and y_r are the variables of integration respectively over the y extension of the flat mass and of the rib, θ_r is the variable of integration over the angular extension of the curved rib and x_r over its x extension (see fig.3.2). The result of the integration of the previous equation over on the thickness of the flat mass in the y direction is the expression:

$$\Phi(d_x,d_y)=-2\pi G(\rho_1-\rho_2)\int_{-W/2}^{W/2}\int_{-\Theta}^{\Theta}\int_{\frac{R\theta^2}{2}}^{L_y+\frac{R\theta^2}{2}}R\cos\theta[(-\frac{W}{\Lambda}(\frac{L_y^2}{2}+L_y\cdot(d_y+y^r)))+$$

$$+\sum_{n=1}^{K}\left(\frac{\Lambda}{2n\pi}\right)^2\frac{2\sin(\frac{n\pi W}{\Lambda})}{\pi n}\cos(\frac{2n\pi}{\Lambda}(x_r+d_x))\left(1-e^{-\frac{2\pi nL_y}{\Lambda}}\right)e^{-\frac{2n\pi}{\Lambda}(d_y+y^r)}]dy_r d\theta dx_r \tag{A.2}$$

I exclude therefore the constant term proportional to $WL_y^2/(2\Lambda)$ because it will give origin just to a constant additive term of the potential, which is independent of d_y and d_x. The result of integration over the rib thickness in the y direction is then given by the equation:

$$\Phi(d_x,d_y)=-2\pi G(\rho_1-\rho_2)\int_{-W/2-\Theta}^{W/2}\int^{\Theta}R\cos\theta[-\frac{R\theta^2L_y^3W}{2\Lambda}-\frac{L_y^4W}{2\Lambda}-\frac{L_y^3W}{\Lambda}d_y+$$
$$+\sum_{n=1}^{K}\left(\frac{\Lambda}{2n\pi}\right)^3\frac{2\sin(\frac{n\pi W}{\Lambda})}{\pi n}\cos(\frac{2n\pi}{\Lambda}(x_r+d_x))\left(1-e^{-\frac{2\pi nL_y}{\Lambda}}\right)^2e^{-\frac{2n\pi}{\Lambda}(\frac{R\theta^2}{2}+d_y)}]d\theta dx_r \tag{A.3}$$

I exclude again all the constant terms, which are independent of d_y and d_x. Hence I integrate on the angular extension of the rib, obtaining:

$$\Phi(d_x,d_y)=-2\pi G(\rho_1-\rho_2)\int_{-W/2}^{W/2}[-\frac{2RL_y^3W\sin\Theta}{\Lambda}d_y+\sum_{n=1}^{K}\left(\frac{\Lambda}{2n\pi}\right)^3\frac{2\sin(\frac{n\pi W}{\Lambda})}{\pi n}\cdot$$
$$\cdot\cos(\frac{2n\pi}{\Lambda}(x_r+d_x))\left(1-e^{-\frac{2\pi nL_y}{\Lambda}}\right)^2e^{-\frac{2n\pi d_y}{\Lambda}}\sqrt{\frac{\Lambda R}{n}}\,\mathrm{erf}(\sqrt{\frac{n\pi R}{\Lambda}}\Theta)]dx_r \tag{A.4}$$

where $\mathrm{erf}(z)$ is the error function, integral of the Gaussian distribution and is given by the equation:

$$\mathrm{erf}(z)=\frac{2}{\sqrt{\pi}}\int_0^z e^{-t^2}dt \tag{A.5}$$

I finally integrate over the rib thickness in the x direction and find the equation:

$$\Phi(d_x, d_y) = -2\pi G(\rho_1 - \rho_2)[-\frac{2RL_y^3W^2\sin\Theta}{\Lambda}d_y + \sum_{n=1}^{K}\left(\frac{\Lambda}{2n\pi}\right)^4 \frac{\left(2\sin(\frac{n\pi W}{\Lambda})\right)^2}{\pi n}\cdot$$
$$\cdot\cos(\frac{n2\pi}{\Lambda}d_x)\left(1 - e^{-\frac{2\pi n L_y}{\Lambda}}\right)^2 e^{-\frac{2n\pi d_y}{\Lambda}}\sqrt{\frac{\Lambda R}{n}}\,\mathrm{erf}(\sqrt{\frac{n\pi R}{\Lambda}}\Theta)] \qquad (A.6)$$

where I used the trigonometric identity:

$$\sin\alpha - \sin\beta = 2\cos\left(\frac{\alpha-\beta}{2}\right)\sin\left(\frac{\alpha+\beta}{2}\right) \qquad (A.7)$$

Hence I multiply the integral by the mass density contrast $(\rho_1 - \rho_2)$ of the curved mass and the number of ribs L_x/Λ where L_x is the total length of the mass in the x direction, obtaining eq.3.22:

$$\Phi\left(d_x, d_y\right) = -2\pi G(\rho_1 - \rho_2)^2\frac{L_x}{\Lambda}[-\frac{2R\sin\Theta L_y^3W^2d_y}{\Lambda} + \sum_{l=1}^{K}\left(\frac{\Lambda}{2n\pi}\right)^4 \frac{\left(2\sin(\frac{n\pi W}{\Lambda})\right)^2}{n\pi}$$
$$\cdot\cos(\frac{n2\pi}{\Lambda}d_x)\left(1 - e^{-\frac{2\pi n L_y}{\Lambda}}\right)^2 e^{-\frac{2n\pi d_y}{\Lambda}}\sqrt{\frac{\Lambda R}{n}}\,\mathrm{erf}(\sqrt{\frac{n\pi R}{\Lambda}}\Theta)] \qquad (A.8)$$

Appendix B

Dia-paramagnetic torque

For completeness we report here the analysis of [74] about the expected magnetic torques due to the contrast in magnetic susceptibilities between the gold and aluminium stripes and to the presence of a magnetic field B_0 perpendicular to the mass surface (see fig.3.18). According to [78] the energy density for unit area of a parallel plane configuration is given by the equation:

$$E_{pp} = \frac{1}{\mu_0} \iint \frac{1}{(2\pi/\Lambda)\sinh(2\pi/\Lambda a)} \tilde{C}_{12}(k) e^{ik\xi} \frac{d^2k}{(2\pi)^2} \tag{B.1}$$

with $\tilde{C}_{12}(k)$ the Fourier transform of the 2-d cross correlation function per unit of area of the B-fields, B_m, measured at the surfaces of the masses. If the masses are in an uniform background magnetic field, $\vec{B}_0$, the bulk of the masses will be polarised and have magnetisation field:

$$\vec{M} = \frac{\chi}{1+\chi} \vec{B}_0 \tag{B.2}$$

At the surface of the masses the magnetisation gives origin to the field H:

$$\vec{B} = \mu_0 \left(\vec{M} + \vec{H} \right) \tag{B.3}$$

For the continuity of the magnetic fields B at the surfaces we have $\vec{H} = -\vec{M}$. Hence the expected value of B at the surfaces of the masses is given by the equation:

$$\vec{B}_m(x) = -\mu_0 \frac{\chi(x)}{1+\chi(x)} \vec{B}_0 \tag{B.4}$$

$$\approx -\mu_0 \chi(x) \vec{B}_0 \tag{B.5}$$

If the susceptibility contrast depends just on x and not on z we have that:

$$E_{pp} = \frac{1}{\mu_0} \frac{C_{12}(d_x)}{2\pi/\Lambda \sinh(2\pi/\Lambda a)} \tag{B.6}$$

with

$$C_{12}(d_x) = \frac{1}{L_x} \int_0^{L_x} \vec{B}_{m1}(x) \vec{B}_{m2}(x - d_x) dx \tag{B.7}$$

If we assume also the susceptibility contrasts are sin functions of x with amplitude $\Delta\chi/2$ given by the equations:

$$\vec{B}_{m1}(x) = \mu_0 \frac{\Delta\chi}{2} \sin(2\pi/\Lambda x) \vec{B}_0 \tag{B.8}$$

$$\vec{B}_{m2}(x - d_x) = -\mu_0 \frac{\Delta\chi}{2} \sin(2\pi/\Lambda (x - d_x)) \vec{B}_0 \tag{B.9}$$

The total energy integrated over all curved surface is therefore given by the equation:

$$E_{pp} = -\frac{L_x \Delta\chi^2 B_0^2}{8\mu_0} \frac{\cos(2\pi/\Lambda d_x)}{2\pi/\Lambda} \int_{-Lz/2}^{Lz/2} \frac{dz}{\sinh(2\pi/\Lambda (d_y + z^2/(2R)))} \tag{B.10}$$

The force acting between the masses is therefore given by the expression:

$$F_{\Delta\chi} \approx -\frac{(\Delta\chi B_0)^2 L_x}{8\mu_0} \sin(2\pi/\Lambda d_x) \int_{-Lz/2}^{Lz/2} \frac{dz}{\sinh(2\pi/\Lambda (d_y + z^2/(2R)))} \tag{B.11}$$

from which we obtain the torque given by eq.3.72.

Appendix C

The capacitive bridge: transfer function and noise analysis

To model the output current of the capacitive bridge to the input of the pre-amplifier, I write its mesh equations [20], [34] (see fig.C.1). Supposing that the coupling between Is_1 and Is_2 is negligible and that $L_1 = L_2 = L_3 = L$, the mesh equations describing the capacitive bridge are the following ones:

$$I_p i\omega L - i\omega M I_{s1} + i\omega I_{s2} = V_0 \tag{C.1}$$

$$-i\omega M I_p + I_{s1}\left(\frac{1}{i\omega C_1} + i\omega L\right) - I_{s2} i\omega M = 0 \tag{C.2}$$

$$i\omega M I_p - I_{s1} i\omega M + I_{s2}\left(\frac{1}{i\omega C_2} + i\omega L\right) = 0 \tag{C.3}$$

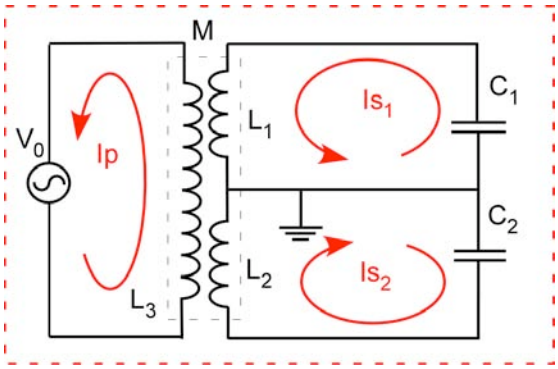

Figure C.1: Capacitor bridge in the measurement configuration.

The previous system when solved will give the solution for I_{s1} and I_{s2} whose sum is given by the simple formula:

$$I_s = I_{s1} + I_{s2} = i\Delta C\omega V_0 \tag{C.4}$$

with $\Delta C = C_1 - C_2$.

The pre amplification stage of the measurement mode is given by a charge amplifier (see fig.6.3) whose voltage output can be written as [88]:

$$V_{out} = -Z_f I_s \tag{C.5}$$

with Z_f the impedance of the feedback line given by the parallel impedance of C_f and R_f. $|V_{out}|$ is given by the equation

$$|V_{out}| = \frac{R_f}{\sqrt{1+\omega^2 R_f^2 C_f^2}} I_s \tag{C.6}$$

By substituting I_s with eq.C.4 I find:

$$\left|\frac{dV_{out}}{d\Delta C}\right|_{meas.} = \frac{R_f}{\sqrt{1+\omega_0^2 R_f^2 C_f^2}} \omega_0 V_0 \tag{C.7}$$

Thanks to the Norton theorem the capacitive bridge of the measurement mode can be modelled as an ideal current source, I_s, in parallel with an output impedance Z_s which is approximated by the equation:

$$Z_s \approx \frac{1}{i\omega(C_1 + C_2)} \tag{C.8}$$

The noise model for the amplification stage is shown in fig.C.2 where four noise sources have been considered [87]: the voltage (E_n) and current noise (I_n) source of the op-amp AD745 and the voltage Johnson noise sources (V_{nf} and V_{np}) of the resistances, R_f and R_p. C_{coax} is the capacitance to ground of the coaxial cable connecting the float to the pre amplifier input. Assuming that the compensation impedance is chosen to minimize the effect of the bias current and that all the mentioned noise sources are not correlated, the voltage noise at the output V_{nout} is given by the following formula [87]:

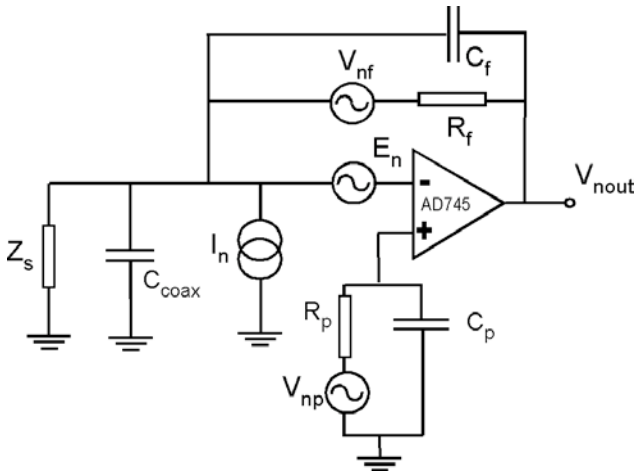

Figure C.2: Noise model for the amplifier in the masurement mode.

$$V_{nout} = \sqrt{(I_n Z_f)^2 + \left(\frac{V_{nf}}{\sqrt{1+(\omega R_f C_f)^2}}\right)^2 + (E_n G_{ninv})^2 + \left(\frac{V_{np} G_{ninv}}{\sqrt{1+(\omega R_p C_p)^2}}\right)^2} \tag{C.9}$$

The amplitude spectrum densities of the Johnson voltage noises, V_{nf} and V_{np}, are given as white noise level as $V/\sqrt{Hz}$ by the equations [87]:

$$V_{np} = \sqrt{4K_B T R_p} \tag{C.10}$$

$$V_{nf} = \sqrt{4K_B T R_f} \tag{C.11}$$

with K_B the Boltzman constant and T the ambient temperature of the amplifier. If Z_{in} is the input impedance of the pre amplifier, which is given by the parallel impedance of Z_s and C_{coax}, the not inverting gain, G_{ninv}, is given by the equation:

$$G_{ninv} = 1 + \frac{Z_f}{Z_{in}} \tag{C.12}$$

$$= 1 + \frac{i\omega R_f C_{coax}}{1 + i\omega C_f R_f} \tag{C.13}$$

$$\approx 1 + \frac{C_{coax}}{C_f} \tag{C.14}$$

Noise source	**Output Voltage noise** $(nV/\sqrt{Hz})$
I_n	1.5
E_n	118
R_p	30
R_f	23
Total	124

Table C.1: Table of the contribution to the output voltage noise of the pre amplifier of the capacitive sensor.

where the last equation as been obtained in the limit of $\omega \gg 1/C_f R_f$.

In the measurement mode the adopted operational amplifier AD745 has current noise $I_n = 6.9fA/\sqrt{Hz}$ and voltage noise $E_n \approx 2.9nV/\sqrt{Hz}$ at $70kHz$. The capacitance to the ground C_{coax} was measured to be $C_{coax} = 400pF$ and the operational amplifier has $R_p = 1.5M\Omega$ and $C_p = 0.33nF$ (see fig.6.3). The working temperature is the room temperature one $T = 293K$. In the table C.1 I report the output noise contribution for each element according of the predictions of the eq.C.9.

The actual noise level predicted for the amplifier output is given mainly by the voltage noise of the op-amp which is amplified due to the high capacitance to ground of the coaxial bringing the current from the float to the amplifier input. This noise has to be summed in quadrature with the measured input noise of our lock-in amplifier $\approx 200nV/\sqrt{Hz}$ to obtain the total lock-in input noise.

Appendix D

General transfer function for a servo loop

The demonstration of eq.6.48 is quite straightforward. From fig.6.14 I can write that:

$$Y_j = \prod^{1\leq n\leq j} H_n \prod^{i<n\leq N} H_n B \tag{D.1}$$

$$B = \prod^{j<n\leq i} H_n Y_j + R_i \tag{D.2}$$

Hence by substitution of eq.D.2 in eq.D.1

$$Y_j = \frac{\prod^{i<n\leq N} H_n \prod^{1\leq n\leq j} H_n}{1 - \prod^{all} H_n} R_i \tag{D.3}$$

The transfer function between R_i and Y_j is therefore given by the equation

$$T_{CL}(R_i, Y_j) = \frac{Y_j}{R_i} \tag{D.4}$$

$$= \frac{\prod^{i<n\leq j} H_n}{1 - \prod^{all} H_n} \tag{D.5}$$

where $i < n \leq j$ stands for $(i < n \leq N)\&(1 \leq n \leq j)$.